



ALBERT-LUDWIGS-UNIVERSITÄT FREIBURG

FAKULTÄT FÜR DI MATHEMATIK UND PHYSIK

DOCTOR RERUM NATURALIUM

**Higher Order and Heavy Quark Mass Effects
in the Determination of
Parton Distribution Functions**

CANDIDATE:
VALERIO BERTONE

SUPERVISOR:
PROF. DR. JOCHUM J. VAN DER BIJ

COSUPERVISOR:
DR. ALBERTO GUFFANTI

*“Non mi soffermo
sul primo o sul secondo,
indico soltanto l’alternanza”*

Contents

Introduction	v
1 Parton Distribution Functions	1
1.1 The Asymptotic Freedom	1
1.2 The Collinear Factorization	2
1.3 DIS in QCD	3
1.4 The DGLAP Equation	10
1.5 Recent PDF Determinations	12
2 Treatment of Heavy Flavours	15
2.1 FFNS and VFNS	16
2.2 The ACOT Method	20
2.2.1 The S-ACOT Variant	22
2.2.2 The ACOT- χ Variant	23
2.3 The TR Method	24
2.3.1 The TR' Variant	27
2.4 The FONLL Method	28
2.5 The BMSN Method	32
3 Implementation of the FONLL Method	35
3.1 Practical Implementation	35
3.1.1 Light Structure Functions at order α_s^2	39
3.1.2 Perturbative Ordering	41
3.2 Electro-weak Structure Functions	41
3.3 Mellin Space Implementation	45
3.3.1 Splitting Functions	47
3.3.2 Coefficient Functions	50
4 Structure Functions with $\overline{\text{MS}}$ Masses	57
4.1 $\overline{\text{MS}}$ Running Mass vs. Pole Mass	57
4.2 RGE Solution for the $\overline{\text{MS}}$ Running Mass	58
4.3 Matching Conditions	60
4.3.1 Matching of $\alpha_s(\mu)$	60
4.3.2 Matching of $m(\mu)$	61
4.3.3 Matching of the PDFs	61
4.3.4 Benchmark of the Evolution	63

4.4	Structure Functions	63
4.4.1	Neutral Current	63
4.4.2	Charged Current	66
4.4.3	Benchmark of the Structure Functions	66
5	The NNPDF Methodology	67
5.1	Monte Carlo Generation	68
5.2	Neural Networks and Fitting Strategy	70
5.2.1	Neural Network Parametrization	71
5.2.2	Genetic Algorithm Minimization	74
5.2.3	Cross-Validation Method	75
5.3	Statistical Tools	76
6	Impact of Higher Orders and Heavy Flavours on PDFs	79
6.1	Experimental Data	79
6.1.1	Kinematic Cuts	79
6.1.2	The Dataset	80
6.1.3	Positivity constraints	80
6.1.4	Treatment of Hadronic Data	83
6.2	Results	84
6.2.1	Impact of the Higher Order Corrections	85
6.2.2	Impact of the Heavy Flavour Corrections	88
6.2.3	Impact of the Threshold Prescription	96
6.3	LHC Phenomenology	98
7	Summary and Conclusions	103
A	Massive Coefficient Functions Mellin Transform	107
A.1	NC Processes	107
A.1.1	Order α_s	107
A.1.2	Order α_s^2	113
A.2	CC Processes	123
B	Mellin Transform of the $\overline{\text{MS}}$ Coefficient Functions	133
B.1	Neutral Current	133
B.1.1	F_2	133
B.1.2	F_L	135
B.2	Charged Current	135
	Acknowledgments	149

Introduction

The formulation of Quantum Chromodynamics (QCD) as a theory to describe the strong interactions was certainly one of the most impressive achievements of Physics in the 20-th century. As a matter of fact, QCD proved to be able to account for a wide variety of observed phenomena. Some of the most famous examples are: confinement [1], hadron spectroscopy [2], asymptotic freedom [3] and Bjorken scaling violation in Deep Inelastic Scattering of leptons and hadrons [4].

Since the establishment of QCD in the early '70s, a huge effort has been devoted to find suitable tools that permit the extraction of quantitative predictions out of it. The non-abelian nature of QCD, and the consequent asymptotic freedom, strongly suggests that perturbation theory could offer a valuable handle for the calculation of the cross sections in the high-energy region where perturbativity is supposed to hold. Nonetheless, perturbativity is not always sufficient. In fact, a more careful analysis of the QCD structure reveals that a general high-energy cross section is a mix of high- and low-energy contributions, and thus is not directly computable in perturbation theory. In practice, it turns out that a direct calculation is affected by infrared (low-energy) divergences.

It should be remarked that the appearance of infrared singularities is a feature of non-inclusive observables. It has been proven that fully inclusive observables without hadrons in the initial state, like for instance e^+e^- annihilation into hadrons, are free of any infrared divergence (KLN-theorem [5, 6]). Therefore in these cases perturbativity alone is enough to perform the calculation. On the other hand, this excludes a widely studied category of observables, namely the hadron-lepton and the hadron-hadron cross sections, which are of extreme interest in the Large Hadron Collider (LHC) era. However, these processes can still be treated in a manner which is reminiscent of the renormalization procedure, and that is based on the concept of collinear factorization. Unfortunately, until now the applicability of the factorization procedure to all orders in perturbation theory has been proven only for a limited number of processes [7]. For the remaining processes, instead, the collinear factorization is simply assumed to hold up to the perturbative order under consideration.

The collinear factorization property of QCD states that any high-energy cross section σ can be systematically separated (factorized) into a high-energy contribution $\hat{\sigma}$ and a low-energy contribution f , according to the formula:

$$\sigma = \hat{\sigma} \otimes f. \tag{1}$$

The infrared singularities that may appear in an explicit perturbative calculation of $\hat{\sigma}$ (coefficient functions) can be factorized out and essentially moved into the low-energy part f . This is similar to what happens in the renormalization procedure, where the

ultraviolet singularities are absorbed into the renormalization constants. In the factorization framework, the role of the renormalization constants is played by the parton distribution functions (PDFs). The essential difference between renormalization constants and PDFs is that, while the former are still computable in perturbation theory, the latter are not. Hence, one is forced to find an alternative way to determine PDFs and, up to now, the by far most efficient method is the extraction from experimental data.

Any PDF determination from experimental data basically proceeds through the fit of eq. (1) to data, where the function f is parametrized by some empirical functional form. Therefore, the reliability of PDFs deeply depends on the accuracy with which coefficient functions $\hat{\sigma}$ have been calculated. As a consequence, a lot of effort has been invested in obtaining as accurate as possible computations. In this context, the inclusion of higher-order perturbative corrections and the formulation of a factorization scheme able to properly account for the heavy quark mass effects were certainly two of the main guidelines.

The importance of having precise PDF sets at one's disposal is manifest in the present historical moment. In fact, PDFs are one of the dominant sources of systematic uncertainty in many of the LHC cross section measurements relevant for Standard Model precision physics, Higgs boson characterization and new physics searches. In parallel, the copious amount of precise measurements coming from the LHC itself will certainly lead to a substantial improvement in the determination of PDFs.

This thesis is mainly concerned with the effects of the inclusion of the heavy quark mass contributions in PDF determinations up to the highest possible perturbative order. The more general scope is to obtain a PDF set which combines the most up to date available data with the most precise calculations. To this end a wide dataset, ranging from Deep-Inelastic-Scattering (DIS) data to the most recent LHC data, has been fitted using a theoretical framework where heavy quark mass effects are consistently included up to next-to-next-to-leading order. This resulted in the arguably most accurate PDF set currently available: the NNPDF2.3 set.

This thesis is organized as follows. In the first chapter the concept of PDF will be introduced in the context of QCD. Considering the DIS process at next-to-leading order, it will be shown how the presence of PDFs is needed to reabsorb the infrared divergences that arise in the calculation. Such a procedure will finally lead to the formulation of the DGLAP equation which is one of the basic ingredients for a PDF determination.

In the second chapter a general overview of the presently available factorization schemes commonly used in DIS to include heavy quark mass effects in PDF fits is presented. The main features, and the possible variants, of each scheme will be discussed showing how they behave in the low- and high-energy regions.

In the third chapter the implementation of the FONLL method (already introduced in Chapter 2) up to order α_s^2 (being α_s the strong coupling) will be described thoroughly. This will go through the precise definition of heavy and light structure functions for both neutral-current (NC) and charged-current (CC) processes. In addition, the Mellin space formalism, which is used for the implementation of the FONLL method presented in this thesis, will be introduced. In the last part of the chapter a benchmark of the implementation of the structure functions will also be presented.

In the fourth chapter a detailed description of the implementation of the heavy

quark masses in the $\overline{\text{MS}}$ renormalization scheme for the DIS structure functions will be illustrated and benchmarked. The implementation of the $\overline{\text{MS}}$ scheme for the heavy quark masses, as compared to the more common pole mass scheme, requires two main modifications: the consistent replacement of the pole masses with the respective $\overline{\text{MS}}$ masses in coefficient functions and the modification of the PDF matching at the heavy quark thresholds. Both the NC and CC cases are considered here.

The implementation of the FONLL method to extract PDFs has been performed in the NNPDF framework. In the fifth chapter the main features of the NNPDF methodology as a framework for the determination of PDFs will be summarized.

Finally, in the sixth chapter, the results obtained from the implementation of the FONLL scheme up to next-to-next-to-leading order in the NNPDF framework to obtain the proton PDFs will be presented. After a brief description of the dataset included in the fits, the impact of the higher-order corrections and of the heavy quark mass effects will be assessed. Thereafter, a short discussion on some of the implication on the LHC phenomenology will be presented and, at the end, a brief comparison to the other PDF sets presently available will be given.

Chapter 1

Parton Distribution Functions

The main goal of this Chapter is the introduction of the concept of Parton Distribution Function (PDF) in the context of the Quantum-Chromodynamics (QCD). This in particular will lead to the formulation of the DGLAP equation which is one of the most important ingredient of the present PDF determinations.

The Deep-Inelastic-Scattering (DIS) context is doubtless the most suitable playground where to discuss such concepts. In fact, DIS is one of the few processes for which the all-order factorization theorem has been proved [7], therefore it provides a well-established framework. In addition, DIS data are still massively used in the determination of the PDFs.

The so-called “naive” parton model, proposed by Feynman in the late '60s [8], regards hadrons (*e.g.* protons) as composed of point-like constituents, named *partons*, from which any incoming particle scatters *instantaneously* and *incoherently*. Such a simple model, applied immediately after to DIS [9], was able to predict the (approximate) Bjorken scaling of the structure functions, that not much later was experimentally observed. In addition the verification of the *Callan-Gross* relation, derived in the same context, ascertained the spin- $\frac{1}{2}$ property of the partons [10]. As a “byproduct”, the idea of PDF $f_i(\xi)$ was also introduced, $f_i(\xi)d\xi$ being the probability that the parton type i carries a momentum fraction of the hadron between ξ and $\xi + d\xi$. It should be stressed here that, in the naive parton model, the PDFs have a purely probabilistic interpretation.

The naive parton model existed before the invention of QCD. Once the QCD was invented [11], it was straightforward to match partons to quarks and gluons, giving the parton model a solid theoretical foundation. In particular, it was found that the naive parton model is the leading-order (LO) approximation of QCD. Higher-order corrections to DIS were soon calculated and this resulted in one of the most impressive achievements of QCD: the prediction of the so-called *Bjorken scaling violation* that later was experimentally observed in DIS. This striking success is based on two main features of QCD: the *asymptotic freedom* and the *collinear factorization*.

1.1 The Asymptotic Freedom

Asymptotic freedom [4] is a property of QCD according to which the coupling α_s between constituents becomes asymptotically weaker as the energy Q at which the “matter” is

probed increases. At LO in perturbation theory the equation for the evolution of α_s (running) is given by:

$$Q^2 \frac{\partial \alpha_s}{\partial Q^2} = \beta_0 \alpha_s^2 + \mathcal{O}(\alpha_s^3), \quad (1.1)$$

with:

$$\beta_0 = \frac{1}{6\pi} N_f - \frac{11}{12\pi} C_A, \quad (1.2)$$

being N_f is the number of quark flavours and $C_A = 3$ one of the $SU(3)$ color factors. The second term on the r.h.s. of eq. (1.2) is a consequence of the “non-abelianity” of QCD (gauge group $SU(3)$) which gives rise to gluon self-interaction diagrams. It is evident that this *negative* contribution is dominant if $N_f \leq 16$. In QCD this is always the case, therefore, while $\beta_0 < 0$, eq. (1.1) states that α_s is a decreasing function of Q or, in other words, that QCD is asymptotically free. The asymptotic freedom is an extremely important feature of QCD because, for Q sufficiently large, the coupling constant α_s is small enough to allow the use of perturbation theory.

A rough estimate of the minimal energy where perturbation theory is still applicable can be obtained considering the “experimental” value of $\Lambda_{\text{QCD}} \simeq 200$ MeV which is, by definition, the energy where the coupling constant α_s diverges. Given that for $Q \rightarrow \Lambda_{\text{QCD}} \Rightarrow \alpha_s \rightarrow \infty$, the requirement for perturbativity $\alpha_s \ll 1$ to be applicable leads to $Q \gg \Lambda_{\text{QCD}}$. More quantitatively, for $Q \simeq 2$ GeV, $\alpha_s(Q) \simeq 0.3$ which is already a small enough value to use perturbation theory.

1.2 The Collinear Factorization

The collinear factorization is a very central ingredient in the definition of PDFs.

As discussed in Ref. [7], order by order in a perturbative expansion, any physical quantity in QCD is a combination of low- and high-energy contributions, and hence, due to the presence of the low-energy part, it is not computable directly in perturbation theory. This is the basic statement of the *factorization theorem*. There are actually exceptions to this rule. These are inclusive cross sections without hadrons in the initial state, such as the total cross section for e^+e^- annihilation into hadrons, or into jets (infrared safe observables). Nevertheless, this leaves out the majority of experimentally studied processes like lepton-hadron and hadron-hadron cross sections, as well as inclusive cross sections in e^+e^- annihilation with detected hadrons in the final state. The factorization theorem allows to derive predictions for these cross sections, by separating (factorizing) low-energy from high-energy behavior in a systematic fashion. Thus, almost all applications of perturbative QCD use factorization properties of some kind.

The original factorization theorem [7] was based of the assumption that the typical kinematic energy scale of the process Q is much bigger than all the masses involved. However, this assumption is not always valid. Presently, a substantial fraction of the DIS measured cross sections place themselves in a region where the heavy quark masses are not negligible with respect to the scale Q and, *a priori*, the “standard” factorization theorem could be questionable. However, in Ref. [12] a general proof of factorization in DIS including heavy-quark effects to all orders was given, establishing once and for all the validity of the factorization theorem also in the presence of non-negligible heavy

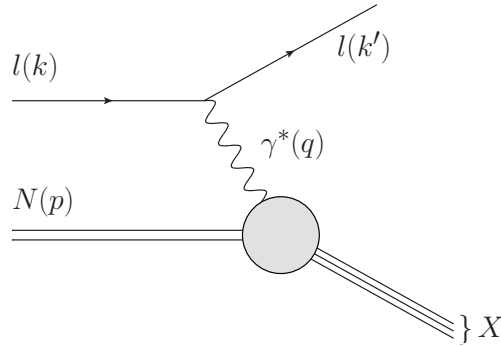


Figure 1.1: Deep inelastic charged lepton-hadron scattering.

quark masses. This is indeed the real theoretical foundation of the so-called general mass factorization schemes extensively discussed in Chapter 2.

In the following a sketchy calculation of the DIS process at next-to-leading-order (NLO) in QCD focusing on the infrared divergences will be presented. This will serve to exhibit the need for factorizing out the initial-state collinear divergences into the PDFs. Such a factorization will in turn result in the appearance of an unphysical factorization scale and in the DGLAP evolution equation for PDFs.

1.3 DIS in QCD

Consider the scattering of a high-energy charged lepton off a hadron target (typically a proton) mediated by the exchange of a virtual (space-like) photon, like in Fig. 1.1. The standard DIS variables commonly used to study this kind of processes are:

$$\begin{aligned}
 \text{Momentum transfer (virtuality):} \quad & Q^2 = -q^2, \\
 \text{Target Mass:} \quad & p^2 = M^2, \\
 \text{Energy transfer:} \quad & \nu = q \cdot p = M(E' - E), \quad (1.3) \\
 \text{Bjorken variable:} \quad & x = \frac{Q^2}{2(p \cdot q)} = \frac{Q^2}{2M(E' - E)}, \\
 \text{Fractional energy transfer (inelasticity):} \quad & y = \frac{q \cdot p}{k \cdot p} = 1 - \frac{E'}{E},
 \end{aligned}$$

where the energy variables on the r.h.s. of eq. (1.3) refer to the target rest frame and serve to give an idea of the physical meaning of the respective variables.

As is well known, the cross section for this process can be factored into a leptonic and a hadronic tensor as:

$$\frac{d^2\sigma}{dx dy} \propto L_{\mu\nu} W^{\mu\nu}. \quad (1.4)$$

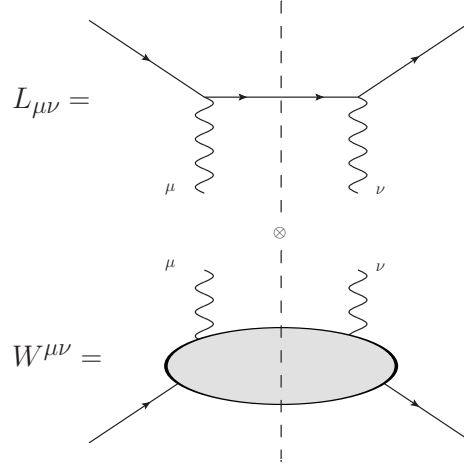


Figure 1.2: Pictorial representation of the factorization of the cross section into a leptonic and a hadronic tensor for a DIS cross section.

This is pictorially illustrated in Fig. 1.2.

The leptonic tensor, assuming photon exchange only, is completely determined by QED and is equal to:

$$L_{\mu\nu} = e^2 \text{Tr}[k' \gamma_\mu k \gamma_\nu] = 4e^2 (k_\mu k'_\nu + k_\nu k'_\mu - g_{\mu\nu} k \cdot k'), \quad (1.5)$$

being e the electric charge of the incoming lepton.

The hadronic tensor, instead, cannot be completely determined. However, requiring the current conservation $q_\mu W^{\mu\nu} = 0$ and the hermiticity $W^{\mu\nu*} = W^{\nu\mu}$, it can be parametrized in terms of two real scalar structure functions F_1 and F_2 that contain all the information about the structure of the hadron as seen by the virtual photon:

$$W^{\mu\nu}(x, Q) = \left(g^{\mu\nu} - \frac{q^\mu q^\nu}{q^2} \right) F_1(x, Q^2) + \frac{1}{\nu} \left(p^\mu + \frac{1}{2x} q^\mu \right) \left(p^\nu + \frac{1}{2x} q^\nu \right) F_2(x, Q^2). \quad (1.6)$$

The contraction of the leptonic tensor in eq. (1.5) with the hadronic tensor in eq. (1.6) gives the scattering cross section in terms of the structure functions F_1 and F_2 .

The question is how to explicitly explicit expressions for the structure functions F_1 and F_2 . At this point let us assume that QCD is at work, *i.e.* the proton is made up of (massless) quarks interacting by means of gluons. This allows to make use of the factorization theorem [7] that states that the generic structure function $F = F_1, F_2$ can be factorized into a low- and a high-energy contribution as follows:

$$\begin{aligned} F(x, Q) &= \sum_{i=q,g} \int_0^1 dy \int_0^1 dz C_i^0(z, Q) f_i^0(y) \delta(x - yz) \\ &= \sum_{i=q,g} \int_x^1 \frac{dy}{y} C_i^0\left(\frac{x}{y}, Q\right) f_i^0(y) = \sum_{i=q,g} \int_x^1 \frac{dz}{z} C_i^0(z, Q) f_i^0\left(\frac{x}{z}\right) \\ &\equiv \sum_{i=q,g} C_i^0(x, Q) \otimes f_i^0(x) = \sum_{i=q,g} f_i^0(x) \otimes C_i^0(x, Q), \end{aligned} \quad (1.7)$$

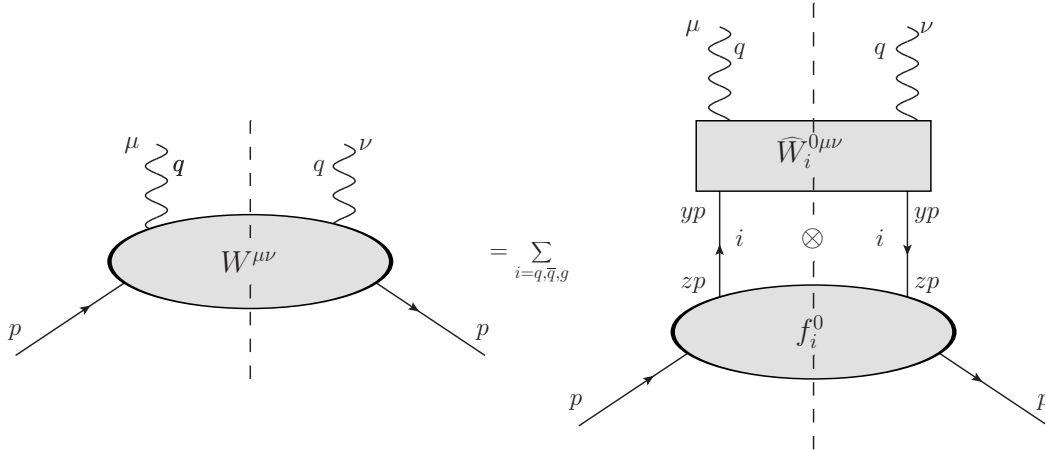


Figure 1.3: Pictorial representation of the factorization of the hadronic tensor into a long- and a short- distance contribution.

where \otimes denotes the Mellin convolution defined as:

$$\begin{aligned}
 f(x) \otimes g(x) &\equiv \int_0^1 dy \int_0^1 dz f(y)g(z)\delta(x - yz) \\
 &= \int_x^1 \frac{dy}{y} f(y)g\left(\frac{x}{y}\right) = \int_x^1 \frac{dz}{z} f\left(\frac{x}{z}\right)g(z).
 \end{aligned} \tag{1.8}$$

In eq. (1.7) C_i^0 are the so-called *coefficient functions* or Wilson coefficients and embody the high-energy contributions and thus, thanks to the QCD asymptotic freedom, they are computable in perturbation theory. The functions f_i^0 , instead, are the PDFs and embody the low-energy contributions. As a consequence, PDFs are non-perturbative quantities. PDFs do not depend on the process under consideration (DIS in the case), but rather they are an “intrinsic” characteristic of the hadron (the proton in this case), while the whole information about the specific process is contained in the coefficient functions C_i^0 . It is this *universality* that the possibility to determine the PDFs of the proton by fitting different categories of data is based on. Fig. 1.3 represents a pictorial representation of the factorization formula in eq. (1.7).

The superscript 0 in the quantities appearing on the r.h.s. of eq. (1.7) denotes the fact that they are “bare” quantities that need to be regularized and eventually renormalized. In fact, when using the perturbation theory to calculate the coefficient functions C_i^0 beyond LO, the result turns out to be divergent. As is well known, there are two different categories of divergences appearing in such a calculation: *ultraviolet* and *infrared*.

The first category of divergences, the ultraviolet ones, arise from the loop contributions and therefore they are explicit divergences of the matrix element associated to the high-energy region. They are treated using the standard procedure, *i.e.* regularizing the divergent integrals, typically using the dimensional regularization, and subtracting the divergences, typically in the $\overline{\text{MS}}$ scheme. This kind of divergences will not be addressed here and the ultraviolet renormalization will be understood in the following.

The infrared divergences, instead, are not originally present in the matrix element but appear only when the integration over the phase-space is performed. Some of the infrared divergences, also called *mass singularities*, arise from the fact that partons, *i.e.* quarks and gluons, are treated as massless particles. This causes the propagators to blow up when approaching the small energy region. A natural way to regularize this kind of divergences would be to assign the massless particle a mass and, after having subtracted the divergent terms, take the limit of vanishing mass. However, it has been shown in Ref. [13] that for a non-abelian theory like QCD this leads to a wrong result. In fact, it was proved that a zero-mass gluon is *not* the limiting case of a finite-mass gluon. On the other hand, the use of dimensional regularization also for the treatment of the infrared divergences does not present any sort of problem and therefore is presently systematically employed. In the following it will be used to study the structure of the infrared divergences in DIS.

As already mentioned, the coefficient functions C_i^0 can be calculated in perturbation theory. As a consequence, they admit the following perturbative expansion⁽¹⁾:

$$\begin{aligned} C_i^0 &= \int \left| \mathcal{A}_i^{\mu\nu,(0)} + g_s \mathcal{A}_i^{\mu\nu,(1)} + g_s^2 \mathcal{A}_i^{\mu\nu,(2)} + \mathcal{O}(g_s^2) \right|^2 d\Phi \\ &= C_i^{0,(0)} + \frac{\alpha_s}{4\pi} C_i^{0,(1)} + \mathcal{O}(\alpha_s^2), \quad i = q, g, \end{aligned} \quad (1.9)$$

being $\alpha_s = g_s^2/4\pi$ and $d\Phi$ the phase-space element. The expression in eq. (1.9) should be understood in $4 - 2\epsilon$ dimensions with $\epsilon < 0$, so that all the infrared divergences are regularized and appear as $1/\epsilon$ poles. For simplicity only the case $i = q$ will be considered here. In Fig. 1.4 a pictorial representation of eq. (1.9) for $i = q$ is also given.

We will consider one by one the diagrams in the bottom of Fig. 1.4, highlighting the structure of the infrared divergences (if any) [14].

Let us start with the only LO diagram contributing to $C_q^{0,(0)}$. In this case no infrared (as well as ultraviolet) divergences appear and thus no regularization is needed at all. Moreover, the calculation of this diagram is totally equivalent to that for the leptonic tensor in eq. (1.5) and, for both the structure functions (apart from a factor $\frac{1}{2}$), the result is⁽²⁾:

$$C_q^{0,(0)}(x, Q) = C_q^{(0)}(x) = \delta(1 - x). \quad (1.10)$$

Notice that $C_q^{(0)}$, without the superscript 0, denotes the renormalized (finite) coefficient function.

Now we consider the order α_s coefficient function $C_q^{0,(1)}$. To this end, we start considering the diagram (a) at the bottom of Fig. 1.4. In the case the result is infrared divergent and the divergent part has the form:

$$(a) = \mathcal{V}(\epsilon) C_q^{(0)}(x) + \dots, \quad (1.11)$$

where dots denote terms which are finite in the limit $\epsilon \rightarrow 0$, with:

$$\mathcal{V}(\epsilon) = 2C_F \frac{\alpha_s}{4\pi} \left(\frac{4\pi\mu^2}{Q^2} \right)^\epsilon \frac{\Gamma(1 - \epsilon)}{\Gamma(1 - 2\epsilon)} \left[-\frac{2}{\epsilon^2} - \frac{3}{\epsilon} \right], \quad (1.12)$$

¹Note that the strong coupling constant α_s in eq. (1.9) has already been renormalized and thus depends on the renormalization scale μ_R which is taken to be of the order of Q .

²For simplicity we are assuming that the electric charge of the quarks is equal to one.

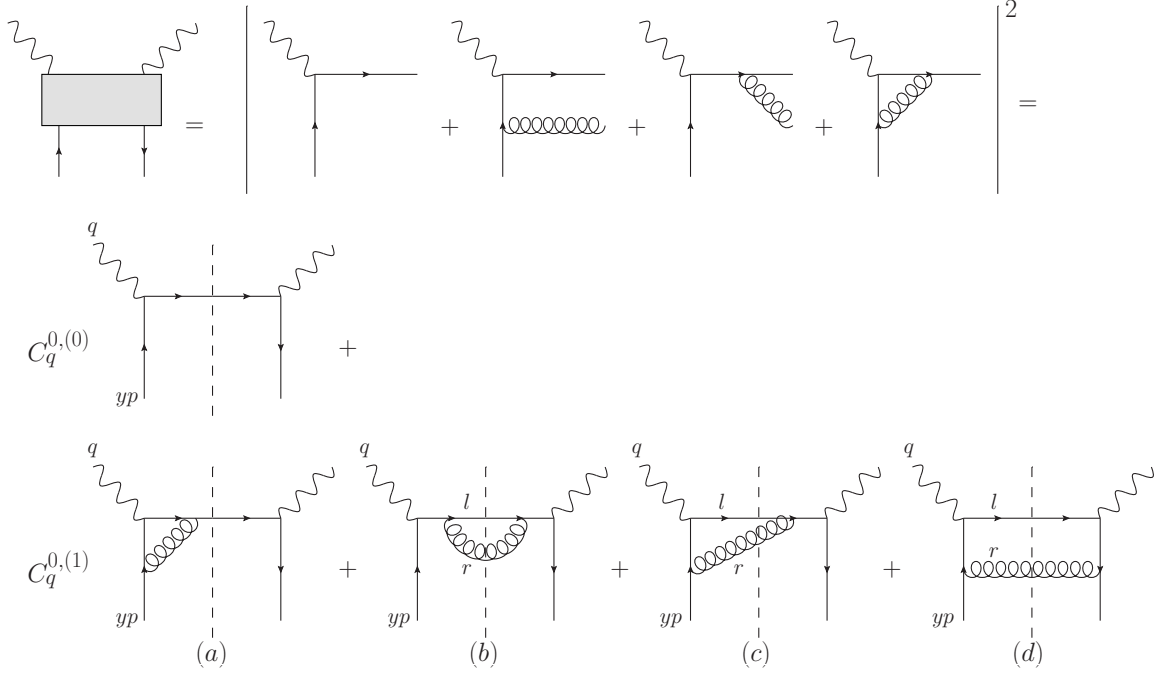


Figure 1.4: Pictorial representation of eq. (1.9).

being $C_F = \frac{4}{3}$ another $SU(3)$ color factor. Notice the appearance of the arbitrary scale μ which has been introduced in order to preserve the dimension of the coupling.

Considering the diagram (b) in Fig. 1.4, one finds that the divergent part is equal to:

$$(b) = 2C_F \frac{\alpha_s}{4\pi} \left(\frac{4\pi\mu^2}{Q^2} \right)^\epsilon \frac{\Gamma(1-\epsilon)}{\Gamma(1-2\epsilon)} \left[-\frac{1}{\epsilon}(1-x) \right] + \dots \quad (1.13)$$

The diagram (c) instead gives the result:

$$(c) = 2C_F \frac{\alpha_s}{4\pi} \left(\frac{4\pi\mu^2}{Q^2} \right)^\epsilon \frac{\Gamma(1-\epsilon)}{\Gamma(1-2\epsilon)} \left[-2x \left(\frac{1}{\epsilon} + 1 \right) \frac{x^\epsilon}{(1-x)^{1+\epsilon}} \right] + \dots \quad (1.14)$$

This expression can be manipulated using the expansion [14]:

$$\frac{x^\epsilon}{(1-x)^{1+\epsilon}} = -\frac{1}{\epsilon} \delta(1-x) + \frac{1}{(1-x)_+} + \mathcal{O}(\epsilon), \quad (1.15)$$

where the so-called *plus prescription* in the second term on the r.h.s. of eq. (1.15) is defined in such a way that:

$$\int_0^1 dx \frac{f(x)}{(1-x)_+} = \int_0^1 dx \frac{f(x) - f(1)}{1-x}, \quad (1.16)$$

being $f(x)$ some test function. Therefore, plugging eq. (1.15) into eq. (1.14), one gets:

$$(c) = 2C_F \frac{\alpha_s}{4\pi} \left(\frac{4\pi\mu^2}{Q^2} \right)^\epsilon \frac{\Gamma(1-\epsilon)}{\Gamma(1-2\epsilon)} \left[\left(\frac{2}{\epsilon^2} + \frac{2}{\epsilon} \right) C_q^{(0)}(x) - \frac{1}{\epsilon} \frac{2x}{(1-x)_+} \right] + \dots \quad (1.17)$$

Finally, considering the diagram (d), one finds:

$$(d) = 2C_F \frac{\alpha_s}{4\pi} \left(\frac{4\pi\mu^2}{Q^2} \right)^\epsilon \frac{\Gamma(1-\epsilon)}{\Gamma(1-2\epsilon)} \left[-\frac{1}{2\epsilon} \right] C_q^{(0)}(x) + \dots \quad (1.18)$$

Summing diagrams (b), (c) and (d), we find:

$$(b) + (c) + (d) = 2C_F \frac{\alpha_s}{4\pi} \left(\frac{4\pi\mu^2}{Q^2} \right)^\epsilon \frac{\Gamma(1-\epsilon)}{\Gamma(1-2\epsilon)} \left[\left(\frac{2}{\epsilon^2} + \frac{3}{2\epsilon} \right) C_q^{(0)}(x) - \frac{1}{\epsilon} \frac{1+x^2}{(1-x)_+} \right] + \dots, \quad (1.19)$$

which can also be written as:

$$(b) + (c) + (d) = -\mathcal{V}(\epsilon) C_q^{(0)}(x) - \frac{\alpha_s}{4\pi} \left(\frac{4\pi\mu^2}{Q^2} \right)^\epsilon \frac{\Gamma(1-\epsilon)}{\Gamma(1-2\epsilon)} \frac{1}{\epsilon} 2C_F \left[\frac{1+x^2}{1-x} \right]_+ + \dots, \quad (1.20)$$

where we have used the identity:

$$\frac{1+x^2}{(1-x)_+} + \frac{3}{2}\delta(1-x) = \left[\frac{1+x^2}{1-x} \right]_+. \quad (1.21)$$

In conclusion, summing eqs. (1.11) and (1.20), we have the order α_s bare coefficient function $C_q^{0,(1)}$ is given by:

$$C_q^{0,(1)}(x, Q) = C_q^{(1)}(x, Q) - \left(\frac{4\pi\mu^2}{Q^2} \right)^\epsilon \frac{\Gamma(1-\epsilon)}{\Gamma(1-2\epsilon)} \frac{1}{\epsilon} P_{qq}^{(0)}(x), \quad (1.22)$$

where we have defined:

$$P_{qq}^{(0)}(x) \equiv 2C_F \left[\frac{1+x^2}{1-x} \right]_+. \quad (1.23)$$

On the r.h.s. of eq. (1.22) the function $C_q^{(1)}$ is the part of the calculation that remains finite as $\epsilon \rightarrow 0$ and that we omitted in the previous calculations. The net result is that almost all the infrared singularities cancel in the calculation ($\mathcal{V}(\epsilon)$ disappears), except a leftover initial-state $1/\epsilon$ singularity of collinear origin. The physical reason for the missing cancellation stems from the fact that the collinear emission changes the momentum fraction of the incoming parton that scatters off the virtual photon, causing a momentum unbalancing that spoils the ‘‘inclusivity’’ of the process.

The bare quark coefficient function up to order α_s can be finally written as:

$$C_q^0(x, Q) = C_q^{(0)}(x) + \frac{\alpha_s}{4\pi} C_q^{(1)}(x, Q) - \frac{\alpha_s}{4\pi} \left(\frac{4\pi\mu^2}{Q^2} \right)^\epsilon \frac{\Gamma(1-\epsilon)}{\Gamma(1-2\epsilon)} \frac{1}{\epsilon} P_{qq}^{(0)}(x) + \mathcal{O}(\alpha_s^2). \quad (1.24)$$

The same procedure can be applied for the calculation of the gluon coefficient function appearing in eq. (1.7). In this case, since the gluon does not couple directly to the photon, this causes the vanishing of the order α_s^0 contribution, *i.e.*:

$$C_g^{0,(0)}(x, Q) = 0, \quad (1.25)$$

while for the order α_s coefficient function one finds:

$$C_g^{0,(1)}(x, Q) = C_g^{(1)}(x, Q) - \left(\frac{4\pi\mu^2}{Q^2} \right)^\epsilon \frac{\Gamma(1-\epsilon)}{\Gamma(1-2\epsilon)} \frac{1}{\epsilon} P_{gg}^{(0)}(x), \quad (1.26)$$

where:

$$P_{qg}^{(0)}(x) \equiv 2T_R [x^2 + (1-x)^2], \quad (1.27)$$

with $T_R = \frac{1}{2}$, so that:

$$C_g^0(x, Q) = \frac{\alpha_s}{4\pi} C_g^{(1)}(x, Q) - \frac{\alpha_s}{4\pi} \left(\frac{4\pi\mu^2}{Q^2} \right)^\epsilon \frac{\Gamma(1-\epsilon)}{\Gamma(1-2\epsilon)} \frac{1}{\epsilon} P_{qg}^{(0)}(x) + \mathcal{O}(\alpha_s^2). \quad (1.28)$$

Finally, plugging eqs. (1.24) and (1.28) into eq. (1.7), one gets:

$$\begin{aligned} F(x, Q) &= \sum_q \left[C_q^{(0)}(x) + \frac{\alpha_s}{4\pi} C_q^{(1)}(x, Q) - \frac{\alpha_s}{4\pi} \left(\frac{4\pi\mu^2}{Q^2} \right)^\epsilon \frac{\Gamma(1-\epsilon)}{\Gamma(1-2\epsilon)} \frac{1}{\epsilon} P_{qq}^{(0)}(x) \right] \otimes f_q^0(x) \\ &+ \left[\frac{\alpha_s}{4\pi} C_g^{(1)}(x, Q) - \frac{\alpha_s}{4\pi} \left(\frac{4\pi\mu^2}{Q^2} \right)^\epsilon \frac{\Gamma(1-\epsilon)}{\Gamma(1-2\epsilon)} \frac{1}{\epsilon} P_{qg}^{(0)}(x) \right] \otimes f_g^0(x) + \mathcal{O}(\alpha_s^2). \end{aligned} \quad (1.29)$$

The definition of $\overline{\text{MS}}$ renormalized PDFs is:

$$\begin{aligned} f_q^0(x) &= f_q(x, \mu_F) + \frac{\alpha_s}{4\pi} \left(\frac{4\pi\mu^2}{\mu_F^2} \right)^\epsilon \frac{\Gamma(1-\epsilon)}{\Gamma(1-2\epsilon)} \frac{1}{\epsilon} P_{qq}^{(0)}(x) \otimes f_q(x, \mu) \\ &+ \frac{\alpha_s}{4\pi} \left(\frac{4\pi\mu^2}{\mu_F^2} \right)^\epsilon \frac{\Gamma(1-\epsilon)}{\Gamma(1-2\epsilon)} \frac{1}{\epsilon} P_{qg}^{(0)}(x) \otimes f_g(x, \mu) + \mathcal{O}(\alpha_s^2) \end{aligned} \quad (1.30)$$

$$f_g^0(x) = f_g(x, \mu_F) + \mathcal{O}(\alpha_s),$$

where the arbitrary scale μ_F^2 , called *factorization scale*, has been introduced. The reason of the definition in eq. (1.30) is, of course, the subtraction of the poles in eq. (1.29). However, the finite contributions can be treated arbitrarily. In fact, using the expansion:

$$\frac{1}{\epsilon} \left(\frac{4\pi\mu^2}{Q^2} \right)^\epsilon \frac{\Gamma(1-\epsilon)}{\Gamma(1-2\epsilon)} \frac{1}{\epsilon} = \left(\frac{1}{\epsilon} + \ln 4\pi - \gamma_E \right) + \ln \frac{\mu^2}{Q^2} + \mathcal{O}(\epsilon), \quad (1.31)$$

where γ_E is the Euler-Mascheroni constant, it is evident that the poles come typically with finite terms containing a logarithmic contribution. Therefore, plugging the definitions given in eq. (1.30) into eq. (1.29), using the fact that $C_q^{(0)}(x) \otimes f_i(x, \mu_F) = f_i(x, \mu_F)$ and finally taking the limit $\epsilon \rightarrow 0$, one obtains:

$$\begin{aligned} F(x, Q) &= \sum_q \left[C_q^{(0)}(x) + \frac{\alpha_s}{4\pi} \left(C_q^{(1)}(x, Q) + P_{qq}^{(0)}(x) \ln \frac{Q^2}{\mu_F^2} \right) \right] \otimes f_q(x, \mu_F) \\ &+ \frac{\alpha_s}{4\pi} \left(C_g^{(1)}(x, Q) + P_{qg}^{(0)}(x) \ln \frac{Q^2}{\mu_F^2} \right) \otimes f_g(x, \mu_F) + \mathcal{O}(\alpha_s^2), \end{aligned} \quad (1.32)$$

which is the order α_s prediction for the structure function F .

Before moving to discuss the scale dependence of PDFs it is worth making some remarks. First of all we see that the r.h.s. of eq. (1.32) contains logarithms of μ_F/Q . If the (arbitrary) factorization scale μ_F is taken to be very different from Q , these

logarithms become large spoiling the usefulness of perturbation theory, because they overcome the small coupling α_s that each logarithm multiplies. For this reason, the choice for μ_F should be such that $\ln(\mu_F/Q)$ is not large. In particular, very often one chooses $\mu_F = Q$. Commonly, however, the factorization scale is also varied in the range $Q/2 < \mu_F < 2Q$ in order to give an estimate of the missing higher-order corrections.

As a second remark, we recall that the naive parton model gave as a prediction the so-called *Bjorken scaling* according to which, in the Bjorken limit defined as $Q \rightarrow \infty$ with x fixed, the structure functions exhibit the scaling law:

$$F(x, Q) \longrightarrow F(x). \quad (1.33)$$

In other words, the structure functions are only functions of the Bjorken variable x . However, as we already mentioned, the naive parton model is equivalent to the LO approximation of QCD. Considering the NLO corrections to the DIS structure functions, we obtained eq. (1.32) where, at order α_s , terms proportional to $\ln(Q^2/\mu_F^2)$ appear. The presence of such terms violates the scaling law of eq. (1.33), leading to the so-called *Bjorken scaling violation*, *i.e.* an explicit dependence on Q of the structure functions. In addition, the predicted scaling violation has a peculiar behavior. It can be shown that the structure functions decrease with increasing Q at large x and increase with increasing Q at small x . The later experimental observation of the scaling violation as predicted by eq. (1.33) represents one of the most remarkable success of QCD. In Fig. 1.5 the experimental data published by the ZEUS, NMC, BCDMS and E665 experiments are compared to the NLO QCD predictions [15]: the agreement is excellent.

1.4 The DGLAP Equation

As already stated before, PDFs cannot be determined in perturbation theory and presently they are extracted from experimental data. However, the way how PDFs evolve with the factorization scale μ_F is instead perturbatively predictable. The starting point is the observation that, by definition, any physical quantity is independent from the factorization scale μ_F , and so should be the structure function in eq. (1.32) if all the perturbative orders were included. Therefore the (logarithmic) derivative of F with respect to μ_F is required to be zero, *i.e.*:

$$\frac{\partial F(x, Q)}{\partial \ln \mu_F^2} = 0. \quad (1.34)$$

As a consequence, also the derivative of r.h.s. of eq. (1.32) must be zero and this leads to the equation for the quark PDF:

$$\frac{\partial f_q(x, \mu_F)}{\partial \ln \mu_F^2} = \frac{\alpha_s}{4\pi} \sum_{i=q,g} P_{qi}^{(0)}(x) \otimes f_i(x, \mu_F). \quad (1.35)$$

A similar equation for the gluon PDF f_g can be obtained calculating the order α_s^2 corrections to F in eq. (1.32) in the gluon-initiated channel. Therefore, one has to

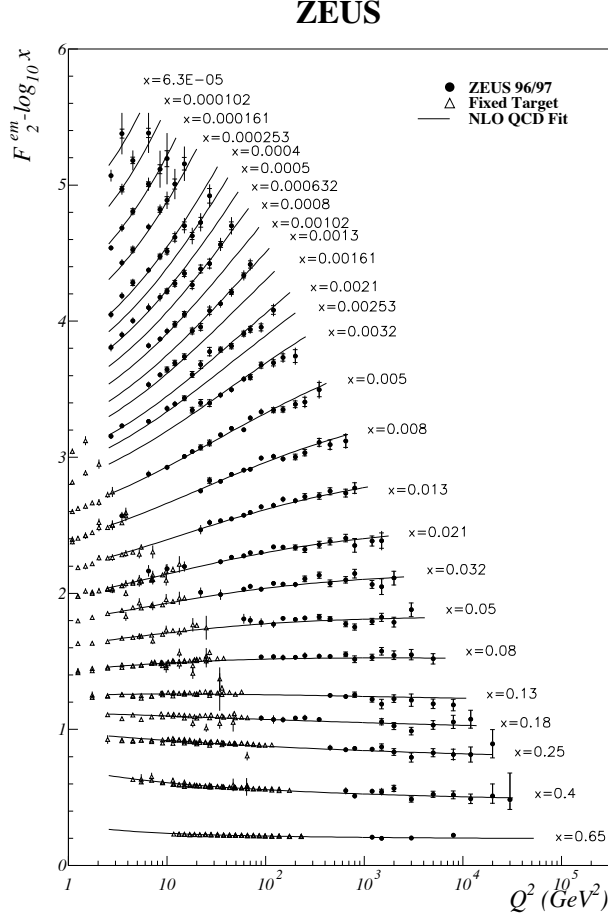


Figure 1.5: F_2 versus Q^2 for fixed x . Results from ZEUS (points) and the fixed target experiments NMC, BCDMS and E665 (triangles) are shown. The NLO QCD predictions (curve) are also displayed [15].

consider the order α_s correction for the gluon PDF in eq. (1.30), that reads:

$$\begin{aligned}
 f_g^0(x) = f_g(x, \mu_F) &+ \frac{\alpha_s}{4\pi} \left(\frac{4\pi\mu^2}{\mu_F^2} \right)^\epsilon \frac{\Gamma(1-\epsilon)}{\Gamma(1-2\epsilon)} \frac{1}{\epsilon} P_{gq}^{(0)}(x) \otimes f_q(x, \mu) \\
 &+ \frac{\alpha_s}{4\pi} \left(\frac{4\pi\mu^2}{\mu_F^2} \right)^\epsilon \frac{\Gamma(1-\epsilon)}{\Gamma(1-2\epsilon)} \frac{1}{\epsilon} P_{gg}^{(0)}(x) \otimes f_g(x, \mu) + \mathcal{O}(\alpha_s^2),
 \end{aligned} \tag{1.36}$$

where the functions $P_{gq}^{(0)}$ and $P_{gg}^{(0)}$ can be derived in a similar way as $P_{qq}^{(0)}$ and $P_{qg}^{(0)}$ and their explicit form will be given in Chapter 3. This in turn leads to the analogous equation for the gluon PDF:

$$\frac{\partial f_g(x, \mu_F)}{\partial \ln \mu_F^2} = \frac{\alpha_s}{4\pi} \sum_{i=q,g} P_{gi}^{(0)}(x) \otimes f_i(x, \mu_F). \tag{1.37}$$

The system of coupled integro-differential equations given in eqs. (1.35) and (1.37) is commonly known as Dokshitzer-Gribov-Lipatov-Altarelli-Parisi (DGLAP) equation [16, 17, 18]. It should be noticed that Eqs. (1.35) and (1.37) represent only the LO approximation of the all-order equation system that reads:

$$\frac{\partial f_i(x, \mu_F)}{\partial \ln \mu_F^2} = \frac{\alpha_s(\mu_F)}{4\pi} \sum_{j=q,g} P_{ij}(x, \alpha_s(\mu_F)) \otimes f_j(x, \mu_F), \quad i = q, g, \quad (1.38)$$

where the evolution kernels P_{ij} admit the perturbative expansion:

$$P_{ij}(x, \alpha_s(\mu_F)) = P_{ij}^{(0)}(x) + \frac{\alpha_s(\mu_F)}{4\pi} P_{ij}^{(1)}(x) + \dots \quad (1.39)$$

and the functions $P_{ij}^{(k)}$, commonly called splitting functions, are derived considering more and more perturbative orders in the definition of renormalized PDFs in eqs. (1.30) and (1.37). Presently, the splitting functions have been analytically calculated up to three loops [16, 19, 20, 21, 22], *i.e.* the first three terms of the expansion in eq. (1.39) are known.

The DGLAP equation (1.38) describes the evolution of PDFs with the factorization scale μ_F . As any differential equation, to be univocally solved the DGLAP equation needs some boundary condition. In practice this means that knowing the PDFs at some initial scale μ_{F0} , eq. (1.38) allows to predict how they change from the scale μ_{F0} to any other scale μ_F . This has a big impact on PDF determination. In fact, thanks to the DGLAP equation, the dependence on the variable μ_F of PDFs is known and it is then sufficient to determine the dependence of PDFs on the Bjorken variable x at some particular initial scale μ_{F0} .

1.5 Recent PDF Determinations

To conclude this chapter, we only mention the main groups that perform PDF fits and their most recent determinations. A more detailed description regarding the method used to include heavy quark mass effects is given in Chapter 2, while a quantitative comparison between PDFs will be given in Chapter 6. Here we limit ourselves to list the collaborations and give a very brief description of the main features of their most recent PDF determinations. It is however worth mentioning that there are some main differences that distinguish the following PDF sets which essentially are: the treatment of the heavy quark flavour effects, the perturbative order at which PDFs are determined, the data set included in the fit and the functional form adopted to parametrize PDFs. In this respect, the choices adopted by the PDF collaborations can give rise in some cases to relevant quantitative differences.

- The ABM collaboration provides PDF sets at NLO and NNLO based on DIS and Drell-Yan data. They parametrize six independent PDFs using polynomials for a total of 25 free parameters and determine the PDF uncertainties by means of the Hessian method. Their most recent determination is the ABM11 set [23] where the heavy quark mass effects are included using the fixed-flavour-number scheme.

- The CTEQ/TEA collaboration produces PDF sets at LO, NLO and NNLO using a global dataset that includes DIS data, Drell-Yan data, collider vector boson production data and jet data. They also use polynomials to parametrize 6 independent PDFs with 26 free parameters in total and determine the PDF errors by means of the Hessian method. Their most recent determination of the CTEQ collaboration is the CT10 PDF set [24] where the heavy quark mass effects are included using the S-ACOT- χ general-mass-variable-flavour-number scheme.
- The GJR collaboration provides PDF sets at NLO and NNLO based on DIS, Drell-Yan data and jet data. They have 5 independent polynomial PDFs with 15 free parameters in total and determine the PDF uncertainties again using the Hessian method. The JR09 set [25] is their most recent fit and employs the fixed-flavour-number scheme.
- The HERAPDF collaboration produces PDF sets at NLO and NNLO which are based only on HERA DIS data. The HERAPDF fits are performed using the Hessian method and assuming 5 independent polynomial PDFs and 14 free parameters. Their last release is the HERAPDF1.5 fit [26, 27] which employs the TR general-mass-variable-flavour-number scheme.
- The MSTW collaboration produces PDF sets at LO, NLO and NNLO using a global dataset that includes DIS data, Drell-Yan data, collider vector boson production data and jet data. They fit 7 independent PDFs, again using polynomials, for a total of 20 free parameters using the Hessian method. Their most recent determination is MSTW08 set [28] which is based on the TR general-mass-variable-flavour-number scheme.
- The NNPDF collaboration, finally, provides LO, NLO and NNLO PDF sets based on a global dataset like the MSTW and the CTEQ collaborations but, at present, it is the only collaboration that includes the most recent vector boson production data and jet data published by the LHC experiments. The NNPDF collaboration parametrizes 7 PDFs at the initial scale using neural networks, for a total of 259 free parameters while the errors are determined using the Monte Carlo sampling method (see Chapter 5). The most up to date release is the NNPDF2.3 set [29] which is based on the FONLL general-mass-variable-flavour-number scheme.

Chapter 2

Treatment of Heavy Flavours

Interest in the inclusion the effects of heavy flavours in DIS structure functions was revived by the discovery [30] that different treatments of mass-suppressed terms in global parton fits can affect predictions for the total W and Z production at the LHC by almost 10%.

A technique for the inclusion of these mass-suppressed contributions to structure functions was developed long ago [12, 31], based upon a renormalization scheme with explicit heavy quark decoupling [32]. Several variants of this method (usually called ACOT after Aivazis, Collins, Olness and Tung) were subsequently proposed, such as S-ACOT [33] and ACOT- χ [34, 35]. The ACOT method is presently used by the CTEQ collaboration since 2007 when the CTEQ6.5 set [36] was made public.

An alternative method (sometimes called TR after Thorne and Roberts) has also been advocated [37, 38] and used for all MRST parton fits until 2004 [39, 40, 41, 42]. However, the methods used by the CTEQ [30] and MRST/MSTW [28, 36] groups for their current parton fits, based respectively on the ACOT [12, 31] and TR' [43] procedures, have adopted at least in part a common framework. They have been compared in Refs. [44, 45], thereby elucidating differences and common aspects.

A somewhat different technique for the inclusion of heavy-quark-mass effects, the so-called FONLL method (which stands for fixed-order next-to-leading log), was introduced in Ref. [46] in the context of hadro-production of heavy quarks. The FONLL method only relies on standard QCD factorization and calculations with massive quarks in the decoupling scheme of Ref. [32] and with massless quarks in the $\overline{\text{MS}}$ scheme. The name FONLL is motivated by the fact that the method was originally used to combine a fixed (second) order (FO) calculation with a next-to-leading-log (NLL) one. However, the method is entirely general and can be used to combine consistently a fixed-order with a resummed calculations to any order. The application of the FONLL scheme to DIS structure functions was presented in Ref. [47] and is presently used by the NNPDF collaboration.

It is also worth mentioning that there exists another method, usually referred to as BMSN prescription [48, 49] (after Buza, Matiounine, Smith and van Neerven), that resembles quite closely the FONLL method. The main differences, however, will be briefly mentioned in Sec. 2.5. The BMSN has been employed in the ABKM09 analysis [50] but has been abandoned in favor of a purely fixed-order approach in the more recent ABM11 analysis [23].

In this chapter we will give a detailed overview of the techniques described above and used to include heavy quark masses to the DIS structure functions, with some emphasis on the FONLL method. This will serve as a theoretical background for the next chapter where the implementation of the FONLL method will be described in detail. A numerical benchmark of these methods (except the BMSN scheme) has been recently presented in Ref. [51].

2.1 FFNS and VFNS

In order to explain how the inclusion of heavy quark mass effects works in DIS, we consider a general lepton-hadron process:

$$l_1(p_1) + N(P) \rightarrow l_2(p_2) + H(p_H) + X(P_X), \quad (2.1)$$

at the lowest order in the electro-weak interactions, as depicted in Fig. 2.1, and where we require a heavy quark H of momentum p_H^μ and mass M_H in the final state⁽¹⁾. This

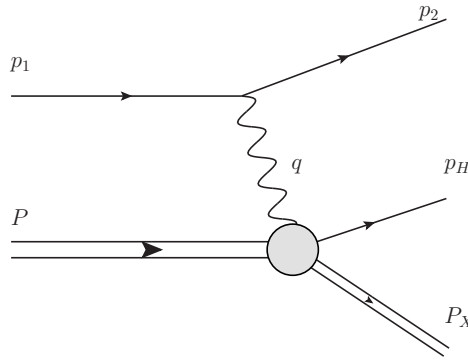


Figure 2.1: Lepton Hadron production amplitude for a heavy quark.

process takes place by the exchange of a vector boson $B = \gamma, W, Z$ having momentum q .

As already shown in Chapter 1, the differential cross section of this process can be factorized as follows:

$$\frac{d^2\sigma}{dx dy} \propto L_{\mu\nu} W^{\mu\nu}, \quad (2.2)$$

where $L_{\mu\nu}$ is the leptonic tensor given in eq. (1.5) and $W^{\mu\nu}$ is the hadronic tensor that here we write in the more general form:

$$W^{\mu\nu} = \frac{1}{4\pi} \sum \overline{\langle P | J^\mu | p_H, P_X \rangle} (2\pi)^4 \delta^{(4)}(P + q - p_H - P_X) \langle P_X, p_H | J^{\nu\dagger} | P \rangle, \quad (2.3)$$

¹The requirement of having a heavy quark in the final state is the way heavy quark structure functions are experimentally measured. Nonetheless, this definition, when considering higher-order corrections, is infrared unsafe, thus perturbative calculations are usually carried out using a different definition of heavy quark structure function. This issue, anyhow, appears only at higher orders and it is irrelevant for the qualitative description of the mass schemes which follows. We will instead return on this in Chapter 3 where the implementation of the FONLL method up to order α_s^2 will be considered.

where $\overline{\sum}$ denotes a sum over all hadronic states containing the final-state quark H of momentum p_H and the average over the incoming helicity states.

The factorization theorem asserts that, to the leading power in $1/Q^2$ (leading twist), the hadronic tensor can be factorized as:

$$W^{\mu\nu}(x, Q, M_H) = \sum_i w_i^{\mu\nu}(x, Q, M_H, \alpha_s(\mu)) \otimes f_i(x, \mu), \quad (2.4)$$

where the short notation \otimes denotes the Mellin convolution already defined in eq. (1.7). We recall here that f_i and $w_i^{\mu\nu}$ are the PDFs and coefficient functions, respectively. Moreover, for simplicity renormalization and the factorization scales have been set to $\mu_R = \mu_F = \mu$.

In the presence of non-zero masses, the helicity amplitudes provide the simplest connection between the physical (scalar) structure functions and the corresponding parton-level quantities $w_i^{\mu\nu}$. Projecting out the helicity components of the hadronic tensor, eq. (2.4) reads:

$$W^\lambda = \sum_i w_i^\lambda \otimes f_i, \quad (2.5)$$

where:

$$W^\lambda = \epsilon_\mu^{(\lambda)*}(q, P) W^{\mu\nu} \epsilon_\nu^{(\lambda)}(q, P) \quad \text{and} \quad w_i^\lambda = \epsilon_\mu^{(\lambda)*}(q, k) w_i^{\mu\nu} \epsilon_\nu^{(\lambda)}(q, k), \quad (2.6)$$

being $\epsilon_\nu^{(\lambda)}(q, r)$ the polarization vector of the vector boson with momentum q and helicity $\lambda = +, 0, -$ defined with respect to the reference vector r . The more familiar structure functions F_1 , F_2 and F_3 are then given by a linear combination of the helicity structure functions according to the following relations (*cf.* Appendix B of [52]):

$$\begin{aligned} W^+ &= F_1^H - \frac{1}{2} \sqrt{1 + \frac{Q^2}{\nu^2}} F_3^H \\ W^- &= F_1^H + \frac{1}{2} \sqrt{1 + \frac{Q^2}{\nu^2}} F_3^H \\ W^0 &= -F_1^H + \frac{1}{2x} \left(1 + \frac{Q^2}{\nu^2} \right) F_2^H. \end{aligned} \quad (2.7)$$

In addition, the *longitudinal* structure function F_L^H is defined in terms of the structure functions F_1^H and F_2^H as:

$$F_L^H = F_2^H - 2x F_1^H. \quad (2.8)$$

From now on, we will only refer to the heavy quark structure functions F_k^H . Moreover, in order to avoid unnecessary complications arising from higher-order corrections, we will work only with expressions up to order α_s . Using these simplifications, the DIS

heavy quark structure functions reduce to the following factorization formula⁽²⁾:

$$\begin{aligned}
F_k^H(x, Q, M_H) &= \sum_{i=g, H, \bar{H}} C_{k,i}(x, Q, M_H, \alpha_s(\mu)) \otimes f_i(x, \mu) \\
&= C_{k,H}^{(0)} \otimes f_H^+ + \frac{\alpha_s}{4\pi} \sum_{i=g, H, \bar{H}} C_{k,i}^{(1)} \otimes f_i,
\end{aligned} \tag{2.9}$$

where $C_{k,i}^{(j)}$ are the coefficient functions and $f_H^+ \equiv f_H + f_{\bar{H}}$. Notice that the sum runs only over the gluon and the heavy quark PDFs. In fact, limiting ourselves to order α_s , the only graphs that contribute to the heavy quark structure functions are either gluon-initiated or heavy quark-initiated graphs. Moreover, since no gluon-initiated graph is present at LO, we have explicitly set to zero the order α_s^0 gluon coefficient function in the second line of eq. (2.9).

One possibility to calculate the coefficient functions $C_{k,i}^{(j)}$ is to set to zero the masses of the internal lines and external partons in graphs for the partonic subprocesses. This way, the calculation presents infrared (IR) divergences that are usually regularized using the dimensional regularization and subtracted in the $\overline{\text{MS}}$ scheme (see Chapter 1), obtaining the structure functions in the *zero-mass* (ZM) scheme:

$$\begin{aligned}
F_k^{H,\text{ZM}}(x, Q) &= \sum_{i=g, H, \bar{H}} C_{k,i}^{\text{ZM}}(x, Q, \alpha_s(\mu)) \otimes f_i(x, \mu) \\
&= C_{k,H}^{\text{ZM},(0)} \otimes f_H^+ + \frac{\alpha_s}{4\pi} \sum_{i=g, H, \bar{H}} C_{k,i}^{\text{ZM},(1)} \otimes f_i.
\end{aligned} \tag{2.10}$$

where and $C_{k,i}^{\text{ZM},(j)}$ are the ZM $\overline{\text{MS}}$ coefficient functions. The IR singularities arising from setting $M_H = 0$ in the coefficient functions reflect the presence of large collinear logarithms of the kind $\ln(Q/M_H)$ and the natural way to resum these contributions is to reabsorb them into the heavy quark PDFs f_H and $f_{\bar{H}}$ which, as a consequence, start evolving according to the standard DGLAP evolution equation as discussed in Chapter 1. Of course, this scheme does not depend explicitly on the value of the heavy quark mass M_H , however both coefficient functions and DGLAP evolution will depend on the number of *active* (*i.e.* massless) flavours, which we take to be $(N + 1)$, and only the lightest $(N + 1)$ flavours and the gluon will have an associated PDF, while the remaining heavy flavour PDFs will be identically zero. As a consequence, there will be as many such schemes as there are flavours. Of course, the lightest flavours up, down and strange will always be considered massless. Therefore eq. (2.10) can be written in the ZM 3-flavour scheme, where the number of active flavours entering the coefficient functions and the DGLAP evolution equation is three and only up, down and strange have a non-vanishing PDF, or in the ZM 4-flavour scheme, where the number of active flavours entering the coefficient functions and the DGLAP evolution equation is now four and up, down, strange and charm have a non-vanishing PDF, and so on.

²Here and for the rest of this chapter an overall factor e_H^2 , being e_H the electric charge of the heavy quark H , is understood in the definition of the structure functions as a convolution between coefficient functions and PDFs. In addition in the case of F_2^H also a factor x is understood.

Although schemes with different numbers of active flavours come from different renormalization and factorization procedures, the relation between them is just a matter of a transformation between different schemes and can be calculated order by order in α_s . The corresponding matching conditions are presently known up to $\mathcal{O}(\alpha_s^2)$ [48] and such conditions allow to match the ZM N -flavour with the $(N + 1)$ -flavour scheme at any given scale μ_{match} . For a question of naturalness, μ_{match} is usually taken to be the mass of the $(N + 1)$ -th flavour M_H ³. In practice, the matching can be done in such a way that if $Q < M_c$ eq. (2.4) is evaluated in the ZM 3-flavour scheme, if $M_c \leq Q < M_b$ the ZM 4-flavour scheme is used, and so on. This defines the so-called ZM Variable-Flavour-Number Scheme (ZM-VFNS).

The ZM-VFNS works well if the scale Q is sufficiently distant from any heavy quark mass threshold. When, instead, $Q \simeq M_H$ this approach turns out not to be accurate because it neglects potentially large contributions proportional to powers of M_H/Q in the coefficient functions.

Alternatively to the ZM scheme, one can retain the full dependence on the heavy quark mass M_H in the calculation of $C_{k,i}$ in eq. (2.9). The presence of the mass M_H provides a natural regulator for the IR collinear divergences which, therefore, do not need to be resummed requiring the DGLAP evolution for the heavy quark PDF f_H^+ .

However, this approach gives rise to terms proportional to $\ln(Q/M_H)$ in the coefficient functions which blow up either if $Q \ll M_H$ or if $Q \gg M_H$. Particularly in the limit $Q \ll M_H$, these logarithms prevent the desirable decoupling of the heavy flavour H . The natural solution to this problem is provided by the so-called Collins-Wilczek-Zee (CWZ) method [32]. Assuming that H is the $(N + 1)$ -th flavour (*e.g.*, if H is the charm, $N = 3$), the CWZ prescription is very simple: for $Q < M_H$ switch to the ZM N -flavour scheme. This method has the following advantages: satisfies manifest decoupling of the $(N + 1)$ -th flavour, the evolution equations for α_s and PDFs are the same for QCD with N flavours with pure $\overline{\text{MS}}$ subtraction, the parton distribution of the $(N + 1)$ -th flavour is identically zero and the quark mass M_H only appears in the coefficient functions for $Q > M_H$.

The procedure described above is called Fixed Flavour Number Scheme (FFNS) and in practice in this scheme one sets at the beginning the number of active flavours to N and keeps the contributions due to the mass of the $(N + 1)$ -th flavour only in the coefficient functions for scales above the heavy quark mass threshold. In the FFNS, given that the heavy quark PDFs are identically zero, the structure functions look like this:

$$F_k^{H,\text{FF}}(x, Q, M_H) = \frac{\alpha_s}{4\pi} C_{k,g}^{\text{FF},(1)}(x, Q, M_H) \otimes f_g(x, \mu). \quad (2.11)$$

Of course, using the CWZ prescription one can define a FFNS for any number of active flavours: the 3-flavour FFNS where up, down and strange are the only active flavours but with the charm mass contributions in the coefficient functions, the 4-flavour FFNS where now up, down, strange and charm are the active flavours and with the bottom mass contributions in the coefficient function, and so on.

³This choice is somehow arbitrary but it simplifies substantially the matching conditions because all the terms proportional to powers of $\ln(\mu_{\text{match}}/M_H)$ vanish. Accidentally, with this choice the matching is continuous up to order α_s , meaning that α_s and PDFs are equal in $\mu_{\text{match}} = M_H$ when switching from the N -flavour to the $(N + 1)$ -flavour scheme. Unfortunately, this is no longer true at order α_s^2 .

The CWZ prescription, however, does not solve the problems for $Q \gg M_H$. Therefore the FFNS turns out to be accurate for scales Q of the order or below M_H but, due to the presence of unresummed large logarithms $\ln(M_H/Q)$, it becomes unreliable when $Q \gg M_H$.

The ZM-VFNS and the FFNS are therefore two distinct mass schemes that are accurate in two complementary energy regions: $Q \gg M_H$ and $Q \lesssim M_H$, respectively.

What is actually needed then is a mass scheme able to interpolate smoothly between the FFNS for $Q \lesssim M_H$ and the ZM-VFNS for $Q \gg M_H$. As we will see, there are several prescriptions that achieve this goal and they are commonly referred to as General-Mass Variable-Flavour-Number Schemes (GM-VFNS). In the following a description of such schemes, along with their possible variants, will be given.

2.2 The ACOT Method

The ACOT scheme [31, 52], used by the CTEQ collaboration, provides a framework to incorporate the heavy quark mass effects into the theoretical calculation of heavy quark production. This is built upon the CWZ renormalization procedure [32] which provides a formal foundation for the ACOT scheme which is valid to all orders.

As already explained in Sec. 2.1, the CWZ renormalization yields manifest decoupling of the heavy quarks in the $Q \ll M_H$ limit. In addition, in 1998 Collins [12] extended the factorization theorem to address the case of heavy quarks ensuring that heavy quark processes can be computed to all orders. Based on these ingredients, the ACOT scheme yields the complete quark mass dependence from the low- to high-energy regime: for $Q \ll M_H$ it ensures manifest decoupling behaving like the FFNS, and in the limit $Q \gg M_H$ it reduces precisely to the ZM-VFNS.

To describe the ACOT method in more details, we will focus on the relation between the ACOT coefficient functions $C_{k,i}^{\text{ACOT},(j)}$ and the coefficient functions $C_{k,i}^{(j)}$ appearing in eq. (2.9) that come from a straight calculation of the DIS heavy quark production amplitude retaining the heavy quark mass M_H . The basic relation is established by applying the factorization formula at the parton amplitude level. This provides the definition for the ACOT coefficient functions:

$$C_{k,i} \equiv \sum_{j=g,H,\bar{H}} C_{k,j}^{\text{ACOT}} \otimes \Gamma_{ji}, \quad (2.12)$$

where the functions Γ_{ji} , which admit the following perturbative expansion:

$$\Gamma_{ji}(x) = \delta_{ji} \delta(1-x) + \frac{\alpha_s}{4\pi} \ln \frac{Q^2}{M_H^2} P_{ji}^{(0)}(x) + \mathcal{O}(\alpha_s^2), \quad (2.13)$$

where $P_{ji}^{(0)}$, the LO splitting functions introduced in Chapter 1, account for the splitting of the incoming partons. Notice that the logarithm $\ln(Q^2/M_H^2)$ in eq. (2.13) embodies the collinear divergence in the limit $Q \gg M_H$. At the same time we have the expansion:

$$C_{k,j}^{\text{ACOT}}(x) = C_{k,j}^{\text{ACOT},(0)}(x) + \frac{\alpha_s}{4\pi} C_{k,j}^{\text{ACOT},(1)}(x) + \mathcal{O}(\alpha_s^2), \quad (2.14)$$

with $C_{k,g}^{\text{ACOT},(0)}(x) = 0$, given that at order α_s^0 the gluon does not couple to the photon. Plugging eqs. (2.13) and (2.14) into eq. (2.12) we get:

$$\begin{aligned} C_{k,i} &= C_{k,i}^{(0)} + \frac{\alpha_s}{4\pi} C_{k,i}^{(1)} + \mathcal{O}(\alpha_s^2) \\ &= C_{k,i}^{\text{ACOT},(0)} + \frac{\alpha_s}{4\pi} \left(\sum_j C_{k,j}^{\text{ACOT},(0)} \otimes \Gamma_{ji} + C_{k,i}^{\text{ACOT},(1)} \right) + \mathcal{O}(\alpha_s^2), \end{aligned} \quad (2.15)$$

so that:

$$C_{k,i}^{\text{ACOT},(0)} = C_{k,i}^{(0)}, \quad (2.16)$$

consistent with the fact that $C_{k,i}^{(0)}$ comes from a tree level diagram and therefore does not contain any collinear divergence, while:

$$C_{k,i}^{\text{ACOT},(1)} = C_{k,i}^{(1)} - \ln \frac{Q^2}{M_H^2} \sum_j C_{k,j}^{(0)} \otimes P_{ji}^{(0)}. \quad (2.17)$$

Gathering everything, the ACOT coefficient functions are given by:

$$C_{k,i}^{\text{ACOT}} = C_{k,i}^{(0)} + \frac{\alpha_s}{4\pi} \left[C_{k,i}^{(1)} - \ln \frac{Q^2}{M_H^2} \sum_j C_{k,j}^{(0)} \otimes P_{ji}^{(0)} \right] + \mathcal{O}(\alpha_s^2), \quad (2.18)$$

so that the order α_s heavy quark structure functions take the form:

$$\begin{aligned} F_k^{H,\text{ACOT}} &= C_{k,H}^{(0)} \otimes f_H^+ + \frac{\alpha_s}{4\pi} \left[C_{k,H}^{(1)} - \ln \frac{Q^2}{M_H^2} \sum_j C_{k,j}^{(0)} \otimes P_{jH}^{(0)} \right] \otimes f_H^+ \\ &\quad + \frac{\alpha_s}{4\pi} \left[C_{k,g}^{(1)} - \ln \frac{Q^2}{M_H^2} \sum_j C_{k,j}^{(0)} \otimes P_{j,g}^{(0)} \right] \otimes f_g. \end{aligned} \quad (2.19)$$

Eq. (2.19) is the master formula for heavy quark structure functions in the ACOT scheme and Fig. 2.2 is its pictorial representation.

This scheme contains all the ingredients of a consistent QCD theory of heavy quark production over a wide range of energy scales. In particular, if the initial-state quark is massive and the energy scale Q is of the same order of its mass M_H , the terms proportional to $\ln(Q^2/M_H^2)$ (subtraction terms) in eq. (2.19) vanish. Moreover, applying the CWZ prescription, the PDF f_H^+ is either identically zero or very small for $Q < M_H$, thus the result is:

$$F_k^{H,\text{ACOT}} \xrightarrow{Q \lesssim M_H} \frac{\alpha_s}{4\pi} C_{k,g}^{\text{FF},(1)} \otimes f_g, \quad (2.20)$$

i.e. dominance of the gluon-fusion mechanism which reproduces the usual picture of heavy quark production in the FFNS.

On the other hand, if either H is a usual light quark (*i.e.*, $M_H \simeq 0$) or H is massive but $Q \gg M_H$, the subtraction terms become large (collinear divergence), hence the

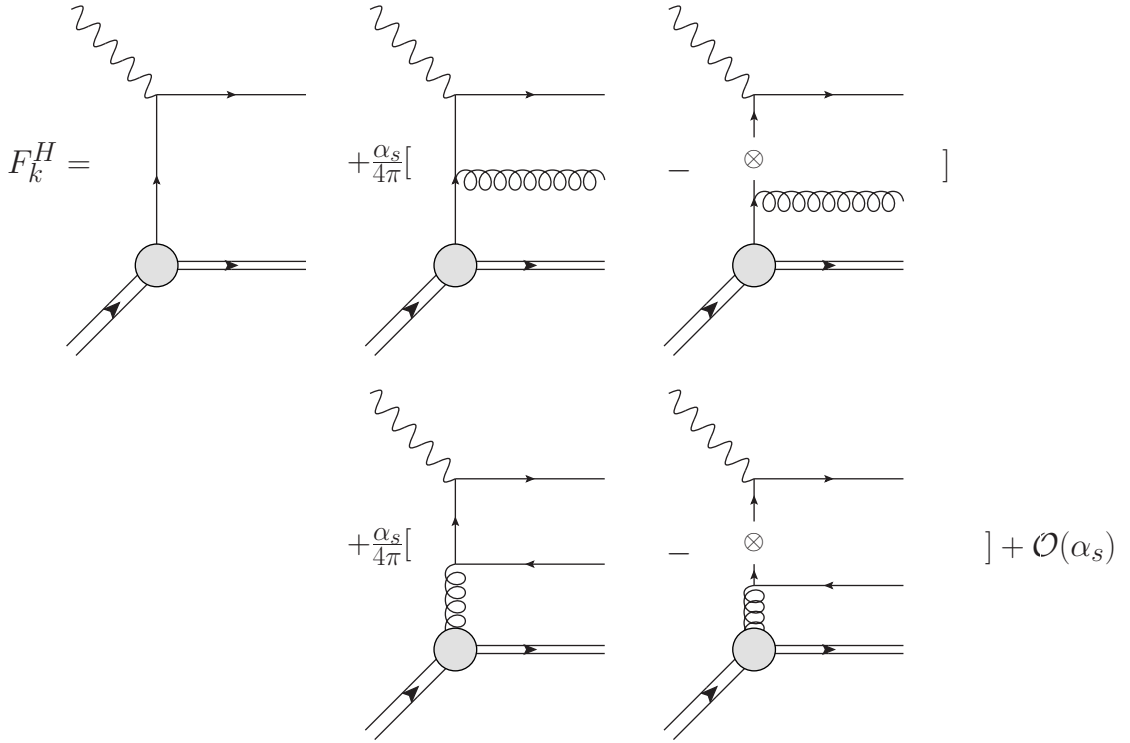


Figure 2.2: Graphical representation of the master equation eq. (2.19) for the helicity structure functions.

collinear divergences of the terms in brackets in eq. (2.19) cancel leaving only a correction term of order α_s with no large logarithmic factors. This way, we obtain:

$$F_k^{H, \text{ACOT}} \xrightarrow{Q \gg M_H} C_{k,H}^{\text{ZM},(0)} \otimes f_H^+ + \frac{\alpha_s}{4\pi} (C_{k,q}^{\text{ZM},(1)} \otimes f_H^+ + C_{k,g}^{\text{ZM},(1)} \otimes f_g) \quad (2.21)$$

which reproduces the ZM-VFNS, appropriate for energies much higher than all masses.

In conclusion, eq. (2.19) provides a smooth interpolation between FFNS and ZM-VFNS, and contains both as special cases.

As an example, in Fig. 2.3 we show the order α_s heavy quark structure function F_2^c as a function of the energy Q calculated in the ZM-VFNS, FFNS, ACOT and S-ACOT schemes (see Sec. 2.2.1). We see that the ACOT scheme coincides with the FFNS for small values of Q and tends to the ZM-VFNS for large values of Q .

2.2.1 The S-ACOT Variant

In the application of the ACOT method, it was observed that the heavy quark mass could be set to zero in certain pieces of the hard scattering terms without any loss of accuracy. This modification of the ACOT scheme goes by the name Simplified-ACOT (S-ACOT) and can be summarized as follows [33]: for hard-scattering processes with *incoming heavy quarks* or with *internal on-shell cuts on a heavy quark line*, the heavy quark mass can be set to zero ($M_H = 0$) for these pieces.

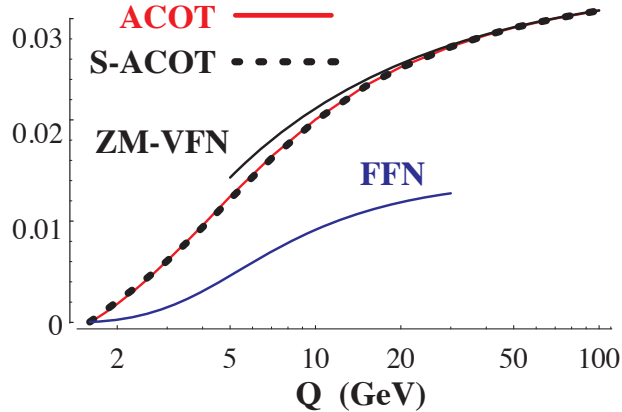


Figure 2.3: F_2^c for $x = 0.1$ for order α_s DIS heavy quark production as a function of the energy Q . We display calculations using the schemes ACOT, S-ACOT, FFNS and ZM-VFNS [53].

Considering the order α_s DIS heavy quark production, this prescription states that one can set $M_H = 0$ for the order α_s^0 and for the heavy quark-initiated terms of the order α_s contributions (first two terms on the r.h.s. of eq. (2.19)), and for the subtraction terms (on-shell cut on an internal heavy quark line, third and fifth terms on the r.h.s. of eq. (2.19)). Hence, the only contribution which requires a calculation for finite values of M_H is the order α_s gluon coefficient function⁽⁴⁾. Fig. 2.3 displays a comparison of a calculation using the plain ACOT scheme with the S-ACOT scheme. As expected, these two results match throughout the full kinematic region.

It is important to notice that the S-ACOT scheme is not an approximation, this is an exact renormalization scheme extensible to all orders. On the other hand, the S-ACOT prescription has the advantage of being more straightforward to state and simpler to implement than the plain ACOT method.

2.2.2 The ACOT- χ Variant

A crucial point of any GM-VFNS and more in particular of the ACOT method is that the appearance of the mass M_H has both a dynamical origin, in the coefficient functions, and a kinematic origin in the phase space of the process. In fact, for a process where one or more heavy quarks are present in the final state, any convolution between PDFs and coefficient functions should be correctly written as:

$$C_{k,i} \otimes f_i = \int_{\chi}^1 \frac{dy}{y} C_{k,i} \left(\frac{x}{y}, M_H, Q, \alpha_s(\mu) \right) f_i(y, \mu), \quad (2.22)$$

⁴The S-ACOT prescription is not to be taken literally. In fact, the procedure described above would lead to logarithmic divergences when setting M_H to zero in the subtraction terms. This, of course, is not the way the S-ACOT proceeds. Perhaps, a more comprehensible way to understand the S-ACOT prescription could be seen in terms “relocation” of the power terms of the form M_H/Q . As stated in [33], essentially one has the freedom to move all the power suppressed terms of the kind M_H/Q from the quark to the gluon coefficient function and afterwards apply the limit $M_H \rightarrow 0$ in the remaining terms, making sure that appropriate cancellation of logarithmic divergent terms takes place.

where χ takes into account the reduction of the phase space of the final state due to heavy quarks having mass M_H . In particular, if n heavy quarks of mass M_H are produced in the final state, by requiring that the partonic invariant mass $W^2 = Q^2(1-x)/x > (n M_H)^2$, one finds that the lower kinematic bound is given by:

$$\chi = x \left[1 + \left(\frac{n M_H}{Q} \right)^2 \right]. \quad (2.23)$$

This was the original idea behind the slow-rescaling prescription of Ref. [54], which considered DIS charm production (e.g. $\gamma c \rightarrow c$) introducing the shift $x \rightarrow \chi = x[1 + (M_c/Q)^2]$.

The generalization of this prescription is implemented in the variant of the ACOT scheme called ACOT- χ that accounts for the charm quark mass by effectively reducing the phase space for the final state relative to the lighter quarks by an amount proportional to $(M_c/Q)^2$.

More details on this scheme can be found in Ref. [53], where it was shown that (up to order α_s) the phase space mass dependence is generally the dominant contribution with respect to the dynamical dependence to the DIS heavy quark structure functions.

As a last remark, we point out that the S-ACOT and the ACOT- χ schemes are not incompatible and can be combined into the so-called S-ACOT- χ scheme.

2.3 The TR Method

The TR scheme, presently used by the MSTW collaboration, was introduced in Refs. [37, 38] as an alternative to the ACOT scheme [31] with more emphasis on correct threshold behavior of the structure functions.

Like ACOT, the TR scheme is based on the existence of two different regions separated by a transition point, chosen by default to be the heavy quark mass M_H . Below this point a heavy quark is not an active parton but is generated in the final state using the FFNS coefficient functions, while above this point the heavy quark becomes a new parton, evolving according to the massless evolution equations, and the structure functions are obtained using the GM-VFNS coefficient functions which must tend to the correct ZM-VFNS limits as $Q \gg M_H$, up to possibly higher-order corrections.

Apart from these similarities, the basic difference, and somehow the improvement with respect to the ACOT method, is the demand of a smooth transition when crossing the heavy quark mass thresholds. In fact, when crossing the threshold $Q = M_H$ the ACOT scheme leads to an abrupt rise of the heavy quark structure functions, which is in contrast with the smooth behavior required physically. In particular, though the structure function itself is continuous at the threshold, its derivative is not.

In order to better reflect the true physics around the heavy quark thresholds, the TR scheme imposes the continuity of the derivative of the structure functions at the thresholds.

Assuming that the structure function in the TR scheme admits the perturbative expansion:

$$F_k^{H,\text{TR}} = C_{k,H}^{\text{TR},(0)} \otimes f_H^+ + \frac{\alpha_s}{4\pi} \left[C_{k,H}^{\text{TR},(1)} \otimes f_H^+ + C_{k,g}^{\text{TR},(1)} \otimes f_g \right] + \mathcal{O}(\alpha_s^2), \quad (2.24)$$

the aim is to determine the coefficient functions $C_{k,j}^{\text{TR},(i)}$ in such a way that eq. (2.24) extrapolates smoothly from the FFNS at low Q to the ZM-VFNS at high Q with a smooth transition at the heavy quark threshold M_H .

First of all, the equivalence of the structure function in the TR scheme $F_k^{H,\text{TR}}$ with that in the FFNS $F_k^{H,\text{FF}}$ in eq. (2.11) for $Q \lesssim M_H$ is required. However, in the FFNS the flavour H is not active while the TR scheme it is. Therefore, before equating the two structure functions, one needs to express the PDFs in eq. (2.24) in terms of the PDFs in eq. (2.11) and this can be done using the matching conditions evaluated in Ref. [48] and that we report here up to order α_s :

$$\begin{aligned} f_H^+(x, Q) &= \frac{\alpha_s}{4\pi} \ln \frac{Q^2}{M_H^2} P_{qg}^{(0)}(x) \otimes f_g^{(N)}(x, Q) \\ f_g^{(N+1)}(x, Q) &= \left[1 + \frac{\alpha_s}{6\pi} \ln \frac{Q^2}{M_H^2} \right] f_g^{(N)}(x, Q), \end{aligned} \quad (2.25)$$

where the upper index in the gluon PDF (N) or ($N+1$) denotes the factorization scheme, *i.e.* the number of active flavours. Therefore, plugging eq. (2.25) into eq. (2.24), retaining the terms up order α_s and equating it to eq. (2.11), we obtain the relation:

$$C_{k,g}^{\text{FF},(1)} = C_{k,g}^{\text{TR},(1)} + \ln \frac{Q^2}{M_H^2} C_{k,H}^{\text{TR},(0)} \otimes P_{qg}^{(0)}, \quad (2.26)$$

connecting the gluon coefficient functions in the FFNS and in the TR scheme. Eq. (2.26), rearranged as:

$$C_{k,g}^{\text{TR},(1)} = C_{k,g}^{\text{FF},(1)} - \ln \left(\frac{Q^2}{M_H^2} \right) C_{k,H}^{\text{TR},(0)} \otimes P_{qg}^{(0)}, \quad (2.27)$$

can be read as the iterative definition of $C_{k,g}^{\text{TR},(1)}$ in terms $C_{k,g}^{\text{TR},(0)}$. Any choice of $C_{k,g}^{\text{TR},(1)}$ and $C_{k,g}^{\text{TR},(0)}$ satisfying eq. (2.26) is equally correct. Therefore it is possible to use this freedom⁽⁵⁾ to choose $C_{k,g}^{\text{TR},(0)}$ in such a way that the transition of the structure function at the heavy quark threshold M_H is smooth.

To this end, we take the derivative with respect to $\ln Q^2$ of the LO term of eq. (2.24) obtaining:

$$\frac{dF_k^{H,\text{TR}}}{d \ln Q^2} = \frac{dC_{k,H}^{\text{TR},(0)}}{d \ln Q^2} \otimes f_H^+ + \frac{\alpha_s}{4\pi} C_{k,H}^{\text{TR},(0)} \otimes \left(P_{qg}^{(0)} \otimes f_H^+ + P_{qg}^{(0)} \otimes f_g \right) + \dots, \quad (2.28)$$

where we used the DGLAP equation for f_H^+ which reads:

$$\frac{df_H^+}{d \ln Q^2} = \frac{\alpha_s}{4\pi} \left(P_{qg}^{(0)} \otimes f_H^+ + P_{qg}^{(0)} \otimes f_g \right). \quad (2.29)$$

The derivative of the heavy quark structure function in the FFNS in eq. (2.11) instead is:

$$\frac{dF_k^{H,\text{FF}}}{d \ln Q^2} = \frac{\alpha_s}{4\pi} \frac{dC_{k,g}^{\text{FF},(1)}}{d \ln Q^2} \otimes f_g, \quad (2.30)$$

⁵This is exactly the same freedom that allowed to define S-ACOT from the ACOT scheme.

where we have omitted the order α_s^2 terms coming from the derivative of the gluon parton density f_g .

In order to have a smooth transition at the heavy quark threshold, the TR method requires that:

$$\left. \frac{dF_k^{H,\text{TR}}}{d \ln Q^2} \right|_{Q=M_H} = \left. \frac{dF_k^{H,\text{FF}}}{d \ln Q^2} \right|_{Q=M_H} \quad (2.31)$$

The choice of the matching threshold $Q = M_H$ leads to a further simplification in eq. (2.28). In fact, using eq. (2.25), we find that $f_H^+(x, M_H) = 0$ and finally we have that:

$$\left[C_{k,H}^{\text{TR},(0)} \otimes P_{qg}^{(0)} = \frac{dC_{k,g}^{\text{FF},(1)}}{d \ln Q^2} \right] \Big|_{Q=M_H}. \quad (2.32)$$

This relations allows to achieve the required smooth transition at the heavy quark threshold. Generalizing eq. (2.32) to be the definition of $C_{k,H}^{\text{TR},(0)}$ for all Q , identifies the TR scheme at LO.

From a phenomenological point of view, eq. (2.32) guarantees a smooth passage for the heavy quark structure function from $Q < M_H$ to $Q > M_H$. Moreover, taking the explicit derivative of $C_{k,g}^{\text{FF},(1)}$ in the limit $Q \rightarrow \infty$ one easily finds that:

$$\frac{dC_{k,g}^{\text{FF},(1)}}{d \ln Q^2} \rightarrow P_{qg}^{(0)}(x). \quad (2.33)$$

Hence, from eq. (2.32), we see that $C_{k,H}^{\text{TR},(0)}$ must indeed tend to $\delta(1-x)$ reproducing this way the correct ZM limit.

Furthermore, since $C_{k,g}^{\text{FF},(1)}$ contains the factor $\theta(W^2 - 4M_H^2)$, that ensures the correct threshold behavior, so does its derivative and in turn also $C_{k,H}^{\text{TR},(0)}$. Using eq. (2.32), then, guarantees the correct threshold behavior for $F_k^{H,\text{TR}}$ at LO.

Moreover, once $C_{k,H}^{\text{TR},(0)}$ is known, eq. (2.27) allows to calculate $C_{k,g}^{\text{TR},(1)}$ that again, due to the presence of the θ -function in both terms on the r.h.s., has the same threshold behavior as $C_{k,g}^{\text{FF},(1)}$.

Finally, using the explicit form of $C_{k,g}^{\text{FF},(1)}$, it is easy to check that in the limit $Q \rightarrow \infty$, $C_{k,g}^{\text{TR},(1)}$ does indeed tend to the correct asymptotic ZM $\overline{\text{MS}}$ limit.

In order to obtain the full order α_s structure function $F_k^{H,\text{TR}}$, only the coefficient function $C_{k,H}^{\text{TR},(1)}$ is missing. This contribution, though very small, requires the extension of $F_k^{H,\text{FF}}$ and of the matching conditions in eq. (2.25) to order α_s^2 and again $C_{k,H}^{\text{TR},(1)}$ is determined by imposing the continuity in the gluon sector. The details of the calculation are extensively worked out in Ref. [37].

In Fig. 2.4 the LO calculation for F_2^c in the TR scheme for two values of x is shown. It is evident that also the TR scheme, like the ACOT scheme, ensures a smooth transition from the description at low Q in terms of the FFNS to high Q in terms of the ZM-VFNS.

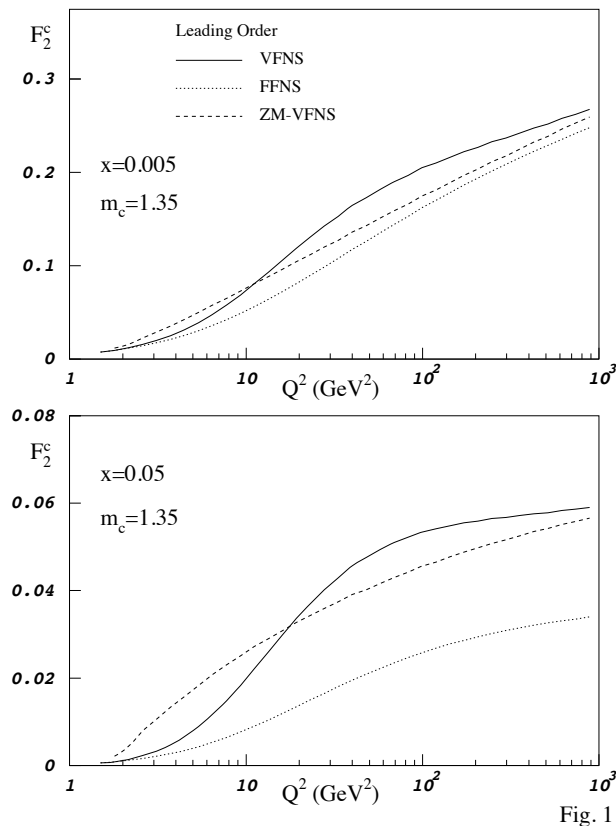


Figure 2.4: F_2^c for $x = 0.05$ and $x = 0.005$ calculated using the TR prescription at LO. Also shown are the LO FFNS and ZM-VFNS expressions [38].

2.3.1 The TR' Variant

The pure TR method, as described in the previous section, was used in the global analyses up to MRST 2004 [42]. However, it results in expressions which become increasingly more and more complicated at higher orders. Moreover, as clear from Fig. 2.4, it overshoots the ZM-VFNS before approaching it asymptotically from above. Here the need for a mass scheme that had the same threshold behavior as the TR scheme but simpler and more well-behaved in the central region.

In Ref. [34] the correct threshold behavior was already achieved simply by replacing the lower limit x of convolution integrals with the rescaled variable $\chi = x(1 + 4M_H^2/Q^2)$. If the heavy flavour coefficient functions are just the ZM ones, with this restriction, one obtains the ACOT- χ scheme. A very similar definition for heavy flavour coefficient functions was then adopted in Ref. [43], resulting in the TR' scheme, and extended explicitly to NNLO. The TR' scheme was first used in the MRST 2006 analysis [36] and for all the subsequent MSTW analyses.

The basic point of the TR' scheme is the requirement that the following relation for

the quark coefficient functions holds at any order⁽⁶⁾:

$$C_{k,H}^{\text{TR}',(n)}(Q/M_H, x) = C_{k,H}^{\text{ZM},(n)}(x/x_{\text{max}}), \quad x_{\text{max}} = \frac{Q^2}{Q^2 + M_H^2}. \quad (2.34)$$

This way, the TR' coefficient functions tend to the standard ZM-VFNS coefficient functions in the limit $Q \gg M_H$ but respect the threshold requirement $W^2 \geq 4M_H^2$ for heavy pair production.

Adopting this convention for the quark coefficient functions, one can easily derive the gluon coefficient functions using the usual matching conditions. In particular eq. (2.27) to derive the order α_s gluon coefficient function $C_{k,g}^{\text{TR}',(1)}$ knowing the α_s^0 quark coefficient function $C_{k,H}^{\text{TR}',(0)}$.

In the 'TR/TR' schemes there is an ambiguity stemming from the fact that ZM-VFNS and FFNS expressions for F_k^H in eqs. (2.10) and (2.11) have a different absolute perturbative ordering. Indeed the LO of the former is order α_s^0 while the LO of the latter is order α_s . Since any GM-VFNS interpolates between the two, there are two possible choices. One could simply adopt the absolute ordering, *i.e.* the same power of α_s , above and below the transition point $Q = M_H$. But at order α_s this would mean to use the LO expression for the FFNS contribution and the NLO for the ZM-VFNS contribution. In the TR/TR' schemes instead adopt a relative ordering where LO FFNS goes with LO ZM-VFNS, NLO FFNS goes with NLO ZM-VFNS and so on. The problem here is that at NNLO this requires the knowledge of the order α_s^3 FFNS coefficient functions which have not been calculated yet. In the MSTW NNLO analyses, however, the small- x and threshold limits are employed to this purpose [43].

2.4 The FONLL Method

The FONLL scheme was first introduced in the context of heavy flavour (bottom) hadro-production in Ref. [46]. It is based upon the idea of looking at both the massless and massive scheme calculations as power expansions in the strong coupling constant α_s , and replacing the coefficients of the expansion in the former with their exact massive counterparts in the latter, when available. The FONLL method has been subsequently applied to DIS in Ref. [47].

The FONLL method is presently implemented in the NNPDF analyses since 2011. The first set to implement it was the NNPDF2.1 set at NLO presented in Ref. [55], which was at a later stage extended to NNLO in Ref. [56]. The implementation of the FONLL method up to NNLO in the NNPDF framework is the central topic of this thesis and in Chapter 3 a detailed description of the method will be given. In this chapter, instead, we limit ourselves to a general introduction.

Exactly like the other GM-VFNS presented above, also the FONLL method is intended to provide a framework capable to be accurate over a wide range of energies. But differently from ACOT and TR, the FONLL method is simply based on the idea of combining the FFNS with the ZM-VFNS and subtracting the double counting terms between the two order by order in the expansion in powers of α_s and $\ln(Q^2/M_H^2)$. In

⁶This relation is strictly valid only for F_2^H , while for F_L^H it becomes a proportionally relation due to requirement that F_L^H is zero at $Q = M_H$.

practice, starting from the α_s expansion of ZM-VFNS expression, one replaces all the terms whose mass dependence is known with their exact massive expression.

Let us now see explicitly how the FONLL scheme works in the case of the heavy quark structure functions F_k^H [47]. Again the starting point are the structure functions in the FFNS and in the ZM-VFNS. Given that in Chapter 3 we will work out the full expressions of the FONLL scheme to NNLO, in the following we will not limit ourselves to order α_s as we did to illustrate the ACOT and the TR schemes. As a consequence, eqs. (2.10) and (2.11) will need to be generalized to order α_s^2 . At order α_s^2 it is no longer true that only the gluon and the heavy quark H contribute to the structure function F_k^H , but also the light quark-initiated channels open up⁽⁷⁾. Furthermore, the matching conditions to splice schemes having different number of active flavours are necessarily discontinuous at order α_s^2 , meaning that even performing the match at $Q = M_H$, both α_s and PDFs present a step in the matching point.

For the sake of simplicity, for the rest of the discussion we will assume N light flavours q and one single heavy flavour H having mass M_H . Moreover, we take the factorization and the renormalization scales μ_F and μ_R equal to each other and to the transferred energy Q , *i.e.* $\mu_F = \mu_R = \mu = Q$.

Under these assumptions, we can write in a more general form the structure functions in the ZM-VFNS as:

$$F_k^{H,\text{ZM}}(x, Q) = \sum_{i=g,q,\bar{q},H,\bar{H}} C_{k,i}^{\text{ZM}}(x, \alpha_s^{(N+1)}(Q)) \otimes f_i^{(N+1)}(x, Q). \quad (2.35)$$

Notice that in eq. (2.35) the sum runs over gluon, light and heavy flavours and the number of active flavours is explicitly shown in α_s and in the PDFs. Here, indeed, the heavy quarks are treated on the same footing as the light flavours and α_s and PDFs satisfy the standard evolution equations with $(N + 1)$ flavours.

The expression for the structure functions in the FFNS is instead given by:

$$F_k^{H,\text{FF}}(x, Q) = \sum_{i=g,q,\bar{q}} C_{k,i}^{\text{FF}}\left(x, \frac{M_H}{Q}, \alpha_s^{(N)}(Q)\right) \otimes f_i^{(N)}(x, Q). \quad (2.36)$$

Here the sum runs only over gluon and light flavours and the number of active flavours in the α_s and PDFs is equal to N .

We recall here that the ZM coefficient functions $C_{k,i}^{\text{ZM}}$ in eq. (2.35) at any given order k in α_s are obtained by setting explicitly $M_H = 0$ in the calculation and the arising IR singularities are subtracted in the $\overline{\text{MS}}$ scheme. This is equivalent to resumming the logarithmic terms $\alpha_s \ln(Q/M_H)$ up to $N^k\text{LL}$.

The FFNS coefficient functions $C_{k,i}^{\text{FF}}$ in eq. (2.36), instead, are obtained retaining the full dependence on M_H which in turn works as a regulator for the IR singularities. This is a pure $N^k\text{LO}$ fixed order calculation. Furthermore, in order to ensure the decoupling of the heavy flavour H , only N active flavours are present.

In order to work out the FONLL method, we first need to express the structure functions in the FFNS in eq. (2.36) in terms of $\alpha_s^{(N+1)}$ and $f_i^{(N+1)}$ for $i \neq H, \bar{H}$. Exactly

⁷This complication, apart from making the implementation much more involved, also causes an ambiguity in the definition of heavy quark structure function which is absent up to order α_s . We will return on this issues in Chapter 3.

like in the TR scheme, this is done using the matching conditions for α_s and PDFs reported in Refs. [57] and [48], respectively. In general, they have the form:

$$a_s^{(N+1)}(Q) = a_s^{(N)}(Q) \left[1 + \sum_{k=1}^P c_k(L) \left[a_s^{(N)}(Q) \right]^k \right] \quad (2.37)$$

$$f_i^{(N+1)}(x, Q) = f_j^{(N)}(x, Q) \otimes \left[\delta_{ij} \delta(1-x) + \sum_{k=1}^P \left[a_s^{(N)}(Q) \right]^k \sum_{j=g, q, \bar{q}} K_{ij}^{(k)}(x, L) \right],$$

where $i, j = g, q, \bar{q}, H, \bar{H}$ and:

$$a_s \equiv \frac{\alpha_s(Q)}{4\pi}, \quad L \equiv \ln \left(\frac{M_H}{Q} \right). \quad (2.38)$$

Both the coefficients $c_k(L)$ and the functions $K_{ij}^{(k)}(x, L)$ are polynomials in L and they have the general form:

$$c_k(L) = \sum_{n=0}^k b_n L^n \quad (2.39)$$

$$K_{ij}^{(k)}(x, L) = \sum_{n=0}^k g_{ij}^{(n)}(x) L^n.$$

Inverting both the equations in eq. (2.37), in such a way to express $\alpha_s^{(N)}$ in terms of $\alpha_s^{(N+1)}$ and $f_i^{(N)}$ in terms of $f_i^{(N+1)}$, and plugging the result into eq. (2.36), one obtains the expression for $F_k^{H, \text{FF}}$ in terms of $\alpha_s^{(N+1)}$ and $f_i^{(N+1)}$:

$$F_k^{H, \text{FF}}(x, Q) = \sum_{i=g, q, \bar{q}} B_{k,i}^{\text{FF}} \left(x, \frac{M_H}{Q}, \alpha_s^{(N+1)}(Q) \right) \otimes f_i^{(N+1)}(x, Q), \quad (2.40)$$

where the coefficient functions $B_{k,i}^{\text{FF}}$ are such that, substituting the matching conditions given in eq. (2.37) into eq. (2.40), one gets back the original expression in eq. (2.36) up to subleading terms. The expression given in eq. (2.40) for $F_k^{H, \text{FF}}$ allows one to avoid any further reference to $\alpha_s^{(N)}$ and $f_i^{(N)}$.

In order to match the two expressions for F_k^H in the ZM-VFNS, eq. (2.35), and in the FFNS, eq. (2.40), we need to work out the perturbative expansion of the respective coefficient functions.

In the ZM-VFNS at order $N^P \text{LO}$ (or better to say $N^P \text{LL}$) we have that:

$$\begin{aligned} C_{k,i}^{\text{ZM}}(x, \alpha_s^{(N+1)}(Q)) &= \sum_{p=0}^P \left[a_s^{(N+1)}(Q) \right]^p C_{k,i}^{\text{ZM},(p)}(x) \\ &= \sum_{p=0}^P \left[a_s^{(N+1)}(Q) \right]^p \sum_{j=0}^{\infty} A_{k,i}^{(p,j)}(x) \left[a_s^{(N+1)}(Q) L \right]^j, \end{aligned} \quad (2.41)$$

where the resummation of the logarithms L is embedded in the infinite series in j in the second line of eq. (2.41). Ordering the powers of α_s , eq. (2.41) can be rearranged in the following way:

$$C_{k,i}^{\text{ZM}}(x, \alpha_s^{(N+1)}(Q)) = \sum_{p=0}^P \left[a_s^{(N+1)}(Q) \right]^p \sum_{j=0}^p A_{k,i}^{(p-j,j)}(x) L^j + \mathcal{O} \left(\left[a_s^{(N+1)}(Q) \right]^{P+1} \right). \quad (2.42)$$

The massive FFNS coefficient functions $B_{k,i}^{\text{FF}}$, instead, admit a fixed order expansion of the form:

$$B_{k,i}^{\text{FF}} \left(x, \frac{M_H}{Q}, \alpha_s^{(N+1)}(Q) \right) = \sum_{p=0}^P \left[a_s^{(N+1)}(Q) \right]^p B_{k,i}^{\text{FF},(p)} \left(x, \frac{M_H}{Q} \right). \quad (2.43)$$

Each of the perturbative contributions $B_{k,i}^{\text{FF},(p)}$ to the FFNS coefficient functions in eq. (2.43) can be decomposed into a power suppressed part, which vanishes when $Q \gg M_H$, and a logarithmically enhanced part which instead blows up in the same limit. In particular, we can write:

$$B_{k,i}^{\text{FF},(p)} \left(x, \frac{M_H}{Q} \right) = B_{k,i}^{\text{FF0},(p)}(x, L) + \mathcal{O} \left(\frac{M_H}{Q} \right), \quad (2.44)$$

so that:

$$B_{k,i}^{\text{FF},(p)} \left(x, \frac{M_H}{Q} \right) \xrightarrow{Q \gg M_H} B_{k,i}^{\text{FF0},(p)}(x, L). \quad (2.45)$$

We can then define the so-called *zero mass limit* of the FFNS coefficient functions (FF0) as follows:

$$B_{k,i}^{\text{FF0}} \left(x, L, \alpha_s^{(N+1)}(Q) \right) = \sum_{p=0}^P \left[a_s^{(N+1)}(Q) \right]^p B_{k,i}^{\text{FF0},(p)}(x, L), \quad (2.46)$$

from which we define the *zero mass limit* of the structure functions in the FFNS as:

$$F_k^{H,\text{FF0}}(x, Q) = \sum_{i=g,q,\bar{q}} B_{k,i}^{\text{FF0}} \left(x, L, \alpha_s^{(N+1)}(Q) \right) \otimes f_i^{(N+1)}(x, Q). \quad (2.47)$$

Now, all the contributions to the FFNS coefficient functions in eq. (2.43) which do not vanish when $Q \gg M_H$ must also be present in the ZM-VFNS coefficient functions in eq. (2.42). But this terms are exactly the FF0 coefficient functions defined in eq. (2.45). Therefore, comparing eq. (2.42) with eq. (2.46), we deduce that:

$$B_{k,i}^{\text{FF0},(p)}(x, L) = \sum_{j=0}^p A_{k,i}^{(p-j,j)}(x) L^j. \quad (2.48)$$

This allows us to formulate the FONLL scheme as follows:

$$F_k^{H,\text{FONLL}}(x, Q) = F_k^{H,\text{FF}}(x, Q) + F_k^{H,\text{ZM}}(x, Q) - F_k^{H,\text{FF0}}(x, Q). \quad (2.49)$$

The interpretation of eq. (2.49) is straightforward: we start from $F_k^{H,ZM}$, then we subtract from it all the constant and logarithmically enhanced terms subtracting $F_k^{H,FF0}$, and finally we replace these terms with the exact massive contributions adding $F_k^{H,FF}$.

Now let us see how the FONLL scheme behaves in the two different energy regimes $Q \gg M_H$ and $Q \lesssim M_H$. Because of eq. (2.45), when $Q \gg M_H$ the massive structure functions $F_k^{H,FF}$ and $F_k^{H,FF0}$ cancel in eq. (2.49) so that $F_k^{H,FONLL}$ reduces to $F_k^{H,ZM}$. When instead $Q \lesssim M_H$, $F_k^{H,FONLL}$ tends to $F_k^{H,FF}$ because in this regime the difference $F_k^{H,ZM} - F_k^{H,FF0}$, due to eq. (2.48) and to the fact that the logarithm L is not large, is genuinely subleading in α_s .

As a conclusion, the FONLL scheme has the features that a GM-VFNS needs to have: it tends to the ZM-VFNS for $Q \gg M_H$ and to the FFNS for $Q \lesssim M_H$.

It should be observed that near the threshold the difference $F_k^{H,ZM} - F_k^{H,FF0}$, though formally subleading, could in practice be non-negligible. It may thus be convenient to suppress this term through a suitable kinematic factor when Q is near M_H . The suppression can be obtained modifying eq. (2.49) in the following way:

$$F_k^{H,FONLL}(x, Q) = F_k^{H,FF}(x, Q) + D_{\text{th}}(Q) \left[F_k^{H,ZM}(x, Q) - F_k^{H,FF0}(x, Q) \right], \quad (2.50)$$

where the empirical function D_{th} should be monotonically increasing, approach to one when $Q \gg M_H$ and be identically zero for $Q \leq M_H$. A suitable choice is then:

$$D_{\text{th}}(Q) = \theta(Q^2 - M_H^2) \left(1 - \frac{M_H^2}{Q^2} \right)^2. \quad (2.51)$$

This particular choice guarantees a smooth transition from zero to one as Q increases, ensuring also a continuous derivative in $Q = M_H$. In Chapter 6 the impact of the inclusion of the damping function D_{th} for the determination of the proton PDFs will be discussed.

Finally, in Fig. 2.5 the results for F_2^c in the FONLL-C scheme, which is the order α_s^2 implementation of the FONLL scheme (see Chapter 3), for two values of x are shown. This proves that, like the ACOT and the TR schemes, also the FONLL scheme presents a smooth transition from low Q , where it tends to the FFNS, to high Q , where it tends to the ZM-VFNS.

2.5 The BMSN Method

The structure functions in the FONLL scheme eq. (2.49) may look similar to a prescription suggested in Ref. [48], and then further discussed in Ref. [49] (see in particular eq. (5) of the latter), sometimes referred to as the BMSN prescription. This scheme is also based on the idea of combining computations performed in schemes which differ in the number of active flavours. However, in the BMSN method the issue of using PDFs defined in a single factorization scheme in all terms is not addressed (unlike in FONLL, where it is accomplished by expressing everything in terms of $\alpha_s^{(N+1)}$ and $f_i^{(N+1)}$). This

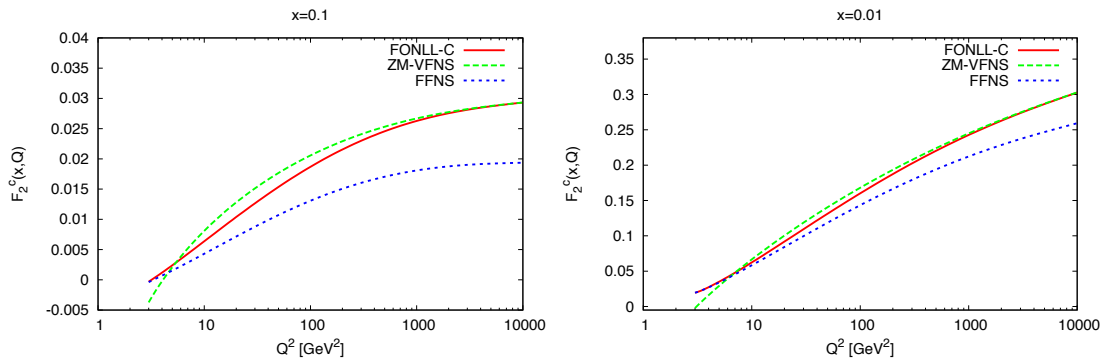


Figure 2.5: F_2^c for $x = 0.1$ and $x = 0.01$ calculated using the FONLL-C scheme (see Sec. 3.1.2). Also shown are the NNLO FFNS and ZM-VFNS predictions.

leads to inconsistent results beyond order α_s , as stated in Ref. [49], where it is argued that the inconsistency is however numerically small in practice.

Also, contributions proportional to the light or heavy quark electric charge are not easily separated in the BMSN method, again leading to (possibly small [49]) inconsistencies beyond order α_s , unlike in FONLL where this separation can be treated in a fully consistent way up to order α_s^2 as we will explicitly do in Chapter 3.

Chapter 3

Implementation of the FONLL Method

In this chapter the practical implementation of the FONLL scheme up to order α_s^2 will be discussed. In order to elucidate the details of the method, in Sec. 3.1 we shall first assume that the generic heavy quark structure functions F_k^H refer to the electromagnetic DIS structure functions, where only a virtual photon is exchanged between the incoming lepton and hadron. The more general case of the electro-weak boson mediated DIS structure functions will be instead presented in Sec. 3.2. Finally, in Sec. 3.3, the Mellin space implementation of the FONLL scheme is discussed.

3.1 Practical Implementation

First of all, we need to write the FONLL heavy quark structure functions explicitly in terms of coefficient functions and PDFs. To this end, we plug eqs. (2.35), (2.40) and (2.47) into eq. (2.49), obtaining:

$$F_k^{H,\text{FONLL}} = \sum_{i=g,q,\bar{q}} [B_{k,i}^{\text{FF}} + C_{k,i}^{\text{ZM}} - B_{k,i}^{\text{FF0}}] \otimes f_i^{(N+1)} + \sum_{i=H,\bar{H}} C_{k,i}^{\text{ZM}} \otimes f_i^{(N+1)}, \quad (3.1)$$

where, to simplify the notation, in eq. (3.1) all the dependencies on x and Q have been dropped. The sum on the r.h.s. of eq. (3.1) has been split in two pieces because the heavy quark PDFs f_H and $f_{\bar{H}}$ are convoluted only with the ZM-VFNS coefficient functions. This stems from the fact that heavy quark-initiated diagrams are present only in the ZM-VFNS and not in the FFNS. Finally, PDFs f_i and α_s entering eq. (3.1) are all expressed in the $(N+1)$ scheme. This is an important simplification that makes the method particularly suitable for PDF fits. The price to pay is that the coefficient functions $B_{k,i}^{\text{FF}}$ and $B_{k,i}^{\text{FF0}}$ are obtained from the combination of the standard FFNS coefficient functions with the matching conditions.

The next step is the perturbative expansion in α_s of eq. (3.1). This is the right point to get back to the issue that we raised in the previous chapter regarding the definition of heavy quark structure function. In Sec. 2.1, to define the heavy quark structure functions, we required a heavy quark in the final state as this is indeed the only possible experimental definition. Notwithstanding this fact, from the theoretical point of view

this is not a particularly suitable definition because the resulting observable is affected by final-state mass singularities in the limit $M_H \rightarrow 0$, which are due to the absence of virtual diagrams that prevent the cancellation of the collinear and soft singularities arising from the real diagrams [47]. For this reason the following definition is adopted here: *the heavy quark structure functions F_k^H are obtained from the inclusive structure functions F_k when only the electric charge e_H of the heavy quark H is different from zero.* In practice this means that the incoming virtual vector boson γ^* couples only to H and not to the other light quarks. It can be shown that this definition is free of mass singularities for $M_H \rightarrow 0$.

Now we can expand eq. (3.1) using eqs. (2.41), (2.43) and (2.46) as follows:

$$\begin{aligned}
F_k^{H,\text{FONLL}} &= e_H^2 \sum_{p=1}^P \left[a_s^{(N+1)} \right]^p \left[B_{k,g}^{\text{FF},(p)} + C_{k,g}^{\text{ZM},(p)} - B_{k,g}^{\text{FF0},(p)} \right] \otimes f_g^{(N+1)} \\
&+ e_H^2 \sum_{i=q,\bar{q}} \sum_{p=2}^P \left[a_s^{(N+1)} \right]^p \left[B_{k,i}^{\text{FF},(p)} + C_{k,i}^{\text{ZM},(p)} - B_{k,i}^{\text{FF0},(p)} \right] \otimes f_i^{(N+1)} \\
&+ e_H^2 \sum_{i=H,\bar{H}} \sum_{p=0}^P \left[a_s^{(N+1)} \right]^p C_{k,i}^{\text{ZM},(p)} \otimes f_i^{(N+1)}. \tag{3.2}
\end{aligned}$$

Notice that the overall factor e_H^2 , which had been omitted in Chapter 2, has been restored here.

The first line on the r.h.s. of eq. (3.2) corresponds to the gluon-initiated diagrams. All such diagrams, up to order α_s^2 , are shown in Fig. 3.1. Notice that the LO diagram is order α_s , and this is reflected in the sum over p in the first line of eq. (3.2) that starts from one. Furthermore, in the FONLL scheme both ZM-VFNS and FFNS contribute to this channel, thus all the coefficient functions $B_{k,g}^{\text{FF},(p)}$, $C_{k,g}^{\text{ZM},(p)}$ and $B_{k,g}^{\text{FF0},(p)}$ are present.

The second line on the r.h.s. of eq. (3.2), instead, corresponds to the light quark-initiated diagrams. Up to order α_s^2 , the only diagram that contributes to this channel is shown in Fig. 3.2. This is an order- α_s^2 diagram and thus the sum over p in the second line of eq. (3.2) starts from two. Again, both ZM-VFNS and FFNS contribute here.

Finally, the third line on the r.h.s. of eq. (3.2) corresponds to the heavy quark-initiated diagrams. Given that in the FFNS there are no such diagrams, this channel is purely ZM-VFNS, and indeed only the ZM coefficient functions $C_{k,i}^{\text{ZM},(p)}$ appear. In this case, the first non-vanishing order is α_s^0 , thus the sum over p starts from zero.

In order to completely work out the FONLL scheme for the heavy quark structure functions F_k^H , one essentially needs to express the r.h.s. of eq. (3.2) in terms of the basic ingredients currently available, that are:

- the ZM-VFNS coefficient functions $C_{k,i}^{\text{ZM},(p)}$ whose exact expressions are presently known up to order α_s^3 [58, 59, 60, 61, 62, 63],
- the FFNS coefficient functions $C_{k,i}^{\text{FF},(p)}$ and $C_{k,i}^{\text{FF0},(p)}$, whose exact expressions are known, only for $k = 1, 2$ and not for $k = 3$, up to order α_s^2 for the Neutral Current process [64] and up to order α_s for the Charged Current process [65],

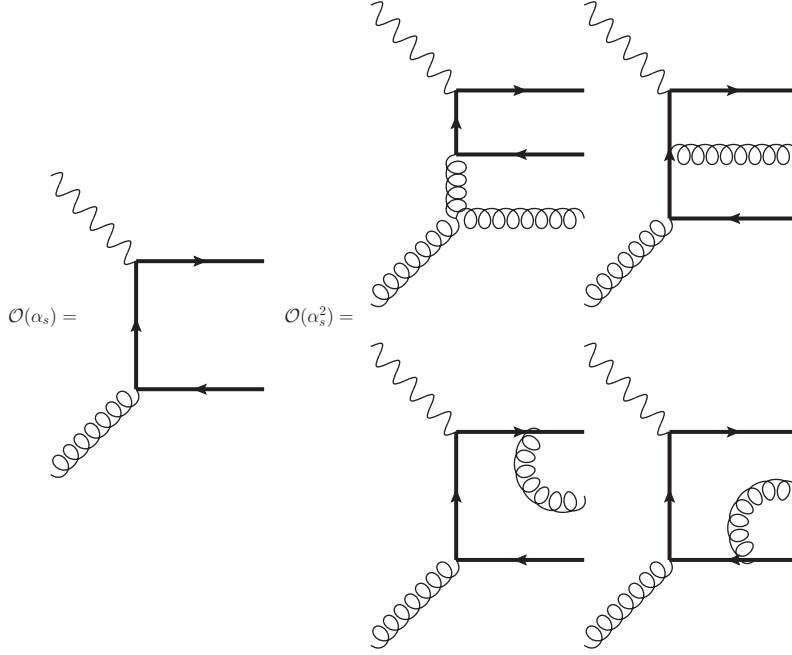


Figure 3.1: Gluon-initiated diagrams contributing to the heavy quark structure functions F_k^H up to order α_s^2 according to the definition given in the text. In these diagrams the thicker lines correspond to the heavy quark H while the thinner lines correspond to any light quark.

- the matching conditions for α_s and PDFs given by the functions $c_k(L)$ and $K_{ij}^{(k)}(x, L)$ in eq. (2.39), which are currently known up to order α_s^2 [48].

Starting from expansion in terms $\alpha_s^{(N)}$ of the massive coefficient functions:

$$C_{k,i}^{\text{FF}} = \sum_p \left[a_s^{(N)} \right]^p C_{k,i}^{\text{FF},(p)} \quad \text{and} \quad C_{k,i}^{\text{FF0}} = \sum_p \left[a_s^{(N)} \right]^p C_{k,i}^{\text{FF0},(p)}, \quad (3.3)$$

where the first P terms are assumed to be known, what we need to do in practice is to solve the equations:

$$\sum_p \left[a_s^{(N+1)} \right]^p B_{k,i}^{m,(p)} \otimes f_i^{(N+1)} = \sum_p \left[a_s^{(N)} \right]^p C_{k,i}^{m,(p)} \otimes f_i^{(N)} \quad (3.4)$$

with $m = \text{FF}, \text{FF0}$, with respect to $B_{k,i}^{m,(p)}$ order by order, using the matching conditions for α_s and PDFs given in eq. (2.37). This requires the inversion of the matching conditions in order to express the quantities in the N -flavour scheme in terms of the corresponding quantities in the $(N+1)$ -flavour scheme.

In the light quark-initiated channel the first non-vanishing order is α_s^2 , therefore eq. (3.4) reduces to:

$$\left[a_s^{(N+1)} \right]^2 B_{k,q}^{m,(2)} \otimes f_q^{(N+1)} = \left[a_s^{(N)} \right]^2 C_{k,q}^{m,(2)} \otimes f_q^{(N)}, \quad (3.5)$$

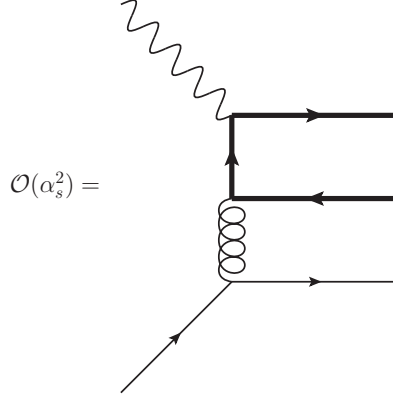


Figure 3.2: Light quark-initiated diagram contributing to the heavy quark structure functions F_k^H up to order α_s^2 according to the definition given in the text.

and given that $a_s^{(N)} = a_s^{(N+1)} + \mathcal{O}(\alpha_s^2)$ and $f_i^{(N)} = f_i^{(N+1)} + \mathcal{O}(\alpha_s)$ (cf. eq. (2.37)), one does not really need to invert the matching conditions because:

$$\left[a_s^{(N+1)} \right]^2 B_{k,q}^{m,(2)} \otimes f_q^{(N+1)} = \left[a_s^{(N+1)} \right]^2 C_{k,q}^{m,(2)} \otimes f_q^{(N+1)} + \mathcal{O}(\alpha_s^3), \quad (3.6)$$

so that:

$$B_{k,q}^{m,(2)} = C_{k,q}^{m,(2)}. \quad (3.7)$$

Of course, the corresponding quantity for the antiquark \bar{q} is identical to that for the quark q . Therefore, in the second line of the r.h.s. of eq. (3.2), up to order α_s^2 , one needs to replace $B_{k,i}^{m,(p)}$ with $C_{k,i}^{m,(p)}$.

For the gluon-initiated channel, instead, the matching conditions need to be explicitly inverted. However, since in this case the first non-vanishing order is α_s , we just need to invert the matching conditions only up to order α_s .

From eq. (2.37), for α_s we have:

$$a_s^{(N+1)}(Q) = a_s^{(N)}(Q) \left[1 + c_1(L) a_s^{(N)}(Q) + \mathcal{O}(\alpha_s^2) \right], \quad (3.8)$$

whose inverse is:

$$a_s^{(N)}(Q) = a_s^{(N+1)}(Q) \left[1 - c_1(L) a_s^{(N+1)}(Q) + \mathcal{O}(\alpha_s^2) \right]. \quad (3.9)$$

Similarly, for the PDFs we have:

$$f_i^{(N+1)} = \left[\delta_{ij} \delta(1-x) + a_s^{(N)} \sum_{j=g,q,\bar{q}} K_{ij}^{(1)}(x,L) + \mathcal{O}(\alpha_s^2) \right] \otimes f_j^{(N)}, \quad (3.10)$$

that, again, are easily inverted as:

$$f_i^{(N)} = \left[\delta_{ij} \delta(1-x) - a_s^{(N+1)} \sum_{j=g,q,\bar{q}} K_{ij}^{(1)}(x,L) + \mathcal{O}(\alpha_s^2) \right] \otimes f_j^{(N+1)}. \quad (3.11)$$

Now, plugging eqs. (3.9) and (3.11) into eq. (3.4), for the gluon coefficient functions one gets:

$$\begin{aligned} a_s^{(N+1)} B_{k,g}^{m,(1)} \otimes f_g^{(N+1)} + \left[a_s^{(N+1)} \right]^2 B_{k,g}^{m,(2)} \otimes f_g^{(N+1)} \\ = a_s^{(N+1)} C_{k,g}^{m,(1)} \otimes f_g^{(N+1)} \end{aligned} \quad (3.12)$$

$$+ \left[a_s^{(N+1)} \right]^2 \left[C_{k,g}^{m,(2)} - c_1(L) \delta(1-x) - K_{gg}^{(1)}(x, L) \right] \otimes f_g^{(N+1)} + \mathcal{O}(\alpha_s^3).$$

In the third line of eq. (3.12), we have used the fact that $K_{gg}^{(1)}(x, L) = 0$ [48]. Moreover, quite fortuitously, it turns out that:

$$K_{gg}^{(1)}(x, L) = -c_1(L) \delta(1-x), \quad (3.13)$$

so that the second and the third term in the square brackets in the third line of eq. (3.12) cancel. This leaves us with:

$$\begin{aligned} B_{k,g}^{m,(1)} &= C_{k,g}^{m,(1)} \\ B_{k,g}^{m,(2)} &= C_{k,g}^{m,(2)}. \end{aligned} \quad (3.14)$$

Finally, inserting eqs. (3.7) and (3.14) into eq. (3.2) and truncating the series at order α_s^2 ($P = 2$), we have that the heavy quark structure functions in the FONLL scheme in terms of the basic ingredients take the following form:

$$\begin{aligned} F_k^{H,\text{FONLL}} &= \sum_{p=1}^2 \left[a_s^{(N+1)} \right]^p \left[C_{k,g}^{\text{FF},(p)} + C_{k,g}^{\text{ZM},(p)} - C_{k,g}^{\text{FF0},(p)} \right] \otimes f_g^{(N+1)} \\ &+ \left[a_s^{(N+1)} \right]^2 \sum_{i=q,\bar{q}} \left[C_{k,i}^{\text{FF},(2)} + C_{k,i}^{\text{ZM},(2)} - C_{k,i}^{\text{FF0},(2)} \right] \otimes f_i^{(N+1)} \\ &+ \sum_{i=H,\bar{H}} \sum_{p=0}^2 \left[a_s^{(N+1)} \right]^p C_{k,i}^{\text{ZM},(p)} \otimes f_i^{(N+1)} + \mathcal{O}(\alpha_s^3). \end{aligned} \quad (3.15)$$

3.1.1 Light Structure Functions at order α_s^2

So far we have only considered the heavy quark structure functions F_k^H , whose exact definition has been given above. Given this definition, it is easy to deduce the complementary definition of *light quark structure functions* F_k^l as being the part of the inclusive structure functions F_k setting to zero the electric charge of all the heavy quarks. In practice, this means that the incoming virtual photon γ^* couples only to the light quarks.

In this section we will see how the light structure functions F_k^l are obtained in the FONLL framework. The starting point is the definition of FONLL light structure function, which is identical to that of heavy quark structure function given in eq. (2.49):

$$F_k^{l,\text{FONLL}}(x, Q) = F_k^{l,\text{FF}}(x, Q) + F_k^{l,\text{ZM}}(x, Q) - F_k^{l,\text{FF0}}(x, Q). \quad (3.16)$$

In this case, however, the expansion in powers of α_s gives much simpler results. In fact, the first diagrams involving heavy quarks which contribute to the light structure

functions $F_k^{l,\text{FONLL}}$ are the order α_s^2 light quark-initiated ones shown in Fig. 3.3, where a gluon radiates a heavy-quark pair. In practice, this means that⁽¹⁾:

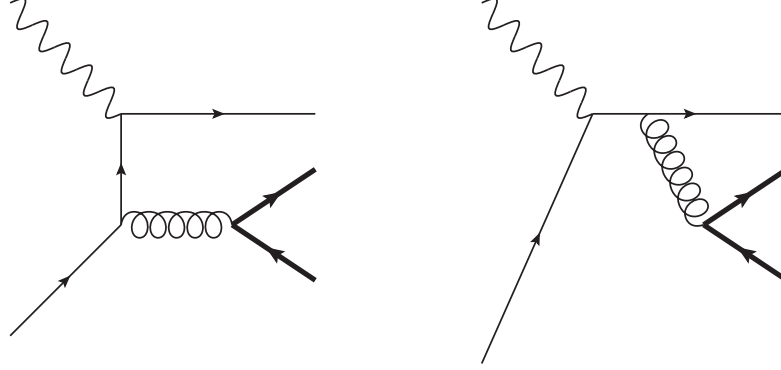


Figure 3.3: Light quark-initiated diagrams contributing to the light quark structure functions F_K^l involving the heavy quark H .

$$F_k^{l,\text{FONLL}}(x, Q) = F_k^{l,\text{ZM}}(x, Q) + \left[a_s^{(N+1)} \right]^2 F_k^{l,\text{GR},(2)} + \mathcal{O}(\alpha_s^3), \quad (3.17)$$

where:

$$F_k^{l,\text{GR},(2)} = \sum_{i=q,\bar{q}} e_i^2 \left[B_{k,\text{GR}}^{\text{FF},(2)} - B_{k,\text{GR}}^{\text{FF0},(2)} \right] \otimes f_i^{(N+1)} \quad (3.18)$$

is the contribution associated to the diagrams in Fig. 3.3. Now we just need to write $B_{k,\text{GR}}^{\text{FF},(2)}$ and $B_{k,\text{GR}}^{\text{FF0},(2)}$, *i.e.* the massive coefficient functions in the $(N+1)$ -flavour scheme, in terms of the coefficient functions $C_{k,\text{GR}}^{\text{FF},(2)}$ and $C_{k,\text{GR}}^{\text{FF0},(2)}$, that are the “standard” massive coefficient functions in the N -flavour scheme. To this end, we use the very same procedure followed to obtain eq. (3.12) but we omit here the calculations that, involving also order α_s^0 coefficient functions are pretty lengthy, and only quote the result:

$$B_{k,\text{GR}}^{m,(2)} = C_{k,\text{GR}}^{m,(2)} - c_1 C_{k,q}^{\text{ZM},(1)} - K_{qq}^{(2)}, \quad (3.19)$$

with $m = \text{FF}, \text{FF0}$.

Once also the light structure functions $F_k^{l,\text{FONLL}}$ has been defined in the FONLL scheme, taking the flavours up, down and strange as light and charm, bottom and top as heavy, one can obtain the *inclusive* FONLL structure functions F_k^{FONLL} as the sum of light and heavy components as follows:

$$F_k^{\text{FONLL}}(x, Q) = F_k^{l,\text{FONLL}}(x, Q) + \sum_{H=c,b,t} F_k^{H,\text{FONLL}}(x, Q). \quad (3.20)$$

¹Actually, this is not as straightforward as it looks. In fact, in principle contributions coming from the inversion of the matching conditions could already appear at order α_s . However, due to the fact that in eq. (2.37) $K_{qq}^{(1)}(x, L) = 0$ [48], it does not happen.

3.1.2 Perturbative Ordering

As already mentioned in Chapter 2, the perturbative ordering in matching ZM-VFNS and FFNS in the FONLL structure functions is somehow a matter of definition. The central point is that the LO contribution to heavy quark production in the ZM-VFNS is order α_s^0 (heavy quark-initiated diagram) while in the FFNS it is order α_s (gluon-initiated diagrams). There are then two possibilities: either the two schemes are combined order by order in α_s (*absolute ordering*) or the combination is done matching LO with LO, NLO with NLO and so on (*relative ordering*). Until now we have worked implicitly assuming the absolute ordering in the construction of the FONLL structure functions. However, this issue is in general non-trivial because in a global parton fit one may want to combine data for observables whose LO starts at different orders in α_s .

One option is then to simply adopt an absolute perturbative ordering, whereby at NLO all quantities are computed at order α_s . We will refer to it as scheme A henceforth.

However, we can also adopt the relative approach and use different accuracies in α_s but same relative ordering in the computation of the different contributions to the FONLL structure functions. At NLO, it is then necessary to compute the ZM coefficient functions $C_{k,i}^{\text{ZM}}$ only up α_s because this is the NLO in the ZM sector, but all massive coefficient functions $B_{k,i}^{\text{FF}}$ and their zero-mass limits $B_{k,i}^{\text{FF0}}$ should be computed to order α_s^2 in order to have the same relative accuracy in the massive sector. However, to ensure consistency of the subtraction of the large logarithms it is sufficient to include only logarithmic terms in $B_{k,i}^{\text{FF0}}$, because the corresponding non-logarithmic terms are not included in the massless coefficient functions $C_{k,i}^{\text{ZM}}$. We will refer to this as scheme B.

We can finally also pursue a full order α_s^2 computation, by simply performing the absolute-ordered computation of scheme A to one extra order. We will refer to this as scheme C.

In summary, there are three options for perturbative ordering, namely:

- Scheme A: the order α_s FONLL of eqs. (3.15) and (3.17).
- Scheme B: the order α_s ZM coefficient functions and retaining the order α_s^2 contributions to the massive coefficient functions in eqs. (3.15) and (3.17). In this case, however, the massive expressions exceed in accuracy the massless ones when $Q \simeq M_H$. Thus, in the zero-mass limit expressions of the FFNS coefficient functions, the non-logarithmic terms of order α_s^2 should not be included.
- Scheme C: the order α_s^2 FONLL of eqs. (3.15) and (3.17).

We should finally remark that schemes A and B, being formally NLO schemes, require α_s and PDFs evolved using the respective NLO evolution equations. The scheme C instead, being a NNLO scheme, requires the NNLO evolution.

3.2 Electro-weak Structure Functions

In the previous sections we have considered the implementation of the DIS heavy quark structure functions only in the case in which the heavy quark was produced in an electron-hadron process via the exchange of virtual photon γ^* . Strictly speaking, this

is correct only if $Q \ll M_W$, *i.e.* when the transferred energy is not sufficient to generate a massive electro-weak vector boson Z^0 or W^\pm . If this is not the case, the above treatment must be generalized and there are essentially two categories to be considered: the Neutral Current (NC) processes, where a neutral massive virtual boson γ^*/Z^0 is exchanged, and the Charged Current (CC) processes, where instead a charged massive virtual boson W^\pm is exchanged.

It is straightforward to generalize the above discussion to the case of a general NC process. The only modifications needed with respect to pure photon exchange is the replacement of the electric charges with the corresponding weak charges.

In the case of the structure functions F_1 and F_2 , one has to perform the following replacement:

$$e_q^2 \rightarrow B_q(Q) = e_q^2 - 2e_q V_e V_q P_Z(Q) + (V_e^2 + A_e^2)(V_q^2 + A_q^2) P_Z^2(Q), \quad (3.21)$$

where:

$$P_Z(Q) = \frac{1}{4 \sin^2 \theta_W (1 - \sin^2 \theta_W)} \left(\frac{Q^2}{Q^2 + M_Z^2} \right), \quad (3.22)$$

being θ_W the weak mixing angle, e_q the electric charge of the quark flavour q and V_f and A_f , with $f = q, e$, the vector and axial couplings of the fermion f to the Z^0 boson. The specific values of the couplings are collected in Tab. 3.1.

f	e_f	V_f	A_f
u, c, t	$+\frac{2}{3}$	$+\frac{1}{2} - \frac{4}{3} \sin^2 \theta_W$	$+\frac{1}{2}$
d, s, b	$-\frac{1}{3}$	$-\frac{1}{2} + \frac{2}{3} \sin^2 \theta_W$	$-\frac{1}{2}$
ν_e, ν_μ, ν_τ	0	$+\frac{1}{2}$	$+\frac{1}{2}$
e, μ, τ	-1	$-\frac{1}{2} + 2 \sin^2 \theta_W$	$-\frac{1}{2}$

Table 3.1: Coupling of fermions to the Z^0 boson.

The structure function F_3 , instead, is absent in a purely electromagnetic scattering. In fact, it embodies the parity violating part of the scattering and it appears only when the Z^0 boson starts contributing. The weak charge to associate to the quark flavour q in F_3 is given by:

$$D_q(Q) = -2e_q A_q A_e P_Z(Q) + 4V_q A_q V_e A_e P_Z^2(Q). \quad (3.23)$$

The generalization to CC process is slightly more complicated. In fact, here we need a different definition for the heavy structure functions and, consequently, for the light ones. To this end, we consider the general form of the inclusive CC proton structure

functions from neutrino scattering F_k^ν , writing explicitly the CKM matrix elements⁽²⁾:

$$\begin{aligned}
F_k^\nu = & 2\left\{ C_{k,q} \otimes \left[(|V_{ud}|^2 + |V_{cd}|^2 + |V_{td}|^2) f_d \right. \right. \\
& \pm (|V_{ud}|^2 + |V_{us}|^2 + |V_{ub}|^2) f_{\bar{u}} \\
& + (|V_{us}|^2 + |V_{cs}|^2 + |V_{ts}|^2) f_s \\
& \pm (|V_{cd}|^2 + |V_{cs}|^2 + |V_{cb}|^2) f_{\bar{c}} \\
& + (|V_{ub}|^2 + |V_{cb}|^2 + |V_{tb}|^2) f_b \\
& \left. \pm (|V_{td}|^2 + |V_{ts}|^2 + |V_{tb}|^2) f_{\bar{t}} \right] \\
& \left. + c_g^{CC} C_{k,g} \otimes f_g \right\}, \tag{3.24}
\end{aligned}$$

where the + signs in eq. (3.24) have to be taken for $k = 1, 2$ and the – signs for $k = 3$, moreover:

$$c_g^{CC} \equiv 2 \sum_{i=u,c,t} \sum_{j=d,s,b} |V_{ij}|^2. \tag{3.25}$$

The CC anti-neutrino structure functions $F_k^{\bar{\nu}}$ can be easily obtained from eq. (3.24) replacing each PDF with the PDF of the respective antiquark and, only for $k = 3$, changing the overall sign.

As in the NC heavy quark structure functions, a suitable definition is based on the use of the couplings, which in this case are the CKM matrix elements: such a definition is indeed free of mass singularity when $M_H \rightarrow \infty$. We adopt then the following definitions:

1. the CC light structure functions are composed by the terms of eq. (3.24) which are proportional to those CKM matrix elements containing *only* light flavours (i.e. u , d and s),
2. the CC heavy structure functions associated to the heavy flavour H are instead given by the terms proportional to V_{HK} or V_{KH} , such that $M_H > M_K$.

In practice, this means dividing the CKM matrix in the following way:

$$V_{CKM} = \begin{pmatrix} V_{ud} & V_{us} & V_{ub} \\ V_{cd} & V_{cs} & V_{cb} \\ V_{td} & V_{ts} & V_{tb} \end{pmatrix} \tag{3.26}$$

where the red terms contribute to the light structure functions, the blue terms to the charm, the green terms to the bottom and the violet terms to the top structure functions.

This definition, that may look a bit peculiar, turns out to be useful when mass effects are taken into account. In fact, one does not want bottom mass effects to contribute to the charm structure functions and this definition is formulated in such a way that, for a given heavy flavour H , no flavour heavier than H itself enters the respective structure functions. In particular, only light flavours contribute to the light structure functions.

²The form eq. (3.24) is strictly valid in the ZM-VFNS and using the unitarity of the CKM matrix it reduces to a much simpler formula where the CKM matrix element do not enter at all (*cf.* eqs. (2.39)-(2.42) of Ref. [66]). However, the FFNS form can be obtained setting to zero the heavy quark PDFs in eq. (3.24) and limiting only to the light flavours the sum in eq. (3.25).

Putting into practice this recipe, the explicit form of the CC structure functions is given by:

$$\begin{aligned}
F_k^{\nu,l} &= 2 \left\{ C_{k,q} \otimes \left[|V_{ud}|^2 f_d + (|V_{ud}|^2 + |V_{us}|^2) f_{\bar{u}} + |V_{us}|^2 f_s \right] \right. \\
&\quad \left. + 2 (|V_{ud}|^2 + |V_{us}|^2) C_{k,g} \otimes f_g \right\} \\
F_k^{\nu,c} &= 2 \left\{ C_{k,q} \otimes \left[|V_{cd}|^2 (f_d + f_{\bar{c}}) + |V_{cs}|^2 (f_s + f_{\bar{c}}) \right] \right. \\
&\quad \left. + 2 (|V_{cd}|^2 + |V_{cs}|^2) C_{k,g} \otimes g \right\} \\
F_k^{\nu,b} &= 2 \left\{ C_{k,q} \otimes \left[|V_{ub}|^2 (f_{\bar{u}} + f_b) + |V_{cb}|^2 (f_{\bar{c}} + f_b) \right] \right. \\
&\quad \left. + 2 (|V_{ub}|^2 + |V_{cb}|^2) C_{k,g} \otimes f_g \right\} \\
F_k^{\nu,t} &= 2 \left\{ C_{k,q} \otimes \left[|V_{td}|^2 (f_d + f_{\bar{t}}) + |V_{ts}|^2 (f_s + f_{\bar{t}}) + |V_{tb}|^2 (f_b + f_{\bar{t}}) \right] \right. \\
&\quad \left. + 2 (|V_{td}|^2 + |V_{ts}|^2 + |V_{tb}|^2) C_{k,g} \otimes f_g \right\},
\end{aligned} \tag{3.27}$$

for $k = 1, 2$ and:

$$\begin{aligned}
F_3^{\nu,l} &= 2 \left\{ C_{3,q} \otimes \left[|V_{ud}|^2 f_d - (|V_{ud}|^2 + |V_{us}|^2) f_{\bar{u}} + |V_{us}|^2 f_s \right] \right. \\
&\quad \left. + (|V_{ud}|^2 + |V_{us}|^2) C_{3,g} \otimes f_g \right\} \\
F_3^{\nu,c} &= 2 \left\{ C_{3,q} \otimes \left[|V_{cd}|^2 (f_d - f_{\bar{c}}) + |V_{cs}|^2 (f_s - f_{\bar{c}}) \right] \right. \\
&\quad \left. + (|V_{cd}|^2 + |V_{cs}|^2) C_{3,g} \otimes f_g \right\} \\
F_3^{\nu,b} &= 2 \left\{ C_{3,q} \otimes \left[|V_{ub}|^2 (-f_{\bar{u}} + f_b) + |V_{cb}|^2 (-f_{\bar{c}} + f_b) \right] \right. \\
&\quad \left. + (|V_{ub}|^2 + |V_{cb}|^2) C_{3,g} \otimes f_g \right\} \\
F_3^{\nu,t} &= 2 \left\{ C_{3,q} \otimes \left[|V_{td}|^2 (f_d - f_{\bar{t}}) + |V_{ts}|^2 (f_s - f_{\bar{t}}) + |V_{tb}|^2 (f_b - f_{\bar{t}}) \right] \right. \\
&\quad \left. + (|V_{td}|^2 + |V_{ts}|^2 + |V_{tb}|^2) C_{3,g} \otimes f_g \right\}.
\end{aligned} \tag{3.28}$$

Finally, it is easy to verify that:

$$F_k^\nu(x, Q) = F_k^{\nu,l}(x, Q) + \sum_{H=c,b,t} F_k^{\nu,H}(x, Q). \tag{3.29}$$

Having eqs. (3.27) and (3.28) for F_k^ν , one can construct the respective FONLL structure functions following the very same procedure described in Sec. 3.1. However, while the full order α_s^2 ZM CC coefficient functions are known (being identical to the NC ones), the order α_s^2 massive CC are not available yet. Only their asymptotic $Q \gg M_H$ limit [67] and their threshold behavior [68] are currently known, so that the FONLL can be fully implemented only up to order α_s . Nonetheless, a partial order α_s^2 implementation, where the respective massive coefficient functions are set to zero, can still be employed.

3.3 Mellin Space Implementation

In order to illustrate how the FONLL scheme is implemented in the NNPDF code, we start recalling here that a generic structure function F is given by the Mellin convolution of coefficient functions with PDFs:

$$F(x, Q) = \sum_i C_i(x, Q) \otimes f_i(x, Q). \quad (3.30)$$

However, one is usually interested in expressing all the observables in terms of the PDFs f_i at some initial scale Q_0 . To do so, one must solve the DGLAP equation whose solution can be written again as the following Mellin convolution:

$$f_i(x, Q) = \sum_j \Gamma_{ij}(x, Q, Q_0) \otimes f_j(x, Q_0), \quad (3.31)$$

where $\Gamma_{ij}(x, Q, Q_0)$ are the evolution operators that evolve PDFs from the scale Q_0 to the scale Q . Plugging eq. (3.31) into eq. (3.30), we get:

$$F(x, Q) = \sum_{ij} C_i(x, Q) \otimes \Gamma_{ij}(x, Q, Q_0) \otimes f_j(x, Q_0). \quad (3.32)$$

The implementation of eq. (3.32) in a numerical code can follow (at least) two ways.

The first is the direct numerical integration of the double convolution between coefficient functions, evolution operators and PDFs. This, of course, requires also a numerical solution of the DGLAP equation, which is an integro-differential equation. This is certainly the most direct and intuitive way to give a prediction for $F(x, Q)$. This approach, however, strongly relies on numerical algorithms given that the convolutions and the solution of the DGLAP equation cannot be performed analytically.

A second and alternative approach, adopted by the NNPDF collaboration, allows for a more analytical treatment of the problem and is the so-called Mellin space (or N -space) method. This is based on the *Mellin transformation* which, for a function $f(x)$, is defined as:

$$f(N) \equiv \mathbf{M}[f(x)](N) = \int_0^1 dx x^{N-1} f(x), \quad N \in \mathbb{C}. \quad (3.33)$$

As is well known, the great advantage of the Mellin transformation is that the Mellin convolution, that understands an integral over the Bjorken variable x , in the N -space is turned into a simple product.

As a consequence, eq. (3.32) in N -space takes the simpler multiplicative form:

$$F(N, Q) = \sum_{ij} C_i(N, Q) \Gamma_{ij}(N, Q, Q_0) f_j(N, Q_0). \quad (3.34)$$

In addition, the N -space evolution operators $\Gamma_{ij}(N, Q, Q_0)$ are the solutions of the DGLAP equation in the N -space that is no longer an integro-differential equation but a much simpler first order differential equation that can be solved analytically.

The better analytical control of the Mellin method with respect to the direct x -space solution however comes with a price to be paid.

First of all, it requires the analytical Mellin transform of all the expressions involved, in particular coefficient functions and evolution operators⁽³⁾. This point will be extensively discussed later.

Secondly, once the structure functions in the N -space have been obtained, in order to have a prediction that can be compared to data, one needs to get back to the x -space. This requires the *inverse Mellin transformation* whose definition is:

$$f(x) = \frac{1}{2\pi i} \int_{c-i\infty}^{c+i\infty} dN x^{-N} f(N), \quad (3.35)$$

where the real number c has to be such that the integral $\int_0^1 dx x^{c-1} f(x)$ is absolutely convergent. Hence c has to lie to the right of the rightmost singularity of $f(N)$ in the complex plane. The contour of the integration in eq. (3.35) is shown in Fig. 3.4 and denoted by the green line while the (hypothetical) poles of $f(N)$ by the blue crosses.

Under the assumption that $f(N)$ is an analytical (or holomorphic) function, the Cauchy theorem states that one can deform the integration path in a continuous way without changing the result of the integral, provided that no pole of the function $f(N)$ is crossed during the deformation. This allows us to cleverly choose a different path that makes the solution of the integral in eq. (3.35) easy to implement in a numerical code. A possible choice is the so-called Talbot path \mathcal{C}_T , such that eq. (3.35) is equivalent to:

$$f(x) = \frac{1}{2\pi i} \int_{\mathcal{C}_T} dN x^{-N} f(N), \quad (3.36)$$

where:

$$\mathcal{C}_T : \{N(\theta) = r\theta(\cot \theta + i); \theta \in (-\pi, +\pi)\} \quad (3.37)$$

being r a parameter possibly depending only on x . The Talbot path in eq. (3.37) is showed in Fig. 3.4 and denoted by the red line.

Performing a variable substitution in eq. (3.36) using eq. (3.37) and defining $t \equiv -\ln x$, one gets:

$$\begin{aligned} f(x) &= \frac{1}{2\pi i} \int_{-\pi}^{+\pi} d\theta \frac{dN(\theta)}{d\theta} e^{tN(\theta)} f(N(\theta)) \\ &= \frac{r}{2\pi} \int_{-\pi}^{+\pi} d\theta [1 + i\sigma(\theta)] e^{tN(\theta)} f(N(\theta)), \end{aligned} \quad (3.38)$$

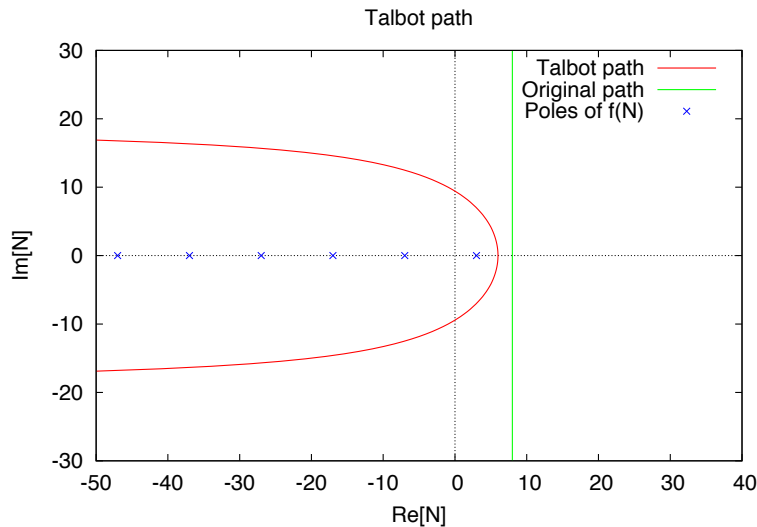
with:

$$\sigma(\theta) = \theta + \cot \theta(\theta \cot \theta - 1). \quad (3.39)$$

From eq. (3.37) one can easily see that $N(-\theta) = N^*(\theta)$, while from eq. (3.39) it is evident that $\sigma(\theta)$ is an odd function of θ . Moreover, $f(N)$ being the Mellin transform of a real function, one automatically has that $f(N^*) = f^*(N)$. Using this information, one gets:

$$f(x) = \frac{r}{\pi} \int_0^{+\pi} d\theta \operatorname{Re} \left\{ [1 + i\sigma(\theta)] e^{tN(\theta)} f(N(\theta)) \right\}, \quad (3.40)$$

³In principle also the Mellin transform of the PDFs would be required but, using the so called **FastKernel** method [69], one can essentially keep the second convolution on the r.h.s. of eq. (3.32) performing the integration interpolating over an x -space grid with a set of cubic Hermite polynomials.

Figure 3.4: Talbot path on the N plane.

where $\text{Re}\{\dots\}$ is the real part of its argument. Finally, eq. (3.40) can be solved numerically using, for instance, the trapezoidal approximation.

Once we know how to get back from the N -space to the x -space, we can go back to the question of the analytical Mellin transforms of coefficient functions and evolution operators appearing in eq. (3.34). We will treat this issue separately for splitting functions, on which evolution operators depend, and coefficient functions in the following sections.

3.3.1 Splitting Functions

The splitting functions $P_{ij}(x, \mu)$ entering the DGLAP equation were already introduced in Chapter 1. As is well known, they admit the perturbative expansion:

$$P_{ij}(x, \mu) = \sum_{k=0}^m a_s^k(\mu) P_{ij}^{(k)}(x), \quad (3.41)$$

where the coefficients of the expansion are presently known up to three loops (*i.e.* $m = 2$) [16, 19, 20, 21, 22]. The LO contributions to eq. (3.41) [16], two of which ($P_{qq}^{(0)}$ and $P_{gq}^{(0)}$) were already given in Chapter 1, are compact enough and we report them in here

along with the corresponding splitting diagrams:

$$\begin{aligned}
& \begin{array}{c} \text{diagram 1} \\ \text{diagram 2} \\ \text{diagram 3} \\ \text{diagram 4} \end{array} \quad P_{qq}^{(0)}(x) = 2C_F \left[\frac{1+x^2}{(1-x)_+} + \frac{3}{2}\delta(1-x) \right] \\
& \begin{array}{c} \text{diagram 5} \\ \text{diagram 6} \end{array} \quad P_{gq}^{(0)}(x) = 2T_R [x^2 + (1-x)^2] \\
& \begin{array}{c} \text{diagram 7} \end{array} \quad P_{gq}^{(0)}(x) = 2C_F \left[\frac{1+(1-x)^2}{x} \right] \\
& \begin{array}{c} \text{diagram 8} \end{array} \quad P_{gq}^{(0)}(x) = 4C_A \left[\frac{x}{(1-x)_+} + \frac{1-x}{x} + x(1-x) \right] + \delta(1-x) \frac{11C_A - 4N_f T_R}{3}.
\end{aligned} \tag{3.42}$$

C_F , T_R and C_A being the usual $SU(3)$ color factors:

$$C_F = \frac{4}{3}, \quad T_R = \frac{1}{2}, \quad C_A = 3. \tag{3.43}$$

Notice that in the splitting functions in eq. (3.42) the so-called *plus prescription* appears which is meant to regulate the soft $x \rightarrow 1$ singularities. Its definition, when the integration bounds are 0 and 1 has already been given in eq. (1.16). However, given the generic function $f(x)$, the following more general definition that holds for any integration bound can be given:

$$[f(x)]_+ \equiv \lim_{\beta \rightarrow 0} \left[\theta(1-\beta-x)f(x) - \delta(1-\beta-x) \int_0^{1-\beta} dy f(y) \right]. \tag{3.44}$$

Using eq. (3.44), it is easy to derive eq. (1.16) as a special case for the function $1/(1-x)$. The plus prescription is an important ingredient for the computation of the Mellin transform of functions like those appearing in eq. (3.42). In fact, using eqs. (3.33) and (3.44) the Mellin transform of the splitting functions in eq. (3.42), called anomalous dimensions, is given by:

$$\begin{aligned}
P_{qq}^{(0)}(N) &= 2C_F \left[\frac{1}{N(N+1)} - 2S_1(N) + \frac{3}{2} \right] \\
P_{gq}^{(0)}(N) &= 2T_R \left[\frac{2+N+N^2}{N(N+1)(N+2)} \right] \\
P_{gq}^{(0)}(N) &= 2C_F \left[\frac{2+N+N^2}{N(N^2-1)} \right] \\
P_{gq}^{(0)}(N) &= 4C_A \left[\frac{1}{N(N-1)} + \frac{1}{(N+1)(N+2)} - S_1(N) + \frac{11}{12} \right] - \frac{4}{3} N_f T_R.
\end{aligned} \tag{3.45}$$

The results in eq. (3.45) are given in terms of the harmonic function $S_1(N)$ whose definition is [70]:

$$S_l(N) \equiv \zeta(l) - \frac{(-1)^l}{(l-1)!} \psi^{(l-1)}(N-1). \quad (3.46)$$

Here $\zeta(1) = \gamma_E$, where γ_E is the Euler-Mascheroni constant, while $\zeta(l > 1)$ is the Riemann ζ -function evaluated in the integer l , and $\psi^{(l-1)}$ is the l -th logarithmic derivative of the Euler Γ -function also called polygamma.

The NLO and NNLO contributions to the splitting functions $P_{ij}^{(1)}(x)$ and $P_{ij}^{(2)}(x)$, reported in Refs. [21, 22], are definitely more involved than $P_{ij}^{(0)}(x)$ and so are their Mellin transforms. However, while the expressions for $P_{ij}^{(1)}(x)$, though pretty lengthy, are still reasonably short to be implemented in an efficient numerical code, the expressions for $P_{ij}^{(2)}(x)$ are instead huge and would require many calls to special external functions (*cf.* for instance eqs. (4.9), (4.10) and (4.11) of Ref. [21] and eqs. (3.10), (3.11), (3.12) and (3.13) of Ref. [22]). This makes their implementation very inefficient. It is then useful to have at one's disposal also compact approximate representations [70] involving, besides powers of x , only simple functions like:

$$D_0 = \frac{1}{(1-x)_+}, \quad L_1 = \ln(1-x), \quad L_0 = \ln(x), \quad (3.47)$$

and possibly their powers.

These compact expressions are determined fitting a template functions, constructed using the simple functions in eq. (3.47) to the exact expressions. Besides the regular functions in eq. (3.47), also a ‘‘local’’ term proportional to $\delta(1-x)$ could be included in the parametrization, and its numerical coefficient is determined fitting the template expression to the exact expression of the first Mellin moments of the coefficient functions. An example of such compact parametrization is the pure-singlet component $P_{ps}^{(2)}$ of splitting functions $P_{qq}^{(2)} \equiv P_{ps}^{(2)} + P_{ns}^{(2)}$ whose parametrized form is [22]:

$$\begin{aligned} P_{ps}^{(2)}(x) \simeq & \left\{ N_f \left(-5.926L_1^3 - 9.751L_1^2 - 72.11L_1 + 177.4 + 392.9x \right. \right. \\ & \left. \left. - 101.4x^2 - 57.04L_0L_1 - 661.6L_0 + 131.4L_0^2 - 400/9L_0^3 \right. \right. \\ & \left. \left. + 160/27L_0^4 - 506.0x^{-1} - 3584/27x^{-1}L_0 \right) \right. \\ & \left. + N_f^2 \left(1.778L_1^2 + 5.944L_1 + 100.1 - 125.2x + 49.26x^2 \right. \right. \\ & \left. \left. - 12.59x^3 - 1.889L_0L_1 + 61.75L_0 + 17.89L_0^2 + 32/27L_0^3 \right. \right. \\ & \left. \left. + 256/81x^{-1} \right) \right\} (1-x). \end{aligned} \quad (3.48)$$

Except for x values very close to zeros of the exact expressions, such parametrizations deviate from the exact results typically by less than one part in thousand, which is a more than sufficient accuracy for any foreseeable numerical application. In Fig. 3.5 we show the comparison for $P_{ps}^{(2)}$ between the exact result and the respective compact parametrization given in eq. (3.48) [22]: no visible difference is observed.

As a consequence of such a simple parametrization, the Mellin transform of the splitting functions can be readily obtained from them to a perfectly sufficient accuracy and their expressions involve only simple harmonic functions $S_l(N)$.

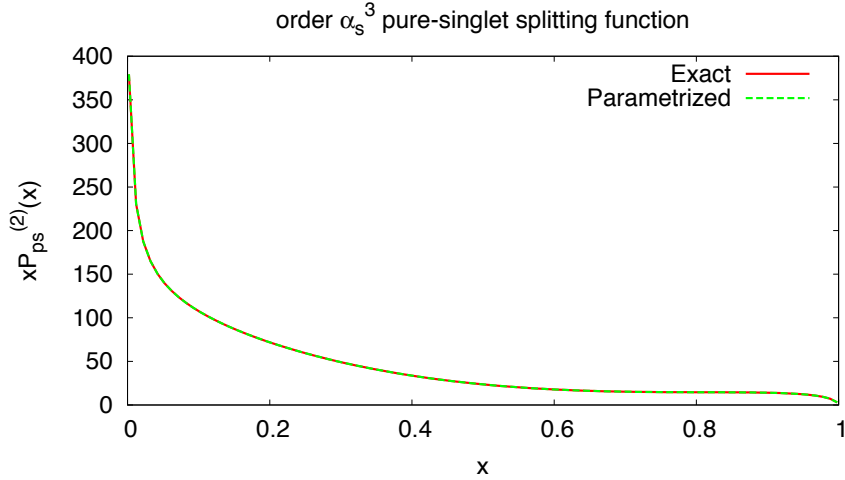


Figure 3.5: The order α_s^3 pure-singlet splitting function, multiplied by x for display purposes: exact vs. parametrization [22].

The splitting functions are responsible for the PDF evolution through the use of the DGLAP equation. In addition, if the evolution is performed in the VFNS (as required by the FONLL method) where the number of active flavours changes when the heavy quark mass thresholds are crossed, also the PDF matching conditions [48] play a role in the evolution. Therefore, for an N -space implementation, also the Mellin transform of the PDF matching conditions needs to be evaluated.

In order to assess the accuracy of the parametrization discussed above as well as the correctness of the implementation, a benchmark of the NNLO PDF evolution in the VFNS as implemented in the NNPDF framework against the Les Houches benchmark tables [71] has been performed [56]. In Table 3.2 the relative difference ϵ_{rel} between the NNPDF implementation and the benchmark tables of Ref. [71] for various combinations of PDFs is shown. It is clear that the accuracy is perfectly satisfactory for precision phenomenology.

3.3.2 Coefficient Functions

Now we come to the issue of the Mellin transform of the coefficient functions. First of all, looking for instance at eq. (3.15) we notice that the FONLL method to order α_s^2 needs three kinds of coefficient functions: the ZM coefficient functions $C_{k,i}^{\text{ZM},(p)}$, the FFNS coefficient functions $C_{k,i}^{\text{FF},(p)}$ and the zero-mass limit of the FFNS coefficient functions $C_{k,i}^{\text{FF0},(p)}$, all of them for $p = 0, 1, 2$ when possible. In the next sections we will address, one by one, the issue of Mellin transforming these typologies of coefficient functions.

ZM Coefficient Functions

Let us first discuss the ZM coefficient functions $C_{k,g}^{\text{ZM},(p)}$. As we already mentioned, the order α_s^2 x -space expressions for the ZM coefficient functions are known since long

x	$\epsilon_{\text{rel}}(f_u - f_{\bar{u}})$	$\epsilon_{\text{rel}}(f_d - f_{\bar{d}})$	$\epsilon_{\text{rel}}(f_{\bar{d}} - f_{\bar{u}})$	$\epsilon_{\text{rel}}(f_{\bar{d}} + f_{\bar{u}})$	$\epsilon_{\text{rel}}(f_s + f_{\bar{s}})$	$\epsilon_{\text{rel}}(f_g)$
10^{-7}	$2.5 \cdot 10^{-4}$	$2.5 \cdot 10^{-4}$	$3.4 \cdot 10^{-5}$	$2.7 \cdot 10^{-5}$	$4.7 \cdot 10^{-5}$	$5.7 \cdot 10^{-5}$
10^{-6}	$1.5 \cdot 10^{-4}$	$1.0 \cdot 10^{-4}$	$1.0 \cdot 10^{-4}$	$6.1 \cdot 10^{-5}$	$5.0 \cdot 10^{-5}$	$5.8 \cdot 10^{-5}$
10^{-5}	$1.7 \cdot 10^{-4}$	$1.6 \cdot 10^{-4}$	$1.1 \cdot 10^{-4}$	$5.2 \cdot 10^{-5}$	$3.6 \cdot 10^{-5}$	$7.8 \cdot 10^{-5}$
10^{-4}	$1.6 \cdot 10^{-4}$	$1.7 \cdot 10^{-4}$	$6.5 \cdot 10^{-5}$	$4.3 \cdot 10^{-5}$	$7.7 \cdot 10^{-5}$	$8.6 \cdot 10^{-5}$
10^{-3}	$9.4 \cdot 10^{-5}$	$6.9 \cdot 10^{-5}$	$1.9 \cdot 10^{-5}$	$7.6 \cdot 10^{-5}$	$7.5 \cdot 10^{-5}$	$1.0 \cdot 10^{-4}$
10^{-2}	$2.9 \cdot 10^{-4}$	$3.2 \cdot 10^{-4}$	$4.5 \cdot 10^{-4}$	$1.0 \cdot 10^{-4}$	$1.3 \cdot 10^{-4}$	$1.2 \cdot 10^{-4}$
10^{-1}	$2.6 \cdot 10^{-4}$	$3.8 \cdot 10^{-4}$	$5.9 \cdot 10^{-4}$	$5.2 \cdot 10^{-4}$	$3.4 \cdot 10^{-4}$	$7.5 \cdot 10^{-5}$
$3 \cdot 10^{-1}$	$1.3 \cdot 10^{-5}$	$1.3 \cdot 10^{-5}$	$4.7 \cdot 10^{-5}$	$1.3 \cdot 10^{-5}$	$9.9 \cdot 10^{-5}$	$4.8 \cdot 10^{-5}$
$5 \cdot 10^{-1}$	$3.8 \cdot 10^{-5}$	$5.8 \cdot 10^{-5}$	$3.1 \cdot 10^{-5}$	$4.2 \cdot 10^{-4}$	$8.5 \cdot 10^{-4}$	$2.3 \cdot 10^{-4}$
$7 \cdot 10^{-1}$	$1.8 \cdot 10^{-4}$	$7.9 \cdot 10^{-5}$	$2.4 \cdot 10^{-3}$	$4.2 \cdot 10^{-3}$	$9.4 \cdot 10^{-3}$	$1.1 \cdot 10^{-3}$

Table 3.2: Relative accuracy of NNLO PDF evolution in the VFNS as implemented in the NNPDF framework in comparison to the Les Houches benchmark tables [71].

time [58, 59, 60, 61] and more recently even the order α_s^3 contributions have been calculated [62, 63]. A nice feature of this kind of calculations, where all the quark masses are set to zero, is that their kinematics is completely determined by the incoming momenta only. This means that, in the lowest order of the electro-weak interactions where the electro-weak coupling factorizes out, NC and CC hard processes are totally equivalent, with the consequence that their coefficient functions are exactly the same. This allows, when treating ZM coefficient functions, not to distinguish between NC and CC processes.

The x -space expressions of the ZM coefficient functions up to order α_s have a reasonably short expression and we can explicitly report some of them here. For example, the order α_s^0 coefficient functions for F_2^{ZM} are:

$$\begin{aligned} C_{2,q}^{\text{ZM},(0)}(x) &= \delta(1-x) \\ C_{2,g}^{\text{ZM},(0)}(x) &= 0, \end{aligned} \quad (3.49)$$

while the order α_s are [72]:

$$\begin{aligned} C_{2,q}^{\text{ZM},(1)}(x) &= 2C_F \left[2 \left(\frac{\ln(1-x)}{1-x} \right)_+ - \frac{3}{2} \left(\frac{1}{1-x} \right)_+ - (1+x) \ln(1-x) \right. \\ &\quad \left. - \frac{1+x^2}{1-x} \ln x + 3 + 2x - \left(\frac{\pi^2}{3} - \frac{9}{2} \right) \delta(1-x) \right] \end{aligned} \quad (3.50)$$

$$C_{2,g}^{\text{ZM},(1)}(x) = 2T_R \left[(2x^2 - 2x + 1) \ln \left(\frac{1-x}{x} \right) - (8x^2 - 8x + 1) \right].$$

The Mellin transform of these coefficient functions can be easily obtained (using, for instance Tabs. A.1 and A.2 in Appendix A) and they read:

$$\begin{aligned} C_{2,q}^{\text{ZM},(0)}(N) &= 1 \\ C_{2,g}^{\text{ZM},(0)}(N) &= 0 \end{aligned} \quad (3.51)$$

and:

$$\begin{aligned}
C_{2,g}^{\text{ZM},(1)}(N) &= 2C_F \left[-S_2(N) + S_1^2(N) - \frac{S_1(N)}{N(N+1)} + \frac{3}{2}S_1(N) \right. \\
&\quad \left. + \frac{1}{N^2} + \frac{2}{N+1} + \frac{3}{2N} - \frac{9}{2} \right] \\
C_{2,g}^{\text{ZM},(1)}(N) &= 2T_R \left[-S_1(N) \left(\frac{2}{N+2} - \frac{2}{N+1} + \frac{1}{N} \right) \right. \\
&\quad \left. - \frac{2}{(N+1)(N+2)} + \frac{1}{N^2} - \frac{8}{N+2} + \frac{8}{N+1} - \frac{1}{N} \right].
\end{aligned} \tag{3.52}$$

Unfortunately, the respective expressions beyond order α_s are much more involved. Therefore, exactly like the case of the splitting functions, in order to implement such expressions in an efficient numerical code, one fits the exact results with more compact parametric functions determining the coefficients. The results of this procedure for F_2 are given in Ref. [63], those for F_L in Ref. [62] and those for F_3 can instead be found in Refs. [70, 73]. They usually ensure an accuracy of order 0.1 % or less. Again, these simplified functions can be easily Mellin transformed and the result involves only simple harmonic functions $S_l(N)$. In Fig. 3.6 we show the relative accuracy of the first even moments ($N = 2, 4, 6, 8$) for $C_{2,g}^{\text{ZM},(2)}(N)$ between the approximated expressions reported in Ref. [63] and the exact results given in Ref. [74]. With an accuracy below 10^{-4} , this confirms the goodness of the parametrized expressions.

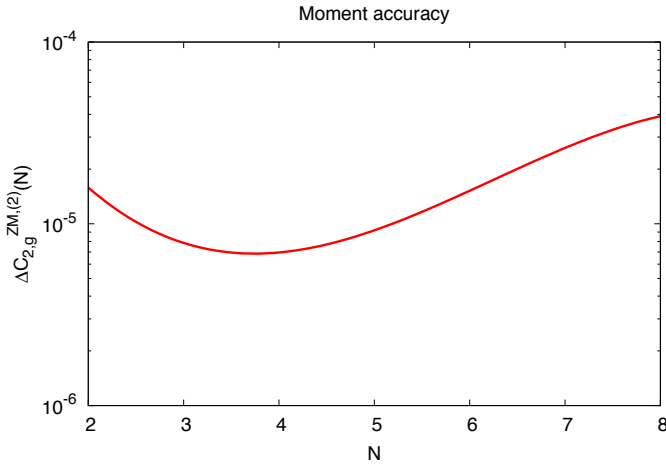


Figure 3.6: Relative accuracy of the first even moments ($N = 2, 4, 6, 8$) for $C_{2,g}^{\text{ZM},(2)}(N)$ of the expressions reported in Ref. [63] with respect to the exact results given in Ref. [74].

Finally, in Fig. 3.7 the relative accuracy for the charm structure functions F_2^c and F_L^c in the ZM-VFNS at order α_s^2 for three different energies $Q^2 = 10, 100, 1000$ GeV² between the NNPDF implementation and the FONLLdis public code [47] is shown. The difference between the two is below the 0.2% all over the relevant range, providing

perfectly satisfactory accuracy. A similar accuracy has been found for the light structure functions F_2^l and F_2^l .

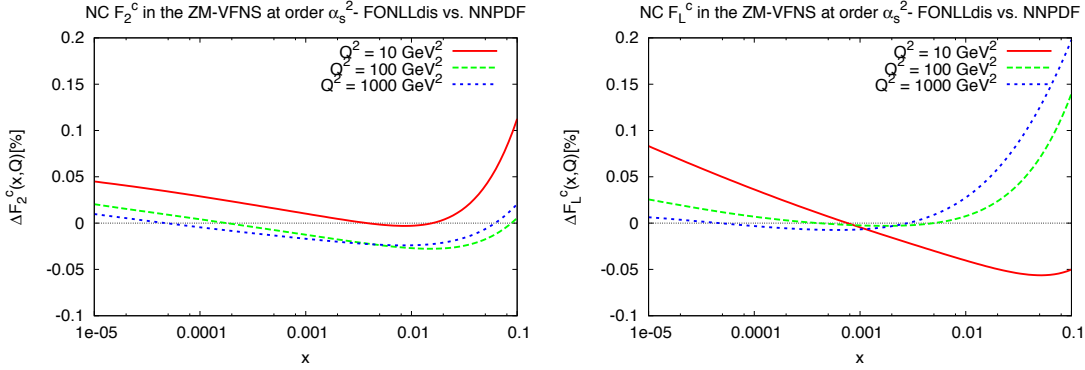


Figure 3.7: Relative difference for the order α_s^2 charm structure function F_2^c (left panel) and F_L^c (right panel) at $Q^2 = 10, 100, 1000 \text{ GeV}^2$ in the ZM-VFNS between the NNPDF code and FONLLdis.

Massive Coefficient Functions

In this Section we consider the FFNS coefficient functions $C_{k,i}^{\text{FF},(p)}$ and $C_{k,i}^{\text{FF}0,(p)}$. In this case, given that the non-vanishing masses affect the kinematics of the process, we need to distinguish between NC and CC.

The Mellin transform of the FFNS coefficient functions represents the trickiest part of the implementation of the FONLL scheme in N -space. In fact, the presence of the mass contributions makes the analytical solution of the Mellin transforms much more involved and requires the use, for instance, of the hypergeometric function for which a suitable implementation becomes necessary. In addition, an analytical x -space solution for the Mellin transforms is not even always possible. This is the case, for instance, for the order α_s^2 FFNS coefficient functions for which fully analytical expressions are not available. The Mellin transform of these coefficient functions has been however possible employing the parametrization presented in Ref. [75].

In Appendix A all the results for the Mellin transform of the FFNS coefficient functions are collected. In particular, the Mellin transform of the NC coefficient functions up to order α_s^2 and the CC ones up to order α_s are presented. A numerical benchmark of their implementation is also included, showing that the derived formulas provide a more than satisfactory accuracy.

Here we limit ourselves to compare the predictions for the FFNS structure functions obtained using NNPDF N -space implementation [69] with other independent codes that instead employ a direct x -space implementation.

As far as the NC structure functions are concerned, the NNPDF implementation has been benchmarked against the x -space code FONLLdis [47]. Regarding CC structure functions, instead, a private x -space benchmark code able to produce predictions for all the CC and NC cross sections included in the NNPDF fits up to order α_s was written

with the precise purpose to benchmark the N -space implementation⁽⁴⁾.

In Fig. 3.8 the relative accuracy for the NC charm structure functions F_2^c and F_L^c in the FFNS at order α_s^2 for three different energies $Q^2 = 10, 100, 1000 \text{ GeV}^2$ between the NNPDF implementation and the FONLLdis public code [47] is shown. A good accuracy well below the 1% level is found.

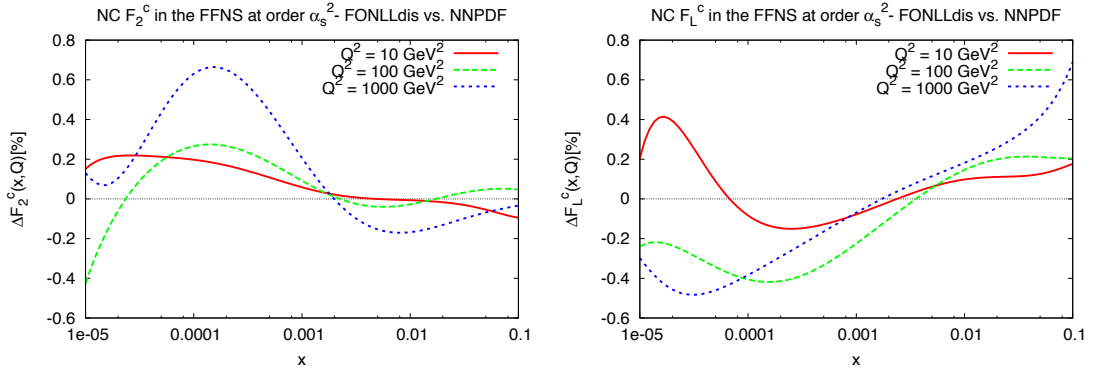


Figure 3.8: Relative difference between the order α_s^2 NC charm structure function F_2^c (left panel) and F_L^c (right panel) at $Q^2 = 10, 100, 1000 \text{ GeV}^2$ in the FFNS.

In Fig. 3.9 the same accuracy plots as in Fig. 3.8 are shown but this time for structure functions in the zero-mass limit of the FFNS (FFNS0) are shown. Here the accuracy is even slightly better than in the FFNS. The reason is that, while in FFNS an approximate parametrization of the order α_s^2 coefficient functions is used [75], in the zero-mass limit of the FFNS the exact analytical Mellin transform of the respective coefficient functions has been employed (see Appendix A).

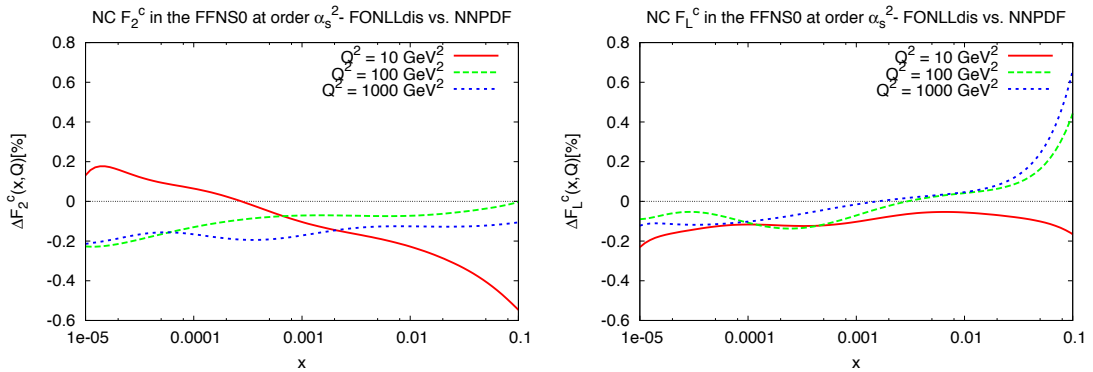


Figure 3.9: Same as Fig 3.8 but in the zero-mass limit of the FFNS (FFNS0).

In Fig. 3.10 the relative accuracy for the CC charm structure function F_2^c and F_L^c in

⁴Presently, also the code `OpenQCDrad` [76], which allows to have predictions for both NC and CC observables, is publicly available but, at the time of our implementation, it was not. However, we have compared *a posteriori* both our N -space and x -space implementation with `OpenQCDrad` [76] finding good agreement.

the FFNS at order α_s for the same energies as before between the NNPDF implementation and the private x -space benchmark code is shown. Also in this case the accuracy is very good.

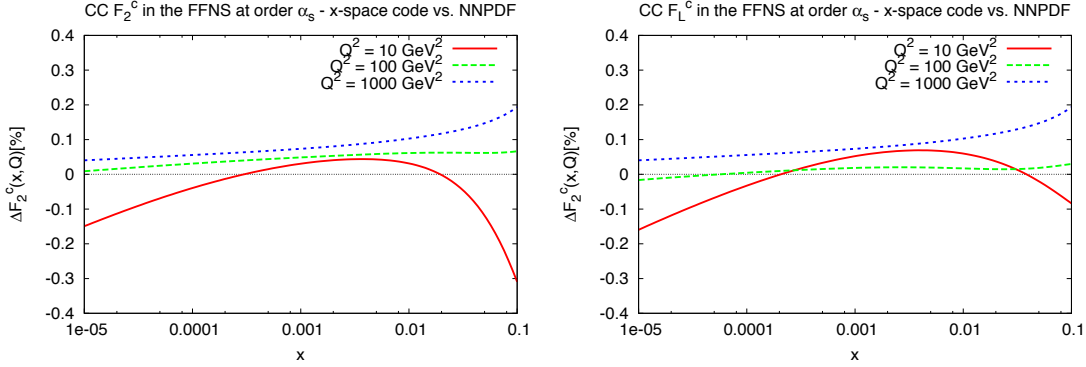


Figure 3.10: Relative difference between the order α_s CC charm structure function F_2^c (left panel) and F_L^c (right panel) at $Q^2 = 10, 100, 1000 \text{ GeV}^2$ in the FFNS.

Finally, in Fig. 3.11 the same accuracy plots as in Fig. 3.10 are shown in for the structure functions in the zero-mass limit of the FFNS. Again, a very good agreement is found.

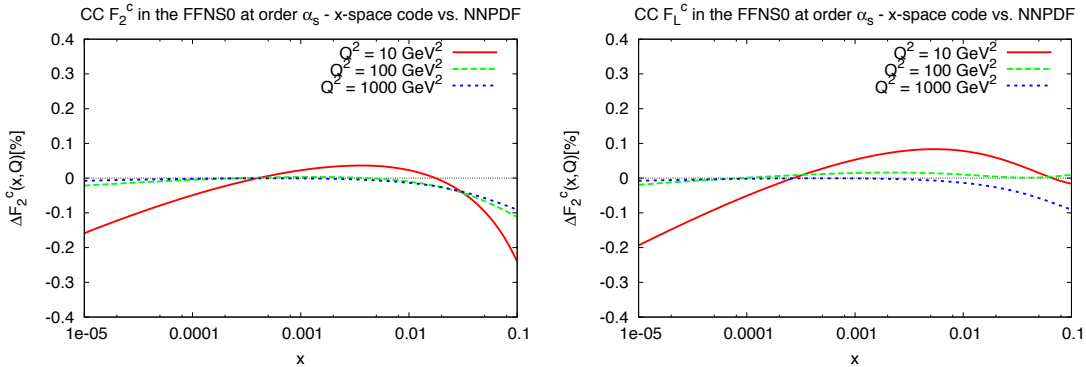


Figure 3.11: Same as Fig 3.10 but in the zero-mass limit of the FFNS (FFNS0).

The same benchmark of NNPDF implementation has been performed also for the respective FFNS light structure functions finding similar accuracies. It should be remarked that a real full benchmark of the order α_s^2 neutral current structure functions was not possible because the FONLLdis code does not implement the gluon radiation term mentioned in Sec. 3.1.1. However, it was shown in Ref. [56] that the contribution due to this term is usually below the 1% level.

After benchmarking the implementation of the structure functions for all three sectors ZM-VFNS, FFNS and zero-mass limit of the FFNS, one can be reasonably sure that also the FONLL prediction, which is a combination of those three schemes, works well. This is indeed the case, as shown in Fig. 3.12 where the predictions for F_2^c at $Q^2 = 10 \text{ GeV}^2$ in

the FONLL-C scheme as implemented in the NNPDF code and in FONLLdis are shown. No visible difference is observed.

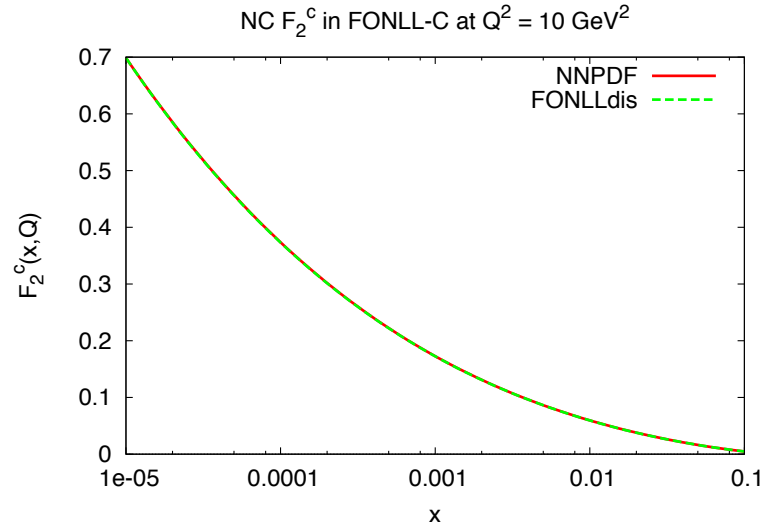


Figure 3.12: F_2^c at $Q^2 = 10 \text{ GeV}^2$ in the FONLL-C scheme as implemented in the NNPDF code and in FONLLdis.

Chapter 4

Structure Functions with $\overline{\text{MS}}$ Masses

In a recent paper [77] it has been claimed that the implementation of the $\overline{\text{MS}}$ masses in the heavy quark structure functions may result in an improvement of the perturbative stability and in a reduction of the theoretical uncertainty due to variations of the renormalization and factorization scales. This turns out to be useful for a PDF determination because it helps to constrain potentially large higher order corrections.

In this chapter a detailed strategy on how to implement heavy quark structure functions in terms of $\overline{\text{MS}}$ masses in the FONLL scheme will be discussed. There are two distinct steps to be taken. The first is the modification of the VFNS PDF and α_s evolution. In fact, introducing the $\overline{\text{MS}}$ masses, the threshold matching conditions, which are usually expressed in terms of pole masses [48], need to be adjusted. The second step consists in expressing the FFNS coefficient functions, which are also usually given in terms of the pole mass, in terms of $\overline{\text{MS}}$ masses. Once these steps have been carried out, given that the ZM coefficient functions do not depend on the heavy quark masses, the FONLL structure functions can be fully expressed in terms of $\overline{\text{MS}}$ masses. With this setup it will be possible to determine the $\overline{\text{MS}}$ charm mass $m_c(m_c)$ in the context of a PDF determination.

4.1 $\overline{\text{MS}}$ Running Mass vs. Pole Mass

For the rest of this chapter, we will only consider a single heavy quark mass and, in order to make the notation lighter, the pole mass will be denoted by M while the $\overline{\text{MS}}$ mass by $m(\mu)$.

The pole (or on-shell) mass M is defined as the pole of the renormalized propagator of the heavy quark. Although M depends on the perturbative order, it is independent from the renormalization scale μ . The $\overline{\text{MS}}$ mass $m(\mu)$ refers instead to the mass parameter in the QCD Lagrangian renormalized according to the $\overline{\text{MS}}$ scheme prescription. Differently from the pole mass, the $\overline{\text{MS}}$ mass is renormalization scale dependent and its evolution is regulated by a differential equation, similar to that for α_s , called the Renormalization Group Equation (RGE).

Therefore M and $m(\mu)$ come from two different renormalization procedures and thus

one can be expressed in terms of the other through a perturbative series in α_s . This is exactly what has been done in Ref. [78] and in particular from eq. (31) one reads:

$$\frac{M}{m(\mu)} = 1 + h^{(1)}a_s + \underbrace{C_F \left[C_F h_1^{(2)} + C_A h_2^{(2)} + T_R \left(N_L h_3^{(2)} + h_4^{(2)} \right) \right]}_{h^{(2)}} a_s^2 + \mathcal{O}(\alpha_s^3), \quad (4.1)$$

with:

$$\begin{aligned} h^{(1)}(\mu, m(\mu)) &= C_F (4 + 3L_{\mu m}) \\ h_1^{(2)}(\mu, m(\mu)) &= -\frac{7}{8} + 30\zeta_2 + 12\zeta_3 - 48\zeta_2 \ln(2) - \frac{9}{2}L_{\mu m} + \frac{9}{2}L_{\mu m}^2 \\ h_2^{(2)}(\mu, m(\mu)) &= \frac{1111}{24} - 8\zeta_2 - 6\zeta_3 + 24\zeta_2 \ln(2) + \frac{185}{6}L_{\mu m} + \frac{11}{2}L_{\mu m}^2 \\ h_3^{(2)}(\mu, m(\mu)) &= -\frac{71}{6} - 8\zeta_2 - \frac{26}{3}L_{\mu m} - 2L_{\mu m}^2 \\ h_4^{(2)}(\mu, m(\mu)) &= -\frac{143}{6} + 16\zeta_2 - \frac{26}{3}L_{\mu m} - 2L_{\mu m}^2, \end{aligned} \quad (4.2)$$

where:

$$L_{\mu m} \equiv \ln \frac{\mu^2}{m^2(\mu)}, \quad (4.3)$$

and N_L is the number of lighter flavours. In practice, if M or $m(\mu)$ is the mass of the n -th flavour, then $N_L = n - 1$. In the following eq. (4.1) will be used to replace the pole mass M with the $\overline{\text{MS}}$ mass $m(\mu)$ wherever needed.

4.2 RGE Solution for the $\overline{\text{MS}}$ Running Mass

As already mentioned, the $\overline{\text{MS}}$ mass $m(\mu)$ is renormalization scale dependent and its evolution is regulated by the RGE which gives rise to the following differential equation for the running:

$$\mu^2 \frac{dm}{d\mu^2} = m(\mu) \gamma_m(a_s) = -m(\mu) \sum_{n=0}^P \gamma_m^{(N)} a_s^{n+1}. \quad (4.4)$$

From eqs. (46), (47) and (48) of Ref.[79] for $SU(3)$ (taking into account a factor four difference in the definition of a_s), the first three coefficients of the series on the r.h.s. of eq. (4.4) read:

$$\gamma_m^{(0)} = 4 \quad (4.5a)$$

$$\gamma_m^{(1)} = \frac{202}{3} - \frac{20}{9}N \quad (4.5b)$$

$$\gamma_m^{(2)} = 1249 - \left(\frac{2216}{27} + \frac{160}{3}\zeta_3 \right) N - \frac{140}{81}N^2, \quad (4.5c)$$

where N is the number of active flavours at the scale μ .

The evolution equation for a_s instead reads:

$$\mu^2 \frac{da_s}{d\mu^2} = \beta(a_s) = - \sum_{n=0}^P \beta_n a_s^{n+2}, \quad (4.6)$$

with:

$$\beta_0 = 11 - \frac{2}{3}N \quad (4.7a)$$

$$\beta_1 = 102 - \frac{38}{3}N \quad (4.7b)$$

$$\beta_2 = \frac{2857}{2} - \frac{5033}{18}N + \frac{325}{54}N^2. \quad (4.7c)$$

Using eq. (4.6), eq. (4.4) can be written as:

$$\frac{dm}{da_s} = \frac{\gamma_m(a_s)}{\beta(a_s)} m(a_s), \quad (4.8)$$

whose solution is:

$$m(\mu) = m(\mu_0) \exp \left[\int_{a_s(\mu_0)}^{a_s(\mu)} \frac{\gamma_m(a_s)}{\beta(a_s)} da_s \right]. \quad (4.9)$$

Expanding the integrand in eq. (4.9) using the perturbative expansions of $\gamma_m(a_s)$ and $\beta(a_s)$ given in eqs. (4.4) and (4.6) respectively, one gets the following polynomial in a_s :

$$\frac{\gamma_m(a)}{\beta(a)} = \frac{1}{a} [c_0 + (c_1 - b_1 c_0)a + (c_2 - c_1 b_1 - b_2 c_0 + b_1^2 c_0)a^2 + \mathcal{O}(a^3)], \quad (4.10)$$

where:

$$b_i \equiv \frac{\beta_i}{\beta_0} \quad \text{and} \quad c_i \equiv \frac{\gamma_m^{(i)}}{\beta_0}. \quad (4.11)$$

Now the integral in eq. (4.9) can be explicitly solved obtaining:

$$\int_{a_0}^a \frac{\gamma_m(a)}{\beta(a)} da = c_0 \ln \frac{a}{a_0} + (c_1 - b_1 c_0)(a - a_0) + \frac{1}{2}(c_2 - c_1 b_1 - b_2 c_0 + b_1^2 c_0)(a^2 - a_0^2), \quad (4.12)$$

where $a \equiv a_s(\mu)$ and $a_0 \equiv a_s(\mu_0)$.

Substituting eq. (4.12) into eq. (4.9) and expanding the exponential functions, one finally obtains:

$$m(\mu) = m(\mu_0) \left(\frac{a}{a_0} \right)^{c_0} \times \frac{1 + (c_1 - b_1 c_0)a + \frac{1}{2}[c_2 - c_1 b_1 - b_2 c_0 + b_1^2 c_0 + (c_1 - b_1 c_0)^2]a^2}{1 + (c_1 - b_1 c_0)a_0 + \frac{1}{2}[c_2 - c_1 b_1 - b_2 c_0 + b_1^2 c_0 + (c_1 - b_1 c_0)^2]a_0^2}, \quad (4.13)$$

which gives the NNLO running for $m(\mu)$. Of course, to obtain the NLO running one has just to disregard the terms proportional to a^2 and a_0^2 in eq. (4.13), while at LO $m(\mu) = m(\mu_0)$, *i.e.* there is no running at all⁽¹⁾.

¹Note that, to be consistent, the evolution of a and a_0 must be done at the same perturbative order as $m(\mu)$.

4.3 Matching Conditions

The matching conditions for PDFs and α_s at the heavy quark thresholds are usually given in terms of the pole mass M [48]. However, in order to consistently implement the $\overline{\text{MS}}$ scheme for the heavy quark masses, they need to be expressed in terms of $m(\mu)$. This will be done in the next sections. In addition, the matching conditions for the running of $m(\mu)$ itself will also be derived. As discussed in Sec. 4.4, since the FFNS coefficient functions will also need to be expressed in terms of $\overline{\text{MS}}$ masses, the knowledge $m(\mu)$ for any value of the renormalization scale μ is required as well.

4.3.1 Matching of $\alpha_s(\mu)$

The explicit expression of the matching condition for α_s between the $(N-1)$ - and the N -flavour scheme can be found in eq. (9) of Ref. [57]. Up to order α_s^2 , it reads:

$$\frac{a^{(N-1)}(\mu)}{a^{(N)}(\mu)} = 1 - \frac{2}{3}L_{\mu M}a^{(N)}(\mu) + \left(\frac{4}{9}L_{\mu M}^2 - \frac{38}{3}L_{\mu M} - \frac{14}{3}\right)[a^{(N)}(\mu)]^2, \quad (4.14)$$

where M is the pole mass of the N -th flavour. But from eq. (4.1) it follows that:

$$\ln M^2 = \ln m^2(\mu) + 2 \ln[1 + h^{(1)}(\mu)a^{(N)}(\mu)], \quad \text{with} \quad h^{(1)}(\mu) = \frac{16}{3} + 4L_{\mu m}, \quad (4.15)$$

that, using the expansion:

$$\ln(1+x) = \sum_{k=1}^{\infty} \frac{(-1)^{k+1}}{k} x^k, \quad (4.16)$$

can be written as:

$$\ln M^2 = \ln m^2(\mu) + 2h^{(1)}(\mu)a^{(N)}(\mu) + \mathcal{O}([a^{(N)}]^2). \quad (4.17)$$

It is straightforward then to see that:

$$L_{\mu M} = L_{\mu m} - 2h^{(1)}a^{(N)} = L_{\mu m} - \left(\frac{32}{3} + 8L_{\mu m}\right)a^{(N)}, \quad (4.18)$$

that, substituted into eq. (4.14), gives the matching condition for α_s in terms of the $\overline{\text{MS}}$ mass $m(\mu)$:

$$\frac{a^{(N-1)}(\mu)}{a^{(N)}(\mu)} = 1 - \frac{2}{3}L_{\mu m}a^{(N)}(\mu) + \left(\frac{4}{9}L_{\mu m}^2 - \frac{22}{3}L_{\mu m} + \frac{22}{9}\right)[a^{(N)}(\mu)]^2. \quad (4.19)$$

In order to get rid of the logarithmic terms, one can choose to match $a^{(N-1)}$ and $a^{(N)}$ at $\mu = m(\mu) = m(m)$, so that eq. (4.19) reduces to:

$$a^{(N-1)}(m) = a^{(N)}(m) \left(1 + \frac{22}{9}[a^{(N)}(m)]^2\right), \quad (4.20)$$

which can be easily inverted obtaining:

$$a^{(N)}(m) = a^{(N-1)}(m) \left(1 - \frac{22}{9}[a^{(N-1)}(m)]^2\right). \quad (4.21)$$

Exactly like in the case of the pole mass [80], also in the $\overline{\text{MS}}$ mass scheme it is possible to choose the matching scale for α_s is such a way that the running is continuous at the heavy quark mass thresholds up to order α_s and the discontinuity appears only at order α_s^2 . The only difference is that the coefficient of the matching is $-22/9$ in the $\overline{\text{MS}}$ mass scheme and $14/3$ in the pole mass scheme. It is interesting to observe that, in order to perform the matching as described above, one just needs to know the value of $m(m)$ which is an input parameter that in the $\overline{\text{MS}}$ scheme plays the role of the M in the pole mass scheme. $m(m)$ is usually referred to as the RG-invariant $\overline{\text{MS}}$ mass.

4.3.2 Matching of $m(\mu)$

Also the running of $m(\mu)$ needs to be matched. In particular, one might need to match the $(N-1)$ -flavour scheme to the N -flavour scheme of the mass $m_q(\mu)$, with $q = c, b, t$, at the N -th heavy quark mass threshold $m_h(\mu)$, with again $h = c, b, t$. From eqs. (26) and (27) of Ref. [81] one reads:

$$\frac{m_q^{(N-1)}(\mu)}{m_q^{(N)}(\mu)} = 1 + \left(\frac{4}{3} L_{\mu m}^{(h)2} - \frac{20}{9} L_{\mu m}^{(h)} + \frac{89}{27} \right) [a^{(N)}(\mu)]^2, \quad (4.22)$$

where:

$$L_{\mu m}^{(h)} = \ln \frac{\mu^2}{m_h^2(\mu)}. \quad (4.23)$$

If one chooses to match the two schemes at the scale $\mu = m_h(\mu) = m_h(m_h)$, the logarithmic terms vanish and one is left with:

$$m_q^{(N-1)}(m_h) = \left(1 + \frac{89}{27} [a^{(N)}(m_h)]^2 \right) m_q^{(N)}(m_h), \quad (4.24)$$

whose inverse is:

$$m_q^{(N)}(m_h) = \left(1 - \frac{89}{27} [a^{(N-1)}(m_h)]^2 \right) m_q^{(N-1)}(m_h). \quad (4.25)$$

4.3.3 Matching of the PDFs

In this section the replacement of the pole mass M with the $\overline{\text{MS}}$ mass $m(\mu)$ in the matching conditions for PDFs is discussed. As is well known, the quark and the gluon PDFs (singlet sector) in the $(N+1)$ -flavour scheme in terms of those in N -flavour scheme at any scale μ are given by the coupled equation:

$$\begin{pmatrix} f_q^{(N+1)} \\ f_g^{(N+1)} \end{pmatrix} = \begin{pmatrix} 1 + a_s^2 [A_{qq,h}^{NS,(2)} + \tilde{A}_{hq}^{S,(2)}] & a_s \tilde{A}_{hg}^{S,(1)} + a_s^2 \tilde{A}_{hg}^{S,(2)} \\ a_s^2 A_{qq,h}^{S,(2)} & 1 + a_s A_{gg,h}^{S,(1)} + a_s^2 A_{gg,h}^{S,(2)} \end{pmatrix} \otimes \begin{pmatrix} f_q^{(N)} \\ f_g^{(N)} \end{pmatrix}, \quad (4.26)$$

where the form of the (x -space) functions entering the transformation matrix above are given in Appendix B of Ref. [48]. It should be noticed that, at the generic scale μ , also the order α_s contributions $\tilde{A}_{hg}^{S,(1)}$ and $A_{gg,h}^{S,(1)}$ are present. However, they are both proportional to $\ln(\mu^2/M^2)$ and therefore they disappear if one chooses $\mu = M$ as a matching threshold. The matching condition for the non-singlet sector, *i.e.* those

combinations of PDFs that evolve multiplicatively, is omitted here because it does not contain any α_s contribution, and therefore it is not affected by the mass scheme change up to order α_s^2 .

In order to replace the pole mass M with the $\overline{\text{MS}}$ mass $m(\mu)$, one just needs to substitute eq. (4.17) into eq. (4.26). In the order α_s^2 functions in eq. (4.26), the second term on the l.h.s. of eq. (4.17) would give rise to subleading terms of order α_s^3 . Therefore in those functions it is enough to replace M with $m(\mu)$. On the other hand, the second term on the l.h.s. of eq. (4.17) is important for the order α_s terms in eq. (4.26). Since both functions $\tilde{A}_{hg}^{S,(1)}$ and $A_{gg,h}^{S,(1)}$ are proportional to $\ln(\mu^2/M^2)$, they can be written as:

$$\begin{aligned}\tilde{A}_{hg}^{S,(1)}\left(x, \frac{\mu^2}{M^2}\right) &= g_1(x) \ln \frac{\mu^2}{M^2} \\ A_{gg,h}^{S,(1)}\left(x, \frac{\mu^2}{M^2}\right) &= g_2(x) \ln \frac{\mu^2}{M^2},\end{aligned}\tag{4.27}$$

where:

$$\begin{aligned}g_1(x) &= 4T_R[x^2 + (1-x)^2] \\ g_2(x) &= -\frac{4}{3}T_R\delta(1-x).\end{aligned}\tag{4.28}$$

Replacing M with m in eq. (4.27) using eq. (4.17), one gets:

$$\begin{aligned}\tilde{A}_{hg}^{S,(1)}\left(x, \frac{\mu^2}{m^2}\right) &= g_1(x) \ln \frac{\mu^2}{m^2} - 2h^{(1)}(\mu)a_s(\mu)g_1(x) \\ A_{gg,h}^{S,(1)}\left(x, \frac{\mu^2}{m^2}\right) &= g_2(x) \ln \frac{\mu^2}{m^2} - 2h^{(1)}(\mu)a_s(\mu)g_2(x).\end{aligned}\tag{4.29}$$

Finally, eq. (4.26) in terms of $m(\mu)$ becomes:

$$\begin{pmatrix} f_q^{(N+1)} \\ f_g^{(N+1)} \end{pmatrix} = \begin{pmatrix} 1 + a_s^2[A_{qq,h}^{NS,(2)} + \tilde{A}_{hq}^{S,(2)}] & a_s\tilde{A}_{hg}^{S,(1)} + a_s^2[\tilde{A}_{hg}^{S,(2)} - 2h^{(1)}g_1] \\ a_s^2A_{gg,h}^{S,(2)} & 1 + a_sA_{gg,h}^{S,(1)} + a_s^2[A_{gg,h}^{S,(2)} - 2h^{(1)}g_2] \end{pmatrix} \otimes \begin{pmatrix} f_q^{(N)} \\ f_g^{(N)} \end{pmatrix}.\tag{4.30}$$

Given that the matching conditions for the PDFs are to be implemented in a code based on the solution of the DGLAP equation in Mellin space, it is necessary to compute the Mellin transform of the functions $g_1(x)$ and $g_2(x)$ which is:

$$\begin{aligned}g_1(N) &= \mathbf{M}[g_1(x)](N) = 4T_R \left[\frac{2}{N+2} - \frac{2}{N+1} + \frac{1}{N} \right] \\ g_2(N) &= \mathbf{M}[g_2(x)](N) = -\frac{4}{3}T_R.\end{aligned}\tag{4.31}$$

Choosing to match the $(N+1)$ -flavour scheme and N -flavour scheme at $\mu = m(\mu) = m(m)$, all the logarithmic terms vanish (including the functions $\tilde{A}_{hg}^{S,(1)}$ and $A_{gg,h}^{S,(1)}$), therefore we obtain:

$$\begin{pmatrix} f_q^{(N+1)} \\ f_g^{(N+1)} \end{pmatrix} = \begin{pmatrix} 1 + a_s^2[A_{qq,h}^{NS,(2)} + \tilde{A}_{hq}^{S,(2)}] & a_s^2[\tilde{A}_{hg}^{S,(2)} - 2h^{(1)}g_1] \\ a_s^2A_{gg,h}^{S,(2)} & 1 + a_s^2[A_{gg,h}^{S,(2)} - 2h^{(1)}g_2] \end{pmatrix} \otimes \begin{pmatrix} f_q^{(N)} \\ f_g^{(N)} \end{pmatrix}.\tag{4.32}$$

x	$\epsilon_{\text{rel}}(f_u - f_{\bar{u}})$	$\epsilon_{\text{rel}}(f_d - f_{\bar{d}})$	$\epsilon_{\text{rel}}(f_{\bar{d}} - f_{\bar{u}})$	$\epsilon_{\text{rel}}(f_{\bar{d}} + f_{\bar{u}})$	$\epsilon_{\text{rel}}(f_s + f_{\bar{s}})$	$\epsilon_{\text{rel}}(f_g)$
10^{-7}	$2.6 \cdot 10^{-4}$	$1.9 \cdot 10^{-4}$	$3.5 \cdot 10^{-5}$	$7.4 \cdot 10^{-5}$	$6.0 \cdot 10^{-5}$	$9.8 \cdot 10^{-5}$
10^{-6}	$1.4 \cdot 10^{-4}$	$1.1 \cdot 10^{-4}$	$1.2 \cdot 10^{-4}$	$5.7 \cdot 10^{-5}$	$5.9 \cdot 10^{-5}$	$6.0 \cdot 10^{-5}$
10^{-5}	$1.9 \cdot 10^{-4}$	$1.6 \cdot 10^{-4}$	$9.3 \cdot 10^{-5}$	$5.9 \cdot 10^{-5}$	$6.1 \cdot 10^{-5}$	$4.4 \cdot 10^{-5}$
10^{-4}	$1.5 \cdot 10^{-4}$	$1.7 \cdot 10^{-4}$	$7.0 \cdot 10^{-5}$	$6.5 \cdot 10^{-5}$	$7.0 \cdot 10^{-5}$	$7.6 \cdot 10^{-5}$
10^{-3}	$1.2 \cdot 10^{-4}$	$8.8 \cdot 10^{-5}$	0.0	$7.8 \cdot 10^{-5}$	$1.1 \cdot 10^{-4}$	$9.5 \cdot 10^{-5}$
10^{-2}	$2.6 \cdot 10^{-4}$	$3.1 \cdot 10^{-4}$	$4.5 \cdot 10^{-4}$	$1.3 \cdot 10^{-4}$	$1.3 \cdot 10^{-4}$	$1.3 \cdot 10^{-4}$
10^{-1}	$2.7 \cdot 10^{-4}$	$3.7 \cdot 10^{-4}$	$6.0 \cdot 10^{-4}$	$5.1 \cdot 10^{-4}$	$3.5 \cdot 10^{-4}$	$1.0 \cdot 10^{-4}$
$3 \cdot 10^{-1}$	0.0	0.0	$6.7 \cdot 10^{-5}$	$5.7 \cdot 10^{-5}$	$5.6 \cdot 10^{-5}$	$3.6 \cdot 10^{-5}$
$5 \cdot 10^{-1}$	0.0	$3.2 \cdot 10^{-5}$	$8.0 \cdot 10^{-5}$	0.0	$3.5 \cdot 10^{-5}$	$1.2 \cdot 10^{-4}$
$7 \cdot 10^{-1}$	$2.0 \cdot 10^{-4}$	$9.8 \cdot 10^{-5}$	$1.4 \cdot 10^{-3}$	$2.2 \cdot 10^{-3}$	$1.2 \cdot 10^{-3}$	$6.0 \cdot 10^{-4}$

Table 4.1: Relative differences at $Q^2 = 10^4 \text{ GeV}^2$ for NNLO PDF evolution in the $\overline{\text{MS}}$ mass scheme as described in Sec. 4.3.3 in comparison to HOPPET for various flavor combinations.

Once again, if the matching point is chosen cleverly, also in the $\overline{\text{MS}}$ mass scheme the matching conditions for PDFs start to play a role only at order α_s^2 , with the only difference that some coefficients of the matching matrix for gluon and singlet is modified by some simple functions.

4.3.4 Benchmark of the Evolution

The implementation of the prescriptions described above for the evolution in the VFNS in the presence of $\overline{\text{MS}}$ masses has been benchmarked against publicly available codes.

The running and the matching for the $\overline{\text{MS}}$ mass $m(\mu)$ described in Sec. 4.3.2 has been checked against the `Mathematica` package `RunDec` [81]; we found a perfect agreement.

In order to assess the goodness of the implementation for the evolution in the VFNS of PDFs and α_s , in Tab. 4.1 the relative accuracy against the x -space evolution code HOPPET [82], that also has the option to perform evolution with $\overline{\text{MS}}$ heavy quark masses, is reported [83]. Evidently, a very good agreement is found.

4.4 Structure Functions

Once the evolution for $\alpha_s(\mu)$, $m(\mu)$ and PDFs is settled, we turn to the implementation in the Mellin space of FFNS structure functions in terms of the $\overline{\text{MS}}$ mass. This will be done separately first for the NC structure functions and then for the CC ones.

4.4.1 Neutral Current

In this section we discuss the explicit substitution of the pole mass with $\overline{\text{MS}}$ mass in the FFNS NC heavy quark structure functions (F_2^H and F_L^H). Dropping all the unnecessary dependencies, the generic FFNS NC structure function has the form:

$$F(M) = a_s F^{(1)}(M) + a_s^2 F^{(2)}(M) + \mathcal{O}(\alpha_s^3). \quad (4.33)$$

The Taylor expansion of $F^{(1)}(M)$ and $F^{(2)}(M)$ around $M = m$ reads:

$$F^{(l)}(M) = \sum_{n=0}^{\infty} \frac{1}{n!} \left. \frac{d^n F^{(l)}}{dM^n} \right|_{M=m} (M-m)^n, \quad l = 1, 2, \quad (4.34)$$

and in particular what is needed are the relations:

$$F^{(1)}(M) = F^{(1)}(m) + a_s m h^{(1)} \left. \frac{dF^{(1)}}{dM} \right|_{M=m} + \mathcal{O}(\alpha_s^2) \quad (4.35)$$

$$F^{(2)}(M) = F^{(2)}(m) + \mathcal{O}(\alpha_s),$$

where eq. (4.1) has been used in the first relation.

Finally, substituting eq. (4.35) into eq. (4.33), one gets:

$$F(M) = a_s F^{(1)}(m) + a_s^2 \left[F^{(2)}(m) + m h^{(1)} \left. \frac{dF^{(1)}}{dM} \right|_{M=m} \right] + \mathcal{O}(\alpha_s^3). \quad (4.36)$$

In the NC case the difference between pole and $\overline{\text{MS}}$ mass scheme is given by a correction of order α_s^2 proportional to the derivative of the order α_s term $F^{(1)}$. Of course, the implementation requires the analytical calculation of such a derivative and the starting point is the relation:

$$F^{(1)}(M) = x \int_x^{x_{\max}(M)} \frac{dz}{z} g\left(\frac{x}{z}\right) C_g^{(1)}(\eta(z, M), \xi(M), \chi(M)), \quad (4.37)$$

where the explicit N -space expressions for $C_g^{(1)}$ are given in Appendix A for both F_2 and F_L . In eq. (4.37) the following definitions are also used:

$$x_{\max} = \frac{1}{1 + \frac{4M^2}{Q^2}}, \quad \eta = \frac{Q^2}{4M^2} \left(\frac{1}{z} - 1 \right) - 1, \quad \xi = \frac{Q^2}{M^2}, \quad \chi = \frac{\mu^2}{M^2}. \quad (4.38)$$

Defining:

$$G(z, M) \equiv \frac{x}{z} g\left(\frac{x}{z}\right) C_g^{(1)}(\eta(z, M), \xi(M), \chi(M)), \quad (4.39)$$

eq. (4.37) can be written as:

$$F^{(1)}(M) = \int_x^{x_{\max}(M)} dz G(z, M). \quad (4.40)$$

Therefore:

$$\frac{dF^{(1)}}{dM} = \frac{d}{dM} \int_x^{x_{\max}(M)} dz G(z, M) = \frac{d\tilde{G}(x_{\max}(M), M)}{dM} - \frac{d\tilde{G}(x, M)}{dM}, \quad (4.41)$$

where $\tilde{G}(z, M)$ is the primitive function of $G(z, M)$ with respect to z (*i.e.* $\partial\tilde{G}/\partial z \equiv G$). But:

$$\frac{d\tilde{G}(x_{\max}(M), M)}{dM} = \frac{\partial\tilde{G}(x_{\max}, M)}{\partial M} + \frac{dx_{\max}}{dM} \underbrace{\frac{\partial\tilde{G}(x_{\max}, M)}{\partial x_{\max}}}_{G(x_{\max}, M)} \quad (4.42)$$

and:

$$\frac{d\tilde{G}(x, M)}{dM} = \frac{\partial\tilde{G}(x, M)}{\partial M}, \quad (4.43)$$

thus:

$$\begin{aligned} \frac{dF^{(1)}}{dM} &= \frac{\partial\tilde{G}(x_{\max}, M)}{\partial M} - \frac{\partial\tilde{G}(x, M)}{\partial M} + \frac{dx_{\max}}{dM} G(x_{\max}, M) \\ &= \int_x^{x_{\max}(M)} dz \frac{\partial G(z, M)}{\partial M} + \frac{dx_{\max}}{dM} G(x_{\max}, M). \end{aligned} \quad (4.44)$$

As discussed in Ref. [77], the boundary term in eq. (4.44) vanishes and thus can be omitted. Finally, since:

$$\frac{\partial G(z, M)}{\partial M} = \frac{x}{z} g\left(\frac{x}{z}\right) \frac{\partial C_g^{(1)}}{\partial M}, \quad (4.45)$$

one has that:

$$\begin{aligned} \left. \frac{dF^{(1)}}{dM} \right|_{M=m} &= \left[x \int_x^{x_{\max}(M)} \frac{dz}{z} g\left(\frac{x}{z}\right) \frac{\partial C_g^{(1)}}{\partial M} \right] \Big|_{M=m} \\ &= x \int_x^{x_{\max}(m)} \frac{dz}{z} g\left(\frac{x}{z}\right) \left[\frac{\partial C_g^{(1)}}{\partial M} \right] \Big|_{M=m}. \end{aligned} \quad (4.46)$$

Now, taking into account the fact that:

$$F^{(2)}(M) = \sum_{i=q, \bar{q}, g} x \int_x^{x_{\max}(M)} \frac{dz}{z} q_i\left(\frac{x}{z}\right) C_i^{(2)}(z, M) \quad (4.47)$$

and using eqs. (4.36) and (4.46), one can explicitly write down the massive structure function up to order α_s^2 in terms of the $\overline{\text{MS}}$ mass as following:

$$\begin{aligned} F(m) &= x \int_x^{x_{\max}(m)} \frac{dz}{z} g\left(\frac{x}{z}\right) \left[a_s C_g^{(1)}(z, m) + a_s^2 \left(C_g^{(2)}(z, m) + m h^{(1)} \left[\frac{\partial C_g^{(1)}}{\partial M} \right] \Big|_{M=m} \right) \right] \\ &+ \sum_{i=q, \bar{q}} x \int_x^{x_{\max}(m)} \frac{dz}{z} q_i\left(\frac{x}{z}\right) a_s^2 C_i^{(2)}(z, m). \end{aligned} \quad (4.48)$$

In conclusion the NC heavy quark FFNS structure function (F_2 or F_L) in terms of the $\overline{\text{MS}}$ mass m can be obtained from the pole mass expression by replacing everywhere the pole mass M with m and correcting the order α_s^2 gluon coefficient function $C_g^{(1)}$ with the term:

$$m(\mu) h^{(1)}(\mu, m(\mu)) \left[\frac{\partial C_g^{(1)}}{\partial M} \right] \Big|_{M=m(\mu)}. \quad (4.49)$$

Of course, for the zero-mass limit of the FFNS structure function the same recipe holds, with the only obvious difference that the correct massive coefficient functions are to be used. The explicit derivative of $C_g^{(1)}$ in eq. (4.48) for the NC massive structure functions F_2 and F_L in the Mellin space have been completely worked out in Appendix B.

4.4.2 Charged Current

In this section the $\overline{\text{MS}}$ mass implementation for the generic CC FFNS heavy quark structure function is discussed. The treatment is exactly the same as for the NC structure functions, with the only difference that in the CC case the perturbative expansion starts at order α_s^0 and presently the full massive coefficient functions are only known up to order α_s , *i.e.* we have:

$$F(M) = F^{(0)}(M) + a_s F^{(1)}(M) + \mathcal{O}(\alpha_s^2). \quad (4.50)$$

Therefore, expanding $F^{(0)}$ and $F^{(1)}$ around $M = m$ and keeping only the terms up to order α_s , one obtains:

$$F(m) = F^{(0)}(m) + a_s \left[F^{(1)}(m) + mh^{(1)} \frac{dF^{(0)}}{dM} \Big|_{M=m} \right] + \mathcal{O}(\alpha_s^2). \quad (4.51)$$

Therefore, in order to consistently replace the pole mass M with the $\overline{\text{MS}}$ mass m in the CC FFNS coefficient functions, one has just to replace M with m and then correct the order α_s quark coefficient functions adding the contributions given in eq. (B.24). For the detail of the calculation, I refer to Appendix B.

4.4.3 Benchmark of the Structure Functions

Finally, in order to check that the above derivation for the massive structure functions is correct, the implementation presented above has been compared to the `OpenQCDrad` code [76]. In Ref. [83] a benchmark table for the NC charm structure function F_2^c was presented and reported here in Tab. 4.2. As one can see, the agreement is good over a wide kinematic range. Also the CC FFNS structure functions have been benchmarked against the same code and the same good accuracy was found.

$x \backslash Q^2$	$\epsilon_{\text{rel}}(Q^2 = 10 \text{ GeV}^2)$	$\epsilon_{\text{rel}}(Q^2 = 100 \text{ GeV}^2)$	$\epsilon_{\text{rel}}(Q^2 = 1000 \text{ GeV}^2)$
10^{-4}	1.8%	1.8%	1.1%
10^{-3}	0.1%	0.1%	0.4%
10^{-2}	0.2%	0.1%	0.8%

Table 4.2: Relative differences between the implementation of the charm structure function F_2^c with $\overline{\text{MS}}$ heavy quark masses discussed in this section and the `OpenQCDrad` results.

Chapter 5

The NNPDF Methodology

The acronym NNPDF stands for Neural Network Parton Distribution Functions and this is the name of the methodology adopted for the determination of PDFs described in this chapter.

The NNPDF approach is based on the combination of the *Monte Carlo* method for the treatment of uncertainties with the use of *neural networks* as basic interpolating functions. The general idea is twofold. First, problems related to the possibility of non-Gaussian errors and non-trivial error propagation are best addressed through the use of a representation whereby central values are obtained from a Monte Carlo sample as averages, uncertainties as standard deviations, and so forth. Second, problems which require the reconstruction of a function through its discrete sampling, without making assumptions on its functional form, are best addressed using neural networks as unbiased interpolants.

In the first stage, one generates a Monte Carlo ensemble of replicas of the original data. The ensemble is generated with the probability distribution of the data, and it is large enough to reproduce the statistical properties of the data to the desired accuracy. In practice, data are assumed to be distributed according to a given multi-Gaussian probability distribution of statistical and systematic errors, described by a covariance matrix and a normalization error, and thus this is the distribution that is used to generate the replicas. However, any other probability distribution can be used if required by the experimental data. Each element in the Monte Carlo set is then a replica of the experimental data and contains as many data points as are originally available. The ensemble contains all the available experimental information, which can be reproduced *a posteriori* by performing statistical operations on the replicas that form the ensemble.

In the second stage, a set of PDFs is extracted from each replica of the data. Each PDF at a given scale is parametrized by an individual neural network. A neural network is just an especially convenient functional form used in place of the more usual polynomials. In practice, one first chooses a basis set of initial PDFs, typically smaller than the maximal set of twelve quarks and antiquarks plus one gluon, and then evolves from the initial scale to the scale at which data are available by using standard DGLAP evolution equations described in Chapter 1. Finally, physical observables are computed by convoluting the evolved PDFs with the coefficient functions. The best fit set of PDFs is finally determined by comparing the theoretical computation of the observable for a given PDF set with the respective experimental values contained in each Monte Carlo

replica. The experimental values will of course be different in each replica, as they will fluctuate according to their distribution in the Monte Carlo ensemble, and the best fit PDFs will be accordingly different for each replica. The ensemble of these best fit PDFs, which contains as many elements as the set of replicas of the data, is the final result of the PDF determination in the NNPDF approach.

The way in which the best fit set of PDFs is determined from each data replica is especially important. A first obvious requirement is that the best fit be independent of any assumption made about the parton parametrization. This requirement is met by adopting a redundant parametrization: the size of the neural networks used, *i.e.* the number of parameters used to parametrize them, is much larger than the minimum required in order to reproduce the data.

A more subtle issue is that of establishing how the best fit is to be determined. A first possible answer might be to determine the best fit as the absolute minimum of the χ^2 (*i.e.* absolute maximum of the likelihood). However, this procedure does not produce the optimal fit. Indeed, even for fully compatible data, independent measurements of the same quantity at the same point will fluctuate within the uncertainty of the measurement. If fitted by maximum likelihood, such independent measurements will automatically be combined into their weighted average. However, assume now that two independent measurements of the same observable are performed, but measured at very close values of the underlying kinematic variables: for example the structure function $F_2(x, Q)$ at the same Q and two different but close values of x . Then, if a redundant parametrization is used, a fit which goes through the central values of both measurements might be possible, but in the limit in which the two measurements are performed at infinitesimally close points this would correspond to a discontinuous behavior of the observable, which is surely unphysical. This problem is exacerbated in the case of incompatible measurements.

It was thus suggested [84] that the best fit should be characterized by a value of the χ^2 which is not the smallest possible, but rather equal to the value expected on the basis of the fluctuations of the data. In order to determine this value, a strategy was developed in Ref. [85], based on the so-called *cross-validation* method used quite generally in neural network studies [86].

In Sec. 5.1 the Monte Carlo generation of artificial data will be described, while in Sec. 5.2 the particular neural network architecture as well as the minimization strategy and the stopping criterion adopted in the NNPDF fits will be exposed. Finally, in Sec. 5.3, some of the statistical estimators that are commonly used to assess the quality and the stability of a given fit will be given for future use.

5.1 Monte Carlo Generation

In order to explain how the Monte Carlo generation of the artificial data works, we start with the observation that the experimental covariance matrix for each experiment can be computed from knowledge of statistical, systematic and normalization uncertainties as follows:

$$\text{cov}_{pq} = \left(\sum_{i=1}^{N_c} \sigma_{p,c}^{(i)} \sigma_{q,c}^{(i)} + \sum_{i=1}^{N_a} \sigma_{p,a}^{(i)} \sigma_{q,a}^{(i)} + \sum_{i=1}^{N_r} \sigma_{p,r}^{(i)} \sigma_{q,r}^{(i)} + \delta_{pq} \sigma_{p,s}^2 \right) F_{p,I} F_{q,J}, \quad (5.1)$$

where the indices p and q run over the experimental points, $F_{I,p} \equiv F_I(x_p, Q_p^2)$ and $F_{J,q} \equiv F_J(x_q, Q_q^2)$ are the measured central values for the observables I and J , and the various uncertainties, given as relative values, are:

- $\sigma_{p,c}^{(i)}$, the N_c correlated systematic uncertainties,
- $\sigma_{p,a(r)}^{(i)}$, the N_a (N_r) absolute (relative) normalization uncertainties,
- $\sigma_{p,s}$ the statistical uncertainty.

The correlation matrix is then defined as:

$$\rho_{pq} = \frac{\text{COV}_{pq}}{\sigma_{p,\text{tot}}\sigma_{q,\text{tot}}F_{I,p}F_{J,q}}, \quad (5.2)$$

where the total uncertainty $\sigma_{p,\text{tot}}$ for the p -th point is given by:

$$\sigma_{p,\text{tot}} = \sqrt{\sigma_{p,s}^2 + \sigma_{p,c}^2 + \sigma_{p,N}^2}, \quad (5.3)$$

being the total correlated uncertainty $\sigma_{p,c}$ the sum of all correlated systematics:

$$\sigma_{p,c}^2 = \sum_{i=1}^{N_c} \left[\sigma_{p,c}^{(i)} \right]^2 \quad (5.4)$$

and the total normalization uncertainty:

$$\sigma_{p,N}^2 = \sum_{i=1}^{N_a} \left[\sigma_{p,a}^{(i)} \right]^2 + \sum_{i=1}^{N_r} \left[\frac{1}{2} \sigma_{p,r}^{(i)} \right]^2. \quad (5.5)$$

The factor one half in the relative normalization uncertainties in eq. (5.5) comes from the first order expansion of eq. (5.7) below.

The statistical sample is obtained by generating N_{rep} artificial replicas of data points following a multi-Gaussian distribution centered around the central value of each data point with the variance given by the experimental uncertainty. More precisely, given the experimental data point $F_{I,p}^{(\text{exp})} \equiv F_I(x_p, Q_p^2)$, the N_{rep} artificial points $F_{I,p}^{(\text{art})^{(k)}}$ are generated as follows:

$$F_{I,p}^{(\text{art})^{(k)}} = S_{p,N}^{(k)} F_{I,p}^{(\text{exp})} \left(1 + \sum_{i=1}^{N_c} r_{p,c}^{(k)} \sigma_{p,c}^{(i)} + r_{p,s}^{(k)} \sigma_{p,s} \right), \quad k = 1, \dots, N_{\text{rep}}, \quad (5.6)$$

where:

$$S_{p,N}^{(k)} = \prod_{i=1}^{N_a} \left(1 + r_{p,a}^{(k)} \sigma_{p,a}^{(i)} \right) \prod_{i=1}^{N_r} \sqrt{1 + r_{p,r}^{(k)} \sigma_{p,r}^{(i)}}. \quad (5.7)$$

The variables $r_{p,c}^{(k)}$, $r_{p,s}^{(k)}$, $r_{p,a}^{(k)}$ and $r_{p,r}^{(k)}$ are all univariate Gaussian random numbers that generate fluctuations of the artificial data around the central value given by the experiments. For each replica k , if two experimental points p and p' have correlated systematic uncertainties, then $r_{p,c}^{(k)} = r_{p',c}^{(k)}$, *i.e.* the fluctuations due to the correlated systematic

uncertainties are the same for both points. A similar condition on $r_{p,n}^{(k)}$ ensures that correlations between normalization uncertainties are properly taken into account.

The treatment of normalization uncertainties needs some more care. As is well known, including normalization uncertainties in the covariance matrix, as done in eq. (5.1), would lead to a fit that is systematically biased to lie below the data: this is the so-called D’Agostini bias. In Ref. [87] an unbiased method based on a self-consistent iterative procedure, called t_0 method, is developed and implemented in the present NNPDF fits since NNPDF2.0 [69].

In Ref. [84] it has been shown that, in order to reach accuracies of order 1% on central values, errors and correlations, a sample of about $N_{\text{rep}} = 1000$ Monte Carlo replicas would be necessary. Nevertheless, such a large number of Monte Carlo replicas would result in as many PDFs and this turns out not to be very practical. In fact, assuming to use such a PDF set with a numerical code that computes a cross section for a specific process, the evaluation of the uncertainty associated to PDFs would require 1000 runs for each kinematical configuration. In addition, the tabulation of such a set would also result in very large files difficult to handle.

However, it has been observed that choosing $N_{\text{rep}} = 100$ is still enough for having accuracies at the percent level for central values and errors and only the accuracy of the correlations slightly worsens reaching a few percent level. Therefore, most of the NNPDF sets come with $N_{\text{rep}} = 100$, though also some sets with $N_{\text{rep}} = 1000$, useful for very accurate statistical studies, have been made public.

5.2 Neural Networks and Fitting Strategy

In this section the parametrization used to represent PDFs at the initial scale, the training (*i.e.* fitting) strategy and the method used to determine the best fit PDF set in the NNPDF analyses is discussed.

In the NNPDF approach the parametrization of PDFs is rather different from that which is most commonly adopted. Instead of choosing an optimized basis of functions with a relatively small number of physically motivated parameters, an unbiased basis of functions (provided by neural networks) parametrized by a very large and redundant set of parameters is used.

The fit of neural networks to data is performed by minimizing a suitably defined error function. This is a complex task because it requires to find the minimum in a very large parameter space of the error function, which is a non-local functional of the functions which are being determined in the minimization. A carefully tuned *genetic algorithm* [86] turns out to provide an efficient solution to this problem. In addition, as already mentioned, the determination of the best fit is not trivial since it is not just given by the absolute minimum of some error function. Indeed, a redundant parametrization may accommodate not only the smooth shape of the “true” underlying PDFs, but also the random fluctuations of the experimental data about it.

This raises the question of how the best fit should be determined. In the NNPDF approach this problem is addressed through the so-called *cross-validation* method [86], which provides the desired stopping criterion.

In summary, the main ingredients of the NNPDF fitting procedure are:

1. neural networks, in order to have a flexible and redundant parametrization of PDFs,
2. genetic algorithm, which allows an efficient minimization on a large parameter space,
3. determination of the best fit by cross-validation, in order to determine the smooth physical law which underlies statistical fluctuations.

In the following each of the above points will be discussed in more detail.

5.2.1 Neural Network Parametrization

In the present NNPDF analyses seven PDFs, parametrized at a initial evolution scale $Q_0^2 = 2 \text{ GeV}^2$, are extracted. The seven parametrized PDFs correspond to the gluon g PDF and to six linear combinations of the light quark PDFs $u, \bar{u}, d, \bar{d}, s$ and \bar{s} . The heavy quark PDFs c, \bar{c}, b, \bar{b} etc., are eventually radiatively generated at higher scales by means of the DGLAP evolution. Any intrinsic heavy quark contributions is thus neglected⁽¹⁾.

Once the PDFs to be determined have been chosen, any linearly independent combination of them is a viable choice to perform the fit. In this respect neural networks are particularly suitable because they provide sufficient flexibility to accommodate any reasonable choice. The specific basis chosen in the NNPDF analyses is given by the following linear combinations:

- gluon: $g(x, Q_0) \equiv f_g(x, Q_0)$,
- singlet: $\Sigma(x, Q_0) \equiv \sum_{q=u,d,s} [f_q(x, Q_0) + f_{\bar{q}}(x, Q_0)]$,
- total valence: $V(x, Q_0) \equiv \sum_{q=u,d,s} [f_q(x, Q_0) - f_{\bar{q}}(x, Q_0)]$,
- non-singlet triplet: $T_3(x, Q_0) \equiv [f_u(x, Q_0) + f_{\bar{u}}(x, Q_0)] - [f_d(x, Q_0) + f_{\bar{d}}(x, Q_0)]$,
- sea asymmetry: $\Delta_S(x, Q_0) \equiv f_{\bar{d}}(x, Q_0) - f_{\bar{u}}(x, Q_0)$,
- total strangeness: $s^+(x, Q_0) \equiv f_s(x, Q_0) + f_{\bar{s}}(x, Q_0)$,
- strange valence: $s^-(x, Q_0) \equiv f_s(x, Q_0) - f_{\bar{s}}(x, Q_0)$.

¹The vanishing of intrinsic heavy flavour contributions is an assumption that in principle could be relaxed. In fact, within the NNPDF collaboration, the inclusion of an intrinsic charm component in a PDF determination is presently being considered.

The assumption that all heavy quark PDFs are generated only radiatively at higher scales, is implemented by requiring that:

$$c(x, Q_0) = \bar{c}(x, Q_0) = b(x, Q_0) = \bar{b}(x, Q_0) = t(x, Q_0) = \bar{t}(x, Q_0) = 0. \quad (5.8)$$

Each independent PDF is parametrized using a multi-layer feed-forward neural network [86]. This typology of neural network can be visualized as composed by neurons arranged into L layers and where the k -th layer contains n_k neurons (see for example Fig. 5.1). The output of the neural network is then given by the neurons in the last layer as a function of the output of all neurons in the preceding layer, which in turn is a function of the output of all neurons in the preceding layer and so on, back to the first layer, which provides the input. Each neuron in a given layer processes the output of *all* the neurons of the preceding layer, in particular the output $\xi_i^{(k)}$ of the i -th neuron in the k -th layer is given by a nonlinear *activation function* $g(x)$ according to the formula:

$$\xi_i^{(k)} = g\left(h_i^{(k)}\right), \quad i = 1, \dots, n_k, \quad k = 2, \dots, L, \quad (5.9)$$

whose argument $h_i^{(k)}$ is the linear combination of the output $\xi_j^{(k-1)}$ of all neurons in the previous layers:

$$h_i^{(k)} = \sum_{j=1}^{n_{k-1}} \omega_{ij}^{(k)} \xi_j^{(k-1)} - \theta_i^{(k)}, \quad (5.10)$$

where $\omega_{ij}^{(k)}$ (weights) and $\theta_i^{(k)}$ (biases) are the free parameters to be determined by the fitting procedure. In the NNPDF approach $g(x)$ is taken to be a sigmoid:

$$g(x) = \frac{1}{1 + e^{-x}} \quad (5.11)$$

in the inner layers and the linear function $g(x) = x$ for the last (output) neurons(s).

In practice, it turns out to be convenient to rescale both the input and the output of the neural network, in such a way that they both take values between 0 and 1: this avoids having weights $\omega_{ij}^{(k)}$ and biases $\theta_i^{(k)}$ whose numerical values span many orders of magnitude.

In short, a neural network outputs the value(s) $\xi_j^{(L)}$ as a function of the input value(s) $\xi_j^{(1)}$ and the parameters $\omega_{ij}^{(k)}$ and $\theta_i^{(k)}$. The training of such a neural network consists in the determination of the best fit values of these parameters.

The choice of the architecture of the neural network cannot be derived from general rules and it must be adapted to each specific problem. One can roughly guess the size of the neural network and then determine by actual fitting the critical size above which results become independent of the size of the networks. Finally, one chooses a size which is somewhat larger than the critical one.

It was found that a neural network with architecture 2-5-3-1, as shown in Fig. 5.1 (*i.e.* two neurons in the input layer, five neurons in the first hidden layer, three neurons in the second hidden layer and one neuron in the output layer), for all PDFs is an adequate choice for this particular task. In fact, it turned out to be more efficient for the fitting procedure to take simultaneously as input both x and $\ln x$ as inputs.

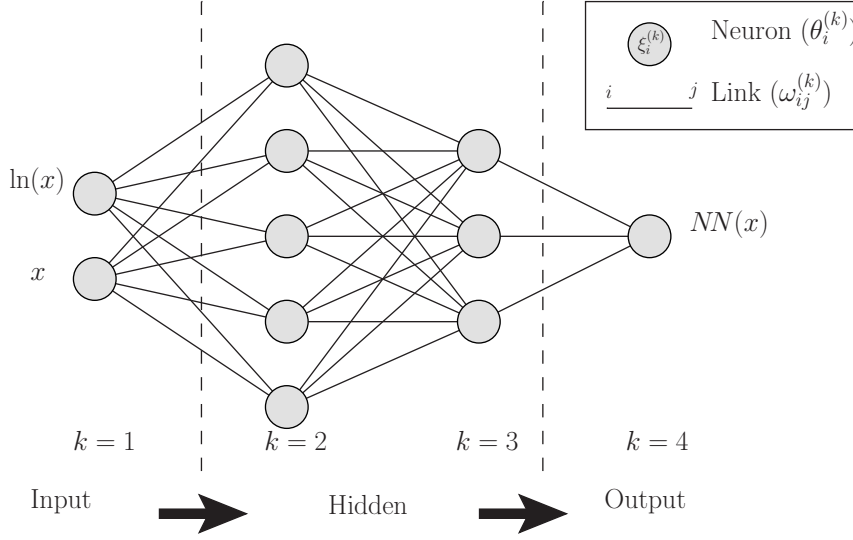


Figure 5.1: Neural network having architecture 2-5-3-1. This architecture is chosen to parametrize the independent PDFs in the NNPDF fits.

This configuration corresponds to 37 free parameters for each PDF, *i.e.* a total of 259 free parameters⁽²⁾. The use of such a redundant architecture reduces a priori the possibility of a functional bias. The absence of any bias has been explicitly checked in Ref. [88], by verifying the independence of results on the choice of architecture.

Large enough neural networks can reproduce any functional form. However, the training can be made more efficient by adding a preprocessing step, *i.e.* by multiplying the output of the neural networks by an appropriately chosen function. The neural network then only fits the deviation from this function.

In practice, the input PDF basis in terms of the neural networks $NN_i(x)$ and preprocessing functions is:

$$\begin{aligned}
 g(x, Q_0) &= A_g \quad x^{\alpha_g} \quad (1-x)^{\beta_g} \quad NN_g(x), \\
 \Sigma(x, Q_0) &= \quad \quad x^{\alpha_\Sigma} \quad (1-x)^{\beta_\Sigma} \quad NN_\Sigma(x), \\
 V(x, Q_0) &= A_V \quad x^{\alpha_V} \quad (1-x)^{\beta_V} \quad NN_V(x), \\
 T_3(x, Q_0) &= \quad \quad x^{\alpha_{T_3}} \quad (1-x)^{\beta_{T_3}} \quad NN_{T_3}(x), \\
 \Delta_S(x, Q_0) &= A_{\Delta_S} \quad x^{\alpha_{\Delta_S}} \quad (1-x)^{\beta_{\Delta_S}} \quad NN_{\Delta_S}(x), \\
 s^+(x, Q_0) &= \quad \quad x^{\alpha_{s^+}} \quad (1-x)^{\beta_{s^+}} \quad NN_{s^+}(x), \\
 s^-(x, Q_0) &= \quad \quad x^{\alpha_{s^-}} \quad (1-x)^{\beta_{s^-}} \quad NN_{s^-}(x) - s_{\text{aux}}(x, Q_0),
 \end{aligned} \tag{5.12}$$

where:

$$s_{\text{aux}}(x, Q_0) = A_{s^-} x^{r_{s^-}} (1-x)^{t_{s^-}}. \tag{5.13}$$

The values of the preprocessing exponents α and β are randomly chosen, replica by replica, within a reasonably wide range that ensures the integrability of PDFs and the absence of any bias at the same time. The exponents r_{s^-} and t_{s^-} , instead, are chosen in

²To be compared to less than a total of 30 free parameters for parton fits based on standard functional parametrizations [24, 23, 28].

such a way that $s_{\text{aux}}(x, Q_0)$ peaks in the valence region ($x \sim 0.1 \div 0.5$), and that the small- x and large- x behavior of $s^-(x, Q_0)$ are not controlled by the $s_{\text{aux}}(x, Q_0)$ contribution. The four normalization constants A_g , A_V , A_{Δ_S} and A_{s^-} that have been factored out, are instead determined dynamically during the fit requiring that the momentum sum rule:

$$\int_0^1 dx x [\Sigma(x, Q_0) + g(x, Q_0)] = 1 \quad (5.14)$$

and the valence sum rules:

$$\begin{aligned} \int_0^1 dx [f_u(x, Q_0) - f_{\bar{u}}(x, Q_0)] &= 2 \\ \int_0^1 dx [f_d(x, Q_0) - f_{\bar{d}}(x, Q_0)] &= 1 \\ \int_0^1 dx [f_s(x, Q_0) - f_{\bar{s}}(x, Q_0)] &= 0 \end{aligned} \quad (5.15)$$

be satisfied.

5.2.2 Genetic Algorithm Minimization

Now we turn to the fitting strategy for the parametrized PDFs. The fit of neural networks on the k -th Monte Carlo replica is performed by minimizing the error function:

$$E^{(k)} = \frac{1}{N_{\text{dat}}} \sum_{p,q=1}^{N_{\text{dat}}} \left[F_{I,p}^{(\text{art})^{(k)}} - F_{I,p}^{(\text{net})^{(k)}} \right] \left[\left(\overline{\text{cov}}^{(k)} \right)^{-1} \right]_{pq} \left[F_{J,q}^{(\text{art})^{(k)}} - F_{J,q}^{(\text{net})^{(k)}} \right], \quad (5.16)$$

where $F_{I,p}^{(\text{art})^{(k)}}$ is defined in eq. (5.6) while $F_{I,p}^{(\text{net})^{(k)}}$ is the prediction of the observable F_I for the i -th experimental data point computed with the PDF set which is being fitted. Notice that the covariance matrix $\overline{\text{cov}}^{(k)}$ used in eq. (5.16) for the minimization is *not* that defined in eq. (5.1), but it is constructed from it using the t_0 prescription [87] that ensures a proper treatment of the normalization errors. The precise definition of $\overline{\text{cov}}^{(k)}$ can be found in Appendix A of Ref. [89].

Due to the non-local nature of the error function (5.16) and the complex structure of the parameter space, the *genetic algorithm* [90] turns out to be the most efficient method for its minimization.

The genetic algorithm applied to this problem works in the following way. For each Monte Carlo replica and for each independent PDF, the state of the corresponding neural network is represented by the state vector:

$$\boldsymbol{\omega} = (\omega_1, \omega_2, \dots, \omega_{N_{\text{par}}}) , \quad (5.17)$$

where each element ω_i corresponds either to a weight $\omega_{ij}^{(k)}$ or to threshold $\theta_i^{(k)}$ of the neural network, being N_{par} the total number of free parameters. At each iteration of the genetic algorithm, $N_{\text{cop}} - 1$ copies of the state vector $\boldsymbol{\omega}$ are generated. For each copy, N_{mut} randomly chosen elements of the state vector $\boldsymbol{\omega}$ are replaced by new values, according to the rule:

$$\omega_k \rightarrow \omega_k + \eta \left(r - \frac{1}{2} \right), \quad (5.18)$$

where r is a uniform random number between 0 and 1 and η (mutation rate) is a free parameter of the minimization algorithm which can be optimized either for the given problem or dynamically during the minimization. At the end of this procedure, there will be $N_{\text{cop}} - 1$ variants of the starting state vector ω (mutants) plus the starting state vector itself. At this point the error function in eq. (5.16) is computed for each one of the N_{cop} state vectors and the one that yields the lowest value (which could possibly be the starting configuration) is then chosen as a starting point for the following iteration.

The procedure is then iterated until the vector with smallest value of the error function $E^{(k)}$ meets a suitable stopping criterion. Notice that the minimization procedure is such that the value of the error function $E^{(k)}$ never increases.

The main advantage of genetic minimization is that it is able to explore many regions of parameter space simultaneously. This lowers the possibility of getting trapped into local minima of the error function allowing a more reliable determination of the best fit configuration.

5.2.3 Cross-Validation Method

The crucial feature which guarantees a bias-free fit is the possibility of stopping the training, not at the lowest value of the error function (which might not reflect the true underlying physical law), but rather when suitable criteria are met. These criteria should single out the point where the fit reproduces the information contained in the data, but not the statistical noise. Namely, the best fit should have the lowest possible value of the error function compatible with the requirement of not fitting statistical fluctuations.

To this end, the so-called *cross-validation* criterion is adopted and it works as follows. The dataset is separated into two disjoint sets and the error function $E^{(k)}$ in eq. (5.16) minimized only using the data points of the first set (*training set*). During the minimization process, the error function from the data of the second set (*validation set*) is however computed. The best fit is reached when the error function computed on the validation set ceases to decrease. In fact, a situation where the training error function keeps decreasing (recall that the training error function only decreases if the genetic algorithm is used) while the validation error function starts increasing, signals that the fit is merely reproducing the fluctuations of the specific training set. This procedure does not lead to loss of information if both the training and the validation sets reproduce the features of the full dataset. This can be simply achieved on average by choosing a different random partition for each Monte Carlo replica of the dataset.

In practice, the stopping criterion is implemented as follows. One first defines the training fraction $0 \leq f_{\text{tr}} \leq 1$ (typically $f_{\text{tr}} = 0.5$, *i.e.* half of the data go into the training set and half into the validation set) and for each Monte Carlo replica selects randomly a fraction f_{tr} of points for each experiment, which are used for training, while the remaining points are assigned to the validation set. At the l -th iteration of the genetic algorithm the error function in eq. (5.16) is separately computed on both the training and validation sets defining the quantities $E_{\text{tr}}^{(k)}(l)$ and $E_{\text{val}}^{(k)}(l)$. The training proceeds at least until $E_{\text{tr}}^{(k)}$ has reached the threshold value $E_{\text{tr}}^{(k)} = E_{\text{min}}$, typically $E_{\text{min}} \simeq 3$. This ensures that the training does not stop due to fluctuations in the early stages. If $E_{\text{tr}}^{(k)} \leq E_{\text{min}}$, the training is stopped at the l -th generation if the following conditions

are met:

$$r_{\text{tr}} < 1 - \delta_{\text{tr}}, \quad r_{\text{val}} > 1 + \delta_{\text{val}}, \quad (5.19)$$

where the slopes r_{tr} and r_{val} are defined as:

$$r_{\text{tr, val}} \equiv \frac{\langle E_{\text{tr, val}}(l) \rangle}{\langle E_{\text{tr, val}}(l - \Delta_{\text{sm}}) \rangle}, \quad (5.20)$$

and the moving averages $\langle E_{\text{tr}}^{(k)}(l) \rangle$ and $\langle E_{\text{val}}^{(k)}(l) \rangle$ as:

$$\langle E_{\text{tr, val}}^{(k)}(l) \rangle \equiv \frac{1}{N_{\text{sm}}} \sum_{i=l-N_{\text{sm}}+1}^l E_{\text{tr, val}}^{(k)}(i), \quad (5.21)$$

being N_{sm} the width of the smearing interval over which the moving average is computed and Δ_{sm} the distance between two points used to evaluate the slope on the error function profiles. Typically, the values $N_{\text{sm}} = \Delta_{\text{sm}} = 200$ are chosen. In other words, the fit is stopped if the training error function has a negative slope ($r_{\text{tr}} < 1$ up to some tolerance given by δ_{tr}) while the slope of validation error function is positive ($r_{\text{val}} > 1 + \delta_{\text{val}}$). The values of the tolerances δ_{tr} and δ_{val} must be determined by analyzing the behavior of the fit for the particular dataset which is being used for neural network training. It was found that $\delta_{\text{tr}}, \delta_{\text{val}} \sim 10^{-4}$ is a suitable choice.

Finally, in order to avoid unacceptably long fits, an upper length for the training process, *i.e.* a maximum number of iterations N_{gen} of the genetic algorithm, is also set. This is typically chosen to be $N_{\text{gen}} = 50000$. It has been checked that, though about 10% of the Monte Carlo replicas do not meet the stopping criterion before reaching the maximum number of allowed iterations, this does not spoil the overall quality of the fit. This is essentially due to the fact that, after such a big number of iterations, both training and validation error functions have reached a point where they do not decrease any more.

5.3 Statistical Tools

One of the biggest advantages of the Monte Carlo approach is that it allows for the use of the standard statistical tools. In this last section we will briefly review how to compute the most important statistical estimators given a Monte Carlo PDF set $\{\mathbf{f}_k\}$, with $k = 1, \dots, N_{\text{rep}}$.

The expectation value of any observable F_i which depends on PDFs is given by the average over replicas:

$$\langle F_i \rangle = \frac{1}{N_{\text{rep}}} \sum_{k=1}^{N_{\text{rep}}} F_i[\mathbf{f}_k]. \quad (5.22)$$

Similarly the uncertainty is given by the standard deviation:

$$\sigma_i = \sqrt{\frac{N_{\text{rep}}}{N_{\text{rep}} - 1} (\langle F_i^2 \rangle - \langle F_i \rangle^2)}. \quad (5.23)$$

Given a second observable F_j depending on PDFs, the associated covariance is given by:

$$\text{cov}_{ij} = \rho_{ij}\sigma_i\sigma_j, \quad (5.24)$$

with:

$$\rho_{ij} = \frac{N_{\text{rep}}}{N_{\text{rep}} - 1} \frac{\langle F_i F_j \rangle - \langle F_i \rangle \langle F_j \rangle}{\sigma_i \sigma_j}. \quad (5.25)$$

Another important statistical estimator, which will be extensively used in Chapter 6, is the statistical distance between Monte Carlo samples. Given two different sets of Monte Carlo PDFs $\{\mathbf{f}_k^{(1)}\}$ and $\{\mathbf{f}_k^{(2)}\}$ having $N_{\text{rep}}^{(1)}$ and $N_{\text{rep}}^{(2)}$ replicas respectively, the statistical distance of the observable F_i with respect to the two samples $\{\mathbf{f}_k^{(1)}\}$ and $\{\mathbf{f}_k^{(2)}\}$ is defined as:

$$d[\langle F_i \rangle^{(1)}, \langle F_i \rangle^{(2)}] = \sqrt{\frac{(\langle F_i \rangle^{(1)} - \langle F_i \rangle^{(2)})^2}{(\sigma_i^{(1)})^2 + (\sigma_i^{(2)})^2}} \quad (5.26)$$

where the quantities $\langle F_i \rangle^{(i)}$ and $\sigma_{F_i}^{(i)}$ have been evaluated using eqs. (5.22) and (5.23) using the Monte Carlo PDFs $\{\mathbf{f}_k^{(i)}\}$. The analogous definition for the statistical distance between uncertainties can be found in Appendix A of Ref. [69].

In practice the distance d defined in eq. (5.26) measures whether the Monte Carlo samples $\{\mathbf{f}_k^{(1)}\}$ and $\{\mathbf{f}_k^{(2)}\}$ do or do not come from the same underlying probability distribution. In other words, eq. (5.26) and its analogous for the uncertainty test whether the two distributions from which the two samples are taken have respectively the same mean and the same standard deviation.

If $N_{\text{rep}}^{(1)} = N_{\text{rep}}^{(2)} = N_{\text{rep}}$, with N_{rep} large enough, it can be shown that d scales as $\sqrt{N_{\text{rep}}}$. In particular, if the two samples are statistically equivalent, one gets $d \simeq 1$, while if they differ by one standard deviation, one gets $d \simeq \sqrt{N_{\text{rep}}}$.

Notice that the observable F_i in eq. (5.26) could well be a PDF so that d would measure the statistical distance between that PDF belonging to two different Monte Carlo samples. In particular, this is how the statistical distance will be largely used in Chapter 6 to assess the statistical ‘‘compatibility’’ of different sets of PDFs.

Chapter 6

Impact of Higher Orders and Heavy Flavours on PDFs

The implementation of the FONLL scheme up to order α_s^2 , described in detail in Chapter 3, has been recently employed for the determination of the proton PDFs using the NNPDF methodology, presented in Chapter 5. This originally resulted in the PDF sets of the NNPDF2.1 family [55, 56].

The NNPDF2.1 analysis was based on a wide set of data including: DIS, fixed-target Drell-Yan and pre-LHC electro-weak vector boson and inclusive jet production data at colliders. Since its release, however, different LHC data with potential to further constrain PDFs have been released and they have been included in the NNPDF2.3 analysis [29].

In Sec. 6.1 a description of the dataset included in the NNPDF2.3 analysis will be given. In Sec. 6.2 the NNPDF2.3 sets will be presented highlighting the impact of the inclusion high order corrections and heavy quark mass effects. Finally in Sec. 6.3 some phenomenology relevant for the LHC will be studied.

6.1 Experimental Data

In this section the experimental data used for the NNPDF2.3 analysis will be presented. In the first place, the kinematic cuts applied to the dataset and their motivation will be discussed. Secondly, the full dataset included in the fit will be discussed and, finally, the issue of the implementation of positivity constraints on PDFs will be addressed.

6.1.1 Kinematic Cuts

As is well known, DIS structure function data are affected by both power corrections of kinematic origin, due to the mass of the target m_N , as well as corrections related to higher twist contributions to the operator product expansion (OPE). The former can be determined exactly in the form of an expansion in powers of m_N^2/Q^2 , while the latter are of dynamical origin and thus, if included, they must be fitted just like the leading twist PDFs.

The target mass corrections are included up to order m_N^2/Q^2 [85] in the NNPDF2.3 fits. Dynamical higher twist corrections, on the other hand, are not and they are kept

under control by imposing suitable kinematic cuts. In particular, only data having invariant mass of the final state $W^2 = Q^2(1-x)/x \geq W_{\min}^2 = 12.5 \text{ GeV}^2$ and energy $Q^2 \geq Q_{\min}^2 = 3 \text{ GeV}^2$ are included in the fit. Very recently, it has been explicitly shown [91] that, imposing the aforementioned cuts, the higher twist corrections have indeed a negligible impact on the PDF determination.

A further reason for selecting data with $Q^2 \geq Q_{\min}^2$ is the fact that, very close to the charm quark threshold $M_c^2 \simeq 2 \text{ GeV}^2$, the predictions for charm structure function F_2^c in the GM-VFNS might suffer from instabilities due to the threshold behavior. This suggests to use a value of Q_{\min}^2 reasonably larger than M_c^2 and $Q_{\min}^2 = 3 \text{ GeV}^2$ is then a suitable choice.

Furthermore, there is an indication of possible deviations from the NLO DGLAP evolution in the small- x HERA data [92, 93] and these deviations are mostly relevant in the smaller Q^2 region.

On top of the cuts just described, additional cuts on the HERA F_2^c data are applied for the NLO fit. The motivation is discussed in detail in Ref. [47] and essentially is that the FONLL-A scheme, which is used for the NLO fits (see Sec. 3.1.2), provides a poor description of the data in the smallest x and Q^2 region due to missing large order α_s^2 corrections⁽¹⁾. Therefore, the HERA F_2^c data with $Q^2 \leq 4 \text{ GeV}^2$ and with $Q^2 \leq 10 \text{ GeV}^2$ for $x \leq 10^{-3}$ are removed from the fit. These cuts ensure that all F_2^c experimental data included in the fit are well described by a theory accurate at order α_s . These additional cuts on F_2^c are instead removed for the NNLO fits, where all the large order α_s^2 corrections are consistently included.

Finally, it should be remarked that only DIS data undergo kinematic cuts. On the contrary, all the hadronic data are included in the fits because, given their kinematic coverage, they are not affected by power corrections.

6.1.2 The Dataset

The NNPDF2.3 dataset is summarized in Tab. 6.1, where experimental data are separated into DIS, fixed target Drell-Yan production, electro-weak vector boson production and inclusive jet data. For each dataset the number of points after the kinematic cuts described in the previous section as well as and their kinematic ranges are provided.

It should be noticed that, on top of all the data already present in NNPDF2.1, 146 LHC data points have been included in the NNPDF2.3 analysis: the ATLAS W and Z lepton rapidity distributions from the 2010 data set [94], the CMS W electron asymmetry from the 2011 data set [95], the LHCb W lepton rapidity distributions from the 2010 data set [96] and the ATLAS inclusive jet cross sections from the 2010 run [97].

A scatter plot in the (x, Q^2) plane of the dataset included in the NNPDF2.3 fit NNLO (the widest) is displayed in Fig. 6.1, with the values of x determined using LO kinematics.

6.1.3 Positivity constraints

An important theoretical constraint which should be enforced when PDFs are determined is the positivity and, as discussed in Ref. [126], it should be imposed on cross sections

¹Note that this is true for any heavy quark scheme that does not include order α_s^2 corrections.

Experiment	Observable	Ref.	N_{dat}	$[x_{\text{min}}, x_{\text{max}}]$	$[Q_{\text{min}}^2, Q_{\text{max}}^2]$ [GeV ²]
Deep-Inelastic scattering					
NMC pd	F_2^p/F_2^d	[98]	132	[0.008, 0.68]	[3.5, 99.0]
NMC	F_2^p	[99]	224	[0.009, 0.48]	[3.2, 62.3]
SLAC	F_2^p	[100]	37	[0.10, 0.55]	[3.0, 19.5]
	F_2^d	[100]	37	[0.10, 0.55]	[3.3, 19.5]
BCDMS	F_2^p	[101]	333	[0.07, 0.75]	[7.5, 230.0]
	F_2^d	[102]	248	[0.07, 0.75]	[8.8, 230.0]
HERA1-AV	NC red. xsec. e^+	[103]	379	$[4.3 \cdot 10^{-5}, 0.65]$	[3.5, 30000.0]
	NC red. xsec. e^-	[103]	145	$[1.3 \cdot 10^{-3}, 0.65]$	[90.0, 30000.0]
	CC red. xsec. e^+	[103]	34	[0.008, 0.40]	[300.0, 15000.0]
	CC red. xsec. e^-	[103]	34	[0.013, 0.40]	[300.0, 30000.0]
CHORUS	CC red. xsec. ν	[104]	431	[0.045, 0.65]	[3.0, 95.2]
	CC red. xsec. $\bar{\nu}$	[104]	431	[0.045, 0.65]	[3.0, 95.2]
FLH108	F_L	[105]	8	$[2.8 \cdot 10^{-4}, 0.0036]$	[12.0, 90.0]
NuTeV	CC Dimuon ν	[106, 107]	41	[0.021, 0.33]	[3.1, 116.5]
	CC Dimuon $\bar{\nu}$	[106, 107]	38	[0.015, 0.21]	[3.1, 68.3]
ZEUS-H2	NC red. xsec. e^-	[108]	90	[0.005, 0.65]	[200.0, 30000.0]
	CC res. xsec. e^-	[109]	37	[0.015, 0.65]	[280.0, 30000.0]
ZEUS F_2^c	F_2^c '99	[110]	14/18	$[1.3 \cdot 10^{-4}, 0.02]$	[7.0/4.0, 130.0]
	F_2^c '03	[111]	21/27	$[7.0 \cdot 10^{-5}, 0.03]$	[7.0/4.0, 500.0]
	F_2^c '08	[112]	7/9	$[2.2 \cdot 10^{-4}, 0.032]$	[7.0, 112.0]
	F_2^c '09	[113]	8	$[8.0 \cdot 10^{-4}, 0.03]$	[30.0, 1000.0]
H1 F_2^c	F_2^c '01	[114]	6/10	$[1.3 \cdot 10^{-4}, 0.0032]$	[12.0/3.5, 60.0]
	F_2^c '09	[115]	6	$[2.4 \cdot 10^{-3}, 0.025]$	[120.0, 400.0]
	F_2^c '10	[116]	26	$[2.0 \cdot 10^{-4}, 0.05]$	[12.0/5.0, 2000.0]
Fixed Target Drell-Yan production					
DYE605	double diff. distr. d	[117]	119	[0.14, 0.65]	[50.5, 286.0]
DYE866	double diff. distr. p	[118, 119]	184	[0.017, 0.87]	[19.8, 251.2]
	double diff. distr. p/d	[120]	15	[0.026, 0.55]	[21.2, 166.4]
Collider vector boson production					
CDF W asy	W asymmetry	[121]	13	$[3.0 \cdot 10^{-3}, 0.57]$	[6463.8, 6463.8]
CDF Z rap	Z rapidity distr.	[122]	29	$[2.7 \cdot 10^{-3}, 0.80]$	[8315.2, 8315.2]
D0 Z rap	Z rapidity distr.	[123]	28	$[3.0 \cdot 10^{-3}, 0.73]$	[8315.2, 8315.2]
ATLAS W/Z rap	W/Z rapidity distr.	[94]	30	$[4.7 \cdot 10^{-4}, 0.28]$	[6464.0, 6464.0]
CMS W el asy	W electron asymmetry	[95]	11	$[1.2 \cdot 10^{-3}, 0.11]$	[6463.8, 6463.8]
LHCb W	W/Z rapidity distr.	[96]	10	$[1.6 \cdot 10^{-4}, 0.91]$	[6463.8, 8315.2]
Collider inclusive jet production					
CDF RII k_T	k_T jets	[124]	76	$[4.6 \cdot 10^{-3}, 0.90]$	[3364.0, 376382.3]
D0 RII cone	cone jets	[125]	110	$[3.1 \cdot 10^{-3}, 0.97]$	[2970.3, 341991.0]
ATLAS jets	anti- k_T jets	[97]	90	$[5.2 \cdot 10^{-5}, 0.91]$	[400.0, 140000.0]
Total					
Total NLO			3482	$[4.3 \cdot 10^{-5}, 0.97]$	[3.0, 140000.0]
Total NNLO			3501	$[4.3 \cdot 10^{-5}, 0.97]$	[3.0, 140000.0]

Table 6.1: Experimental datasets included in the NNPDF2.3 global analysis. For each experiment the number of data points and the kinematic coverage (after the kinematic cuts described in Sec. 6.1.1) are provided. Notice that for some of the HERA charm structure function datasets there are two values for the number of data points and of the energy ranges: the first corresponds to the data included in the NLO fit and the second in the NNLO fit. For hadronic data the x -ranges are determined using LO kinematics.

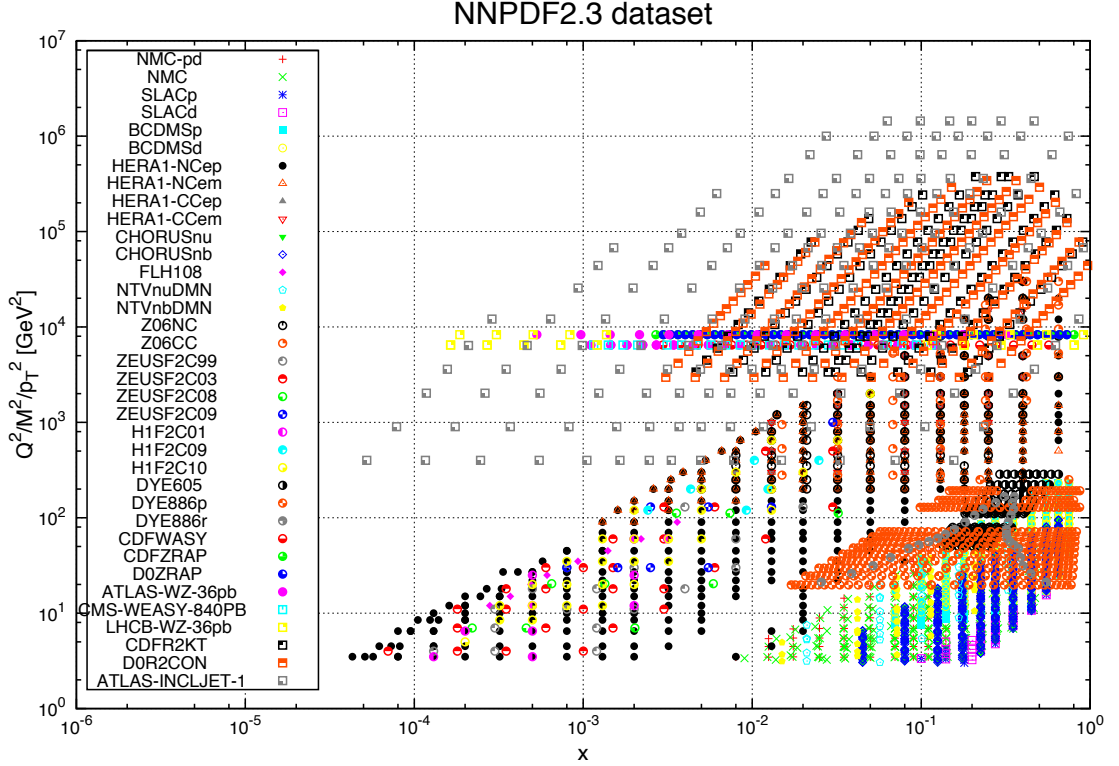


Figure 6.1: Kinematic coverage of the experimental data used in the NNPDF2.3 PDF determination.

rather than directly on PDFs, which do not necessarily satisfy this constraint (except at leading order where the probabilistic interpretation holds).

Positivity constraint may be implemented in various ways and in the NNPDF2.3 fits it is imposed using the so-called the Lagrange multipliers method. In practice, a given number of pseudo-experimental datasets having the desired kinematics are added to the real dataset and they are such that, by construction, the “experimental” value of each point belonging to the pseudo-dataset coincides with theoretical prediction for any set of PDFs. This way the global χ^2 of the fit is not affected by the presence of the positivity constraint datasets. At the k -th iteration of fitting procedure, it is checked whether one or more pseudo-points become negative. If this is the case, the absolute value of the largest violation, say ΔV , multiplied by a given factor λ (Lagrange multiplier) is added to the training error function given in eq. (5.16), in practice the following substitution is performed:

$$E_{\text{tr}}^{(k)} \rightarrow E_{\text{tr}}^{(k)} + \lambda \Delta V. \quad (6.1)$$

This way, configurations of the PDF parameter space that result in negative predictions for the pseudo-data are “discouraged” and the fitting algorithm spontaneously tends to minimize the amount of violation ΔV .

In the NNPDF2.3 fits positivity is imposed producing pseudo datasets for the following observables:

- the DIS longitudinal structure function F_L , which constrains the gluon positivity at small- x .
- The charm production cross section in neutrino DIS, $d^2\sigma^{\nu,c}/dxdy$ [127], which constrains the strange PDFs both at large and at small- x , beyond the reach of existing data.
- The neutral current DIS charm structure function F_2^c , useful to impose the positivity of the gluon at very large- x , where it is not constrained by any experimental dataset.

All the positivity constraints are implemented at a low scale Q_{pos} , that is taken to be $Q_{\text{pos}}^2 = 5 \text{ GeV}^2$, by means of 50 pseudo-data points for each observable logarithmically distributed over the range $x \in [10^{-6}, x_{\text{max}}]$ with $x_{\text{max}} = 0.1$ for the NC observables F_L and F_2^c and $x_{\text{max}} = 0.4$ for CC cross section $d^2\sigma^{\nu,c}/dxdy$. The pseudo-data used to implement positivity are computed consistently at the same perturbative order as all the other physical observables.

6.1.4 Treatment of Hadronic Data

As is clear from Tab. 6.1 and Fig. 6.1, the energies covered by the hadronic data (Drell-Yan, electro-weak boson production and jet production) are typically well above the charm quark threshold. In this regime, as shown in Sec. 2.4, the FONLL schemes reduces automatically to the ZM-VFNS. Therefore, in the NNPDF analyses only the DIS data, which however represent the majority of the whole dataset (around 3000 points out of 3500), are treated using the FONLL scheme. The hadronic data, instead, are treated using the ZM-VFNS. This provides a big practical simplification but does not affect the accuracy of the determination of PDFs.

In the NLO analyses, Drell-Yan and electro-weak vector boson production are consistently included at NLO in perturbative QCD. The extension to NNLO would be in principle straightforward, but in practice challenging because of the distribution structure and intricate choice of kinematic dependence of the NNLO coefficient functions of Ref. [128]. Therefore, an approximate computation is adopted for the NNLO analyses, which leads to an accuracy which is fully adequate for our purposes.

In this approximation, Drell-Yan and electro-weak vector boson production observables are computed with NNLO α_s and PDF evolution but NLO partonic cross sections supplemented by local K -factors that account for the missing order α_s^2 partonic coefficient functions. The K -factors are defined as the ratio of differential cross sections, where in the numerator the full NNLO expression is used, and in the denominator the same expression but with the order α_s^2 corrections to the partonic cross section set to zero. In this definition the same NNLO α_s and PDF evolution are used both in the numerator and the denominator. This minimizes the impact of the NNLO K -factor corrections, which are then reduced to the missing order α_s^2 partonic cross sections.

The K -factors are found to be rather small for most processes of interest, especially for collider kinematics. It turns out that the NNLO K -factors are of order $2 \div 3\%$ for the collider data, while they are more important for fixed-target Drell-Yan data, where they are typically of order 10% but sometimes as large as 25%. However, the average total experimental uncertainty on these data is typically larger than 20%.

As far as the inclusive jet production data are concerned, exact NNLO corrections are not known yet. NNLO theoretical predictions for CDF and D0 inclusive jet data are computed using the approximate NNLO matrix elements obtained from threshold resummation [129] as implemented in the `FastNLO` framework [130, 131]. This provides an approximate NNLO calculation which combines the most accurate perturbative information available. For the ATLAS jet data, instead, the threshold approximation is expected to be worse because of the higher center-of-mass energy, and thus only the NLO matrix elements are used but with NNLO PDF and α_s evolution. However, it was checked in Ref. [56] that the difference between fits with approximate NNLO jet matrix elements and fits with purely NLO matrix elements is significantly smaller than the difference between fits with and without jet data.

6.2 Results

We are finally ready to present the results of the implementation of the FONLL scheme up to order α_s^2 using the NNPDF methodology for the determination of the proton PDFs.

The first step will be the assessment of the higher order corrections. This will be done in Sec. 6.2.1 comparing the NNPDF2.3 NLO set with the NNLO one.

As a second step, the impact of the heavy quark mass effects will be studied in Sec. 6.2.2 by comparing at NNLO the NNPDF2.3 fit obtained using three different mass schemes, namely: FONLL-C scheme, ZM-VFNS and FFNS as described in Chapter 2.

In order to isolate the effects one is interested in, it is necessary that a common setting be used. In particular, a common value for the reference value of α_s and the heavy quark masses should be taken. For this reason, all the NNPDF fits presented in the following have been produced using as a reference for the $\overline{\text{MS}}$ strong coupling the value $\alpha_s(M_Z) = 0.119^{(2)}$, being M_Z the mass of the Z boson. However, it should be stressed that $\alpha_s(M_Z) = 0.119$ is *not* the preferred value for the NNPDF fits. In fact, the NNPDF fits have been produced for all the values of $\alpha_s(M_Z)$ spanning from 0.114 to 0.124 in steps of 0.001 and thus the users can utilize the parton set corresponding to the value of $\alpha_s(M_Z)$ that they find appropriate for their study. Eventually, combined PDF+ α_s uncertainties may be determined by combining replicas from sets corresponding to different values of α_s , as discussed in Sec. 3.2 of Ref. [135].

As for the heavy quark masses, throughout this chapter the pole mass scheme will be used. The use of the $\overline{\text{MS}}$ masses as described in Chapter 4 for a PDF determination, however, is close to its completion and in the near future the NNPDF collaboration will probably be able to release a PDF set based on the $\overline{\text{MS}}$ masses.

In Tab. 6.2 the values for the charm and bottom masses M_c and M_b used in the NNPDF2.3 analysis, along with the values used in other recent PDF determinations, are shown.

As a final remark, we recall that all the NNPDF sets presented in the following sections contain $N_{\text{rep}} = 100$ Monte Carlo replicas.

²Notice that this value is perfectly consistent with the PDG [132] value $\alpha_s(M_Z) = 0.1184 \pm 0.0007$. In addition, in Refs. [133, 134] a determination of $\alpha_s(M_Z)$ at NLO and NNLO using the NNPDF2.1 parton sets [55, 56] has been performed finding similar values.

	M_c [GeV]	M_b [GeV]
NNPDF2.3	$\sqrt{2}$	4.75
CT10 [24]	1.30	4.75
MSTW2008 [28]	1.40	4.75
ABKM09 [50]	1.50	4.50
HERAPDF1.5 [26]	1.40	4.75

Table 6.2: The default values of the heavy quark masses used in NNPDF2.3 and in several recent PDF sets.

NNPDF2.3		
	NLO	NNLO
χ_{tot}^2	1.12	1.13
$\langle \chi^2 \rangle \pm \sigma_{\chi^2}$	1.15 ± 0.06	1.18 ± 0.05
$\langle E \rangle \pm \sigma_E$	2.17 ± 0.05	2.20 ± 0.06
$\langle E_{\text{tr}} \rangle \pm \sigma_{E_{\text{tr}}}$	2.15 ± 0.07	2.18 ± 0.08
$\langle E_{\text{val}} \rangle \pm \sigma_{E_{\text{val}}}$	2.21 ± 0.07	2.24 ± 0.09

Table 6.3: Table of statistical estimators for the NNPDF2.3 NLO and NNLO fits with $N_{\text{rep}} = 100$ replicas.

6.2.1 Impact of the Higher Order Corrections

In this sections the inclusion of the NNLO corrections will be discussed. In Tab. 6.3 the statistical estimators for the NNPDF2.3 NLO and NNLO fits are reported. It should be borne in mind that the NLO fit has been obtained using the FONLL-A scheme, while the NNLO fit using the FONLL-C scheme (see Sec. 3.1.2). In Tab. 6.3 χ_{tot}^2 is computed by comparing the average of the N_{rep} replicas to the original experimental data, $\langle \chi^2 \rangle$ is instead computed by comparing each replica to the data and averaging over replicas, while $\langle E \rangle$ is the quantity that is actually minimized, *i.e.* the error function in eq. (5.16) and it coincides with the χ^2 computed by comparing each replica to the data replica it is fitted to, with the three values given corresponding to the total, training, and validation datasets. The distribution of χ^2 and E_{tr} among the NNPDF2.3 NLO and NNLO replicas are shown in Fig. 6.2. Notice that a value $\langle E \rangle \simeq 2$ is expected for a good fit because, if errors are correctly estimated, the average standard deviation of true values about the measured value should equal the total uncertainty, but replicas are generated about the measured values, so their average standard deviation about the true values should be twice the total uncertainty. It should be finally noticed that all the statistical estimators reported in Tab. 6.3, and specifically the χ^2 , are determined using the t_0 covariance matrix, needed for a proper treatment of the normalization uncertainties [87], and normalized to the total number of data points.

In Tab. 6.4 the χ_{tot}^2 values for the individual experiments for both NNPDF2.3 NLO and NNLO are reported along with the percent difference of the NNLO fit with respect to the NLO one.

From Tabs. 6.3 and 6.4, it is evident that all the statistical indicators are quite similar between NLO and NNLO. More in particular, the χ_{tot}^2 in Tab. 6.4 differ by less

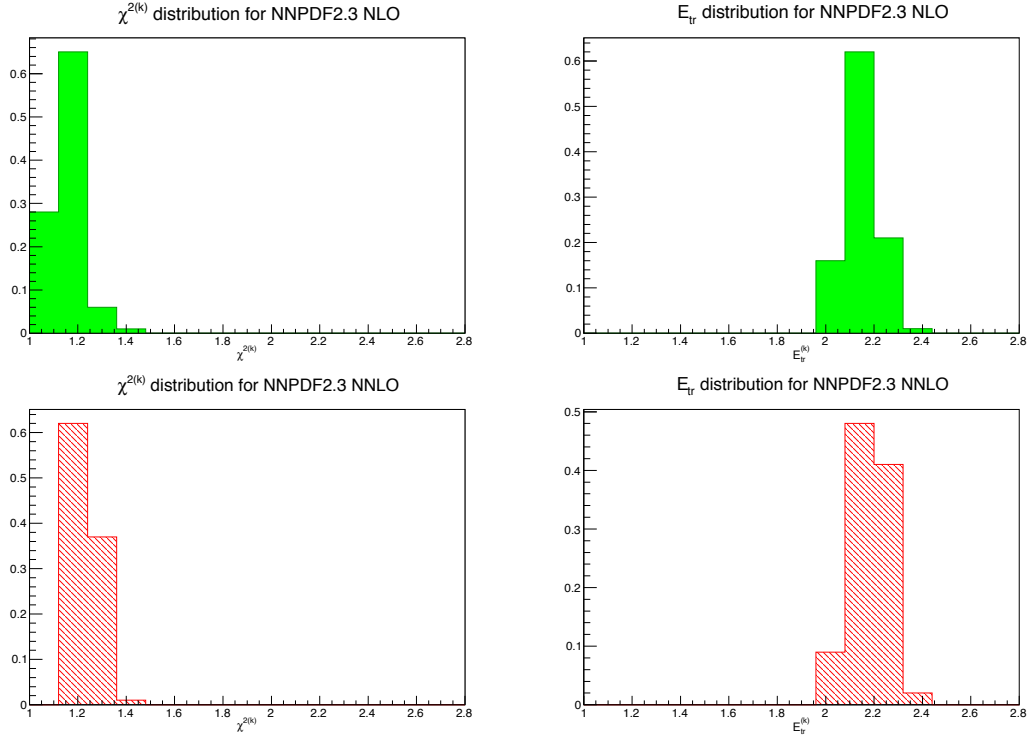


Figure 6.2: Distribution of χ^2 (upper plots) and $E_{tr}^{(k)}$ (lower plots), over the sample of $N_{\text{rep}} = 100$ replicas, for the NNPDF2.3 NLO (left plots) and NNLO (right plots) PDF sets.

than 10% for all experiments, except SLAC and CMS W electron asymmetry data (for which NNLO is better) and the NuTeV, ZEUS F_2^c and LHCb W rapidity distribution data (for which NNLO is worse). It is however interesting to observe that a very good description of the HERA F_2^c data is obtained at NNLO without the need of any *ad hoc* cut as described in Sec. 6.1.1.

A one-to-one comparison for the NNPDF2.3 NLO and NNLO PDFs is given in Figs. 6.3 and 6.4 at the input scale $Q_0^2 = 2 \text{ GeV}^2$, in the basis in which they are parametrized (see Sec. 5.2.1). In each plot the PDF central values are obtained taking the average over the N_{rep} replicas of each set while the error bands are given by the respective standard deviations (see Sec. 5.3). A visual comparison confirms that NLO and NNLO analyses lead to very similar results, but at the same time it also reveals some differences. In order to precisely quantify the statistical significance of the differences between the NNPDF2.3 NLO and NNLO PDFs, we plot in Fig. 6.5 the statistical distances at the initial scale Q_0^2 between central values and uncertainties for each one of the parametrized PDFs. We recall that the statistical distance d between two Monte Carlo samples, defined in eq. (5.26), measures their departure in unit of standard deviations and an average distance $d \simeq 1$ corresponds to statistical equivalence while, for sets of $N_{\text{rep}} = 100$ replicas, an average distance $d \simeq \sqrt{N_{\text{rep}}} = 10$ corresponds to one standard deviation difference.

It is evident that the NLO and NNLO sets are statistically non-equivalent, but differ by typically less than one sigma ($d < 10$). This in particular means that the NNPDF2.3

Experiment	χ_{tot}^2	
	NNPDF2.3 NLO	NNPDF2.3 NNLO
NMC pd	0.95	0.95 (+0.0%)
NMC	1.65	1.63 (-1.2%)
SLAC	1.29	1.00 (-22.5%)
BCDMS	1.25	1.33 (+6.4%)
HERA1-AV	1.02	1.04 (+2.0%)
CHORUS	1.14	1.11 (-2.6%)
FLH108	1.31	1.22 (-6.9%)
NuTeV	0.44	0.57 (+29.5%)
ZEUS-H2	1.27	1.29 (+1.6%)
ZEUS F_2^c	0.83	1.00 (+20.5%)
H1 F_2^c	1.59	1.54 (-3.1%)
DYE886	0.46	0.49 (+6.5%)
DYE605	0.82	0.83 (+1.2%)
CDF W asy	1.56	1.54 (-1.3%)
CDF Z rap	1.70	1.86 (+9.4%)
D0 Z rap	0.61	0.63 (+3.3%)
ATLAS W/Z rap	1.29	1.41 (+9.3%)
CMS W el asy	0.87	0.77 (-11.5%)
LHCb W	0.67	0.76 (+13.4%)
D0 RII cone	0.78	0.82 (+5.1%)
CDF RII k_T	0.78	0.74 (-5.1%)
ATLAS jets	0.84	0.80 (-4.8%)

Table 6.4: χ^2 values per data point for individual experiments computed using NNPDF2.3 NLO and NNLO. In the last column also the percent difference of the NNLO fit with respect to the NLO one is shown.

PDF sets are quite stable when going from NLO to NNLO. The largest variations are observed for the central values of the singlet distribution Σ and the total valence V at $x \sim 0.2 \div 0.4$ where the distances reveal differences slightly above the one sigma level. However, it should be noticed that PDF uncertainties are particularly small in this region and thus relatively small changes in the central value lead to relatively more significant distances. The small- x NNLO PDFs ($x \lesssim 0.01$), instead, are very similar to their NLO counterparts. Finally, it is worth noticing that the distances for the PDF uncertainties in right panel of Fig. 6.5 are all around $d \simeq 1$ all over the x range. This is consistent with the fact that the PDF error bands do not include theory uncertainties and only reflect the experimental uncertainties which are common to NLO and NNLO fits.

In order to assess the impact of NNLO corrections on physical observables, it is useful to compare NLO and NNLO PDFs for individual flavours at a typical hard scale. This is done in Fig. 6.6, where the NLO/NNLO ratio is shown as a function of x at $Q^2 = 10^4$ GeV². The general picture does not change and the biggest differences are observed for the light quarks and, correspondingly by evolution, for the gluon around $x \simeq 10^{-3}$, where the NLO and NNLO bands barely overlap.

From the comparison between NNPDF2.3 NLO and NNLO, it is clear that the inclusion of the NNLO corrections has a visible but small impact on the PDF determination and NLO and NNLO PDFs are (almost) always compatible within one standard devia-

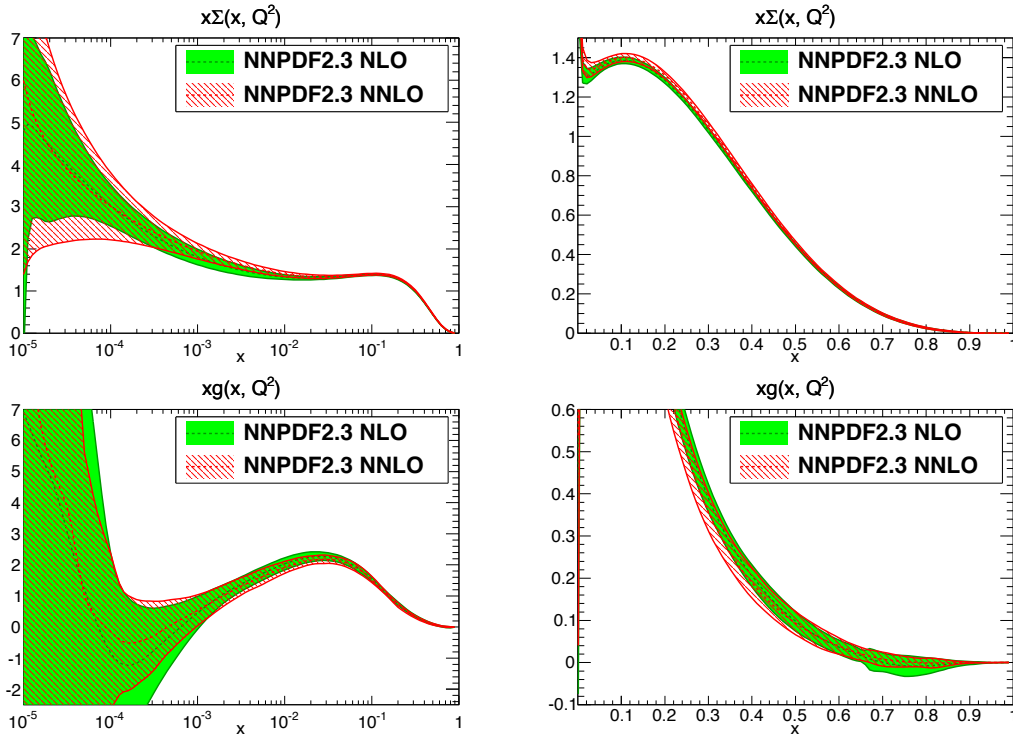


Figure 6.3: Comparison of NNPDF2.3 NLO and NNLO singlet sector PDFs.

tion. This leads to an important conclusion. As already mentioned, PDF uncertainties only reflect experimental errors and do not include the theory uncertainties due to higher perturbative orders, which could be estimated by varying the renormalization and factorization scales. Alternatively, at NLO, an estimate of the impact of the higher order corrections could be assessed by means of a direct comparison to the NNLO results. This is exactly what has been done in this sections and the result shows that, at NLO (and beyond), it is at present a reasonable approximation to neglect PDF theoretical uncertainties, since they are usually smaller than the experimental ones.

6.2.2 Impact of the Heavy Flavour Corrections

To assess the impact of the inclusion of the heavy quark mass corrections, in this section the baseline NNPDF2.3 NNLO set, which implements the FONLL-C mass scheme, will be compared to two variants obtained employing the FFNS and the ZM-VFNS, described in Chapter 2, as mass schemes.

In Tab. 6.5 the main statistical estimators for NNPDF2.3 NNLO FONLL-C, FFNS and ZM-VFNS are compared. The total χ^2_{tot} , in particular, indicates that the description of data provided by FONLL-C scheme is very good ($\chi^2_{\text{tot}} = 1.13$), the FFNS is instead slightly worse but still adequate ($\chi^2_{\text{tot}} = 1.16$), while the ZM-VFNS turns out to be worse ($\chi^2_{\text{tot}} = 1.26$). The χ^2 and E_{tr} distributions for NNPDF2.3 NNLO in the FFNS and in the ZM-VFNS, to be compared with the lower plots of Fig. 6.2, are shown in Fig. 6.7.

In Tab. 6.6 the χ^2_{tot} values for the single experiments are reported. As expected

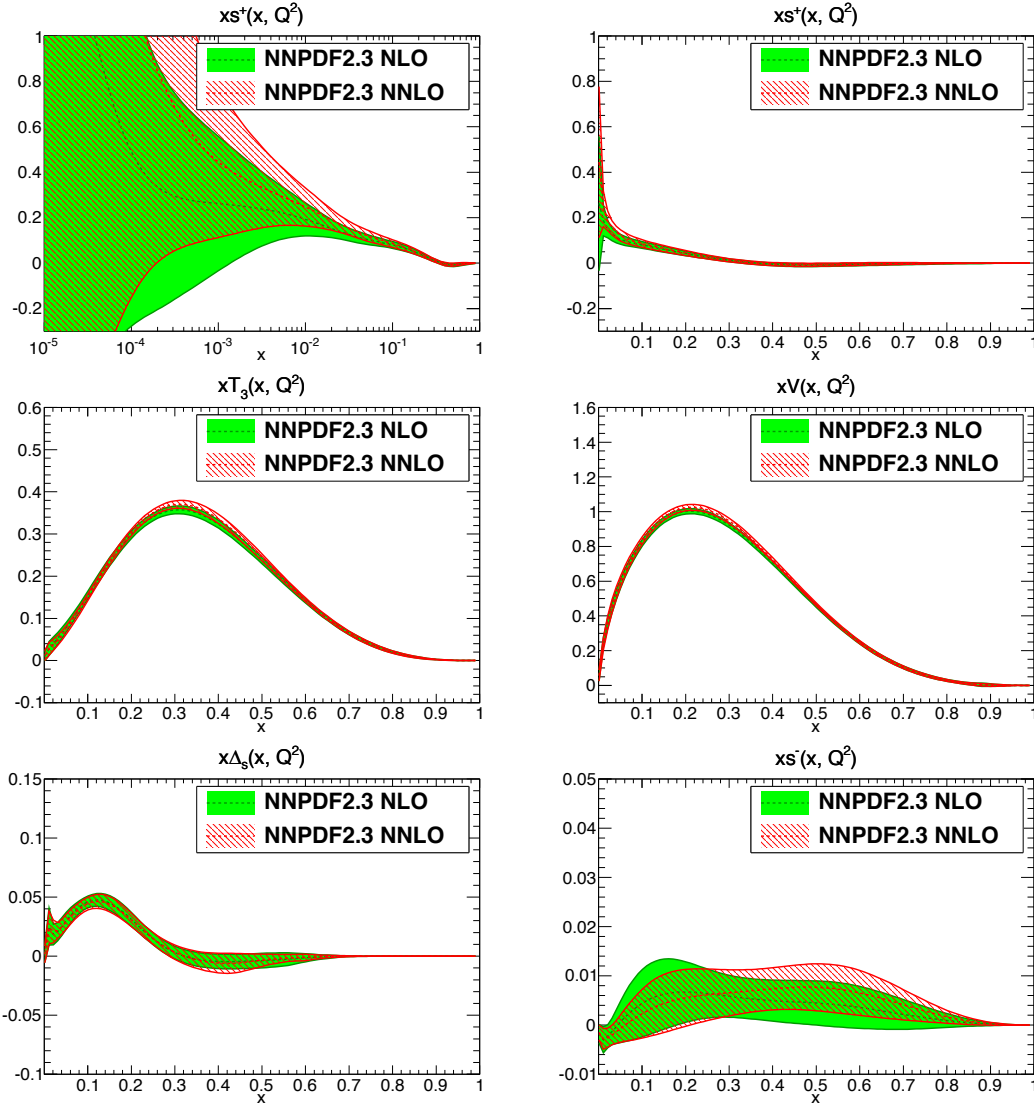


Figure 6.4: Same as Fig. 6.3 for the non-singlet sector PDFs.

from the global χ_{tot}^2 , the differences between FONLL-C and FFNS are rather small and typically below 10% with a few exceptions. In particular, data from SLAC, BCDMS, ZEUS-H2, LHCb W and CDF RII jets are sensibly better described by the FONLL-C scheme, while the ZEUS F_2^c structure functions are better described by the FFNS.

The differences between FONLL-C and ZM-VFNS are instead more pronounced. In particular, the entire DIS sector is indeed much better described by the FONLL-C (see, for instance, NMC and ZEUS F_2^c). On the other hand, as expected, the description of the hadronic sector is in better agreement.

In the following, in order to find out the source of the differences, a more detailed one-to-one comparison between FONLL-C and FFNS first and FONLL-C and ZM-VFNS will be presented.

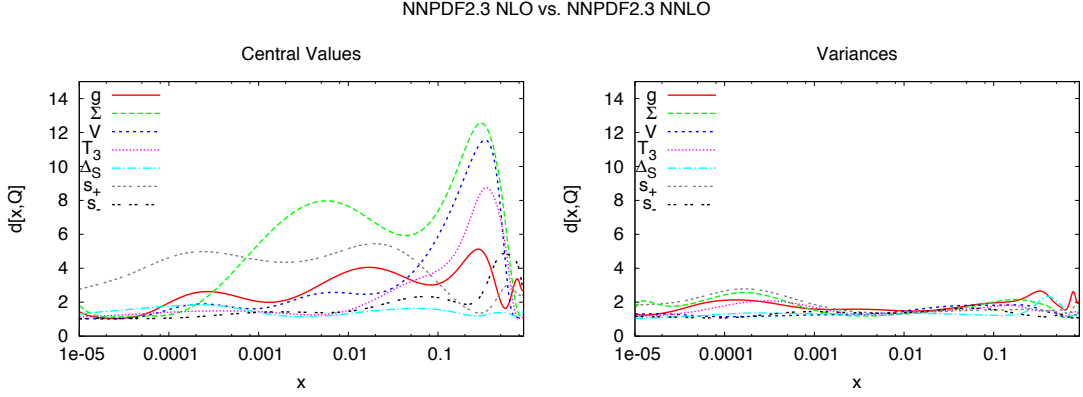


Figure 6.5: Distances between the NNPDF2.3 NLO and NNLO parton sets shown in Figs. 6.3 and 6.4. All distances are computed from sets of $N_{\text{rep}} = 100$ replicas.

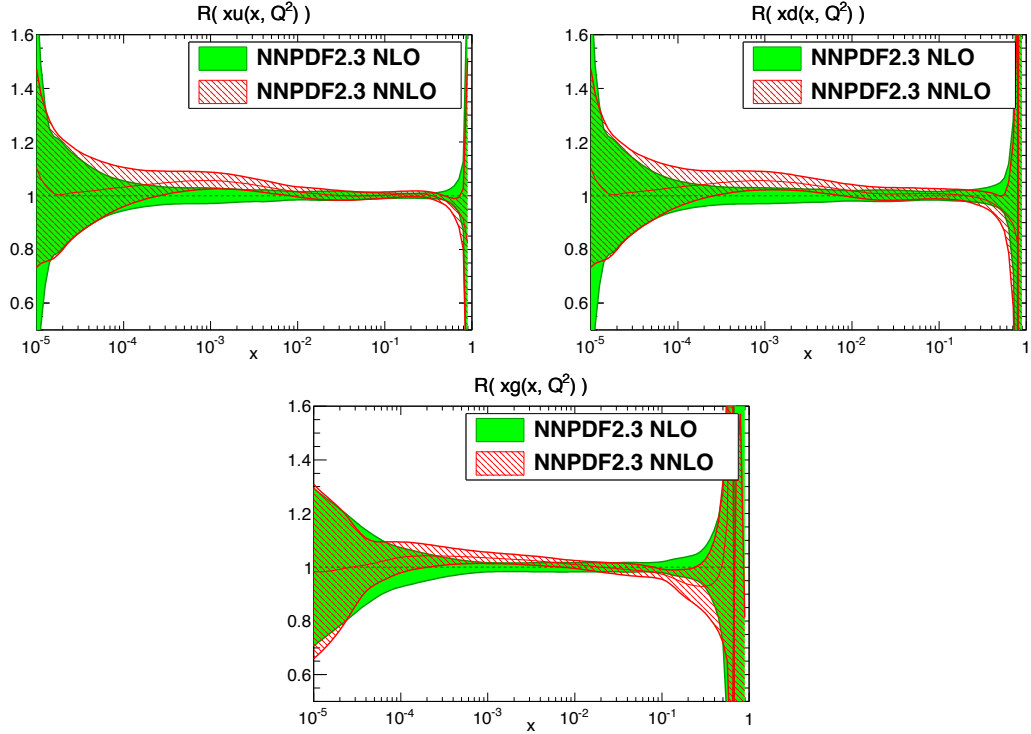


Figure 6.6: Comparison between NNPDF2.3 NLO and NNLO light quark and gluon PDFs at $Q^2 = 10^4 \text{ GeV}^2$. The results have been obtained with $N_{\text{rep}} = 100$ replicas. All curves are shown as ratios to the central NNPDF2.3 NLO result.

FONLL-C vs. FFNS

In Fig. 6.8 the distances between NNPDF2.3 NNLO FONLL-C and FFNS at the initial scale $Q_0^2 = 2 \text{ GeV}^2$ are shown. It is clear that the two fits are statistically non-equivalent, but differences are moderate, at the half sigma level ($d \sim 5$) or so, with the largest change

NNPDF2.3			
	FONLL-C	FFNS	ZM-VFNS
χ^2_{tot}	1.13	1.16	1.26
$\langle \chi^2 \rangle \pm \sigma_{\chi^2}$	1.18 ± 0.05	1.20 ± 0.05	1.26 ± 0.05
$\langle E \rangle \pm \sigma_E$	2.20 ± 0.06	2.21 ± 0.06	2.31 ± 0.06
$\langle E_{\text{tr}} \rangle \pm \sigma_{E_{\text{tr}}}$	2.18 ± 0.08	2.21 ± 0.08	2.27 ± 0.08
$\langle E_{\text{val}} \rangle \pm \sigma_{E_{\text{val}}}$	2.24 ± 0.09	2.27 ± 0.08	2.37 ± 0.10

Table 6.5: Table of statistical estimators for the NNPDF2.3 NNLO fits with $N_{\text{rep}} = 100$ replicas in the FONLL-C scheme, FFNS and ZM-VFNS.

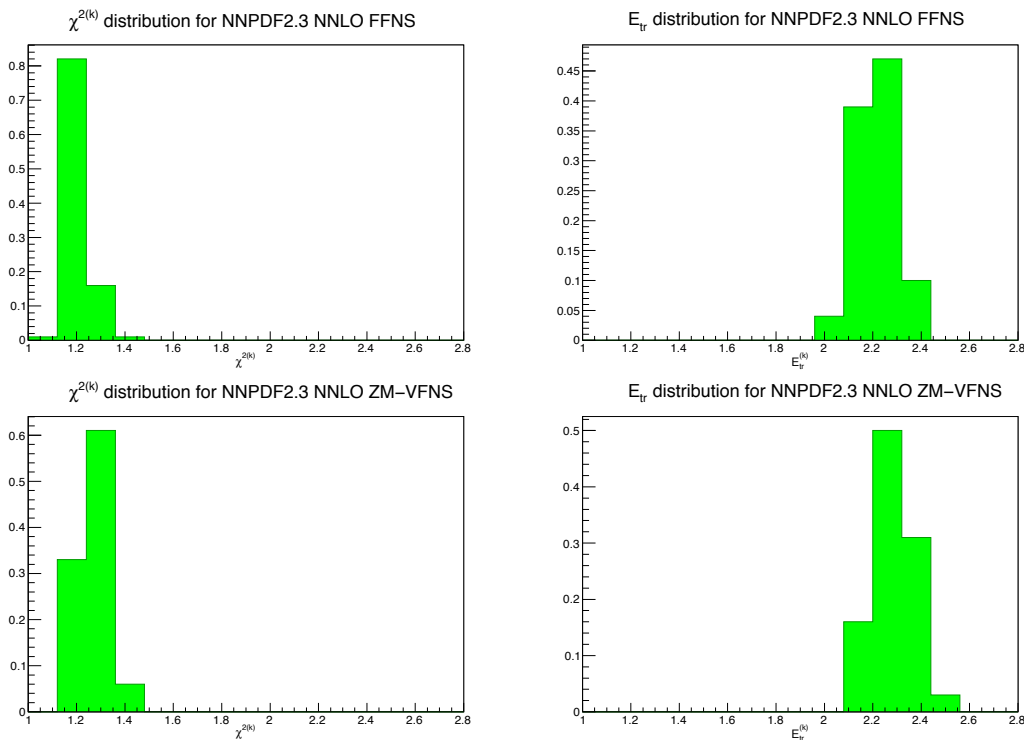


Figure 6.7: Distribution of χ^2 (upper plots) and $E_{\text{tr}}^{(k)}$ (lower plots), over the sample of $N_{\text{rep}} = 100$ replicas, for the NNPDF2.3 NLO (left plots) and NNLO (right plots) PDF sets.

observed in the central values and with no significant change in uncertainties. The PDF which varies most is the gluon: this is easily understandable given that the gluon is mostly determined by scaling violations, which are different in the two cases. As a consequence of the evolution, also the singlet Σ and the total strangeness s^+ present differences of the same order.

For collider physics applications, the initial PDFs, regardless whether determined in a GM-VFNS or in a FFNS [50, 23], are evolved upwards using the usual VFNS evolution equations. It turns out that this evolution amplifies differences between FONLL-C and FFNS PDFs. The amplification is demonstrated in Fig. 6.9, where the same distances of Fig. 6.8 are shown, but now at the scale $Q^2 = 10^4 \text{ GeV}^2$ (relevant e.g. for W , Z

Experiment	χ^2_{tot}		
	FONLL-C	FFNS	ZM-VFNS
NMC pd	0.95	0.96 (+1.1%)	0.95 (+0.0%)
NMC	1.63	1.56 (-4.3%)	2.35 (+44.2%)
SLAC	1.00	1.20 (+20.0%)	1.05 (+5.0%)
BCDMS	1.33	1.50 (+12.8%)	1.31 (-1.5%)
HERA1-AV	1.04	1.05 (+1.0%)	1.42 (+36.5%)
CHORUS	1.11	1.08 (-2.7%)	1.12 (+0.9%)
FLH108	1.22	1.24 (+1.6%)	1.29 (+5.7%)
NuTeV	0.57	0.53 (-7.0%)	0.62 (+8.8%)
ZEUS-H2	1.29	1.46 (+13.2%)	1.31 (+1.6%)
ZEUS F_2^c	1.00	0.88 (-12.0%)	1.22 (+22.0%)
H1 F_2^c	1.54	1.52 (-1.3%)	1.77 (+14.9%)
DYE886	0.49	0.51 (+4.1%)	0.48 (-2.0%)
DYE605	0.83	0.83 (+0.0%)	0.81 (-2.4%)
CDF W asy	1.54	1.54 (+0.0%)	1.55 (+0.6%)
CDF Z rap	1.86	1.89 (+1.6%)	1.97 (+5.9%)
D0 Z rap	0.63	0.62 (-1.6%)	0.65 (+3.2%)
ATLAS W/Z rap	1.41	1.37 (-2.8%)	1.56 (+10.6%)
CMS W el asy	0.77	0.77 (+0.0%)	0.76 (-1.3%)
LHCb W	0.76	0.92 (+21.1%)	0.78 (+2.6%)
D0 RII cone	0.82	0.83 (+1.2%)	0.86 (+4.9%)
CDF RII k_T	0.74	0.99 (+33.8%)	0.71 (-4.1%)
ATLAS jets	0.80	0.83 (+3.8%)	0.89 (+11.3%)

Table 6.6: χ^2 values per data point for individual experiments computed using NNPDF2.3 NNLO FONLL-C, FFNS and ZM-VFNS. In the last two columns also the percent difference with respect to the FONLL-C fit are shown.

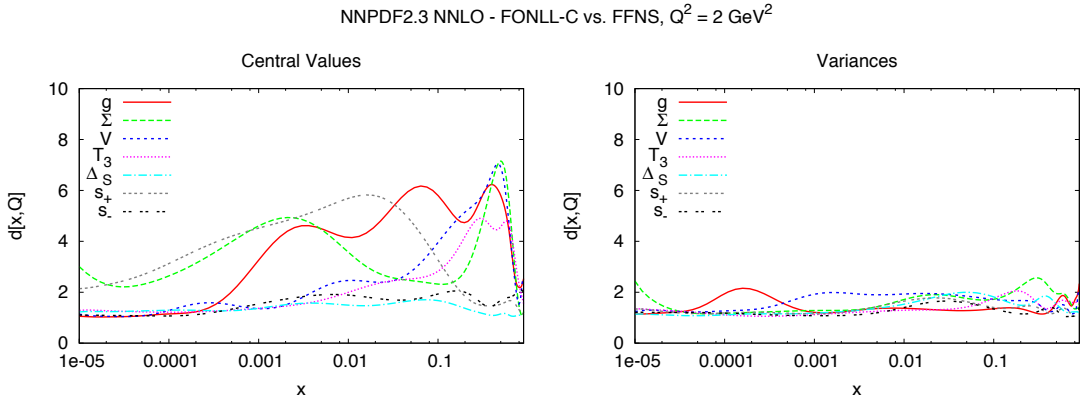


Figure 6.8: Distances between NNPDF2.3 NNLO FONLL-C and FFNS. Distances are shown at the scale $Q^2 = 2 \text{ GeV}^2$ at which PDFs are parametrized, both between central values (left) and uncertainties (right).

or Higgs production). While uncertainties are still unchanged, central values for some PDFs (specifically the gluon and the quark singlet Σ) now differ by more than one sigma.

The increase of the differences when evolving to higher scales can be understood as a consequence of the fact that differences in the large- x region (where uncertainties are large) at low scale lead upon evolution to high scale to differences in the small- x region, where uncertainties are relatively small. In addition the coupled evolution between Σ and gluon tends to amplify the differences even further. In Fig. 6.10 the most different

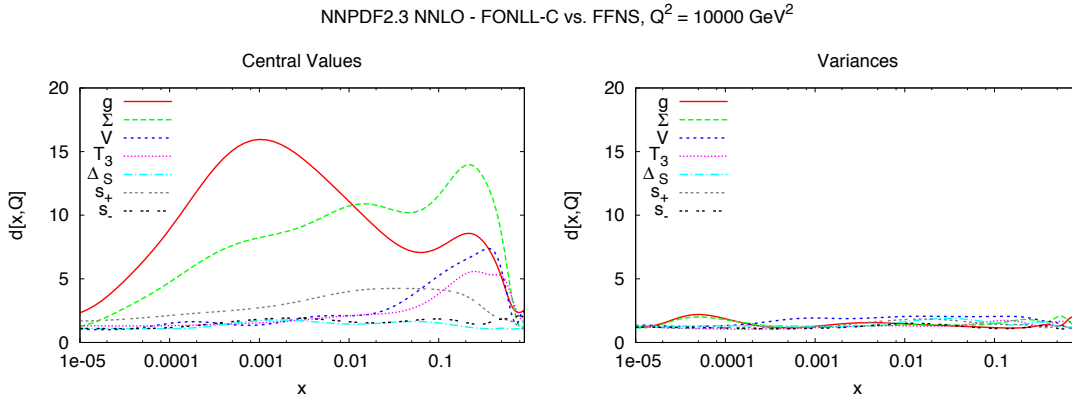


Figure 6.9: Same as Fig. 6.8, but at $Q^2 = 10000 \text{ GeV}^2$. All PDFs have been evolved upwards using the same VFNS evolution equations.

PDFs between FONLL-C and FFNS are shown as a ratio to FONLL-C.

Having ascertained that the difference between PDFs obtained in the FONLL-C scheme and FFNS is not negligible, one can ask what is the source of the difference. In order to understand this, the statistical quality of the two fits needs to be carefully studied [91]. In Fig. 6.11 we show the kinematic coverage of the DIS datasets whose χ^2 in the FFNS worsens (left panel) and improves (right panel) in a substantial way as compared to the FONLL-C scheme. It is clear that the data with worse χ^2 place themselves mainly in the large- x region ($x \gtrsim 0.1$).

This is consistent with the behavior observed for the heavy quark structure functions. In Fig. 6.12 we show the predictions for the charm structure function F_2^c as a function of the energy Q^2 for four different values of x in the three mass schemes considered here, *i.e.* FONLL-C scheme, FFNS and ZM-VFNS. It is clear that at smaller values of x the three predictions are very close to each other over the whole Q^2 range considered. As the values of x becomes larger, instead, the three predictions start to diverge and, while at smaller values of Q^2 ($\lesssim 10 \text{ GeV}^2$) as expected the FONLL-C scheme is closer to the FFNS, for larger values of Q^2 ($\gtrsim 10 \text{ GeV}^2$) the FONLL-C and the FFNS predictions markedly depart from each other.

In conclusion, the difference between FONLL-C and FFNS fits stems from data placed in a particular kinematic region (large- Q and large- x) which, according to the fit quality, are more accurately described by the FONLL scheme.

FONLL-C vs. ZM-VFNS

We now turn to the direct comparison between NNPDF2.3 NNLO FONLL-C and ZM-VFNS. In Fig. 6.13 the distances at the initial scale $Q^2 = 2 \text{ GeV}^2$ are shown. In this

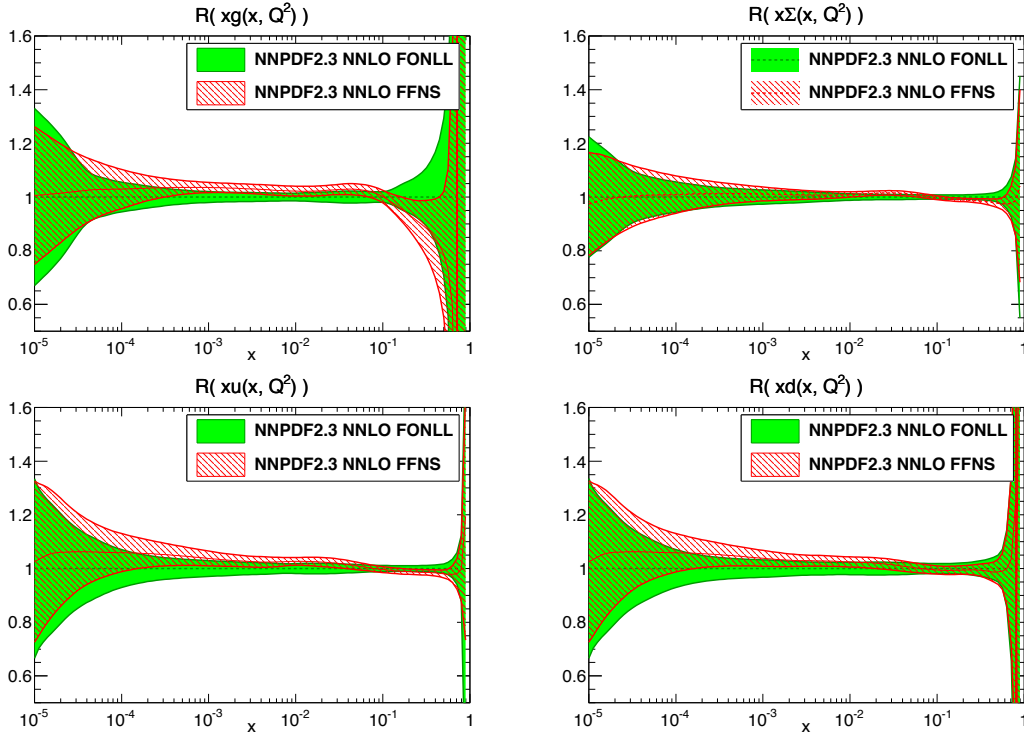


Figure 6.10: Comparison between NNPDF2.3 NNLO FONLL-C and FFNS PDFs, displayed as a ratio to FONLL-C at $Q^2 = 10^4$ GeV²: gluon (top left), quark singlet (top right), up (bottom left) and down (bottom right).

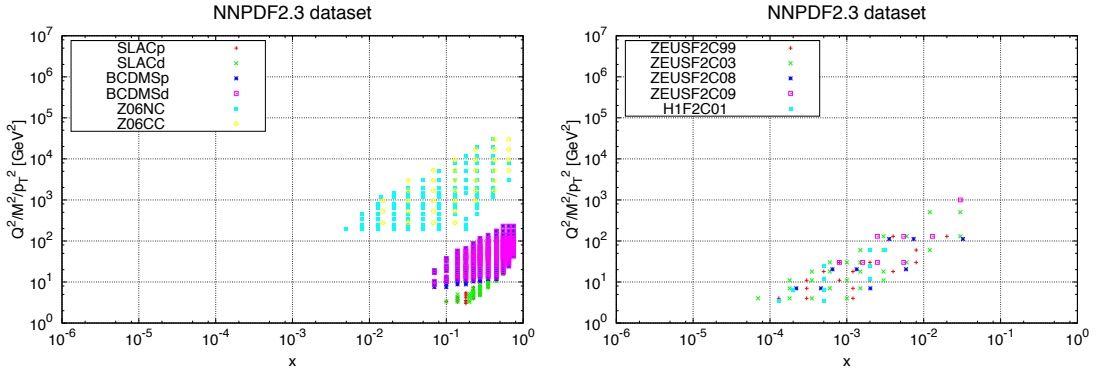


Figure 6.11: Kinematic coverage of the experimental datasets whose χ^2 worsens (left panel) and improves (right panel) in the FFNS as compared to the FONLL-C scheme in the NNPDF2.3 NNLO PDF determination.

case the departure is much more pronounced and in particular the medium- x gluons differ by almost two sigmas. As already observed for the FFNS case, the discrepancy results amplified at higher scales. Indeed Fig. 6.14, where the distances at $Q^2 = 10^4$ GeV² are displayed, shows that at the typical collider energies the difference can reach

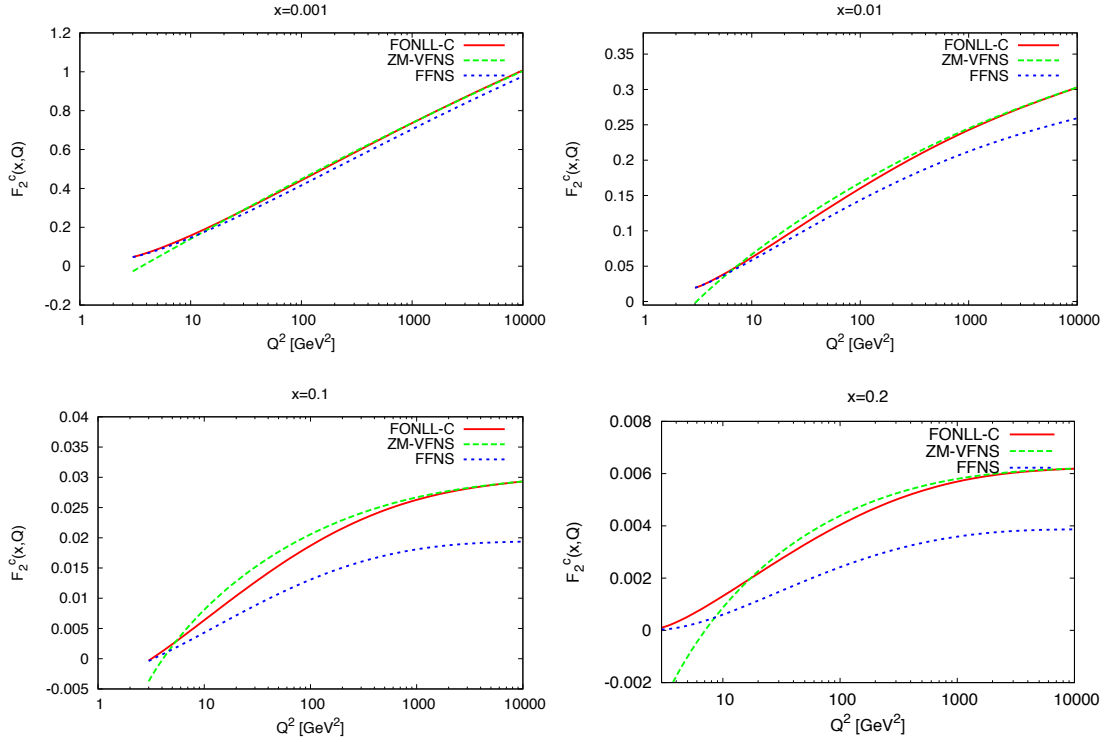


Figure 6.12: Theoretical predictions for the charm structure function F_2^c as a function of Q^2 for four different values of $x = 0.001, 0.01, 0.1, 0.2$ in the three mass schemes considered in this section, *i.e.* FONLL-C scheme, FFNS and ZM-VFNS.

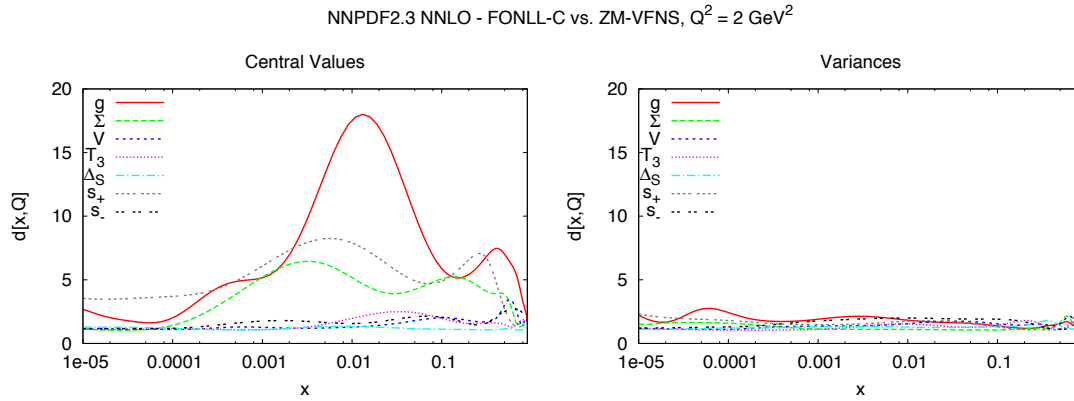


Figure 6.13: Distances between NNPDF2.3 NNLO FONLL-C and ZM-VFNS. Distances are shown at the scale $Q^2 = 2 \text{ GeV}^2$ at which PDFs are parametrized, both between central values (left) and uncertainties (right).

the 3.5 sigma level. In Fig. 6.15 the most different PDFs, *i.e.* the singlet Σ and the gluon, between FONLL-C and ZM-VFNS are shown as a ratio to FONLL-C.

The origin of the discrepancy between FONLL-C and ZM-VFNS can be traced back

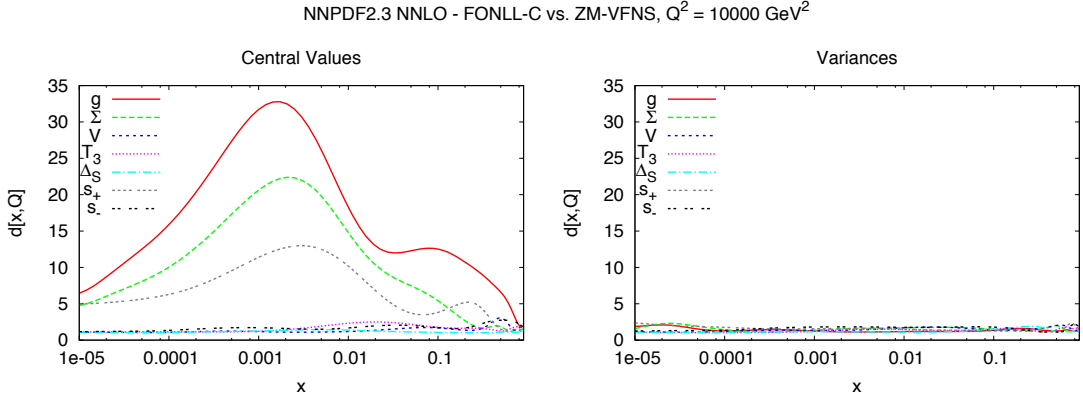


Figure 6.14: Same as Fig. 6.13, but at $Q^2 = 10000 \text{ GeV}^2$. All PDFs have been evolved upwards using the same VFNS evolution equations.

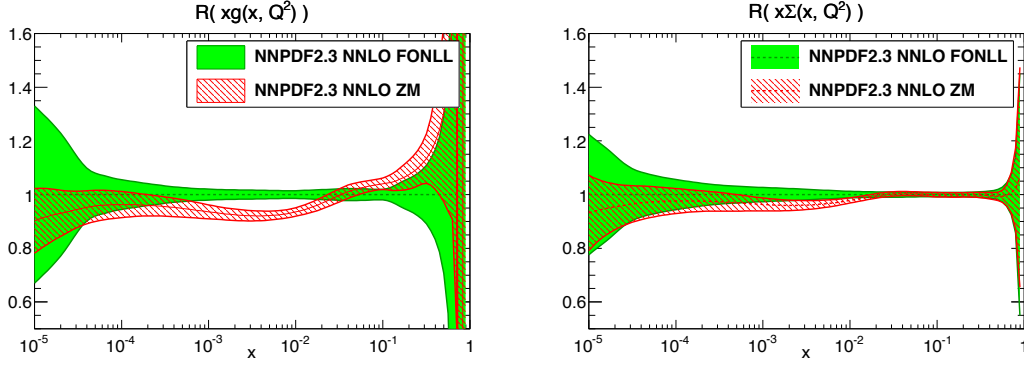


Figure 6.15: Comparison between NNPDF2.3 NNLO FONLL-C and ZM-VFNS (ZM), displayed as a ratio to FONLL-C at $Q^2 = 10^4 \text{ GeV}^2$, for gluon (left) and quark singlet (right) PDFs.

to the NC low-energy data. In fact, looking at Tab. 6.6, the experiments whose deterioration of χ^2 with respect to the FONLL-C scheme is more pronounced are NMC, HERA1-AV the H1 and ZEUS charm structure functions which contain indeed many low energy data (see Fig. 6.16). Here, the absence of the power terms M_H/Q in the ZM-VFNS as compared to the FONLL-C scheme causes the gluon to be much softer in the small- x region ($x < 0.1$) and consequently, due to the momentum sum rule, harder in the large- x region. The low-energy inaccuracy of the ZM-VFNS as compared to the FONLL-C scheme is also confirmed by Fig. 6.12, where the ZM-VFNS predictions for $Q^2 \lesssim 10 \text{ GeV}^2$ and more markedly in the larger- x region ($x \gtrsim 0.1$), where many of the NMC data lay, tend to depart from the FONLL-C predictions with a consequent deterioration of the χ^2 .

6.2.3 Impact of the Threshold Prescription

Finally, we consider the impact of the threshold prescription introduced in eq. (2.50) to damp down the potentially large subleading terms around the heavy quark mass

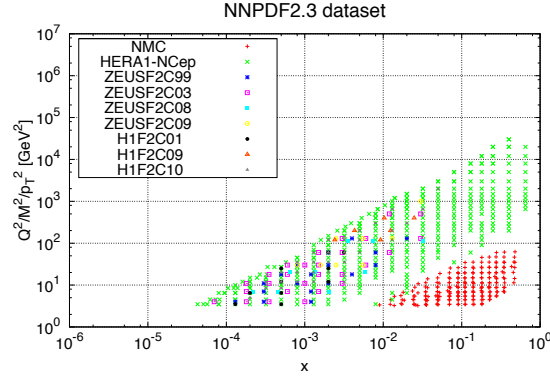


Figure 6.16: Kinematic coverage of the experimental datasets whose χ^2 worsens in the ZM-VFNS as compared to the FONLL-C scheme in the NNPDF2.3 NNLO PDF determination.

threshold in the definition of the FONLL structure function. The explicit form of the damping function implemented if the NNPDF2.3 fits is given in eq. (2.51). This is an “artificial” factor introduced to keep under control potential numerical instabilities and thus one can ask whether the inclusion of such an empirical factor has some impact on the determination of PDFs. To this end the NNPDF2.3 NNLO fit in the FONLL-C scheme has been repeated switching off the damping function ($D_{\text{th}}(Q) = 1$).

The distances between the NNPDF2.3 NNLO FONLL-C with and without the damping functions are shown in Fig. 6.17: it is evident that the two fits are statistically equivalent. One can then conclude that the inclusion of a damping function has no visible impact on the PDF determination.

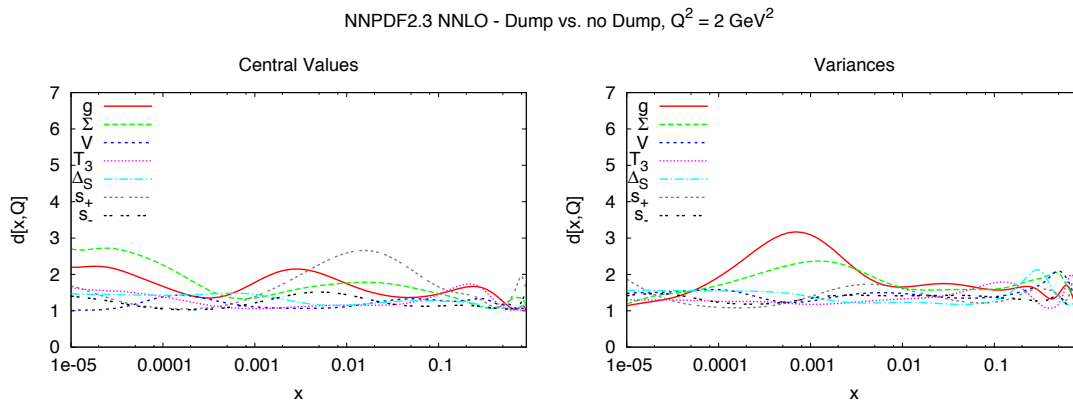


Figure 6.17: Distances between the NNPDF2.3 NNLO FONLL-C with and without damping factor give in eq. 2.51. All distances are computed from sets of $N_{\text{rep}} = 100$ replicas.

6.3 LHC Phenomenology

Once the impact of the heavy quark mass corrections at the level of PDFs has been assessed, in this section we turn to present some results relevant for the phenomenology at the LHC at $\sqrt{s} = 8$ TeV.

As is well known, at a hadron collider the factorized observables depend on PDFs through the parton luminosities [136], which can be defined as:

$$\Phi_{ij}(M_X) \equiv \frac{1}{s} \int_{\tau}^1 \frac{dx}{x} f_i(x, M_X) f_j\left(\frac{\tau}{x}, M_X\right), \quad (6.2)$$

where s is the center of mass energy of the collider, M_X is the invariant mass of the partonic system and $\tau \equiv M_X^2/s$. In the following we will mostly consider gluon-gluon luminosity Φ_{gg} and the total quark-antiquark and quark-gluon luminosities, respectively defined as:

$$\Phi_{q\bar{q}} \equiv \sum_{i=u,\dots,t} \Phi_{i\bar{i}} \quad \text{and} \quad \Phi_{qg} \equiv \sum_{i=u,\dots,t} \Phi_{ig}. \quad (6.3)$$

These luminosities at $\sqrt{s} = 8$ TeV are plotted in Fig. 6.18 as a function of M_x for NNPDF2.3 NNLO FONLL-C, FFNS and ZM-VFNS, all normalized to the FONLL-C central value.

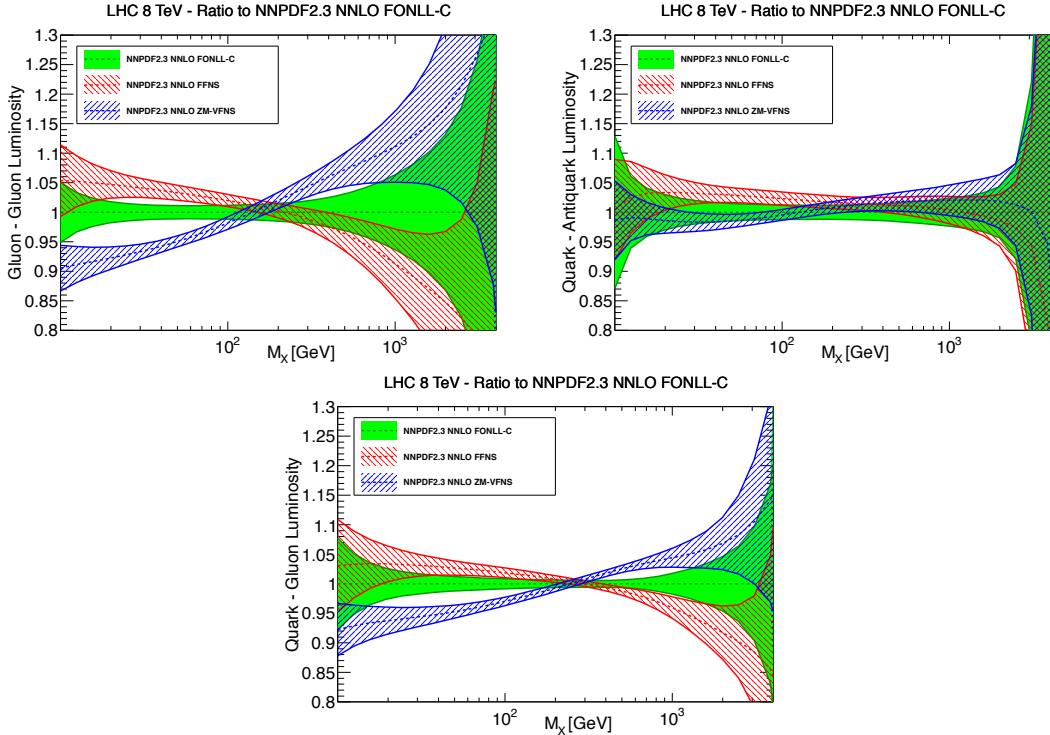


Figure 6.18: Comparison between NNPDF2.3 NNLO FONLL-C, FFNS and ZM-VFNS parton luminosities at LHC 8 TeV, displayed as a ratio to FONLL-C. The for the gluon-gluon (top-left), the quark-antiquark (top-right) and the quark-gluon (bottom) luminosities are shown.

As expected from the direct comparison between PDFs, the gluon-gluon luminosity Φ_{gg} (upper-left panel in Fig. 6.18) is the most affected by the different treatment of the heavy quark contributions. In particular, as compared to the FONLL-C scheme, the FFNS gluon-gluon luminosity is sensibly larger at smaller invariant values of the invariant mass $M_X < 100$ GeV while it is smaller for $M_X > 100$ GeV, though still compatible within the error band. The ZM-VFNS gluon-gluon luminosity, instead, behaves in the opposite way, but the discrepancies both at small and large values of M_X are even more enhanced and only in the range $M_X \simeq 100 \div 200$ GeV there is agreement with the FONLL-C determination. Regarding the quark-antiquark luminosities $\Phi_{q\bar{q}}$ (upper-right panel in Fig. 6.18), we observe a much better agreement all over the M_X range and essentially both FFNS and ZM-VFNS are in agreement with FONLL-C within errors. Finally the quark-gluon luminosities Φ_{qg} (bottom panel in Fig. 6.18), driven by the gluon PDF, have a very similar relative behavior as the gluon-gluon luminosity Φ_{gg} .

In order to assess the impact of the mass scheme choice for PDFs in the hadronic sector, in the following we will present the results for some benchmark total cross sections at the LHC 8 TeV comparing, when possible, the theoretical predictions obtained with the NNPDF2.3 NNLO FONLL-C, FFNS and ZM-VFNS sets to the most recent experimental data.

We will consider the following observables:

- electro-weak vector boson production total cross sections and the W^+/W^- and W/Z cross-section ratios at NNLO using the `Vrap` code [128].
- Top-pair production total cross section using the `top++` code [137] which implements the full NNLO+NNLL corrections. The top quark mass is taken to be $M_t = 173.3$ GeV.
- Standard Model Higgs boson production cross sections via gluon-gluon fusion at NNLO as implemented in the `iHixs` code [138]. Here the Higgs mass is taken to be $M_{\text{Higgs}} = 125$ GeV.

It should be stressed that all the errors associated with the theoretical predictions presented in this section are PDF uncertainties only, thus they do not include α_s as well as theoretical uncertainties due to missing higher orders, usually estimated by varying renormalization and factorization scales.

The numerical results for the electro-weak vector boson production are reported in Tab. 6.7 and in Fig. 6.19 their graphical representation, along with the most recent experimental measurements provided by the CMS collaboration [139], is shown. We start noticing that all the theoretical predictions are in general good agreement amongst themselves. This is a consequence of the fact that the quark-antiquark luminosity $\Phi_{q\bar{q}}$ associated with the $q\bar{q}$ production channel, which is the dominant one in the electro-weak vector boson production, is very similar for all the three PDF determinations considered (see Fig. 6.18). In addition, the predictions are in general good agreement with data. Only the ratio $\sigma(W^+)/\sigma(W^-)$ seems to be slightly overshooting the experimental determination and a difference at the two-sigma level is observed.

Now we turn to top-pair production for which the theoretical predictions are given in Tab. 6.8 and the respective graphical representation, along with the experimental value measured by CMS [140] and ATLAS [141], is shown in Fig. 6.8. The top-pair

	NNPDF2.3 NNLO				
	$\sigma(W^+)$ [nb]	$\sigma(W^-)$ [nb]	$\sigma(Z)$ [nb]	$\sigma(W)/\sigma(Z)$	$\sigma(W^+)/\sigma(W^-)$
FONLL-C	7.027 ± 0.101	4.908 ± 0.073	1.126 ± 0.015	10.599 ± 0.031	1.432 ± 0.012
FFNS	7.209 ± 0.095	5.047 ± 0.064	1.152 ± 0.013	10.637 ± 0.027	1.428 ± 0.013
ZM-VFNS	7.014 ± 0.073	4.890 ± 0.054	1.122 ± 0.011	10.607 ± 0.024	1.434 ± 0.011

Table 6.7: Predictions for the inclusive cross sections for W and Z production at the LHC at $\sqrt{s} = 8$ TeV at NNLO using the `Vrap` code [128], obtained with the PDF sets NNPDF2.3 NNLO FONLL-C, FFNS and ZM-VFNS. All the uncertainties are one sigma and are due only to PDFs. The branching ratios are understood.

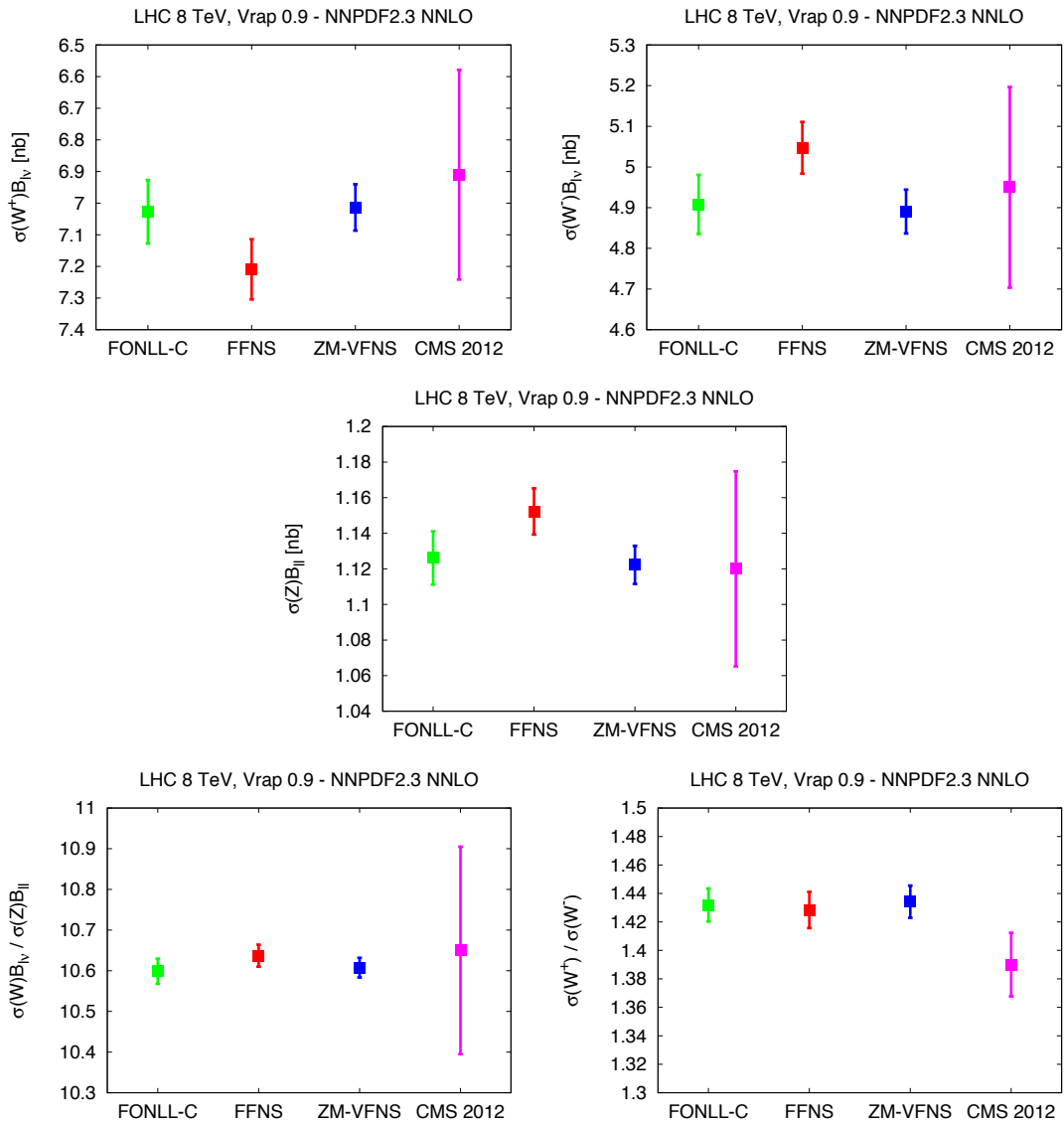


Figure 6.19: Graphical representation of Tab. 6.7 along with the CMS results [139].

production at LHC 8 TeV is dominated by the gluon-gluon fusion channel [142], therefore the predictions are particularly sensitive to the gluon-gluon luminosity Φ_{gg} around $M_X \simeq 2M_t \simeq 350$ GeV. Looking at Fig. 6.18, it is evident that the ZM-VFNS gluon-gluon luminosity in this region is much larger than the FONLL-C one which in turn is larger but compatible with the FFNS determination. This is exactly the same trend observed for the theoretical predictions in Tab. 6.8. However, given the large experimental uncertainties, at present all the determinations obtained with the three NNPDF2.3 NNLO sets considered here are in agreement with (at least one of) the experimental measurements.

	NNPDF2.3 NNLO
	$\sigma(t\bar{t})$ [pb]
FONLL-C	252.8 ± 6.1
FFNS	247.3 ± 5.7
ZM-VFNS	267.7 ± 5.5

Table 6.8: Predictions for the inclusive cross sections for the Higgs production at the LHC at $\sqrt{s} = 8$ TeV at NNLO using the `iHixs` code [138], obtained with the PDF sets NNPDF2.3 NNLO FONLL-C, FFNS and ZM-VFNS. All the uncertainties are one sigma and are due only to PDFs.

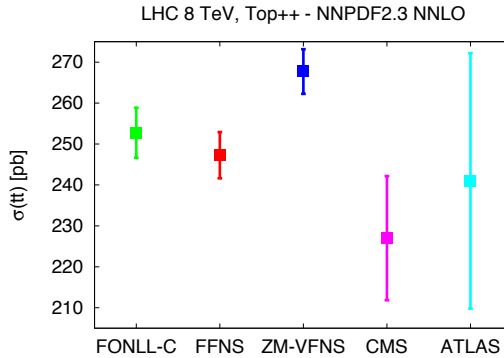


Figure 6.20: Graphical representation of Tab. 6.8 along with the CMS results [140].

Finally, we consider the Higgs production via gluon-gluon fusion. The values for the theoretical predictions are reported in Tab. 6.9 and their graphical representation is given in Fig. 6.21. By definition, this observable is mostly sensitive to the gluon-gluon luminosity around $M_X \simeq M_H = 125$ GeV. From Fig. 6.18 we see that, in this particular region, all the three gluon-gluon luminosities are in good agreement. As a consequence, the predictions shown in Fig. 6.21 are all compatible within uncertainties. However, we also observe that the FFNS luminosity is slightly larger than the FONLL-C while ZM-VFNS one is slightly smaller and, as expected, the predictions for the Higgs production cross section in Fig. 6.21 follow the same trend.

	NNPDF2.3 NNLO
	$\sigma(H)$ [pb]
FONLL-C	19.54 ± 0.24
FFNS	19.84 ± 0.20
ZM-VFNS	19.37 ± 0.22

Table 6.9: Predictions for the inclusive cross sections for $t\bar{t}$ production at the LHC at $\sqrt{s} = 8$ TeV at NNLO using the `Top++` code [137], obtained with the PDF sets NNPDF2.3 NNLO FONLL-C, FFNS and ZM-VFNS. All the uncertainties are one sigma and are due only to PDFs.

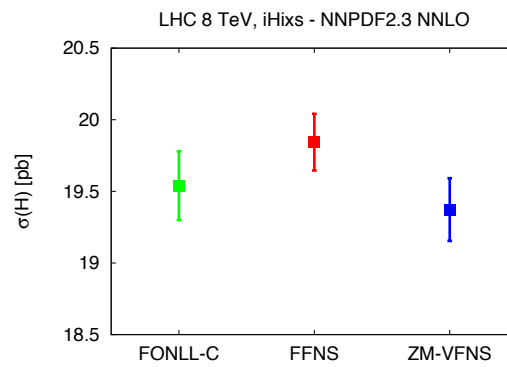


Figure 6.21: Graphical representation of Tab. 6.9.

Chapter 7

Summary and Conclusions

The present thesis was devoted to the study of the inclusion of higher-order corrections and heavy quark mass effects in a PDF determination. This has been carried out in the NNPDF framework resulting originally in the NNPDF2.1 sets [55, 56], which were at a later stage supplemented by the first LHC data leading to the most recent NNPDF2.3 sets [29].

In Chapter 1 the concept of Parton Distribution Function (PDF) was introduced. We have shown how the analytical computation of the Deep-Inelastic-Scattering (DIS) process at order α_s in QCD leads to initial-state collinear divergences which, using the factorization theorem, can be reabsorbed into the PDFs. This “relocation” of divergences from hard coefficients (coefficient functions) to PDFs can be performed only at the price of introducing an arbitrary scale μ_F , called factorization scale, on which both the renormalized coefficient functions and PDFs start depending. The requirement that physical observables do not depend on μ_F , imposed by demanding the logarithmic derivative to vanish, leads to the formulation of the DGLAP equation that regulates the energy dependence of PDFs. The DGLAP equation is one of the most important ingredients for the present PDF determinations. In fact, thanks to it, the energy dependence of PDFs is fully determined and the task is then reduced to the determination of the x (Bjorken variable) dependence.

In Chapter 2 a detailed discussion of the factorization schemes presently available to include heavy quark mass effects into DIS structure functions has been given. It emerged that there are two possible basic approaches to the calculation of the DIS structure functions. In the first approach, the so-called Fixed-Flavour-Number Scheme (FFNS), the calculation is performed retaining the quark mass of the heavy flavours which provide a “natural” regulator for the infrared divergences. As a consequence, there is no need to introduce a PDF for the heavy quark flavours so that the number of active flavours is kept fixed and in particular it does not change with the energy. In the second approach, called Zero-Mass Variable-Flavour-Number Scheme (ZM-VFNS), the heavy quark masses are instead set to zero and this gives rise to the usual final-state collinear divergences that are absorbed into the PDFs. In addition, in the ZM-VFNS, the number of active flavours is assumed to increase by one unity as the energy of the process crosses the energy threshold of a given heavy quark.

It turns out that the FFNS provides an accurate description for energies around and below the heavy quark mass while it deteriorates at high energies. The ZM-VFNS

is instead more accurate when the energy is much larger than the heavy quark mass thresholds and conversely it becomes less and less accurate as the energy approaches them.

In order to obtain a factorization scheme that is accurate both at large and low energies, several prescriptions that interpolate between FFNS at low energy and ZM-VFNS at large energy have been proposed and implemented in as many PDF fits. In Chapter 2 they have been described showing how they behave for different energy regimes. They are: the ACOT, the TR, the FONLL and the BMSN schemes, more generally called General-Mass Variable-Flavour-Number Schemes (GM-VFNS).

The topic of Chapter 3 was the implementation of the FONLL scheme, which is the scheme adopted by the NNPDF collaboration. All the relevant formulas have been derived up to order α_s^2 , discussing how a suitable definition of heavy quark structure functions for both Neutral-Current (NC) and Charged-Current (CC) processes emerges from the requirement of infrared safety in the limit of vanishing heavy quark mass. In a second stage the formalism of the Mellin transformation has been introduced showing how it provides a more analytical approach to the implementation of the structure functions. In fact, the only non-analytical step required is the inverse Mellin transformation, which makes possible to go back from the N -space to the x -space. In addition, this procedure requires the computation of the Mellin transform of all the expressions involved, *i.e.* splitting functions and coefficient functions, up to the desired perturbative order. Some of the higher-order coefficient functions were unknown and they have been derived and benchmarked in Appendix A. Finally, the heavy quark structure functions have been benchmarked.

In Chapter 4 the implementation of the $\overline{\text{MS}}$ heavy quark masses in the DIS structure functions has been worked out. All the relevant formulas for PDF, α_s and mass evolution in the presence of $\overline{\text{MS}}$ heavy quark masses have been derived and benchmarked against publicly available codes. In addition, the heavy quark coefficient functions, which are commonly given in terms of pole masses, have been adapted to the $\overline{\text{MS}}$ and benchmarked. The Mellin transform of the relevant expressions have been collected in Appendix B.

All the expressions presented in the previous chapters for the inclusion of the heavy quark mass effects into a PDF determination have been implemented in the NNPDF framework which thus needs to be properly introduced. Chapter 5 was then devoted to the description of the NNPDF methodology. The main features of the NNPDF methodology are the use of the Monte Carlo method for the treatment of uncertainties combined with neural networks as basic interpolating functions.

The PDF sets resulting from the implementation of the FONLL method up to order α_s^2 in the NNPDF framework have been finally presented in Chapter 6. In the first place, a description of the dataset included in the fits has been given. Secondly, the impact of the inclusion of the order α_s^2 corrections has been assessed comparing the NNPDF2.3 NLO set, obtained using the FONLL-A scheme, to the NNPDF2.3 NNLO set, obtained using the NNLO. It emerged that the NLO and the NNLO sets, though statistically non-equivalent, give rise to only moderate differences. In particular, it turned out that the inclusion on the order α_s^2 corrections in a PDF determination based on a global dataset has presently an impact which is typically smaller than the experimental uncertainties. As a consequence, we could conclude that neglecting the systematic uncertainty due to the higher order corrections is presently a good approximation for NLO or higher PDF

determination.

We then turned to the impact of the heavy quark mass effects in a PDF determination. To this end, we have compared the NNPDF2.3 NNLO fit obtained in the FONLL-C scheme, the FFNS and the ZM-VFNS, which include heavy quark mass effects in three different ways. Based on the quality of the fits, we observed that the FONLL-C scheme provides the best description of data. In order to spot the sources of the differences, we have also performed the one-to-one comparisons FONLL-C vs. FFNS and FONLL-C vs. ZM-VFNS. In both cases it emerged that the differences arise from data placed in specific kinematic regions. In particular, the FFNS as compared to the FONLL-C scheme provides a worse description of data placed in the large- x and large-energy region while the ZM-VFNS is not able to properly describe the low-energy data.

After having ascertained that the implementation of the FONLL scheme in a PDF fit leads to an improvement in the accuracy, we turned to study some phenomenological implications of such a determination. The theoretical predictions for some of the standard candles at the LHC 8 TeV, that is electro-weak vector boson production, top-pair production and Higgs production via gluon-gluon fusion, have been evaluated using the most up to date public codes using the NNPDF2.3 NNLO fits in the three different mass schemes discussed above and compared, when possible, to the most recent experimental measurements. The essential outcome of the comparison is that the present accuracy of LHC measurements is not enough yet to discriminate between different mass schemes.

Appendix A

Massive Coefficient Functions Mellin Transform

In this appendix we collect all the analytical results for the Mellin transforms that has been possible to derive for the massive coefficient functions.

A.1 NC Processes

We first consider the NC processes. In this case, the first non-vanishing massive contribution is given by the order α_s diagram shown on the left side of Fig. 3.1, which is proportional to the gluon density. Moreover, in FFNS this is the only contribution of order α_s to the structure function.

We will first evaluate the Mellin transform of the order α_s coefficient function contributing to $F_2^{H,FF}$ and then to the longitudinal component $F_L^{H,FF}$. After that we will take the limit $M_H \rightarrow 0$ of the massive expressions in order to obtain the Mellin transform of the order α_s coefficient functions for F_2^{FF0} and F_L^{FF0} .

A.1.1 Order α_s

The explicit expression of the order α_s massive coefficient function for the gluon contributing to $F_2^{H,FF}$ is given in eq. (50) of [47] and we report it here:

$$\begin{aligned} C_{2,g}^{FF,(1)}(z, Q, M_H) &= \theta(a-z) T_R \left\{ [2(1-6\epsilon-4\epsilon^2)z^2 - 2(1-2\epsilon)z + 1] \ln \frac{1+v}{1-v} \right. \\ &\quad \left. + [-4(2-\epsilon)z^2 + 4(2-\epsilon)z - 1]v \right\}, \end{aligned} \tag{A.1}$$

with:

$$\epsilon \equiv \frac{M_H^2}{Q^2}, \quad v \equiv \sqrt{1 - \chi \frac{z}{1-z}} \quad \text{and} \quad a \equiv \frac{1}{1+\chi}, \tag{A.2}$$

being:

$$\chi = 4\epsilon \equiv \frac{4M_H^2}{Q^2}. \tag{A.3}$$

Now we want to transform the above coefficient function in the Mellin space. In practice, we must evaluate the following integral:

$$C_{2,g}^{\text{FF},(1)}(N, Q, M_H) = \int_0^1 dz z^{N-1} C_{2,g}^{\text{FF},(1)}(z, Q) = \int_0^a dz z^{N-1} C_{2,g}^{\text{FF},(1)}(z, Q). \quad (\text{A.4})$$

where in the r.h.s. we already let the θ -function act.

At first, let us deal only with the first line of eq. (A.1), *i.e.* the term proportional to the logarithm. We are essentially dealing with integrals of the form:

$$I_q(N) = \int_0^{z_{th}} dz z^{N-1} z^q \ln \frac{1+v}{1-v}, \quad (\text{A.5})$$

with $q = 0, 1, 2$.

Now we perform the following change of variable in eq. (A.5):

$$t = \frac{z}{a} \Rightarrow z = at \Rightarrow dz = a dt \Rightarrow \begin{cases} z = 0 \rightarrow t = 0 \\ z = a \rightarrow t = 1 \end{cases}, \quad (\text{A.6})$$

so that:

$$v = (1-t)^{1/2}(1-at)^{-1/2}. \quad (\text{A.7})$$

Therefore $I_q(N)$ becomes:

$$I_q(N) = a^N a^q \int_0^1 dt t^{N+q-1} \ln \left(\frac{1+v}{1-v} \right). \quad (\text{A.8})$$

The integral above can be integrated by parts and to this end we need:

$$\begin{aligned} \frac{d}{dt} \ln \left(\frac{1+v}{1-v} \right) &= \frac{dv}{dt} \frac{d}{dv} \ln \left(\frac{1+v}{1-v} \right) \\ &= \left(-\frac{1}{2} \frac{1-a}{(1-t)^{1/2}(1-at)^{3/2}} \right) \left(\frac{2(1-at)}{(1-a)t} \right) \\ &= -\frac{1}{t} \frac{1}{(1-t)^{1/2}(1-at)^{1/2}}, \end{aligned} \quad (\text{A.9})$$

thus:

$$I_q(N) = \frac{a^N a^q}{N+q} \int_0^1 dt t^{N+q-1} (1-t)^{-1/2} (1-at)^{-1/2}. \quad (\text{A.10})$$

But, since the Gauss hypergeometric function has the following integral representation⁽¹⁾:

$${}_2F_1(a, b, c; z) = \frac{\Gamma(c)}{\Gamma(b)\Gamma(c-b)} \int_0^1 dx x^{b-1} (1-x)^{c-b-1} (1-zx)^{-a}, \quad (\text{A.11})$$

¹Note that this integral representation of the hypergeometric function converges only if $\text{Re}(c) > \text{Re}(b) > 0$ and $|\arg(1-z)| < \pi$. The first condition is needed to ensure the convergence of the integral at 0 and 1 and also to avoid the poles of the functions, while the second is needed to avoid the crossing of any cut in the complex plane.

we can match eqs. (A.10) and (A.11) obtaining:

$$\begin{cases} b-1 = N+q-1 \\ c-b-1 = -\frac{1}{2} \\ a = \frac{1}{2} \end{cases} \Rightarrow \begin{cases} a = \frac{1}{2} \\ b = N+q \\ c = N+q + \frac{1}{2} = a+b \end{cases}, \quad (\text{A.12})$$

so that we get the following close form:

$$I_q(N) = \frac{a^N a^q}{N+q} \frac{\Gamma(N+q)\Gamma(\frac{1}{2})}{\Gamma(N+q+\frac{1}{2})} {}_2F_1\left(\frac{1}{2}, N+q, N+q+\frac{1}{2}; a\right). \quad (\text{A.13})$$

It follows that the Mellin transform of the first line of eq. (A.1) is:

$$T_R \{2(1-6\epsilon-4\epsilon^2)I_2(N) - 2(1-2\epsilon)I_1(N) + I_0(N)\}. \quad (\text{A.14})$$

Now, we consider the second line of eq. (A.1). In this case we should solve the integrals:

$$J_q(N) = \int_0^{z^{th}} dz z^{N-1} z^q v = \int_0^{z^{th}} dz z^{N-1} z^q \sqrt{1 - \chi \frac{z}{1-z}} \quad (\text{A.15})$$

with $q = 0, 1, 2$. Once again we perform the following change of variable:

$$t = \frac{z}{a}, \quad (\text{A.16})$$

so that, considering eq. (A.7), we have:

$$J_q(N) = a^N a^q \int_0^1 dt t^{N+q-1} (1-t)^{1/2} (1-at)^{1/2}, \quad (\text{A.17})$$

which can be written as:

$$\begin{aligned} J_q(N) &= a^N a^q \left\{ \int_0^1 dt t^{N+q-1} (1-t)^{-1/2} (1-at)^{1/2} \right. \\ &\quad \left. - \int_0^1 dt t^{N+q} (1-t)^{-1/2} (1-at)^{1/2} \right\}. \end{aligned} \quad (\text{A.18})$$

which in turn, given eq. (A.11), reduces to:

$$\begin{aligned} J_q(N) &= a^N a^q \left\{ \frac{\Gamma(N+q)\Gamma(\frac{1}{2})}{\Gamma(N+q+\frac{1}{2})} {}_2F_1\left(\frac{1}{2}, N+q, N+q+\frac{1}{2}; a\right) \right. \\ &\quad \left. - \frac{\Gamma(N+q+1)\Gamma(\frac{1}{2})}{\Gamma(N+q+\frac{3}{2})} {}_2F_1\left(\frac{1}{2}, N+q+1, N+q+\frac{3}{2}; a\right) \right\} \\ &= a^N a^q \frac{\Gamma(N+q)\Gamma(\frac{1}{2})}{\Gamma(N+q+\frac{1}{2})} \left\{ {}_2F_1\left(\frac{1}{2}, N+q, N+q+\frac{1}{2}; a\right) \right. \\ &\quad \left. - \frac{N+q}{N+q+\frac{1}{2}} {}_2F_1\left(\frac{1}{2}, N+q+1, N+q+\frac{3}{2}; a\right) \right\}. \end{aligned} \quad (\text{A.19})$$

Finally, The Mellin transform of the second line of eq. (A.1) takes the form:

$$T_R \{-4(2 - \epsilon)J_2(N) + 4(2 - \epsilon)J_1(N) - J_0(N)\} . \quad (\text{A.20})$$

At the end of the day we have that the final expression for the order α_s massive gluon coefficient function for $F_2^{H,\text{FF}}$ in the Mellin space is:

$$\begin{aligned} C_{2,g}^{\text{FF},(1)}(N, Q, M_H) = & T_R \left\{ 2(1 - 6\epsilon - 4\epsilon^2)I_2(N) - 2(1 - 2\epsilon)I_1(N) + I_0(N) \right. \\ & \left. - 4(2 - \epsilon)J_2(N) + 4(2 - \epsilon)J_1(N) - J_0(N) \right\} . \end{aligned} \quad (\text{A.21})$$

Notice that the arguments of both the hypergeometric functions contained in $I_q(N)$ (eq. (A.13)) and $J_q(N)$ (eq. (A.19)) are such that $c = a + b$. This is useful for numerical reasons. In fact, as we will show below, the code responsible for the evaluation of the hypergeometric functions can be made much more efficient if the assumption $c = a + b$ is taken.

Now we consider the order α_s massive coefficient function for the gluon contributing to $F_L^{H,\text{FF}}$ whose explicit x -space expression of can be found in eq. (7) of Ref. [75] (up to a factor $4\pi\epsilon z$) and reads:

$$C_{L,g}^{\text{FF},(1)}(z, Q, M_H) = \theta(a - z) T_R \left[-8\epsilon z^2 \ln \frac{1+v}{1-v} - 4z^2 v + 4zv \right] . \quad (\text{A.22})$$

Using the results obtained for $F_2^{H,\text{FF}}$, the evaluation of the Mellin transform of the expression is straightforward and gives:

$$C_{L,g}^{\text{FF},(1)}(N, Q, M_H) = T_R [8\epsilon I_2(N) - 4J_2(N) + 4J_1(N)] , \quad (\text{A.23})$$

where $I_q(N)$ and $J_q(N)$ are given in eqs. (A.13) and (A.19), respectively.

In order to check the correctness of the results given in eqs. (A.21) and (A.23), we have compared their numerical inverse Mellin, using the inversion algorithm based on the Talbot path presented in Sec. 3.3, with exact x -space expressions of Ref. [64] obtaining an excellent accuracy. As an example, Fig. A.1 shows that the relative accuracy of the numerical Mellin inverse of $C_{2,g}^{\text{FF},(1)}$ with respect to exact x -space expression is always better than 10^{-6} all over the range in x .

Implementation of the Gauss Hypergeometric Function

As we mentioned before, we have written the result for the Mellin transforms of the order α_s NC gluon massive coefficient function in terms of the Gauss hypergeometric functions having the form ${}_2F_1(a, b, a + b; z)$. Moreover the rightmost argument of all the hypergeometric functions entering the expressions for $I_q(N)$ in eq. (A.13) and $J_q(N)$ in eq. (A.19) is always a (defined in eq. (A.2)) which is evidently a real variable such that $0 < a < 1$. Therefore we need a numerical implementation of the hypergeometric function ${}_2F_1(a, b, c; z)$ such that $c = a + b$ which is accurate on the interval $z \in (0, 1)$. To this end, we have implemented an ‘‘hybrid’’ routine that makes use of the hypergeometric series:

$${}_2F_1(a, b, c; z) = \sum_{n=0}^{\infty} \frac{(a)_n (b)_n}{c_n} \frac{z^n}{n!} , \quad (\text{A.24})$$

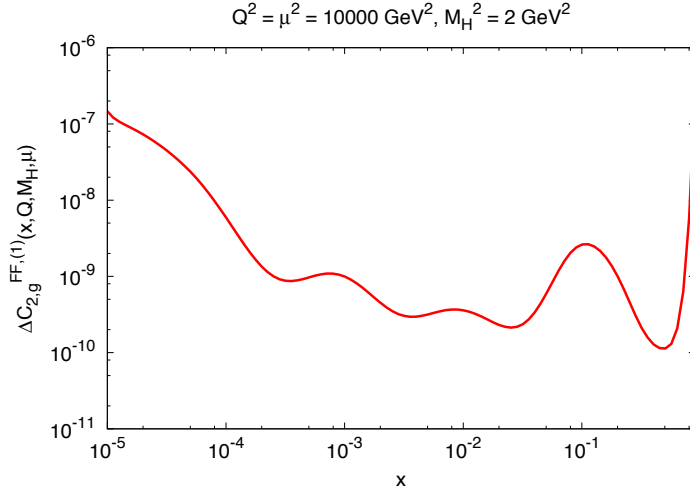


Figure A.1: Relative accuracy of the numerical Mellin inverse of $C_{2,g}^{\text{FF},(1)}$ in eq. (A.21) with respect to exact x -space expression of Ref. [64].

where $(x)_n$ is the so-called Pochhammer symbol defined as:

$$(x)_n = \frac{\Gamma(x+n)}{\Gamma(x)}, \quad (\text{A.25})$$

which converges for $|z| < 1$ and is accurate for $z \simeq 0$, and the expansion of ${}_2F_1(a, b, a+b; z)$ around $z = 1$ [143] that reads:

$$\begin{aligned} {}_2F_1(a, b, c; z) &= \frac{\Gamma(a+b)}{\Gamma(a)\Gamma(b)} \sum_{n=0}^{\infty} \frac{(a)_n (b)_n}{(n!)^2} [2\psi(n+1) - \psi(a+n) \\ &\quad - \psi(b+n) - \ln(1-z)] (1-z)^n, \end{aligned} \quad (\text{A.26})$$

which is indeed more accurate for $z \simeq 1$. In our implementation we use the expansion given in eq. (A.24) for $z \leq 0.1$ and the expansion in eq. (A.26) for $z > 0.1$ and in both case we take the first 81 terms of the series. This provides an approximation for the hypergeometric function which is accurate enough all over the needed range.

Zero-Mass Limit

Once the order α_s gluon massive coefficient functions have been Mellin transformed, we need to do the same for the respective the zero-mass limit coefficient functions. To this end, there are two possible ways: either we directly take the limit $M_H \rightarrow 0$ of the N -space expressions of the full massive coefficient functions, or we first take the limit $M_H \rightarrow 0$ of the x -space expressions and then we transform them in the Mellin space. Of course, the two approaches must lead to the same result, but we take the second one because, from a computational point of view, it is much simpler. However, as a cross check we have verified that for the easier case of $C_{L,g}^{\text{FF},(1)}$ they actually give the same result.

Using the definitions given in eq. (A.2), in the limit $M_H \rightarrow 0$ we directly have:

$$\begin{aligned} \epsilon &\xrightarrow{M_H \rightarrow 0} 0 \\ v &\xrightarrow{M_H \rightarrow 0} 1 \\ a &\xrightarrow{M_H \rightarrow 0} 1 \end{aligned} , \quad (\text{A.27})$$

while one can easily show that:

$$\ln \left(\frac{1+v}{1-v} \right) \xrightarrow{M_H \rightarrow 0} \ln \frac{Q^2(1-z)}{M_H^2 z} . \quad (\text{A.28})$$

Therefore, in the zero-mass limit, eq. (A.1) is given by:

$$\begin{aligned} C_{2,g}^{\text{FF0,(1)}}(z, Q, M_H) &= T_R \left[(2z^2 - 2z + 1) \ln \frac{Q^2(1-z)}{m_H^2 z} - (8z^2 - 8z + 1) \right] \\ &= T_R \left[2 \left(\ln \frac{Q^2}{m_H^2} - 4 \right) z^2 - 2 \left(\ln \frac{Q^2}{m_H^2} - 4 \right) z \right. \\ &\quad + \left. \left(\ln \frac{Q^2}{m_H^2} - 1 \right) + 2z^2 \ln(1-z) - 2z \ln(1-z) \right. \\ &\quad \left. + \ln(1-z) - 2z^2 \ln z + 2z \ln z - \ln z \right] , \end{aligned} \quad (\text{A.29})$$

while the zero-mass limit of eq. (A.22) is:

$$C_{L,g}^{\text{FF0,(1)}}(z, Q) = T_R [-4z^2 + 4z] . \quad (\text{A.30})$$

It is interesting to notice how both the zero-mass limit of the massive coefficient functions in eqs. (A.29) and (A.30) correspond exactly to the order α_s ZM-VFNS coefficient functions (*cf.* eq. (3.276) of Ref. [14]) plus, in the case of $C_{2,g}^{\text{FF0,(1)}}$, a collinear logarithmic divergent term proportional to the splitting function $P_{qg}^{(0)}(x)$. This structure was expected from eq. (2.48) and is the consequence of the absence, in the FFNS, of the heavy quark parton densities that would reabsorb this divergence by means of the DGLAP evolution.

The Mellin transform of eq. (A.29) is:

$$\begin{aligned} C_{2,g}^{\text{FF0,(1)}}(N, Q, M_H) &= T_R \left[2 \left(\ln \frac{Q^2}{m_h^2} - 4 \right) \frac{1}{N+2} - 2 \left(\ln \frac{Q^2}{m_h^2} - 4 \right) \frac{1}{N+1} \right. \\ &\quad + \left. \left(\ln \frac{Q^2}{m_h^2} - 1 \right) \frac{1}{N} - 2 \frac{S_1(N+2)}{N+2} + 2 \frac{S_1(N+1)}{N+1} \right. \\ &\quad \left. - \frac{S_1(N)}{N} + \frac{2}{(N+2)^2} - \frac{2}{(N+1)^2} + \frac{1}{N^2} \right] , \end{aligned} \quad (\text{A.31})$$

but since:

$$S_1(N+1) = S_1(N) + \frac{1}{N+1}, \quad (\text{A.32})$$

and:

$$S_1(N+2) = S_1(N) + \frac{1}{N+1} + \frac{1}{N+2} \quad (\text{A.33})$$

we finally have:

$$\begin{aligned} C_{2,g}^{\text{FF0,(1)}}(N, Q) &= T_R \left[2 \left(\ln \frac{Q^2}{m_h^2} - 4 \right) \frac{1}{N+2} - 2 \left(\ln \frac{Q^2}{m_h^2} - 4 \right) \frac{1}{N+1} \right. \\ &+ \left(\ln \frac{Q^2}{m_h^2} + 1 \right) \frac{1}{N} + S_1(N) \left(-\frac{2}{N+2} + \frac{2}{N+1} - \frac{1}{N} \right) \\ &\left. - \frac{2}{(N+1)(N+2)} + \frac{1}{N^2} \right]. \end{aligned} \quad (\text{A.34})$$

The Mellin transform of eq. (A.30) is instead much simpler and it is:

$$C_{L,g}^{\text{FF0,(1)}}(N, Q) = T_R \left[-\frac{4}{N+2} + \frac{4}{N+1} \right]. \quad (\text{A.35})$$

A.1.2 Order α_s^2

The complete order α_s^2 x -space massive coefficient functions $C_{2,i}^{\text{FF,(2)}}$ and $C_{L,i}^{\text{FF,(2)}}$ for $F_2^{H,\text{FF}}$ and $F_L^{H,\text{FF}}$ was computed long time ago in Ref. [64]. However, they are given in a semi-numerical form and thus analytic results for their Mellin transforms are impossible to obtain. A very efficient method to represent higher order functions to high precision, employed in Ref. [75], consists in the MINIMAX-method. This method is very similar to what is usually done for higher order splitting functions and ZM coefficient functions. In particular, the exact x -space expressions are fitted with a simpler function that is easy to transform in the Mellin space. The MINIMAX-method uses the following parametrization:

$$C^{\text{FF,(2)}}(x, Q, M_H) \simeq (x-a)^{-\kappa} \sum_{k=0}^K b_k(a) x^k, \quad (\text{A.36})$$

where K is the order at which the series in eq. (A.36) is truncated and it is typically $K = 14$ and:

$$a \equiv \frac{Q^2}{Q^2 + 4M_H^2}. \quad (\text{A.37})$$

The coefficients $b_k(a)$ are then determined fitting the parametrization in eq. (A.36) to the exact expressions for a discrete set of values of a that spans a wide enough range ($a \in [0.4, 10^4]$). Then the result for a generic value of a is evaluated by linear interpolation. The exponent κ is not fitted but appropriately chosen case by case.

The functional form of the series in eq. (A.36) is particularly suitable because, including the kinematic θ -function $\theta(a-z)$ that reduces the phase space available for the

final state in presence of two massive particles having mass M_H , its Mellin transform is given by:

$$C^{\text{FF},(2)}(N, Q, M_H) = \sum_{k=0}^K b_k(a) a^{N+k-\kappa} B(N+k, 1-\kappa). \quad (\text{A.38})$$

Here, B denotes the Euler β -function which can be conveniently written in terms of Γ -functions as:

$$B(N+k, 1-\kappa) = \frac{\Gamma(N+k)\Gamma(1-\kappa)}{\Gamma(N+k+1-\kappa)}, \quad (\text{A.39})$$

and, since the Γ -functions can be iteratively evaluated using the identity $\Gamma(x+1) = x\Gamma(x)$, this provides a particularly fast algorithm to be implemented in a numerical code.

As an example, in Fig. A.2 we show the relative accuracy of the numerical Mellin inverse of $C_{2,g}^{\text{FF},(2)}$ as parametrized in Ref. [75] with respect to exact x -space expression from of Ref. [64]. As one can see, the accuracy is pretty good and totally adequate for the precision required by the present experimental data.

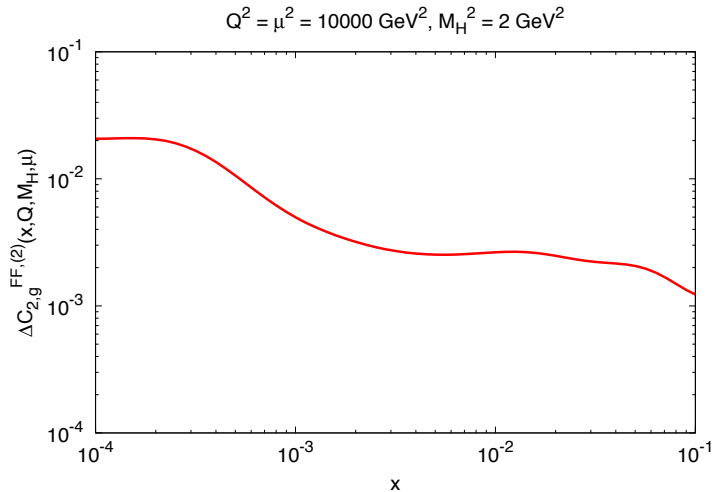


Figure A.2: Relative accuracy of the numerical Mellin inverse of $C_{2,g}^{\text{FF},(2)}$ of the parametrization given in Ref. [75] with respect to exact x -space expression of Ref. [64].

Zero-Mass Limit

Now we turn to the order α_s^2 massive heavy quark coefficient functions in the zero-mass limit. These asymptotic coefficient functions were first computed in Ref. [144] in x -space, but their explicit Mellin transforms were not available yet.

In order to perform the Mellin transformation of those x -space coefficient functions, it is convenient to rewrite them in terms of independent Mellin integrals which we can then tabulate. Following the notation introduced in Ref. [144], we first consider the gluon coefficient function for $F_L^{\text{FF}0}$. The corresponding Mellin transform can be written

as:

$$C_{L,g}^{\text{FF0},(2)} \left(N, \frac{Q^2}{M_H^2}, \frac{\mu^2}{M_H^2} \right) = 4T_R \left[C_{L,g}^{\text{const}}(N) + C_{L,g}^Q(N) \ln \frac{Q^2}{M_H^2} - C_{L,g}^\mu(N) \ln \frac{\mu^2}{M_H^2} \right]. \quad (\text{A.40})$$

The coefficient function has been separated into three terms: a Q^2 -independent term $C^{\text{const}}(N)$, a collinear logarithmic term $C^Q(N)$ and a factorization scale variation term $C^\mu(N)$ that comes from taking $Q \neq \mu$. A similar decomposition will be performed for all the following coefficient functions.

The individual terms can be written as:

$$\begin{aligned} C_{L,g}^{\text{const}} &= C_F \left[\frac{16}{15} A_{10}^{(-2)} - \frac{16}{3} A_{10}^{(1)} + \frac{32}{5} A_{10}^{(3)} + 8A_8^{(1)} + 8A_6^{(1)} - \frac{16}{3} A_3^{(1)} \right. \\ &\quad - \frac{16}{5} A_3^{(3)} - \zeta(2) \left(\frac{16}{3} A_1^{(1)} - \frac{32}{5} A_1^{(3)} \right) + 4A_4^{(0)} + 12A_4^{(1)} \\ &\quad - 16A_4^{(2)} - \frac{16}{15} A_2^{(-1)} - \frac{52}{15} A_2^{(0)} - \frac{104}{5} A_2^{(1)} + \frac{48}{5} A_2^{(2)} \\ &\quad \left. + \frac{16}{15} A_1^{(-1)} - \frac{64}{15} A_1^{(0)} - \frac{152}{5} A_1^{(1)} + \frac{168}{5} A_1^{(2)} \right] \\ &+ C_A \left[16A_{10}^{(1)} + 16A_{10}^{(2)} - 32A_8^{(1)} + 16\zeta(2)A_1^{(2)} - 48A_6^{(1)} + 16A_6^{(2)} \right. \\ &\quad + 8A_5^{(1)} - 8A_5^{(2)} + 24A_3^{(1)} + \frac{8}{3} A_4^{(-1)} - 8A_4^{(0)} - 72A_4^{(1)} \\ &\quad + \frac{232}{3} A_4^{(2)} + 8A_2^{(0)} + 64A_2^{(1)} - 104A_2^{(2)} - \frac{8}{9} A_1^{(-1)} + \frac{8}{3} A_1^{(0)} \\ &\quad \left. + \frac{136}{3} A_1^{(1)} - \frac{424}{9} A_1^{(2)} \right], \end{aligned} \quad (\text{A.41a})$$

$$\begin{aligned} C_{L,g}^Q &= C_F \left[8A_2^{(1)} + 4A_1^{(0)} + 4A_1^{(1)} - 8A_1^{(2)} \right] \\ &+ C_A \left[16A_4^{(1)} - 16A_4^{(2)} - 32A_2^{(1)} + \frac{8}{3} A_1^{(-1)} - 8A_1^{(0)} \right. \\ &\quad \left. - 40A_1^{(1)} + \frac{136}{3} A_1^{(2)} \right], \end{aligned} \quad (\text{A.41b})$$

$$\begin{aligned} C_{L,g}^\mu &= C_A \left[16A_4^{(1)} - 16A_4^{(2)} - 32A_2^{(1)} + \frac{8}{3} A_1^{(-1)} - 8A_1^{(0)} \right. \\ &\quad \left. - 40A_1^{(1)} + \frac{136}{3} A_1^{(2)} \right], \end{aligned} \quad (\text{A.41c})$$

where the $A_N^{(l)}$ are the independent Mellin integrals:

$$A_n^{(l)} \equiv A_n(N+l). \quad (\text{A.42})$$

Those for which we will use closed-form analytic expressions are collected in Tabs. A.1 and A.2. Some of these Mellin transforms were already computed in Ref. [145] and are repeated here for completeness. The remaining terms, for which we will use numerical approximations, are evaluated at the end of this section.

The quark coefficient function for F_L^{FF0} can be similarly written as:

$$C_{L,q}^{\text{FF0},(2)} \left(N, \frac{Q^2}{M_H^2}, \frac{\mu^2}{M_H^2} \right) = 4T_R \left[C_{L,q}^{\text{const}}(N) + C_{L,q}^Q(N) \ln \frac{Q^2}{M_H^2} - C_{L,q}^\mu(N) \ln \frac{\mu^2}{M_H^2} \right], \quad (\text{A.43})$$

where:

$$\begin{aligned} C_{L,q}^{\text{const}} &= C_F \left[-8A_8^{(1)} - 8A_6^{(1)} + 8A_3^{(1)} + \frac{8}{3} A_4^{(-1)} - 8A_4^{(0)} + \frac{16}{3} A_4^{(2)} \right. \\ &\quad + 8A_2^{(0)} - 8A_2^{(1)} - 16A_2^{(2)} - \frac{8}{9} A_1^{(-1)} + \frac{8}{3} A_1^{(0)} \\ &\quad \left. - \frac{32}{3} A_1^{(1)} + \frac{80}{9} A_1^{(2)} \right], \end{aligned} \quad (\text{A.44a})$$

n	$f_n(z)$	$A_n(N) = \mathbf{M}[f_n(z)](N)$
1	1	$\frac{1}{N}$
2	$\ln(z)$	$-\frac{1}{N^2}$
3	$\ln^2(z)$	$\frac{2}{N^3}$
4	$\ln(1-z)$	$-\frac{S_1(N)}{N}$
5	$\ln^2(1-z)$	$\frac{S_1^2(N) + S_2(N)}{N}$
6	$\ln(z)\ln(1-z)$	$\frac{S_1(N)}{N^2} + \frac{S_2(N) - \zeta(2)}{N}$
8	$\text{Li}_2(1-z)$	$-\frac{S_2(N) - \zeta(2)}{N}$
10	$\text{Li}_2(-z) + \ln(z)\ln(1+z)$	$-\frac{\zeta(2)}{2N} - \frac{1}{4N} \left[S_2\left(\frac{N-1}{2}\right) - S_2\left(\frac{N}{2}\right) \right]$
11	$\ln^3(z)$	$-\frac{6}{N^4}$
12	$\ln^2(z)\ln(1-z)$	$\frac{2}{N} \left[\zeta(3) + \frac{\zeta(2)}{N} - \frac{S_1(N)}{N^2} - \frac{S_2(N)}{N} - S_3(N) \right]$
13	$\ln(1-z)\text{Li}_2(1-z) - \text{Li}_3(1-z)$	$\frac{S_1(N)S_2(N) - \zeta(2)S_1(N) + S_3(N) - \zeta(3)}{N}$
14	$\ln(z)\ln^2(1-z)$	$\frac{2}{N} \left\{ \zeta(3) + \zeta(2)S_1(N) - \frac{1}{2N} [S_1^2(N) + S_2(N)] - S_1(N)S_2(N) - S_3(N) \right\}$
15	$S_{1,2}(1-z)$	$-\frac{1}{N} [S_3(N) - \zeta(3)]$
17	$\ln(1+z)$	$\frac{\ln(2)}{N} + \frac{1}{2N} \left[S_1\left(\frac{N-1}{2}\right) - S_1\left(\frac{N}{2}\right) \right]$
18	$\ln^3(1-z)$	$-\frac{S_1^3(N) + 3S_1(N)S_2(N) + 2S_3(N)}{N}$
19	$\text{Li}_3(-z)$	$-\frac{3\zeta(3)}{4N} + \frac{\zeta(2)}{2N^2} - \frac{\ln(2)}{N^3} - \frac{1}{2N^3} \left[S_1\left(\frac{N-1}{2}\right) - S_1\left(\frac{N}{2}\right) \right]$

Table A.1: Elementary transforms used for the computation of the Mellin transform of the order α_s^2 NC zero-mass limit of FFNS coefficient functions.

$$C_{L,q}^Q = C_{L,q}^\mu = C_F \left[-8A_2^{(1)} + \frac{8}{3}A_1^{(-1)} - 8A_1^{(0)} + \frac{16}{3}A_1^{(2)} \right]. \quad (\text{A.44b})$$

n	$f_n(z)$	$A_n(N) = \mathbf{M}[f(z)](N)$
20	$\ln(z)\text{Li}_2(-z)$	$-\frac{1}{2N^2} \left[\frac{2}{N} S_1 \left(\frac{N-1}{2} \right) + \frac{1}{2} S_2 \left(\frac{N-1}{2} \right) + \frac{4 \ln(2)}{N} \right]$ $+\frac{1}{2N^2} \left[\frac{2}{N} S_1 \left(\frac{N}{2} \right) + \frac{1}{2} S_2 \left(\frac{N}{2} \right) + \zeta(2) \right]$
21	$\ln^2(z) \ln(1+z)$	$\frac{1}{2N} \left[\frac{2}{N^2} S_1 \left(\frac{N-1}{2} \right) + \frac{1}{N} S_2 \left(\frac{N-1}{2} \right) + \frac{1}{2} S_3 \left(\frac{N-1}{2} \right) + \frac{4 \ln(2)}{N^2} \right]$ $-\frac{1}{2N} \left[\frac{2}{N^2} S_1 \left(\frac{N}{2} \right) + \frac{1}{N} S_2 \left(\frac{N}{2} \right) + \frac{1}{2} S_3 \left(\frac{N}{2} \right) \right]$
23	$\ln(z)\text{Li}_2(1-z)$	$\frac{1}{N^2} [S_2(N) - \zeta(2)] + \frac{2}{N} [S_3(N) - \zeta(3)]$
27	$\left(\frac{1}{1-z} \right)_+$	$-S_1(N-1)$
28	$\left(\frac{\ln(1-z)}{1-z} \right)_+$	$\frac{1}{2} S_1^2(N-1) + \frac{1}{2} S_2(N-1)$
29	$\frac{\ln(z)}{1-z}$	$S_2(N-1) - \zeta(2)$
30	$\left(\frac{\ln^2(1-z)}{1-z} \right)_+$	$-\frac{1}{3} S_1^2(N-1) - S_1(N-1)S_2(N-1) - \frac{2}{3} S_3(N-1)$
31	$\frac{\ln^2(z)}{1-z}$	$-2[S_3(N-1) - \zeta(3)]$
32	$\frac{\ln(z) \ln(1-z)}{1-z}$	$\zeta(3) + \zeta(2)S_1(N-1) - S_1(N-1)S_2(N-1) - S_3(N-1)$

Table A.2: Continuation of Tab. A.1.

Finally, the gluon radiation coefficient function for $F_L^{\text{FF}0}$, that is the massive coefficient function associated to the diagrams in Fig. 3.2, can be written as:

$$C_{L,\text{GR}}^{\text{FF}0,(2)} \left(N, \frac{Q^2}{M_H^2}, \frac{\mu^2}{M_H^2} \right) = 4T_R \left[C_{L,\text{GR}}^{\text{const}}(N) + C_{L,\text{GR}}^Q(N) \ln \frac{Q^2}{M_H^2} \right], \quad (\text{A.45})$$

where:

$$C_{L,\text{GR}}^{\text{const}} = C_F \left[\frac{4}{3} (A_4^{(1)} - 2A_2^{(1)} + A_1^{(0)}) - \frac{50}{9} A_1^{(1)} \right], \quad (\text{A.46a})$$

and:

$$C_{L,\text{GR}}^Q = C_F \frac{4}{3} A_1^{(1)}. \quad (\text{A.46b})$$

Let us now turn to the $F_2^{\text{FF}0}$ heavy quark coefficient functions. In comparison to the longitudinal structure function, there are extra pieces $C^{2Q}(N)$ and $C^{\mu Q}(N)$ arising from the double collinear logarithm.

The gluon coefficient function for $F_2^{\text{FF}0}$ can be written as:

$$C_{2,g}^{\text{FF}0,(2)} \left(N, \frac{Q^2}{M_H^2}, \frac{\mu^2}{M_H^2} \right) = 4T_R \left[C_{2,g}^{\text{const}}(N) + C_{2,g}^{2Q}(N) \ln^2 \frac{Q^2}{M_H^2} + C_{2,g}^Q(N) \ln \frac{Q^2}{M_H^2} - C_{2,g}^\mu(N) \ln \frac{\mu^2}{M_H^2} - C_{2,g}^{\mu Q}(N) \ln \frac{\mu^2}{M_H^2} \ln \frac{Q^2}{M_H^2} \right], \quad (\text{A.47})$$

where:

$$C_{2,g}^{\text{const}} = C_F \left[4 \left(-2B_{16}^+ - 2\zeta(2)B_{17}^+ + B_{21}^+ - \frac{3}{2}B_8^+ \right) + 2 \left(-4B_{15}^- - 2B_{22}^- + 12B_{19}^- + B_{18}^- - \frac{5}{2}B_{14}^- + 2B_{12}^- + B_{13}^- - 4B_{20}^- + 4\zeta(2)B_2^- - \frac{1}{3}B_{11}^- + 3B_6^- \right) + 2 \left(4A_{15}^{(2)} - 2A_{22}^{(2)} + A_{18}^{(2)} - \frac{7}{2}A_{14}^{(2)} + 4A_{12}^{(2)} - A_{13}^{(2)} - 4\zeta(2)A_4^{(2)} + 4A_{23}^{(2)} + 4\zeta(2)A_2^{(2)} - A_{11}^{(2)} + 11A_8^{(2)} \right) + 32A_{19}^{(1)} + \zeta(3)(28A_1^{(0)} - 24A_1^{(1)} + 48A_1^{(2)}) - 28A_6^{(1)} + 36A_6^{(2)} + \frac{4}{15}A_{10}^{(-2)} + 24A_{10}^{(0)} + \frac{32}{3}A_{10}^{(1)} + \frac{48}{5}A_{10}^{(3)} + \zeta(2)(12A_1^{(0)} - \frac{52}{3}A_1^{(1)} + 26A_1^{(2)} + \frac{48}{5}A_1^{(3)}) - \frac{11}{2}A_5^{(0)} + 22A_5^{(1)} - 21A_5^{(2)} - A_3^{(0)} + \frac{2}{3}A_3^{(1)} - 13A_3^{(2)} - \frac{24}{5}A_3^{(3)} + 7A_4^{(0)} - 33A_4^{(1)} + 24A_4^{(2)} - \frac{4}{15}A_2^{(-1)} - \frac{178}{15}A_2^{(0)} + \frac{34}{5}A_2^{(1)} - \frac{168}{5}A_2^{(2)} + \frac{4}{15}A_1^{(-1)} - \frac{226}{15}A_1^{(0)} + \frac{17}{5}A_1^{(1)} + \frac{82}{5}A_1^{(2)} \right] \quad (\text{A.48a})$$

$$+ C_A \left[4 \left(C_{24} - C_{25} - C_{26} + \frac{3}{4}C_{21} + \frac{3}{2}C_{20} \right) + 2 \left(5(A_{15}^{(0)} + 2A_{15}^{(1)}) + (A_{16}^{(0)} + 2A_{16}^{(1)}) - 3(A_{19}^{(0)} + 2A_{19}^{(1)}) + \zeta(2)(A_{17}^{(0)} + 2A_{17}^{(1)}) \right) + 8 \left(2A_{15}^{(1)} + A_{23}^{(1)} \right) - 16A_{22}^{(1)} + 2A_{21}^{(2)} - 4A_{20}^{(2)} + 12A_{14}^{(1)} - 4A_{14}^{(2)} - 2A_{12}^{(0)} - 16A_{12}^{(1)} + 4A_{12}^{(2)} + 4A_{13}^{(0)} + 16A_{13}^{(1)} - \zeta(2)(10A_4^{(0)} - 12A_4^{(1)} + 16A_4^{(2)}) + \frac{4}{3}A_{11}^{(0)} + 4A_{11}^{(1)} - \zeta(2)(4A_2^{(0)} + 40A_2^{(1)} - 8A_2^{(2)}) - \zeta(3)(3A_1^{(0)} + 14A_1^{(1)} + 2A_1^{(2)}) - \frac{8}{3}A_{10}^{(-1)} - 12A_{10}^{(0)} + 4A_{10}^{(1)} + \frac{52}{3}A_{10}^{(2)} + \frac{16}{3}A_8^{(-1)} + 5A_8^{(0)} - 16A_8^{(1)} + \frac{20}{3}A_8^{(2)} - \zeta(2)(8A_1^{(-1)} + A_1^{(0)} + 52A_1^{(1)} - \frac{199}{3}A_1^{(2)}) + 4A_6^{(0)} - 72A_6^{(1)} + 73A_6^{(2)} + \frac{4}{3}A_5^{(-1)} - \frac{3}{2}A_5^{(0)} + 16A_5^{(1)} - \frac{107}{6}A_5^{(2)} + 46A_3^{(1)} - \frac{57}{2}A_3^{(2)} + \frac{52}{9}A_4^{(-1)} - \frac{28}{3}A_4^{(0)} - \frac{215}{3}A_4^{(1)} + \frac{749}{9}A_4^{(2)} + \frac{73}{3}A_2^{(0)} + 83A_2^{(1)} - \frac{1445}{9}A_2^{(2)} + \frac{20}{9}A_1^{(-1)} + \frac{233}{18}A_1^{(0)} + \frac{65}{9}A_1^{(1)} - \frac{439}{18}A_1^{(2)} \right], \quad (\text{A.48b})$$

$$C_{2,g}^{2Q} = C_F \left[2A_4^{(0)} - 4A_4^{(1)} + 4A_4^{(2)} - A_2^{(0)} + 2A_2^{(1)} - 4A_2^{(2)} - \frac{1}{2}A_1^{(0)} + 2A_1^{(1)} \right] + C_A \left[2A_4^{(0)} - 4A_4^{(1)} + 4A_4^{(2)} + 2A_2^{(0)} + 8A_2^{(1)} + \frac{4}{3}A_1^{(-1)} + A_1^{(0)} + 8A_1^{(1)} - \frac{31}{3}A_1^{(2)} \right], \quad (\text{A.48c})$$

$$\begin{aligned}
C_{2,g}^Q &= C_F \left[2A_8^{(0)} - 4A_8^{(1)} - (8A_1^{(0)} - 16A_1^{(1)} + 16A_1^{(2)})\zeta(2) - 6A_6^{(0)} \right. \\
&\quad + 12A_6^{(1)} - 16A_6^{(2)} + 4A_5^{(0)} - 8A_5^{(1)} + 8A_5^{(2)} + 2A_3^{(0)} - 4A_3^{(1)} \\
&\quad + 8A_3^{(2)} - 7A_4^{(0)} + 24A_4^{(1)} - 20A_4^{(2)} + 2A_2^{(0)} - 12A_2^{(1)} + 20A_2^{(2)} \\
&\quad \left. + 9A_1^{(0)} - 17A_1^{(1)} + 4A_1^{(2)} \right] \\
&\quad + C_A \left[-4A_{10}^{(0)} - 8A_{10}^{(1)} - 8A_{10}^{(2)} + 4A_8^{(0)} + 16A_8^{(1)} \right. \\
&\quad - (4A_1^{(0)} + 8A_1^{(2)})\zeta(2) + 24A_6^{(1)} - 8A_6^{(2)} + 2A_5^{(0)} - 4A_5^{(1)} \\
&\quad + 4A_5^{(2)} - 4A_3^{(0)} - 12A_3^{(1)} + \frac{8}{3}A_4^{(-1)} - 2A_4^{(0)} + 40A_4^{(1)} - \frac{134}{3}A_4^{(2)} \\
&\quad \left. - 48A_2^{(1)} + 50A_2^{(2)} + \frac{52}{9}A_1^{(-1)} - \frac{55}{3}A_1^{(0)} - \frac{92}{3}A_1^{(1)} + \frac{407}{9}A_1^{(2)} \right], \tag{A.48d}
\end{aligned}$$

$$\begin{aligned}
C_{2,g}^\mu &= C_A \left[4A_8^{(0)} + 16A_8^{(1)} - (4A_1^{(0)} - 8A_1^{(1)} + 8A_1^{(2)})\zeta(2) + 24A_6^{(1)} \right. \\
&\quad - 8A_6^{(2)} + 4A_5^{(0)} - 8A_5^{(1)} + 8A_5^{(2)} - 2A_3^{(0)} - 8A_3^{(1)} + \frac{8}{3}A_4^{(-1)} \\
&\quad - 2A_4^{(0)} + 48A_4^{(1)} - \frac{158}{3}A_4^{(2)} - 2A_2^{(0)} - 64A_2^{(1)} \\
&\quad \left. + \frac{62}{3}A_2^{(2)} + \frac{4}{3}A_1^{(-1)} - \frac{43}{3}A_1^{(0)} - \frac{242}{3}A_1^{(1)} + \frac{281}{3}A_1^{(2)} \right], \tag{A.48e}
\end{aligned}$$

$$\begin{aligned}
C_{2,g}^{\mu Q} &= C_A \left[4A_4^{(0)} - 8A_4^{(1)} + 8A_4^{(2)} + 4A_2^{(0)} + 16A_2^{(1)} + \frac{8}{3}A_1^{(-1)} + 2A_1^{(0)} \right. \\
&\quad \left. + 16A_1^{(1)} - \frac{62}{3}A_1^{(2)} \right], \tag{A.48f}
\end{aligned}$$

where:

$$B_n^\pm \equiv A_n^{(0)} \pm 2A_n^{(1)} + A_n^{(2)} \quad \text{and} \quad C_n \equiv A_n^{(0)} + 2A_n^{(1)} + 2A_n^{(2)}. \tag{A.49}$$

The quark coefficient function for $F_2^{\text{FF}0}$ can be written similarly as:

$$\begin{aligned}
C_{2,q}^{\text{FF}0,(2)} \left(N, \frac{Q^2}{M_H^2}, \frac{\mu^2}{M_H^2} \right) &= 4T_R \left[C_{2,q}^{\text{const}}(N) + C_{2,q}^{2Q}(N) \ln^2 \frac{Q^2}{M_H^2} + C_{2,q}^Q(N) \ln \frac{Q^2}{M_H^2} \right. \\
&\quad \left. - C_{2,q}^\mu(N) \ln \frac{\mu^2}{M_H^2} - C_{2,q}^{\mu Q}(N) \ln \frac{\mu^2}{M_H^2} \ln \frac{Q^2}{M_H^2} \right], \tag{A.50}
\end{aligned}$$

where:

$$\begin{aligned}
C_{2,q}^{\text{const}} &= C_F \left[8(A_{15}^{(0)} + A_{15}^{(1)}) + 4(A_{13}^{(0)} + A_{13}^{(1)}) + 2(A_{14}^{(0)} + A_{14}^{(1)}) - 4(A_{12}^{(0)} + A_{12}^{(1)}) \right. \\
&\quad - 8\zeta(2)(A_2^{(0)} + A_2^{(1)}) + \frac{4}{3}(A_{11}^{(0)} + A_{11}^{(1)}) - \frac{8}{3}A_{10}^{(-1)} - 8A_{10}^{(0)} - 8A_{10}^{(1)} \\
&\quad - \frac{8}{3}A_{10}^{(2)} + \frac{16}{3}A_8^{(-1)} + 4A_8^{(0)} - 4A_8^{(1)} + \frac{8}{3}A_8^{(2)} - \zeta(2)(8A_1^{(-1)} + 4A_1^{(0)} \\
&\quad + 4A_1^{(1)} - \frac{16}{3}A_1^{(2)}) + 8A_6^{(2)} + \frac{4}{3}A_5^{(-1)} + A_5^{(0)} - A_5^{(1)} - \frac{4}{3}A_5^{(2)} \\
&\quad + 10A_3^{(1)} - 4A_3^{(2)} + \frac{52}{9}A_4^{(-1)} - \frac{52}{3}A_4^{(0)} + \frac{40}{3}A_4^{(1)} - \frac{16}{9}A_4^{(2)} + \frac{70}{3}A_2^{(0)} \\
&\quad \left. - 22A_2^{(1)} - \frac{176}{9}A_2^{(2)} + \frac{20}{9}A_1^{(-1)} + \frac{76}{9}A_1^{(0)} - \frac{304}{9}A_1^{(1)} + \frac{208}{9}A_1^{(2)} \right], \tag{A.51a}
\end{aligned}$$

$$C_{2,q}^{2Q} = C_F \left[2A_2^{(0)} + 2A_2^{(1)} + \frac{4}{3}A_1^{(-1)} + A_1^{(0)} - A_1^{(1)} - \frac{4}{3}A_1^{(2)} \right], \tag{A.51b}$$

$$\begin{aligned}
C_{2,q}^Q &= C_F \left[4A_8^{(0)} + 4A_8^{(1)} + 4A_6^{(0)} + 4A_6^{(1)} - 4A_3^{(0)} - 4A_3^{(1)} + \frac{8}{3}A_4^{(-1)} \right. \\
&\quad + 2A_4^{(0)} - 2A_4^{(1)} - \frac{8}{3}A_4^{(2)} + 8A_2^{(2)} + \frac{52}{9}A_1^{(-1)} - \frac{52}{3}A_1^{(0)} \\
&\quad \left. + \frac{40}{3}A_1^{(1)} - \frac{16}{9}A_1^{(2)} \right], \tag{A.51c}
\end{aligned}$$

$$C_{2,q}^\mu = C_F \left[4A_8^{(0)} + 4A_8^{(1)} + 4A_6^{(0)} + 4A_6^{(1)} - 2A_3^{(0)} - 2A_3^{(1)} + \frac{8}{3}A_4^{(-1)} + 2A_4^{(0)} - 2A_4^{(1)} - \frac{8}{3}A_4^{(2)} - 2A_2^{(0)} - 10A_2^{(1)} + \frac{8}{3}A_2^{(2)} + \frac{4}{3}A_1^{(-1)} - \frac{40}{3}A_1^{(0)} + \frac{4}{3}A_1^{(1)} + \frac{32}{3}A_1^{(2)} \right], \quad (\text{A.51d})$$

$$C_{2,q}^{\mu Q} = C_F \left[4A_2^{(0)} + 4A_2^{(1)} + \frac{8}{3}A_1^{(-1)} + 2A_1^{(0)} - 2A_1^{(1)} - \frac{8}{3}A_1^{(2)} \right]. \quad (\text{A.51e})$$

The gluon radiation coefficient function for F_2^{FF0} can be written as:

$$C_{2,\text{GR}}^{\text{FF0,(2)}} \left(N, \frac{Q^2}{M_H^2}, \frac{\mu^2}{M_H^2} \right) = 4T_R \left[C_{2,\text{GR}}^{\text{const}}(N) + C_{2,\text{GR}}^{2Q}(N) \ln^2 \frac{Q^2}{M_H^2} + C_{2,\text{GR}}^Q(N) \ln \frac{Q^2}{M_H^2} \right], \quad (\text{A.52})$$

where:

$$C_{2,\text{GR}}^{\text{const}} = C_F \left[-\frac{2}{3}(A_{33}^{(0)} + A_{33}^{(2)}) - \frac{2\zeta(2)}{3}(2A_{27}^{(0)} - A_1^{(0)} - A_1^{(1)}) - \frac{4}{3}(A_{32}^{(0)} + A_{32}^{(2)}) + \frac{1}{3}(2A_{30}^{(0)} - A_5^{(0)} - A_5^{(1)}) + A_{31}^{(0)} + A_{31}^{(2)} - \frac{29}{18}(2A_{28}^{(0)} - A_4^{(0)} - A_4^{(1)}) + \frac{67}{18}(A_{29}^{(0)} + A_{29}^{(2)}) + \frac{359}{108}(2A_{27}^{(0)} - A_1^{(0)} - A_1^{(1)}) + \frac{1}{6}A_4^{(0)} + \frac{13}{6}A_4^{(1)} - \frac{1}{2}A_2^{(0)} - \frac{23}{6}A_2^{(1)} + \frac{29}{36}A_1^{(0)} - \frac{295}{36}A_1^{(1)} + \frac{134\zeta(2)}{18} + \frac{265}{36} \right], \quad (\text{A.53a})$$

$$C_{2,\text{GR}}^{2Q} = C_F \left[\frac{1}{3}(2A_{27}^{(0)} - A_1^{(0)} - A_1^{(1)}) + \frac{1}{2} \right], \quad (\text{A.53b})$$

$$C_{2,\text{GR}}^Q = C_F \left[\frac{2}{3}(2A_{28}^{(0)} - A_4^{(0)} - A_4^{(1)}) - \frac{29}{18}(2A_{27}^{(0)} - A_1^{(0)} - A_1^{(1)}) - \frac{4}{3}(A_{29}^{(0)} + A_{29}^{(2)}) + \frac{1}{6}A_1^{(0)} + \frac{13}{6}A_1^{(1)} - \frac{8\zeta(2)}{3} - \frac{19}{6} \right]. \quad (\text{A.53c})$$

In addition to the elementary Mellin transforms listed in Tabs. A.1 and A.2, the coefficient functions also contain terms whose Mellin transform is known in closed form, but is expressed in terms of generalized harmonic sums $S_{i_1, \dots, i_n}(N)$. Given that, at the best of our knowledge, no numerical implementation of the functions $S_{i_1, \dots, i_n}(N)$, for $N \in \mathbb{C}$, exists, we have evaluated the Mellin transform of these functions through suitable numerical approximations. The x -space expressions whose Mellin transform has been implemented in an approximate way are the following:

$$f_{16}(z) = 2\text{Li}_2(-z) \ln(1+z) + \ln(z) \ln^2(1+z) + 2S_{1,2}(-z), \quad (\text{A.54a})$$

$$f_{22}(z) = \text{Li}_3(1-z), \quad (\text{A.54b})$$

$$f_{24}(z) = \text{Li}_3\left(\frac{1-z}{1+z}\right) - \text{Li}_3\left(-\frac{1-z}{1+z}\right), \quad (\text{A.54c})$$

$$f_{25}(z) = \ln(z) \ln(1-z) \ln(1+z), \quad (\text{A.54d})$$

$$f_{26}(z) = \ln(1-z)\text{Li}_2(-z), \quad (\text{A.54e})$$

$$f_{33}(z) = \frac{\text{Li}_2(1-z)}{1-z}. \quad (\text{A.54f})$$

We will consider one by one each of these functions.

In order to determine the Mellin transform of eq. (A.54a), we use eq. (32) of Ref. [145], which can be written as:

$$A_{16}(N) = \mathbf{M}[f_{16}(z)](N) = \frac{1}{N} \mathbf{M} \left[\frac{z \tilde{\Phi}(z)}{1+z} \right] - \frac{\zeta(2) \ln(2)}{N} + \frac{\zeta(3)}{4N} \\ - \frac{1}{2N} \mathbf{M} \left[\frac{z \ln^2(z)}{1+z} \right] + \frac{\zeta(2)}{N} \mathbf{M} \left[\frac{z}{1+z} \right]. \quad (\text{A.55})$$

The last two Mellin transforms of the r.h.s. of eq. (A.55) are respectively⁽²⁾:

$$\mathbf{M} \left[\frac{z \ln^2(z)}{1+z} \right] = -\frac{1}{4} \left[S_3 \left(\frac{N-1}{2} \right) - S_3 \left(\frac{N}{2} \right) \right], \quad (\text{A.57})$$

and:

$$\mathbf{M} \left[\frac{z}{1+z} \right] = -\frac{1}{2} \left[S_1 \left(\frac{N-1}{2} \right) - S_1 \left(\frac{N}{2} \right) \right]. \quad (\text{A.58})$$

The Mellin transform of the term involving the special function $\tilde{\Phi}(z)$ in eq. (A.55) is instead given in Ref. [145] in terms of the generalized harmonic sum $S_{1,2}(N)$. We instead rewrite it as:

$$\frac{z \tilde{\Phi}(z)}{1+z} \cong \sum_{k=1}^{10} a_k z^k \tilde{\Phi}(z), \quad (\text{A.59})$$

where the values of the coefficients a_k are determined by fitting the polynomial $\sum_{k=1}^{10} a_k z^k$ to the function $z/(1+z)$ on the unit interval. One can then use the Mellin transform of the function $z^k \tilde{\Phi}(z)$, which reads:

$$\mathbf{M}[z^k \tilde{\Phi}(z)] = \frac{1}{(N+k)^3} + \frac{1}{2(N+k)} \left[S_2 \left(\frac{N+k-1}{2} \right) - S_2 \left(\frac{N+k}{2} \right) \right]. \quad (\text{A.60})$$

The desired Mellin transform $A_{16}(N)$ is immediately found combining eqs. (A.57), (A.58), (A.59) and (A.60).

In order to determine the Mellin transform of eq. (A.54b) we use the expansion:

$$\text{Li}_3(z) = \sum_{k=1}^{\infty} \frac{z^k}{k^3}. \quad (\text{A.61})$$

It follows that:

$$A_{22}(N) = \mathbf{M}[f_{22}(z)](N) = \sum_{k=1}^{\infty} \frac{1}{k^3} \int_0^1 z^{N-1} (1-z)^k dz, \quad (\text{A.62})$$

²In general:

$$\mathbf{M} \left[\frac{z \ln^n(z)}{1+z} \right] = \frac{(-1)^{n+1} n!}{2^{n+1}} \left[S_{n+1} \left(\frac{N-1}{2} \right) - S_{n+1} \left(\frac{N}{2} \right) \right]. \quad (\text{A.56})$$

This Mellin transform is superficially different from the Mellin transform number 15 in Appendix of Ref. [145], but they turn out to be equivalent after suitable simplifications. This apparent difference is also responsible for the mismatch between entries 13, 28, 43, and 62 in the Table in Appendix of Ref. [145] and entries 17, 21, 20 and 19 in Tabs. A.1 and A.2, respectively. For the same reason entries number 4 and 57 of [145] look different from our eqs. (A.57) and (A.60).

but:

$$\int_0^1 z^{N-1}(1-z)^k dz = \frac{\Gamma(N)\Gamma(k+1)}{\Gamma(N+k+1)} = \frac{k!}{(N+k)\dots(N+1)N}, \quad (\text{A.63})$$

so that:

$$A_{22}(N) = \sum_{k=1}^{\infty} \frac{k!}{k^3(N+k)\dots(N+1)N}. \quad (\text{A.64})$$

In our implementation we have truncated this series at $k = 30$.

Next, we turn to the Mellin transform of eq. (A.54c). In this case we fit the function:

$$g(z) = (1-z)^{b-1} \sum_{k=0}^{10} c_k z^k \quad (\text{A.65})$$

to the function $f_{24}(z)$. However, one can show that:

$$f_{24}(0) = \text{Li}_3(1) - \text{Li}_3(-1) = \frac{7}{4}\zeta(3) = c_0, \quad (\text{A.66})$$

so that c_0 is fixed, and we only have to fit:

$$g(z) = (1-z)^{b-1} \left[\frac{7}{4}\zeta(3) + \sum_{k=1}^{10} c_k z^k \right]. \quad (\text{A.67})$$

The Mellin transform of eq. (A.54c) follows immediately:

$$\begin{aligned} A_{24}(N) = \mathbf{M}[f_{24}(z)](N) &= \sum_{k=0}^{10} c_k \int_0^1 z^{N+k-1}(1-z)^{b-1} dz \\ &= \frac{\Gamma(N)\Gamma(b)}{\Gamma(N+b)} \sum_{k=0}^{10} c_k \frac{(N+k)\dots(N+1)N}{(N+b+k)\dots(N+b+1)}. \end{aligned} \quad (\text{A.68})$$

In order to determine the Mellin transform of eq. (A.54d), we use the representation given as eq. (21) of Ref. [146], in which the function $\ln(1+z)$ is approximated by the polynomial:

$$\ln(1+z) \cong \sum_{k=1}^8 d_k z^k. \quad (\text{A.69})$$

Using also Tab. A.1, we then get:

$$\begin{aligned} A_{25}(N) &= \mathbf{M}[f_{25}(z)](N) = \sum_{k=1}^8 d_k \mathbf{M}[z^k \ln(z) \ln(1-z)] \\ &= \sum_{k=1}^8 d_k \left[\frac{S_1(N+k)}{(N+k)^2} + \frac{S_2(N+k) - \zeta(2)}{N+k} \right]. \end{aligned} \quad (\text{A.70})$$

In order to determine the Mellin transform of eq. (A.54e), we use the expansion:

$$\text{Li}_2(-z) = \sum_{k=1}^{\infty} \frac{(-1)^k z^k}{k^2}, \quad (\text{A.71})$$

so:

$$A_{26}(N) = \mathbf{M}[f_{26}(z)](N) = \sum_{k=1}^{\infty} \frac{(-1)^k}{k^2} \mathbf{M}[z^k \ln(1-z)] = \sum_{k=1}^{\infty} \frac{(-1)^{k+1}}{k^2} \frac{S_1(N+k)}{N+k}. \quad (\text{A.72})$$

In this case we have chosen to truncate the series at $k = 100$.

Finally, we determine the Mellin transform of eq. (A.54f). In this case we use the geometric series for $1/(1-z)$ so that:

$$A_{33}(N) \mathbf{M}[f_{33}(z)](N) = \sum_{k=0}^{\infty} \mathbf{M}[z^k \text{Li}_2(1-z)] = - \sum_{k=0}^{\infty} \frac{S_2(N+k) - \zeta(2)}{N+k}. \quad (\text{A.73})$$

Also in this case, the series has been truncated at $k = 100$.

Note that the Mellin transform of the x -space coefficient functions involve terms of the form $z^l f_n(z)$. The Mellin transform $\mathbf{M}[z^l f_n(z)](N)$ can be obtained from $\mathbf{M}[f_n(z)](N)$ using the identity $\mathbf{M}[z^l f_n(z)](N) = \mathbf{M}[f_n(z)](N+l)$. Thus the Mellin transform of any of the terms in Tabs. A.1 and A.2 and also any of the terms eqs.(A.54a)-(A.54f) multiplied by a factor z^l can be obtained replacing N with $N+l$.

In conclusion, we have checked our calculation by comparing the inverse Mellin transform of the N -space coefficients with the exact x -space results. In Fig. A.3 we show the relative accuracy of for $C_{2,g}^{\text{FF0},(2)}$, $C_{L,g}^{\text{FF0},(2)}$, $C_{2,q}^{\text{FF0},(2)}$, $C_{L,q}^{\text{FF0},(2)}$, $C_{L,\text{GR}}^{\text{FF0},(2)}$ and $C_{2,\text{GR}}^{\text{FF0},(2)}$. As evident, the accuracy is always excellent.

A.2 CC Processes

As we already mentioned, exact expressions for the CC coefficient functions are known only up to order α_s . We report here their Mellin transforms as implemented in the NNPDF code.

The procedure followed to evaluate the Mellin transform of the CC coefficient functions is slightly different from that used in the NC case. The essential difference comes from the fact that, for the NC coefficient functions, we have Mellin transformed, not only the coefficient function themselves, but also the θ -function that takes into account the reduction of the available phase space for the final state in the presence of massive particles. This allows to extend the integral between coefficient functions and parton densities over the ‘‘massless’’ kinematic range $[x, 1]$. From the point of view of the implementation of the FONLL method, this provides a simplification because it allows to put the massive structure functions on the same footing of the massless ones. In the CC case, instead, the inclusion of the kinematic θ -function in the coefficient functions makes the analytical computation of the Mellin transforms impossible.

Therefore, in order not to rely on numerical approximations, we have chosen to transform in the Mellin space the CC massive coefficient functions without including the

fore-mentioned θ -function, but limiting the convolution with the parton densities only to the allowed phase space.

Furthermore, the kinematics of the CC processes is different with respect to the NC case. In fact, in the NC heavy quark production, up to order α_s^2 , there are two heavy quarks having mass M_H in the final state and this limits the available phase space to $W^2 \geq 4M_H^2$ which is equivalent to $x \leq (1 + 4M_H^2/Q^2)^{-1}$. In the CC heavy quark production, instead, up to order α_s only one heavy quark is present in the final state. This means that $W^2 \geq M_H^2$, *i.e.* $x \leq (1 + M_H^2/Q^2)^{-1}$.

In the following, without loss of generality, we limit ourselves to the charm structure functions whose general definitions are given in eqs. (3.27) and (3.28). In fact, one has just to use the appropriate formula amongst those given in eqs. (3.27) and (3.28) and, for the bottom and top structure functions, use the respective value for the mass in the coefficient functions.

Using the notation of Ref. [65] the order α_s charm structure functions in the FFNS can be written as:

$$\mathcal{F}_k^c(x, Q^2) = \frac{1}{2} f_{s'}(\xi, \mu^2) + \frac{1}{2} \frac{\alpha_s(\mu^2)}{2\pi} \left\{ \int_{\xi}^1 \frac{dz}{z} \left[C_{k,q}^{\text{FF},(1)} \left(z, \frac{Q^2}{M_c^2}, \frac{\mu^2}{M_c^2} \right) f_{s'} \left(\frac{\xi}{z}, \mu^2 \right) + C_{k,g}^{\text{FF},(1)} \left(z, \frac{Q^2}{M_c^2}, \frac{\mu^2}{M_c^2} \right) f_g \left(\frac{\xi}{z}, \mu^2 \right) \right] \right\}, \quad (\text{A.74})$$

with $k = 1, 2, 3$. In the above expression we have used the following definitions:

$$f_{s'} \equiv 2|V_{cs}|^2 f_s + 2|V_{cd}|^2 f_d$$

$$\xi = x \left(1 + \frac{M_c^2}{Q^2} \right) \quad \text{with} \quad \lambda = \frac{Q^2}{Q^2 + M_c^2}. \quad (\text{A.75})$$

The explicit x -space expressions of the order α_s coefficient functions $C_{k,i}^{\text{FF},(1)}$ are given in Refs. [147, 65]. The standard structure functions are related to those defined in Eq. (A.74) through:

$$F_1^c \equiv \mathcal{F}_1^c, \quad F_2^c \equiv 2\xi \mathcal{F}_2^c, \quad F_3^c \equiv 2\mathcal{F}_3^c. \quad (\text{A.76})$$

Reabsorbing the LO term into the integral, eq. (A.74) can be written as:

$$\mathcal{F}_k^c(x, Q^2) = \int_{\xi}^1 \frac{dz}{z} \left\{ \left[C_{k,q}^{\text{FF},(0)}(z) + a_s C_{k,q}^{\text{FF},(1)} \left(z, \frac{Q^2}{M_c^2}, \frac{\mu^2}{M_c^2} \right) \right] f_{s'} \left(\frac{\xi}{z}, \mu^2 \right) + a_s C_{k,f}^{\text{FF},(1)} \left(z, \frac{Q^2}{M_c^2}, \frac{\mu^2}{M_c^2} \right) f_g \left(\frac{\xi}{z}, \mu^2 \right) \right\} \quad (\text{A.77})$$

where, as usual, $a_s = \alpha_s/4\pi$, from which, comparing to eq. (A.74), we read:

$$C_{k,q}^{\text{FF},(0)}(z) = \frac{1}{2} \delta(1-z), \quad (\text{A.78})$$

whose Mellin transform is trivially:

$$C_{k,q}^{\text{FF},(0)}(N) = \frac{1}{2}. \quad (\text{A.79})$$

Therefore, we have that the order α_s^0 quark coefficient functions in the CC case, differently from the NC case, are different from zero.

Now we turn to the order α_s coefficient functions. Before Mellin-transforming the x -space expressions, we rewrite them in the form:

$$C_{k,q}^{\text{FF},(1)}\left(z, \frac{Q^2}{M_c^2}, \frac{\mu^2}{M_c^2}\right) = K\delta(1-z) + f(z) + [g(z)]_+, \quad (\text{A.80})$$

where K is a constant, $f(z)$ is regular function in $z \in [0, 1]$ and $g(z)$ is instead singular in $z = 1$. This way, setting $\mu = Q$ for simplicity, we get:

$$\begin{aligned} C_{1,q}^{\text{FF},(1)}(z) &= -\frac{4}{3}\left(4 + \frac{1}{2\lambda} + \frac{\pi^2}{3} + \frac{1+3\lambda}{2\lambda}K_A\right)\delta(1-z) \\ &+ \frac{4}{3}\left[-\frac{(1+z^2)\ln z}{1-z} - 2(1+z)\ln(1-z) \right. \\ &\quad \left. + (1+z)\ln(1-\lambda z) + (3-z) + \frac{z-z^2}{1-\lambda z}\right] \\ &+ \frac{4}{3}\left[4\frac{\ln(1-z)}{1-z} - 2\frac{\ln(1-\lambda z)}{1-z} - 2\frac{1}{1-z} \right. \\ &\quad \left. + \frac{1}{2}\frac{1-z}{(1-\lambda z)^2} - \frac{1+z^2}{1-z}\ln\lambda\right]_+, \end{aligned} \quad (\text{A.81})$$

$$\begin{aligned} C_{2,q}^{\text{FF},(1)}(z) &= -\frac{4}{3}\left(4 + \frac{1}{2\lambda} + \frac{\pi^2}{3} + \frac{1+\lambda}{2\lambda}K_A\right)\delta(1-z) \\ &+ \frac{4}{3}\left[-\frac{(1+z^2)\ln z}{1-z} - 2(1+z)\ln(1-z) \right. \\ &\quad \left. + (1+z)\ln(1-\lambda z) + \left(2z + 2 - \frac{2}{z}\right) + \frac{\frac{2}{z} - 1 - z}{1-\lambda z}\right] \\ &+ \frac{4}{3}\left[4\frac{\ln(1-z)}{1-z} - 2\frac{\ln(1-\lambda z)}{1-z} - 2\frac{1}{1-z} \right. \\ &\quad \left. + \frac{1}{2}\frac{1-z}{(1-\lambda z)^2} - \frac{1+z^2}{1-z}\ln\lambda\right]_+, \end{aligned} \quad (\text{A.82})$$

$$\begin{aligned}
C_{3,q}^{\text{FF},(1)}(z) &= -\frac{4}{3} \left(4 + \frac{1}{2\lambda} + \frac{\pi^2}{3} + \frac{1+3\lambda}{2\lambda} K_A \right) \delta(1-z) \\
&+ \frac{4}{3} \left[-\frac{(1+z^2) \ln z}{1-z} - 2(1+z) \ln(1-z) \right. \\
&\quad \left. + (1+z) \ln(1-\lambda z) + (1+z) + \frac{1-z}{1-\lambda z} \right] \\
&+ \frac{4}{3} \left[4 \frac{\ln(1-z)}{1-z} - 2 \frac{\ln(1-\lambda z)}{1-z} - 2 \frac{1}{1-z} \right. \\
&\quad \left. + \frac{1}{2} \frac{1-z}{(1-\lambda z)^2} - \frac{1+z^2}{1-z} \ln \lambda \right]_+,
\end{aligned} \tag{A.83}$$

with $K_A = (1-\lambda) \ln(1-\lambda)/\lambda$. The gluon coefficient functions, instead, do not need any further work and are given by:

$$\begin{aligned}
C_{1,g}^{\text{FF},(1)}(z) &= \frac{1}{2} (2z^2 - 2z + 1) \{ 2 \ln(1-z) - 2 \ln z - \ln[\lambda(1-\lambda)] \} \\
&+ [4 - 4(1-\lambda)] z(1-z) + (1-\lambda) \frac{z}{1-\lambda z} \\
&+ 2(1-\lambda) \left[z \ln \frac{1-\lambda z}{(1-\lambda)z} - 2\lambda z^2 \ln \frac{1-\lambda z}{(1-\lambda)z} \right] - 1,
\end{aligned} \tag{A.84}$$

$$\begin{aligned}
C_{2,g}^{\text{FF},(1)}(z) &= \frac{1}{2} (2z^2 - 2z + 1) \{ 2 \ln(1-z) - 2 \ln z - \ln[\lambda(1-\lambda)] \} \\
&+ [8 - 18(1-\lambda) + 12(1-\lambda)^2] z(1-z) + (1-\lambda) \frac{1}{1-\lambda z} \\
&+ 6\lambda(1-\lambda) \left[z \ln \frac{1-\lambda z}{(1-\lambda)z} - 2\lambda z^2 \ln \frac{1-\lambda z}{(1-\lambda)z} \right] - 1,
\end{aligned} \tag{A.85}$$

$$\begin{aligned}
C_{3,g}^{\text{FF},(1)}(z) &= \frac{1}{2} (2z^2 - 2z + 1) \left\{ 2 \ln(1-z) - 2 \ln(1-\lambda z) + \ln \left(\frac{1-\lambda}{\lambda} \right) \right\} \\
&+ 2(1-\lambda) z(1-z) + 2(1-\lambda) \left[(1+\lambda) z^2 \ln \frac{1-\lambda z}{(1-\lambda)z} - z \ln \frac{1-\lambda z}{(1-\lambda)z} \right].
\end{aligned} \tag{A.86}$$

In order to transform to the N -space the above x -space expressions, in Tabs. A.3 and A.4 we have tabulated the Mellin transforms of all terms involved. Naming them B_n , with $n = 1, \dots, 22$, these expressions take the very compact form:

$$\begin{aligned}
C_{1,q}^{\text{FF},(1)}(N) &= -\frac{4}{3} \left(4 + \frac{1}{2\lambda} + \frac{\pi^2}{3} + \frac{1+3\lambda}{2\lambda} K_A \right) \\
&+ \frac{4}{3} [-B_1 - 2B_3 + B_9 + B_{10}] \\
&+ \frac{4}{3} [4B_4 - 2B_5 - 2B_6 + \frac{1}{2}B_7 - B_8 \ln \lambda] .,
\end{aligned} \tag{A.87}$$

$$\begin{aligned}
C_{2,q}^{\text{FF},(1)}(N) &= -\frac{4}{3} \left(4 + \frac{1}{2\lambda} + \frac{\pi^2}{3} + \frac{1+\lambda}{2\lambda} K_A \right) \\
&+ \frac{4}{3} [-B_1 - 2B_2 + B_3 + B_{11} + B_{12}] \\
&+ \frac{4}{3} [4B_4 - 2B_5 - 2B_6 + \frac{1}{2}B_7 - B_8 \ln \lambda] ,
\end{aligned} \tag{A.88}$$

$$\begin{aligned}
C_{3,q}^{\text{FF},(1)}(N) &= -\frac{4}{3} \left(4 + \frac{1}{2\lambda} + \frac{\pi^2}{3} + \frac{1+3\lambda}{2\lambda} K_A \right) \\
&+ \frac{4}{3} [-B_1 - 2B_2 + B_3 + B_{13} + B_{14}] \\
&+ \frac{4}{3} [4B_4 - 2B_5 - 2B_6 + \frac{1}{2}B_7 - B_8 \ln \lambda] ,
\end{aligned} \tag{A.89}$$

$$\begin{aligned}
C_{1,g}^{\text{FF},(1)}(N) &= \frac{1}{2}B_{18} + [4 - 4(1-\lambda)]B_{15} + (1-\lambda)B_{19} \\
&+ 2(1-\lambda)[B_{16} - 2\lambda B_{17}] - B_{20} ,
\end{aligned} \tag{A.90}$$

$$\begin{aligned}
C_{2,g}^{\text{FF},(1)}(N) &= \frac{1}{2}B_{18} + [8 - 18(1-\lambda) + 12(1-\lambda)^2]B_{15} \\
&+ (1-\lambda)B_{21} + 6\lambda(1-\lambda)[B_{16} - 2\lambda B_{17}] - B_{20} ,
\end{aligned} \tag{A.91}$$

$$\begin{aligned}
C_{3,g}^{\text{FF},(1)}(N) &= \frac{1}{2}B_{22} + 2(1-\lambda)B_{15} \\
&+ 2(1-\lambda)[(1+\lambda)B_{17} - B_{16}] .
\end{aligned} \tag{A.92}$$

It is interesting to show how the Mellin transform B_5 has been obtained. In fact, given that we could not find close analytical expression for the Mellin transform of the respective x -space expressions, we can only evaluate it in an approximate way.

We have to evaluate the following integral:

$$B_5 = \mathbf{M} \left[\left[\frac{\ln(1-\lambda z)}{1-z} \right]_+ \right] = \int_0^1 (z^{N-1} - 1) \frac{\ln(1-\lambda z)}{1-z} . \tag{A.93}$$

To this end, let us show how one can evaluate the generic Mellin transform:

$$I_q(N) = \mathbf{M} \left[z^q \left[\frac{\ln(1-\lambda z)}{1-z} \right]_+ \right] = \int_0^1 \frac{z^{N+q-1} - 1}{1-z} \ln(1-\lambda z) , \tag{A.94}$$

where q is an integer.

At first, we assume that N is a positive integer number. Under this hypothesis we can use the geometric series:

$$\frac{z^{N+q-1} - 1}{1-z} = - \sum_{n=0}^{N+q-2} z^n . \tag{A.95}$$

Moreover, we expand the logarithmic function around $\lambda z = 0$, so that we get:

$$\ln(1-\lambda z) = - \sum_{k=1}^{\infty} \frac{\lambda^k z^k}{k} . \tag{A.96}$$

Altogether, we have:

$$\begin{aligned}
I_q(N) &= \sum_{k=1}^{\infty} \frac{\lambda^k}{k} \sum_{n=0}^{N+q-2} \int_0^1 z^{k+n} dz = \sum_{k=1}^{\infty} \frac{\lambda^k}{k} \sum_{n=0}^{N+q-2} \frac{1}{n+k+1} = \\
&\sum_{k=1}^{\infty} \frac{\lambda^k}{k} \sum_{l=k+1}^{N+q+k-1} \frac{1}{l} = \sum_{k=1}^{\infty} \frac{\lambda^k}{k} \left[\underbrace{\sum_{l=1}^{N+q+k-1} \frac{1}{l}}_{S_1(N+q+k-1)} - \underbrace{\sum_{l=1}^k \frac{1}{l}}_{S_1(k)} \right] .
\end{aligned} \tag{A.97}$$

Therefore:

$$B_5 = I_0(N) = \sum_{k=1}^{\infty} \frac{\lambda^k}{k} [S_1(N+k-1) - S_1(k)], \quad (\text{A.98})$$

but since:

$$S_1(N+k-1) = S_1(N+k) - \frac{1}{N+k}, \quad (\text{A.99})$$

at the end of the day we have:

$$B_5 = \sum_{k=1}^{\infty} \frac{\lambda^k}{k} \left[S_1(N+k) - S_1(k) - \frac{1}{N+k} \right]. \quad (\text{A.100})$$

One may notice that there is a certain overlap between the Mellin transforms presented in Tabs. A.1 and A.2 and those presented in Tabs. A.3 and A.4. The point is that they are transforms belonging to two different implementation procedures, namely the order α_s^2 zero-mass limit of the NC massive coefficient functions and the order α_s CC coefficient functions, therefore for completeness we prefer to report both of them separately.

Finally, to check our calculations we compared the Mellin inverse of the order α_s N -space CC coefficient functions to the exact x -expressions given in Ref. [65]. The plots for the relative accuracies are given in Fig. A.4. One more time we have an excellent agreement.

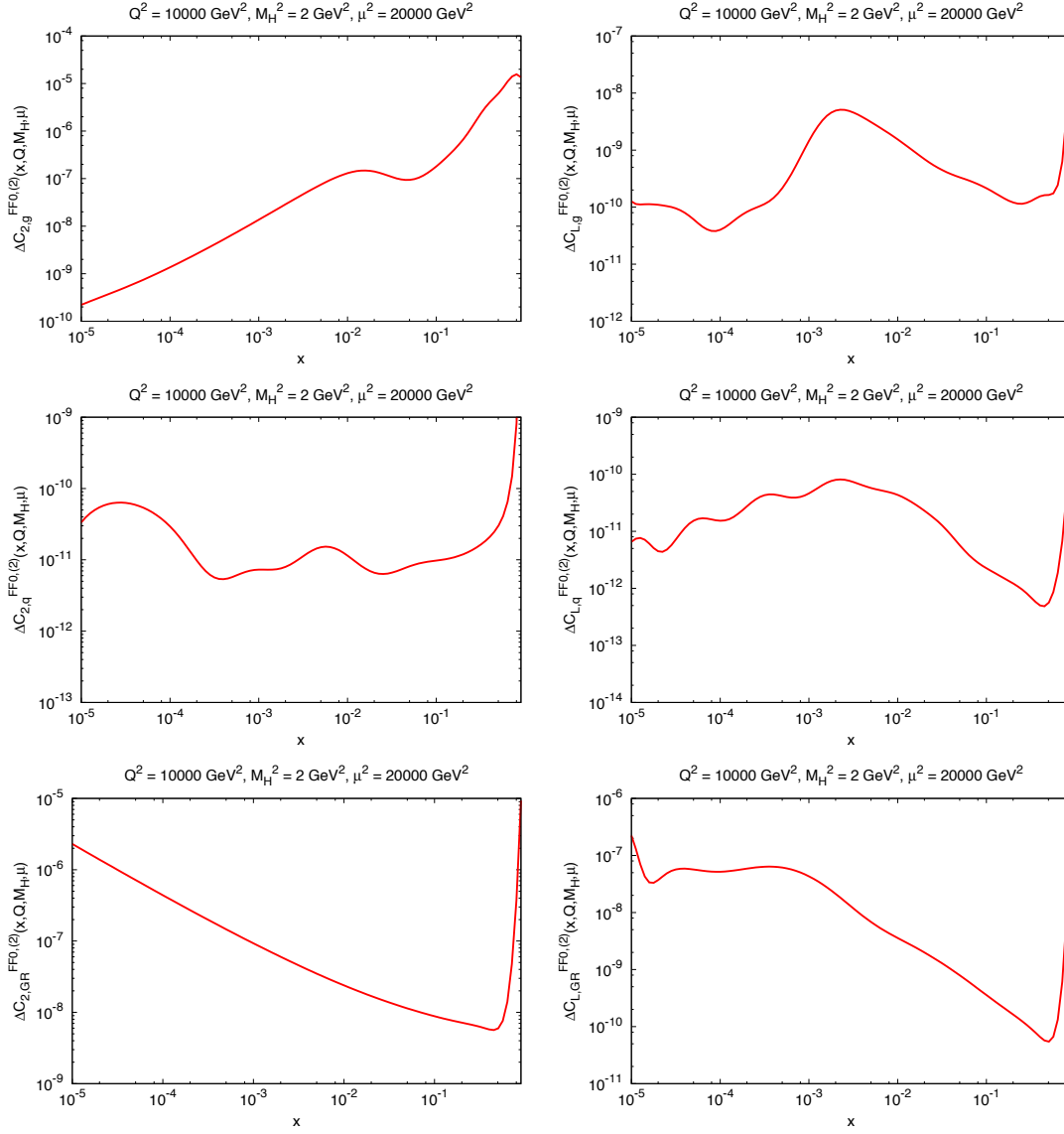


Figure A.3: Relative accuracy for the numerical Mellin inverse of the NC coefficient functions $C_{2,g}^{\text{FF0,(2)}}$, $C_{L,g}^{\text{FF0,(2)}}$, $C_{2,q}^{\text{FF0,(2)}}$, $C_{L,q}^{\text{FF0,(2)}}$, $C_{2,\text{GR}}^{\text{FF0,(2)}}$ and $C_{L,\text{GR}}^{\text{FF0,(2)}}$ of the parametrization given in Ref. [75] with respect to exact x -space expression of Ref. [64].

n	$g_n(z)$	$B_n = \mathbf{M}[g_n(z)](N)$
1	$\frac{(1+z^2)\ln z}{1-z}$	$2(S_2 - \zeta_2) - \frac{1}{N^2} + \frac{1}{(N+1)^2}$
2	$(1+z)\ln(1-z)$	$-\frac{S_1}{N} - \frac{S_1}{N+1} - \frac{1}{(N+1)^2}$
3	$(1+z)\ln(1-\lambda z)$	$\lambda \frac{{}_2F_1(1, N+1, N+2; \lambda)}{N(N+1)} + \frac{\ln(1-\lambda)}{N} +$ $\lambda \frac{{}_2F_1(1, N+2, N+3; \lambda)}{(N+1)(N+2)} + \frac{\ln(1-\lambda)}{N+1}$
4	$\left[\frac{\ln(1-z)}{1-z} \right]_+$	$\frac{1}{2} \left(S_1^2 + S_2 - 2\frac{S_1}{N} \right)$
5	$\left[\frac{\ln(1-\lambda z)}{1-z} \right]_+$	$J_\lambda(N) = \sum_{k=1}^{\infty} \frac{\lambda^k}{k} \left[S_1(N+k) - S_1(k) - \frac{1}{N+k} \right]$
6	$\left[\frac{1}{1-z} \right]_+$	$\frac{1}{N} - S_1$
7	$\left[\frac{1-z}{(1-\lambda z)^2} \right]_+$	$\frac{{}_2F_1(2, N, N+2, \lambda)}{N(N+1)} + \frac{\lambda + \ln(1-\lambda)}{\lambda^2}$
8	$\left[\frac{1+z^2}{1-z} \right]_+$	$\frac{1}{N} - \frac{1}{N+1} - 2S_1 + \frac{3}{2}$
9	$3-z$	$\frac{3}{N} - \frac{1}{N+1}$
10	$\frac{z-z^2}{1-\lambda z}$	$\frac{{}_2F_1(1, N+1, N+2, \lambda)}{N+1} - \frac{{}_2F_1(1, N+2, N+3, \lambda)}{N+2}$
11	$2z+2-\frac{2}{z}$	$\frac{2}{N+1} + \frac{2}{N} - \frac{2}{N-1}$
12	$\frac{\frac{2}{z}-1-z}{1-\lambda z}$	$\frac{{}_2F_1(1, N-1, N, \lambda)}{N-1} - \frac{{}_2F_1(1, N, N+1, \lambda)}{N}$ $- \frac{{}_2F_1(1, N+1, N+2, \lambda)}{N+1}$
13	$1+z$	$\frac{1}{N} + \frac{1}{N+1}$
14	$\frac{1-z}{1-\lambda z}$	$\frac{{}_2F_1(1, N, N+1, \lambda)}{N} - \frac{{}_2F_1(1, N+1, N+2, \lambda)}{N+1}$

Table A.3: Elementary transforms used for the computation of the Mellin transform of the order α_S CC FFNS coefficient functions.

n	$g_n(z)$	$B_n = \mathbf{M}[g_n(z)](N)$
15	$z(1-z)$	$\frac{1}{N+1} - \frac{1}{N+2}$
16	$z \ln \frac{1-\lambda z}{(1-\lambda)z}$	$\frac{{}_2F_1(1, N+1, N+2; \lambda)}{(N+1)^2}$
17	$z^2 \ln \frac{1-\lambda z}{(1-\lambda)z}$	$\frac{{}_2F_1(1, N+1, N+2; \lambda) - 1}{\lambda(N+1)(N+2)}$
18	$[z^2 + (1-z)^2] \times$ $\left\{ 2 \ln \left(\frac{1-z}{z} \right) - \ln[\lambda(1-\lambda)] \right\}$	$\frac{4 - 2N(N-3) - N(N^2 + N + 2)\{2S_1 + \ln[\lambda(1-\lambda)]\}}{N^2(N+1)(N+2)}$
19	$\frac{z}{1-\lambda z}$	$\frac{{}_2F_1(1, N+1, N+2; \lambda)}{N+1}$
20	1	$\frac{1}{N}$
21	$\frac{1}{1-\lambda z}$	$\frac{{}_2F_1(1, N, N+1; \lambda)}{N}$
22	$[z^2 + (1-z)^2] \times$ $\left\{ 2 \ln \left(\frac{1-z}{1-\lambda z} \right) + \ln \left(\frac{1-\lambda}{\lambda} \right) \right\}$	$-\frac{2}{\lambda} \left(\frac{\lambda^2}{N} - \frac{2\lambda}{N+1} + \frac{2}{N+2} \right) \frac{{}_2F_1(1, N+1, N+2, \lambda)}{N+1}$ $-\frac{4(\lambda-1)}{\lambda(N+1)(N+2)} - \frac{(N^2 + N + 2)\{2S_1 - \ln(\frac{1-\lambda}{\lambda})\}}{N(N+1)(N+2)}$

Table A.4: Continuation of Tab. A.3.

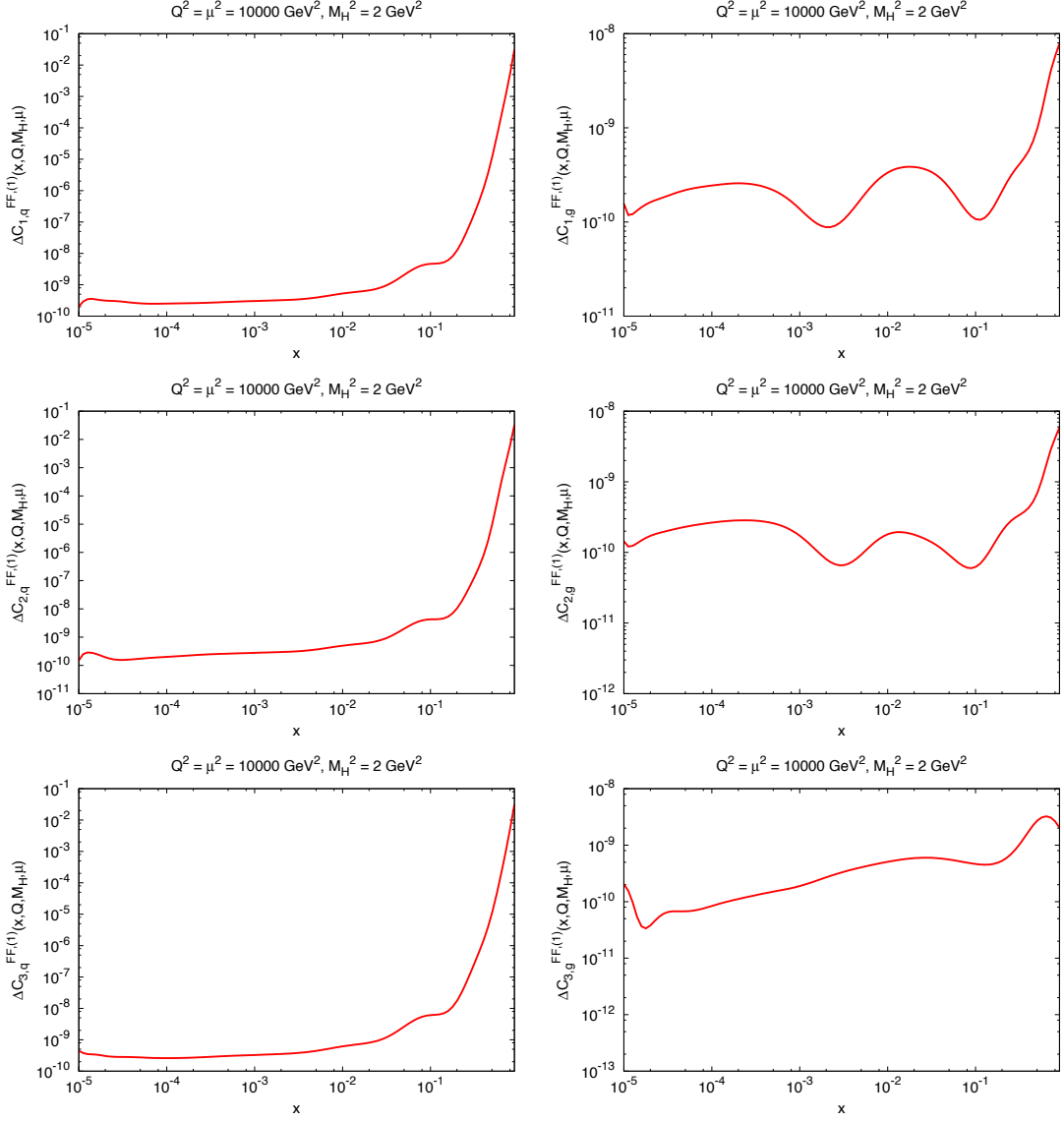


Figure A.4: Relative accuracy of the numerical Mellin inverse of the CC coefficient functions $C_{1,q}^{\text{FF},(1)}$, $C_{1,g}^{\text{FF},(1)}$, $C_{2,q}^{\text{FF},(1)}$, $C_{2,g}^{\text{FF},(1)}$, $C_{3,q}^{\text{FF},(1)}$ and $C_{3,g}^{\text{FF},(1)}$ of our results with respect to exact x -space expression of Ref. [65].

Appendix B

Mellin Transform of the $\overline{\text{MS}}$ Coefficient Functions

In this appendix we collect all the explicit analytical results for the Mellin transforms of the correction terms arising when the heavy quark structure functions are expressed in terms of the $\overline{\text{MS}}$ mass m rather than the pole mass M as discussed in Chapter 4. The NC and the CC cases will be treated separately.

B.1 Neutral Current

In this Section the Mellin transform of the correction term to the gluon massive coefficient function in eq. (4.48) for both F_2 and F_L will be given. In addition, the respective zero mass limit will be evaluated.

B.1.1 F_2

We consider first F_2 . The starting point is the Mellin transform of the gluon massive coefficient function $C_{2,g}^{\text{FF},(1)}$ given in eq. (A.21) of Appendix A. From the definitions given in eq. (A.2), it follows that:

$$\begin{aligned}\frac{\partial}{\partial M} &= \frac{\partial \epsilon}{\partial M} \frac{\partial}{\partial \epsilon} = \frac{2\epsilon}{M} \frac{\partial}{\partial \epsilon}, \\ \frac{\partial}{\partial M} &= \frac{\partial \epsilon}{\partial M} \frac{\partial a}{\partial \epsilon} \frac{\partial}{\partial a} = -\frac{8a^2\epsilon}{M} \frac{\partial}{\partial a}.\end{aligned}\tag{B.1}$$

Therefore:

$$\begin{aligned}
\frac{\partial C_{2,g}^{\text{FF},(1)}}{\partial M} &= T_R \left\{ \frac{2\epsilon}{M} \left[2(-6 - 8\epsilon)I_2 + 4I_1 + 4J_2 - 4J_1 \right] \right. \\
&\quad - \frac{8a^2\epsilon}{M} \left[2(1 - 6\epsilon - 4\epsilon^2) \frac{\partial I_2}{\partial a} - 2(1 - 2\epsilon) \frac{\partial I_1}{\partial a} + \frac{\partial I_0}{\partial a} \right. \\
&\quad \left. \left. - 4(2 - \epsilon) \frac{\partial J_2}{\partial a} + 4(2 - \epsilon) \frac{\partial J_1}{\partial a} - \frac{\partial J_0}{\partial a} \right] \right\}. \tag{B.2}
\end{aligned}$$

Now, starting from eqs. (A.13) and (A.19), the derivative of the functions I_q and J_q can be evaluated using the relation valid for the derivative of the hypergeometric function:

$$\frac{\partial}{\partial x} {}_2F_1(a, b, c; x) = \frac{b}{x} [{}_2F_1(a, b + 1, c; x) - {}_2F_1(a, b, c; x)], \tag{B.3}$$

so that:

$$\begin{aligned}
&\frac{d}{da} a^{N+q} {}_2F_1\left(\frac{1}{2}, N+q, N+q+\frac{1}{2}; a\right) \\
&= a^{N+q-1} (N+q) {}_2F_1\left(\frac{1}{2}, N+q+1, N+q+\frac{1}{2}; a\right), \\
&\frac{d}{da} a^{N+q} {}_2F_1\left(\frac{1}{2}, N+q+1, N+q+\frac{3}{2}; a\right) \\
&= a^{N+q-1} (N+q+1) {}_2F_1\left(\frac{1}{2}, N+q+2, N+q+\frac{3}{2}; a\right) \\
&\quad - a^{N+q-1} {}_2F_1\left(\frac{1}{2}, N+q+1, N+q+\frac{3}{2}; a\right), \tag{B.4}
\end{aligned}$$

and:

$$\begin{aligned}
\frac{\partial I_q}{\partial a} &= a^{N+q-1} \frac{\Gamma(N+q)\Gamma(\frac{1}{2})}{\Gamma(N+q+\frac{1}{2})} {}_2F_1\left(\frac{1}{2}, N+q+1, N+q+\frac{1}{2}; a\right), \\
\frac{\partial J_q}{\partial a} &= a^{N+q-1} \frac{\Gamma(N+q+1)\Gamma(\frac{1}{2})}{\Gamma(N+q+\frac{1}{2})} \left\{ {}_2F_1\left(\frac{1}{2}, N+q+1, N+q+\frac{1}{2}; a\right) \right. \\
&\quad - \frac{N+q+1}{N+q+\frac{1}{2}} {}_2F_1\left(\frac{1}{2}, N+q+2, N+q+\frac{3}{2}; a\right) \\
&\quad \left. + \frac{1}{N+q+\frac{1}{2}} {}_2F_1\left(\frac{1}{2}, N+q+1, N+q+\frac{3}{2}; a\right) \right\}. \tag{B.5}
\end{aligned}$$

Looking at these expressions, one can see that in these derivatives, a part from hypergeometric functions of the form ${}_2F_1(a, b, a+b; x)$ which were already present in

$C_{2,g}^{\text{FF},(1)}$ itself, also hypergeometric functions of the form ${}_2F_1(a, b, a + b - 1; x)$ appear. The implementation of the Gauss hypergeometric function discussed in Appendix A can be extended to the case $c = a + b - 1$ using the expansion around $x = 1$ reported in eq. (15.3.12) of Ref. [143].

The Mellin transform of the zero mass limit $C_{2,g}^{\text{FF}0,(1)}$ of $C_{2,g}^{\text{FF},(1)}$ is given in eq. (A.31). Here, considering that:

$$\frac{\partial}{\partial M} \ln \frac{Q^2}{M^2} = -\frac{2}{M}, \quad (\text{B.6})$$

the derivative of $C_{2,g}^{\text{FF}0,(1)}$ is given by:

$$\frac{\partial C_{2,g}^{\text{FF}0,(1)}}{\partial M} = -T_R \frac{2}{M} \left[\frac{2}{N+2} - \frac{2}{N+1} + \frac{1}{N} \right]. \quad (\text{B.7})$$

B.1.2 F_L

Now we turn to F_L . In this case the Mellin transform of the gluon massive coefficient function $C_{L,g}^{\text{FF},(1)}$ takes the simpler form given in eq. (A.23). Therefore, using eq. (B.1), one gets:

$$\frac{\partial C_{L,g}^{\text{FF},(1)}}{\partial M} = T_R \left\{ -\frac{16\epsilon}{M} I_2 - \frac{8a^2\epsilon}{M} \left[-8\epsilon \frac{\partial I_2}{\partial a} - 4 \frac{\partial J_2}{\partial a} + 4 \frac{\partial J_1}{\partial a} \right] \right\}, \quad (\text{B.8})$$

where the derivatives of I_q and J_q with respect of a are given in eq. (B.5).

The zero mass limit $C_{L,g}^{\text{FF}0,(1)}$, given in eq. (A.35), turns out to be independent from M . This directly means that:

$$\frac{\partial C_{L,g}^{0,(0)}}{\partial M} = 0. \quad (\text{B.9})$$

B.2 Charged Current

As discussed in Sec. A.2, the LO order contribution to the heavy (charm) massive CC structure functions can be written as:

$$F_k^{(0)}(M) = b_k(M) f_{s'}(\xi(M)), \quad (\text{B.10})$$

where:

$$\xi = x \underbrace{\left(1 + \frac{M^2}{Q^2} \right)}_{\frac{1}{\lambda}} = \frac{x}{\lambda} \quad \text{and} \quad \begin{cases} b_1 = \frac{1}{2} \\ b_2 = \xi \\ b_3 = 1 \end{cases} \quad (\text{B.11})$$

and where, for a proton target, one has:

$$f_{s'} \equiv 2|V_{cs}|^2 f_s + 2|V_{cd}|^2 f_d. \quad (\text{B.12})$$

Therefore the derivative in the r.h.s. of eq. (4.51) can be explicitly written as:

$$\begin{aligned} mh^{(1)} \frac{dF_k^{(0)}}{dM} \Big|_{M=m} &= mh^{(1)} \frac{d\xi}{dM} \frac{dF_k^{(0)}}{d\xi} \Big|_{M=m} \\ &= 2h^{(1)}(1-\lambda)\xi \left[\frac{db_k}{d\xi} f_{s'}(\xi) + b_k(\xi) \frac{df_{s'}}{d\xi} \right] \Big|_{M=m}. \end{aligned} \quad (\text{B.13})$$

Eq. (B.13) involves the derivative of the parton density $f_{s'}$ and this makes the implementation a little bit more troublesome. In fact, the functional form of $f_{s'}$ is in general unknown and thus an analytical derivative is impossible to evaluate.

Using the same arguments of eq. (4.44), one can show that:

$$\frac{df_{s'}}{d\xi} = \frac{d}{d\xi} \int_{\xi}^1 \frac{dy}{y} \delta(1-y) f_{s'} \left(\frac{\xi}{y} \right) = \int_{\xi}^1 \frac{dy}{y} \delta(1-y) \frac{d}{d\xi} f_{s'} \left(\frac{\xi}{y} \right). \quad (\text{B.14})$$

Therefore eq. (B.13) can be written as:

$$mh^{(1)} \frac{dF_k^{(0)}}{dM} \Big|_{M=m} = 2h^{(1)}(1-\lambda)\xi \int_{\xi}^1 \frac{dy}{y} \delta(1-y) \left[\frac{db_k}{d\xi} + b_k(\xi) \frac{d}{d\xi} \right] f_{s'} \left(\frac{\xi}{y} \right), \quad (\text{B.15})$$

where in the r.h.s. of eq. (B.15) we are assuming that the pole mass M , which appears only through ξ , has been replaced everywhere by the $\overline{\text{MS}}$ mass m . But since:

$$\frac{d}{dx} f \left(\frac{x}{y} \right) = \frac{1}{y} \frac{d}{d \left(\frac{x}{y} \right)} f \left(\frac{x}{y} \right) = \frac{1}{xy} \frac{d}{d \left(\frac{1}{y} \right)} f \left(\frac{x}{y} \right) \quad (\text{B.16})$$

and:

$$d \left(\frac{1}{y} \right) = -\frac{1}{y^2} dy \quad \Rightarrow \quad \frac{d}{dx} f \left(\frac{x}{y} \right) = -\frac{y}{x} \frac{d}{dy} f \left(\frac{x}{y} \right), \quad (\text{B.17})$$

it follows that:

$$\int_{\xi}^1 \frac{dy}{y} \delta(1-y) \frac{d}{d\xi} f_{s'} \left(\frac{\xi}{y} \right) = - \int_{\xi}^1 \frac{dy}{\xi} \delta(1-y) \frac{d}{dy} f_{s'} \left(\frac{\xi}{y} \right). \quad (\text{B.18})$$

Now, integrating by parts the r.h.s. of the equation above, one gets:

$$\int_{\xi}^1 \frac{dy}{y} \delta(1-y) \frac{d}{d\xi} f_{s'} \left(\frac{\xi}{y} \right) = \int_{\xi}^1 \frac{dy}{y} \left\{ \frac{y}{\xi} \left[\frac{d}{dy} \delta(1-y) \right] \right\} f_{s'} \left(\frac{\xi}{y} \right). \quad (\text{B.19})$$

Therefore eq. (B.15) can be rewritten as:

$$mh^{(1)} \frac{dF_k^{(0)}}{dM} \Big|_{M=m} = 2h^{(1)}(1-\lambda)\xi \int_{\xi}^1 \frac{dy}{y} \left\{ \frac{db_k}{d\xi} \delta(1-y) + \frac{b_k(\xi)}{\xi} \left[y \frac{d}{dy} \delta(1-y) \right] \right\} f_{s'} \left(\frac{\xi}{y} \right). \quad (\text{B.20})$$

In eq. (B.20) a coefficient function can be isolated and, considering the form of b_k given in eq. (B.11), one has:

$$\begin{aligned}\tilde{C}_{1,q}(y) &= h^{(1)}(1-\lambda) \left\{ \delta(1-y) + \left[y \frac{d}{dy} \delta(1-y) \right] \right\} \\ \tilde{C}_{2,q}(y) &= 2h^{(1)}(1-\lambda) \left\{ \delta(1-y) + \left[y \frac{d}{dy} \delta(1-y) \right] \right\} \\ \tilde{C}_{3,q}(y) &= 2h^{(1)}(1-\lambda) \left[y \frac{d}{dy} \delta(1-y) \right],\end{aligned}\tag{B.21}$$

in such a way that:

$$\begin{aligned}mh^{(1)} \frac{dF_2^{(0)}}{dM} \Big|_{M=m} &= \xi \int_{\xi}^1 \frac{dy}{y} \tilde{C}_{2,q}(y) f_{s'} \left(\frac{\xi}{y} \right) \\ mh^{(1)} \frac{dF_k^{(0)}}{dM} \Big|_{M=m} &= \int_{\xi}^1 \frac{dy}{y} \tilde{C}_{k,q}(y) f_{s'} \left(\frac{\xi}{y} \right),\end{aligned}\tag{B.22}$$

where now $k = 1, 3$ and whose Mellin transforms, taking into account that:

$$\mathbf{M} \left[y \frac{d}{dy} \delta(1-y) \right] (N) = -N,\tag{B.23}$$

can be easily evaluated obtaining:

$$\begin{aligned}\tilde{C}_{1,q}(N) &= \mathbf{M}[\tilde{C}_{1,q}(y)](N) = -h^{(1)}(1-\lambda)N \\ \tilde{C}_{2,q}(N) &= \mathbf{M}[\tilde{C}_{2,q}(y)](N) = 2h^{(1)}(1-\lambda)(1-N) \\ \tilde{C}_{3,q}(N) &= \mathbf{M}[\tilde{C}_{3,q}(y)](N) = -2h^{(1)}(1-\lambda)N.\end{aligned}\tag{B.24}$$

Now, since the non-derivative order α_s contributions in (4.51) take the form:

$$F_2^{(1)}(m) = \xi \int_{\xi}^1 \frac{dy}{y} \left\{ C_{2,q}(y) f_{s'} \left(\frac{\xi}{y} \right) + C_{2,g}(y) f_g \left(\frac{\xi}{y} \right) \right\}\tag{B.25a}$$

$$F_k^{(1)}(m) = \int_{\xi}^1 \frac{dy}{y} \left\{ C_{k,q}(y) f_{s'} \left(\frac{\xi}{y} \right) + C_{k,g}(y) f_g \left(\frac{\xi}{y} \right) \right\},\tag{B.25b}$$

the whole order α_s term in eq. (4.51) can be written as:

$$F_2^{(1)}(m) + mh^{(1)} \frac{dF_2^{(0)}}{dM} \Big|_{M=m} = \xi \int_{\xi}^1 \frac{dy}{y} \left\{ [C_{2,q}(y) + \tilde{C}_{2,q}(y)] f_{s'} \left(\frac{\xi}{y} \right) + C_{2,g}(y) f_g \left(\frac{\xi}{y} \right) \right\}\tag{B.26a}$$

$$F_k^{(1)}(m) + mh^{(1)} \frac{dF_k^{(0)}}{dM} \Big|_{M=m} = \int_{\xi}^1 \frac{dy}{y} \left\{ [C_{k,q}(y) + \tilde{C}_{k,q}(y)] f_{s'} \left(\frac{\xi}{y} \right) + C_{k,g}(y) f_g \left(\frac{\xi}{y} \right) \right\}.\tag{B.26b}$$

It is interesting to observe that in the zero-mass limit, where $\lambda \rightarrow 1$, all the coefficient functions in eq. (B.24) vanish. As a consequence, the zero-mass limit of the CC massive structure functions up to order α_s in terms of the pole mass M or the $\overline{\text{MS}}$ mass m have exactly the same form.

Alternative Calculation

We sketch here an alternative calculation that looks more transparent and confirms the result found in eq. (B.24). We start directly calculating the Mellin transform of the term proportional to the derivative in eq. (B.13), that is, disregarding the overall constant:

$$I_k(N) = \int_0^1 d\xi \xi^{N-1} \left[\xi b_k(\xi) \frac{df_{s'}}{d\xi} \right]. \quad (\text{B.27})$$

But since:

$$\frac{d}{d\xi} \xi^N b_k(\xi) f_{s'}(\xi) = \left[\frac{d}{d\xi} \xi^N b_k(\xi) \right] f_{s'}(\xi) + \xi^N b_k(\xi) \frac{df_{s'}}{d\xi}, \quad (\text{B.28})$$

it follows that:

$$I_k(N) = \underbrace{\xi^N b_k(\xi) f_{s'}(\xi)}_{=0} \Big|_0^1 - \int_0^1 d\xi \left[\frac{d}{d\xi} \xi^N b_k(\xi) \right] f_{s'}(\xi). \quad (\text{B.29})$$

Now, using the definition of $b_k(\xi)$ given in eq. (B.11), we can easily find that:

$$\begin{aligned} I_1(N) &= -\frac{1}{2} N f_{s'}(N) \\ I_2(N) &= -(N+1) f_{s'}(N+1) \\ I_3(N) &= -N f_{s'}(N) \end{aligned} \quad (\text{B.30})$$

If one now calculates the Mellin transform of the remaining part of eq. (B.13), one finds the results given in eq. (B.24).

Bibliography

- [1] K. G. Wilson, “Confinement of quarks,” *Phys. Rev. D*, vol. 10, pp. 2445–2459, Oct 1974.
- [2] Z. Fodor and C. Hoelbling, “Light Hadron Masses from Lattice QCD,” *Rev.Mod.Phys.*, vol. 84, p. 449, 2012.
- [3] D. J. Gross and F. Wilczek, “Asymptotically free gauge theories. i,” *Phys. Rev. D*, vol. 8, pp. 3633–3652, Nov 1973.
- [4] D. Gross and F. Wilczek, “Ultraviolet Behavior of Nonabelian Gauge Theories,” *Phys.Rev.Lett.*, vol. 30, pp. 1343–1346, 1973.
- [5] T. Kinoshita, “Mass singularities of Feynman amplitudes,” *J.Math.Phys.*, vol. 3, pp. 650–677, 1962.
- [6] T. D. Lee and M. Nauenberg, “Degenerate systems and mass singularities,” *Phys. Rev.*, vol. 133, pp. B1549–B1562, Mar 1964.
- [7] J. C. Collins, D. E. Soper, and G. F. Sterman, “Factorization of Hard Processes in QCD,” *Adv.Ser.Direct.High Energy Phys.*, vol. 5, pp. 1–91, 1988.
- [8] R. Feynman, “The behavior of hadron collisions at extreme energies,” *Conf.Proc.*, vol. C690905, pp. 237–258, 1969.
- [9] J. Bjorken and E. A. Paschos, “Inelastic Electron Proton and gamma Proton Scattering, and the Structure of the Nucleon,” *Phys.Rev.*, vol. 185, pp. 1975–1982, 1969.
- [10] J. Callan, Curtis G. and D. J. Gross, “High-energy electroproduction and the constitution of the electric current,” *Phys.Rev.Lett.*, vol. 22, pp. 156–159, 1969.
- [11] H. Fritzsch, M. Gell-Mann, and H. Leutwyler, “Advantages of the Color Octet Gluon Picture,” *Phys.Lett.*, vol. B47, pp. 365–368, 1973.
- [12] J. C. Collins, “Hard scattering factorization with heavy quarks: A General treatment,” *Phys.Rev.*, vol. D58, p. 094002, 1998.
- [13] H. van Dam and M. Veltman, “Massive and massless Yang-Mills and gravitational fields,” *Nucl.Phys.*, vol. B22, pp. 397–411, 1970.

- [14] G. Dissertori, I. Knowles, and M. Schmelling, *QCD and Collider Physics*. Oxford University Press, 2003.
- [15] S. Chekanov *et al.*, “Measurement of the neutral current cross section and F_2 structure function for deep inelastic e^+p scattering at HERA,” *Eur. Phys. J.*, vol. C21, pp. 443–471, 2001.
- [16] G. Altarelli and G. Parisi, “Asymptotic Freedom in Parton Language,” *Nucl.Phys.*, vol. B126, p. 298, 1977.
- [17] V. Gribov and L. Lipatov, “Deep inelastic $e p$ scattering in perturbation theory,” *Sov.J.Nucl.Phys.*, vol. 15, pp. 438–450, 1972.
- [18] Y. L. Dokshitzer, “Calculation of the Structure Functions for Deep Inelastic Scattering and $e^+ e^-$ Annihilation by Perturbation Theory in Quantum Chromodynamics,” *Sov.Phys.JETP*, vol. 46, pp. 641–653, 1977.
- [19] G. Curci, W. Furmanski, and R. Petronzio, “Evolution of Parton Densities Beyond Leading Order: The Nonsinglet Case,” *Nucl.Phys.*, vol. B175, p. 27, 1980.
- [20] W. Furmanski and R. Petronzio, “Singlet Parton Densities Beyond Leading Order,” *Phys.Lett.*, vol. B97, p. 437, 1980.
- [21] S. Moch, J. Vermaseren, and A. Vogt, “The Three loop splitting functions in QCD: The Nonsinglet case,” *Nucl.Phys.*, vol. B688, pp. 101–134, 2004.
- [22] A. Vogt, S. Moch, and J. Vermaseren, “The Three-loop splitting functions in QCD: The Singlet case,” *Nucl.Phys.*, vol. B691, pp. 129–181, 2004.
- [23] S. Alekhin, J. Blumlein, and S. Moch, “Parton Distribution Functions and Benchmark Cross Sections at NNLO,” *Phys.Rev.*, vol. D86, p. 054009, 2012.
- [24] J. Gao, M. Guzzi, J. Huston, H.-L. Lai, Z. Li, *et al.*, “The CT10 NNLO Global Analysis of QCD,” 2013.
- [25] P. Jimenez-Delgado and E. Reya, “Variable Flavor Number Parton Distributions and Weak Gauge and Higgs Boson Production at Hadron Colliders at NNLO of QCD,” *Phys.Rev.*, vol. D80, p. 114011, 2009.
- [26] A. Cooper-Sarkar, “PDF Fits at HERA,” *PoS*, vol. EPS-HEP2011, p. 320, 2011.
- [27] V. Radescu, “Parton distributions from HERA,” *AIP Conf.Proc.*, vol. 1369, pp. 37–42, 2011.
- [28] A. Martin, W. Stirling, R. Thorne, and G. Watt, “Parton distributions for the LHC,” *Eur.Phys.J.*, vol. C63, pp. 189–285, 2009.
- [29] R. D. Ball, V. Bertone, S. Carrazza, C. S. Deans, L. Del Debbio, *et al.*, “Parton distributions with LHC data,” *Nucl.Phys.*, vol. B867, pp. 244–289, 2013.
- [30] W. Tung, H. Lai, A. Belyaev, J. Pumplin, D. Stump, *et al.*, “Heavy Quark Mass Effects in Deep Inelastic Scattering and Global QCD Analysis,” *JHEP*, vol. 0702, p. 053, 2007.

- [31] M. Aivazis, J. C. Collins, F. I. Olness, and W.-K. Tung, “Leptoproduction of heavy quarks. 2. A Unified QCD formulation of charged and neutral current processes from fixed target to collider energies,” *Phys.Rev.*, vol. D50, pp. 3102–3118, 1994.
- [32] J. C. Collins, F. Wilczek, and A. Zee, “Low-Energy Manifestations of Heavy Particles: Application to the Neutral Current,” *Phys.Rev.*, vol. D18, p. 242, 1978.
- [33] M. Kramer, F. I. Olness, and D. E. Soper, “Treatment of heavy quarks in deeply inelastic scattering,” *Phys.Rev.*, vol. D62, p. 096007, 2000.
- [34] W.-K. Tung, S. Kretzer, and C. Schmidt, “Open heavy flavor production in QCD: Conceptual framework and implementation issues,” *J.Phys.*, vol. G28, pp. 983–996, 2002.
- [35] S. Kretzer, H. Lai, F. Olness, and W. Tung, “Cteq6 parton distributions with heavy quark mass effects,” *Phys.Rev.*, vol. D69, p. 114005, 2004.
- [36] A. Martin, W. Stirling, R. Thorne, and G. Watt, “Update of parton distributions at NNLO,” *Phys.Lett.*, vol. B652, pp. 292–299, 2007.
- [37] R. Thorne and R. Roberts, “An Ordered analysis of heavy flavor production in deep inelastic scattering,” *Phys.Rev.*, vol. D57, pp. 6871–6898, 1998.
- [38] R. Thorne and R. Roberts, “A Practical procedure for evolving heavy flavor structure functions,” *Phys.Lett.*, vol. B421, pp. 303–311, 1998.
- [39] A. D. Martin, R. Roberts, W. J. Stirling, and R. Thorne, “Parton distributions: A New global analysis,” *Eur.Phys.J.*, vol. C4, pp. 463–496, 1998.
- [40] A. D. Martin, R. Roberts, W. Stirling, and R. Thorne, “MRST2001: Partons and α_s from precise deep inelastic scattering and Tevatron jet data,” *Eur.Phys.J.*, vol. C23, pp. 73–87, 2002.
- [41] A. Martin, R. Roberts, W. Stirling, and R. Thorne, “Uncertainties of predictions from parton distributions. 1: Experimental errors,” *Eur.Phys.J.*, vol. C28, pp. 455–473, 2003.
- [42] A. Martin, R. Roberts, W. Stirling, and R. Thorne, “Physical gluons and high $E(T)$ jets,” *Phys.Lett.*, vol. B604, pp. 61–68, 2004.
- [43] R. Thorne, “A Variable-flavor number scheme for NNLO,” *Phys.Rev.*, vol. D73, p. 054019, 2006.
- [44] R. Thorne and W. Tung, “PQCD Formulations with Heavy Quark Masses and Global Analysis,” 2008.
- [45] F. Olness and I. Schienbein, “Heavy Quarks: Lessons Learned from HERA and Tevatron,” *Nucl.Phys.Proc.Suppl.*, vol. 191, pp. 44–53, 2009.
- [46] M. Cacciari, M. Greco, and P. Nason, “The P(T) spectrum in heavy flavor hadroproduction,” *JHEP*, vol. 9805, p. 007, 1998.

- [47] S. Forte, E. Laenen, P. Nason, and J. Rojo, “Heavy quarks in deep-inelastic scattering,” *Nucl.Phys.*, vol. B834, pp. 116–162, 2010.
- [48] M. Buza, Y. Matiounine, J. Smith, and W. van Neerven, “Charm electroproduction viewed in the variable flavor number scheme versus fixed order perturbation theory,” *Eur.Phys.J.*, vol. C1, pp. 301–320, 1998.
- [49] M. Buza, Y. Matiounine, J. Smith, and W. van Neerven, “Comparison between the various descriptions for charm electroproduction and the HERA data,” *Phys.Lett.*, vol. B411, pp. 211–217, 1997.
- [50] S. Alekhin, J. Blumlein, S. Klein, and S. Moch, “The 3, 4, and 5-flavor NNLO Parton from Deep-Inelastic-Scattering Data and at Hadron Colliders,” *Phys.Rev.*, vol. D81, p. 014032, 2010.
- [51] J. Andersen *et al.*, “The SM and NLO Multileg Working Group: Summary report,” pp. 21–189, 2010.
- [52] M. Aivazis, F. I. Olness, and W.-K. Tung, “Leptoproduction of heavy quarks. 1. General formalism and kinematics of charged current and neutral current production processes,” *Phys.Rev.*, vol. D50, pp. 3085–3101, 1994.
- [53] T. Stavreva, F. Olness, I. Schienbein, T. Jezo, A. Kusina, *et al.*, “Heavy Quark Production in the ACOT Scheme beyond NLO,” *Acta Phys.Polon.*, vol. B43, pp. 1607–1622, 2012.
- [54] R. M. Barnett, “Evidence for New Quarks and New Currents,” *Phys.Rev.Lett.*, vol. 36, pp. 1163–1166, 1976.
- [55] R. D. Ball, V. Bertone, F. Cerutti, L. Del Debbio, S. Forte, *et al.*, “Impact of Heavy Quark Masses on Parton Distributions and LHC Phenomenology,” *Nucl.Phys.*, vol. B849, pp. 296–363, 2011.
- [56] R. D. Ball *et al.*, “Unbiased global determination of parton distributions and their uncertainties at NNLO and at LO,” *Nucl.Phys.*, vol. B855, pp. 153–221, 2012.
- [57] K. Chetyrkin, B. A. Kniehl, and M. Steinhauser, “Strong coupling constant with flavor thresholds at four loops in the $\overline{\text{MS}}$ scheme,” *Phys.Rev.Lett.*, vol. 79, pp. 2184–2187, 1997.
- [58] W. van Neerven and E. Zijlstra, “Order α_s^2 contributions to the deep inelastic Wilson coefficient,” *Phys.Lett.*, vol. B272, pp. 127–133, 1991.
- [59] E. Zijlstra and W. van Neerven, “Contribution of the second order gluonic Wilson coefficient to the deep inelastic structure function,” *Phys.Lett.*, vol. B273, pp. 476–482, 1991.
- [60] E. Zijlstra and W. van Neerven, “Order α_s^2 correction to the structure function $F_3(x, Q^2)$ in deep inelastic neutrino - hadron scattering,” *Phys.Lett.*, vol. B297, pp. 377–384, 1992.

- [61] E. Zijlstra and W. van Neerven, “Order α_s^2 QCD corrections to the deep inelastic proton structure functions $F_2(x, Q^2)$ and $F_L(x, Q^2)$,” *Nucl.Phys.*, vol. B383, pp. 525–574, 1992.
- [62] S. Moch, J. Vermaseren, and A. Vogt, “The Longitudinal structure function at the third order,” *Phys.Lett.*, vol. B606, pp. 123–129, 2005.
- [63] J. Vermaseren, A. Vogt, and S. Moch, “The Third-order QCD corrections to deep-inelastic scattering by photon exchange,” *Nucl.Phys.*, vol. B724, pp. 3–182, 2005.
- [64] E. Laenen, S. Riemersma, J. Smith, and W. van Neerven, “Complete $\mathcal{O}(\alpha_s^2)$ corrections to heavy flavor structure functions in electroproduction,” *Nucl.Phys.*, vol. B392, pp. 162–228, 1993.
- [65] M. Gluck, S. Kretzer, and E. Reya, “The Strange sea density and charm production in deep inelastic charged current processes,” *Phys.Lett.*, vol. B380, pp. 171–176, 1996.
- [66] A. Arbuzov, D. Y. Bardin, J. Blumlein, L. Kalinovskaya, and T. Riemann, “Hector 1.00: A Program for the calculation of QED, QCD and electroweak corrections to e p and lepton+- N deep inelastic neutral and charged current scattering,” *Comput.Phys.Commun.*, vol. 94, pp. 128–184, 1996.
- [67] M. Buza and W. van Neerven, “ $\mathcal{O}(\alpha_s^2)$ contributions to charm production in charged current deep inelastic lepton - hadron scattering,” *Nucl.Phys.*, vol. B500, pp. 301–324, 1997.
- [68] G. Corcella and A. D. Mitov, “Soft gluon resummation for heavy quark production in charged current deep inelastic scattering,” *Nucl.Phys.*, vol. B676, pp. 346–364, 2004.
- [69] R. D. Ball, L. Del Debbio, S. Forte, A. Guffanti, J. I. Latorre, *et al.*, “A first unbiased global NLO determination of parton distributions and their uncertainties,” *Nucl.Phys.*, vol. B838, pp. 136–206, 2010.
- [70] W. van Neerven and A. Vogt, “NNLO evolution of deep inelastic structure functions: The Nonsinglet case,” *Nucl.Phys.*, vol. B568, pp. 263–286, 2000.
- [71] M. Dittmar, S. Forte, A. Glazov, S. Moch, S. Alekhin, *et al.*, “Working Group I: Parton distributions: Summary report for the HERA LHC Workshop Proceedings,” 2005.
- [72] R. K. Ellis, W. J. Stirling, and B. R. Webber, *QCD and Collider Physics*. Cambridge University Press, 1996.
- [73] W. van Neerven and A. Vogt, “NNLO evolution of deep inelastic structure functions: The Singlet case,” *Nucl.Phys.*, vol. B588, pp. 345–373, 2000.
- [74] S. Larin, P. Nogueira, T. van Ritbergen, and J. Vermaseren, “The Three loop QCD calculation of the moments of deep inelastic structure functions,” *Nucl.Phys.*, vol. B492, pp. 338–378, 1997.

- [75] S. I. Alekhin and J. Blumlein, “Mellin representation for the heavy flavor contributions to deep inelastic structure functions,” *Phys.Lett.*, vol. B594, pp. 299–307, 2004.
- [76] OpenQCDrad, <http://www-zeuthen.desy.de/~alekhin/OPENQCDRAD>
- [77] S. Alekhin and S. Moch, “Heavy-quark deep-inelastic scattering with a running mass,” *Phys.Lett.*, vol. B699, pp. 345–353, 2011.
- [78] K. Chetyrkin and M. Steinhauser, “The Relation between the $\overline{\text{MS}}$ and the on-shell quark mass at order α_s^3 ,” *Nucl.Phys.*, vol. B573, pp. 617–651, 2000.
- [79] K. Chetyrkin and A. Retey, “Renormalization and running of quark mass and field in the regularization invariant and $\overline{\text{MS}}$ schemes at three loops and four loops,” *Nucl.Phys.*, vol. B583, pp. 3–34, 2000.
- [80] A. Vogt, “Efficient evolution of unpolarized and polarized parton distributions with QCD-PEGASUS,” *Comput.Phys.Commun.*, vol. 170, pp. 65–92, 2005.
- [81] K. Chetyrkin, J. H. Kuhn, and M. Steinhauser, “RunDec: A Mathematica package for running and decoupling of the strong coupling and quark masses,” *Comput.Phys.Commun.*, vol. 133, pp. 43–65, 2000.
- [82] G. P. Salam and J. Rojo, “A Higher Order Perturbative Parton Evolution Toolkit (HOPPET),” *Comput.Phys.Commun.*, vol. 180, pp. 120–156, 2009.
- [83] V. Bertone and J. Rojo, “Parton Distributions with the Combined HERA Charm Production Cross Sections,” 2012.
- [84] S. Forte, L. Garrido, J. I. Latorre, and A. Piccione, “Neural network parametrization of deep inelastic structure functions,” *JHEP*, vol. 0205, p. 062, 2002.
- [85] L. Del Debbio, S. Forte, J. I. Latorre, A. Piccione, and J. Rojo, “Neural network determination of parton distributions: The Nonsinglet case,” *JHEP*, vol. 0703, p. 039, 2007.
- [86] C. M. Bishop, *Neural Network for Pattern Recognition*. Clarendon Press - Oxford, 1995.
- [87] R. D. Ball *et al.*, “Fitting Parton Distribution Data with Multiplicative Normalization Uncertainties,” *JHEP*, vol. 1005, p. 075, 2010.
- [88] R. D. Ball *et al.*, “A Determination of parton distributions with faithful uncertainty estimation,” *Nucl.Phys.*, vol. B809, pp. 1–63, 2009.
- [89] R. D. Ball, S. Carrazza, L. Del Debbio, S. Forte, J. Gao, *et al.*, “Parton Distribution Benchmarking with LHC Data,” 2012.
- [90] Y. A. Kanev, “Application of neural networks and genetic algorithms in high-energy physics,” 1998.

-
- [91] R. D. Ball *et al.*, “Theoretical issues in PDF determination and associated uncertainties,” 2013.
- [92] F. Caola, S. Forte, and J. Rojo, “HERA data and DGLAP evolution: theory and phenomenology,” 2010. accepted for publication in Nucl. Phys. A.
- [93] F. Caola, S. Forte, and J. Rojo, “Deviations from NLO QCD evolution in inclusive HERA data,” *Phys. Lett.*, vol. B686, pp. 127–135, 2010.
- [94] G. Aad *et al.*, “Measurement of the inclusive W^\pm and Z/γ cross sections in the electron and muon decay channels in pp collisions at $\sqrt{s} = 7$ TeV with the ATLAS detector,” *Phys.Rev.*, vol. D85, p. 072004, 2012.
- [95] S. Chatrchyan *et al.*, “Measurement of the electron charge asymmetry in inclusive W production in pp collisions at $\sqrt{s} = 7$ TeV,” *Phys.Rev.Lett.*, vol. 109, p. 111806, 2012.
- [96] R. Aaij *et al.*, “Inclusive W and Z production in the forward region at $\sqrt{s} = 7$ TeV,” *JHEP*, vol. 1206, p. 058, 2012.
- [97] G. Aad *et al.*, “Measurement of inclusive jet and dijet production in pp collisions at $\sqrt{s} = 7$ TeV using the ATLAS detector,” *Phys.Rev.*, vol. D86, p. 014022, 2012.
- [98] M. Arneodo *et al.*, “Accurate measurement of $F_2(d)/F_2(p)$ and $R(d) - R(p)$,” *Nucl. Phys.*, vol. B487, pp. 3–26, 1997.
- [99] M. Arneodo *et al.*, “Measurement of the proton and deuteron structure functions, $F_2(p)$ and $F_2(d)$, and of the ratio σ_L/σ_T ,” *Nucl. Phys.*, vol. B483, pp. 3–43, 1997.
- [100] L. W. Whitlow, E. M. Riordan, S. Dasu, S. Rock, and A. Bodek, “Precise measurements of the proton and deuteron structure functions from a global analysis of the SLAC deep inelastic electron scattering cross-sections,” *Phys. Lett.*, vol. B282, pp. 475–482, 1992.
- [101] A. C. Benvenuti *et al.*, “A high statistics measurement of the proton structure functions $F_2(x, Q^2)$ and R from Deep Inelastic muon scattering at high Q^2 ,” *Phys. Lett.*, vol. B223, p. 485, 1989.
- [102] A. C. Benvenuti *et al.*, “A high statistics measurement of the deuteron structure functions $F_2(x, Q^2)$ and R from Deep Inelastic muon scattering at high Q^2 ,” *Phys. Lett.*, vol. B237, p. 592, 1990.
- [103] A. F. *et al.*, “Combined Measurement and QCD Analysis of the Inclusive ep Scattering Cross Sections at HERA,” 2009.
- [104] G. Onengut *et al.*, “Measurement of nucleon structure functions in neutrino scattering,” *Phys. Lett.*, vol. B632, pp. 65–75, 2006.
- [105] F. D. Aaron *et al.*, “Measurement of the Proton Structure Function F_L at Low x ,” *Phys. Lett.*, vol. B665, pp. 139–146, 2008.

- [106] M. Goncharov *et al.*, “Precise measurement of dimuon production cross-sections in $\nu/\mu Fe$ and $\bar{\nu}/\mu Fe$ deep inelastic scattering at the Tevatron,” *Phys. Rev.*, vol. D64, p. 112006, 2001.
- [107] D. A. Mason, “Measurement of the strange - antistrange asymmetry at NLO in QCD from NuTeV dimuon data,” FERMILAB-THESIS-2006-01.
- [108] S. Chekanov *et al.*, “Measurement of high Q^2 neutral current deep inelastic e^-p scattering cross sections with a longitudinally polarised electron beam at HERA,” *Eur. Phys. J.*, vol. C62, pp. 625–658, 2009.
- [109] S. Chekanov *et al.*, “Measurement of charged current deep inelastic scattering cross sections with a longitudinally polarised electron beam at HERA,” *Eur. Phys. J.*, vol. C61, pp. 223–235, 2009.
- [110] J. Breitweg *et al.*, “Measurement of $D^{*\pm}$ production and the charm contribution to F_2 in deep inelastic scattering at HERA,” *Eur. Phys. J.*, vol. C12, pp. 35–52, 2000.
- [111] S. Chekanov *et al.*, “Measurement of $D^{*\pm}$ production in deep inelastic $e^\pm p$ scattering at HERA,” *Phys. Rev.*, vol. D69, p. 012004, 2004.
- [112] S. Chekanov *et al.*, “Measurement of D^\pm and D_0 production in deep inelastic scattering using a lifetime tag at HERA,” *Eur. Phys. J.*, vol. C63, pp. 171–188, 2009.
- [113] S. Chekanov *et al.*, “Measurement of charm and beauty production in deep inelastic ep scattering from decays into muons at HERA,” *Eur. Phys. J.*, vol. C65, pp. 65–79, 2010.
- [114] C. Adloff *et al.*, “Measurement of $D^{*\pm}$ meson production and F_2^c in deep inelastic scattering at HERA,” *Phys. Lett.*, vol. B528, pp. 199–214, 2002.
- [115] F. D. Aaron *et al.*, “Measurement of the D^* Meson Production Cross Section and $F_2^{c\bar{c}}$, at High Q^2 , in ep Scattering at HERA,” *Phys. Lett.*, vol. B686, pp. 91–100, 2010.
- [116] F. D. Aaron *et al.*, “Measurement of the Charm and Beauty Structure Functions using the H1 Vertex Detector at HERA,” *Eur. Phys. J.*, vol. C65, pp. 89–109, 2010.
- [117] G. Moreno *et al.*, “Dimuon production in proton - copper collisions at $\sqrt{s} = 38.8$ GeV,” *Phys. Rev.*, vol. D43, pp. 2815–2836, 1991.
- [118] J. C. Webb *et al.*, “Absolute Drell-Yan dimuon cross sections in 800 GeV/ c pp and pd collisions,” 2003.
- [119] J. C. Webb, “Measurement of continuum dimuon production in 800 GeV/ c proton nucleon collisions,” 2003.
- [120] R. S. Towell *et al.*, “Improved measurement of the \bar{d}/\bar{u} asymmetry in the nucleon sea,” *Phys. Rev.*, vol. D64, p. 052002, 2001.

- [121] T. Aaltonen *et al.*, “Direct Measurement of the W Production Charge Asymmetry in $p\bar{p}$ Collisions at $\sqrt{s} = 1.96$ TeV,” *Phys. Rev. Lett.*, vol. 102, p. 181801, 2009.
- [122] V. M. Abazov *et al.*, “Measurement of the shape of the boson rapidity distribution for $p\bar{p} \rightarrow Z/\gamma^* \rightarrow e^+e^- + X$ events produced at \sqrt{s} of 1.96-TeV,” *Phys. Rev.*, vol. D76, p. 012003, 2007.
- [123] T. Aaltonen *et al.*, “Measurement of $d\sigma/dy$ of Drell-Yan e^+e^- pairs in the Z Mass Region from $p\bar{p}$ Collisions at $\sqrt{s} = 1.96$ TeV,” 2009.
- [124] A. Abulencia *et al.*, “Measurement of the Inclusive Jet Cross Section using the k_T algorithm in $p\bar{p}$ Collisions at $\sqrt{s} = 1.96$ TeV with the CDF II Detector,” *Phys. Rev.*, vol. D75, p. 092006, 2007.
- [125] V. M. Abazov *et al.*, “Measurement of the inclusive jet cross-section in $p\bar{p}$ collisions at $s^{91/2} = 1.96$ -TeV,” *Phys. Rev. Lett.*, vol. 101, p. 062001, 2008.
- [126] G. Altarelli, S. Forte, and G. Ridolfi, “On positivity of parton distributions,” *Nucl.Phys.*, vol. B534, pp. 277–296, 1998.
- [127] R. D. Ball *et al.*, “Precision determination of electroweak parameters and the strange content of the proton from neutrino deep-inelastic scattering,” *Nucl.Phys.*, vol. B823, pp. 195–233, 2009.
- [128] C. Anastasiou, L. J. Dixon, K. Melnikov, and F. Petriello, “High precision QCD at hadron colliders: Electroweak gauge boson rapidity distributions at NNLO,” *Phys.Rev.*, vol. D69, p. 094008, 2004.
- [129] N. Kidonakis and J. Owens, “Effects of higher order threshold corrections in high $E(T)$ jet production,” *Phys.Rev.*, vol. D63, p. 054019, 2001.
- [130] T. Kluge, K. Rabbertz, and M. Wobisch, “FastNLO: Fast pQCD calculations for PDF fits,” pp. 483–486, 2006.
- [131] M. Wobisch, D. Britzger, T. Kluge, K. Rabbertz, and F. Stober, “Theory-Data Comparisons for Jet Measurements in Hadron-Induced Processes,” 2011.
- [132] “Review of particle physics,” *Phys. Rev. D*, vol. 86, p. 010001, Jul 2012.
- [133] S. Lionetti, R. D. Ball, V. Bertone, F. Cerutti, L. Del Debbio, *et al.*, “Precision determination of α_s using an unbiased global NLO parton set,” *Phys.Lett.*, vol. B701, pp. 346–352, 2011.
- [134] R. D. Ball, V. Bertone, L. Del Debbio, S. Forte, A. Guffanti, *et al.*, “Precision NNLO determination of $\alpha_s(M_Z)$ using an unbiased global parton set,” *Phys.Lett.*, vol. B707, pp. 66–71, 2012.
- [135] F. Demartin, S. Forte, E. Mariani, J. Rojo, and A. Vicini, “The impact of PDF and α_s uncertainties on Higgs Production in gluon fusion at hadron colliders,” *Phys.Rev.*, vol. D82, p. 014002, 2010.

- [136] J. M. Campbell, J. Huston, and W. Stirling, “Hard Interactions of Quarks and Gluons: A Primer for LHC Physics,” *Rept.Prog.Phys.*, vol. 70, p. 89, 2007.
- [137] M. Czakon, P. Fiedler, and A. Mitov, “The total top quark pair production cross-section at hadron colliders through $\mathcal{O}(\alpha_s^4)$,” 2013.
- [138] C. Anastasiou, S. Buehler, F. Herzog, and A. Lazopoulos, “Total cross-section for Higgs boson hadroproduction with anomalous Standard Model interactions,” *JHEP*, vol. 1112, p. 058, 2011.
- [139] “Inclusive w/z cross section at 8 tev,” Tech. Rep. CMS-PAS-SMP-12-011, CERN, Geneva, 2012.
- [140] “Top pair cross section in dileptons,” Tech. Rep. CMS-PAS-TOP-12-007, CERN, Geneva, 2012.
- [141] “Measurement of the top quark pair production cross section in the single-lepton channel with atlas in proton-proton collisions at 8 tev using kinematic fits with b-tagging,” Tech. Rep. ATLAS-CONF-2012-149, CERN, Geneva, Nov 2012.
- [142] M. Czakon, M. L. Mangano, A. Mitov, and J. Rojo, “Constraints on the gluon PDF from top quark pair production at hadron colliders,” 2013.
- [143] M. Abramowitz and I. A. Stegun, *Handbook of mathematical functions*. National Bureau of Standards Applied Mathematics Series - 55, 1964.
- [144] M. Buza, Y. Matiounine, J. Smith, R. Migneron, and W. van Neerven, “Heavy quark coefficient functions at asymptotic values $Q^2 \gg m_H^2$,” *Nucl.Phys.*, vol. B472, pp. 611–658, 1996.
- [145] J. Blumlein and S. Kurth, “Harmonic sums and Mellin transforms up to two loop order,” *Phys.Rev.*, vol. D60, p. 014018, 1999.
- [146] J. Blumlein and S. Kurth, “On the Mellin transform of the coefficient functions of $F_L(x, Q^2)$,” 1997.
- [147] T. Gottschalk, “Chromodynamic corrections to neutrino production of heavy quarks,” *Phys.Rev.*, vol. D23, p. 56, 1981.